7-1-2008

Flow field analysis in an expanding healthy and emphysematous alveolar model using particle image velocimetry

Jessica Oakes

Recommended Citation

Oakes, Jessica, "Flow field analysis in an expanding healthy and emphysematous alveolar model using particle image velocimetry" (2008). Thesis. Rochester Institute of Technology. Accessed from

Flow Field Analysis in an Expanding Healthy and Emphysematous Alveolar Model Using Particle Image Velocimetry

by

Jessica Oakes

A Thesis Submitted in Partial Fulfillment of the Requirement for the

Master of Science
In
Mechanical Engineering

Approved by:

Dr. Risa Robinson
Department of Mechanical Engineering ______________________________
(Thesis Advisor)

Dr. Steven Day
Department of Mechanical Engineering ______________________________

Dr. Steven Weinstein
Department of Mechanical Engineering ______________________________

Dr. Wayne Walter
Department of Mechanical Engineering ______________________________
(Department Representative)

Department of Mechanical Engineering
Rochester Institute of Technology
July 2008

Permission for Duplication

Permission Granted

Flow Field Analysis in an Expanding Healthy and Emphysematous Alveolar Model Using Particle Image Velocimetry

I, Jessica Oakes, herby grant permission to the Wallace Library of the Rochester Institute of Technology to reproduce my thesis in whole or part. Any reproduction will not be for commercial use or profit.

Date: _______________ Signature of Author: ______________________

Jessica Oakes
7914 Ridge Rd
Gasport, NY 14067
Email: jessica.m.oakes@gmail.com
Phone: 716-870-5273

Acknowledgements

There are numerous people that have helped me in the creation in this thesis. To them, I owe my ultimate thanks and appreciation, for without their support and knowledge I would not have been able to complete this research.

I would first like to thank my family and friends. My family, especially my parents, David and Marie, had been supportive throughout the entire process. Since I was a child, they have always helped me to achieve my dreams and goals. Their dedication to me and my school work had helped me to be successful. Without them, I would never have been able to achieve as much as I have.

I would also like to thank my adviser, Dr. Robinson. Her encouragement helped me to work to my fullest potential. Dr. Robinson continuously guided me to completion, helping to me keep my goals in mind. Her knowledge of the subject matter, as well as her expertise in writing, aided me in producing a thesis that I am proud of.

My committee members, Dr. Day and Dr. Weinstein, have helped me numerous times throughout the two years I have been working on this thesis. Without their expertise, I would not have been able to be successful. I also owe thanks to Dave Hathaway, Steven Kosciol and Rob Kraynik for their help in the machine shop. I thank Bill Finch for always helping me, at a moments notice, with my computer and server needs. Huge thanks to Diane Selleck for always patiently answering my questions. Finally, I would like to thank all of my peers, for their help in answering my questions, being supportive, and helping me through some of the most difficult times.

Abstract

Particle deposition in the acinus region of the lung is a significant area of interest, because particles can potentially travel into the bloodstream through the capillaries in the lung. Drugs, in the form of aerosols, small particulates in a volume of air, may be delivered through the respiratory system. Also, toxic, airborne, particles could enter the body through the pulmonary capillaries in the acinus region of the lung. In order to accurately predict particle deposition, the aspects that influence deposition needs to be understood.

Many physiological features may influence flow and particle deposition in the lung; the geometry of the acinus, expansion and contraction of the alveolar walls due to breathing mechanics, heterogeneities in the lung, breathing flow rate, and the number of breaths. In literature, streamlines and pathlines have been examined, both experimentally and computationally, in models representing the alveolar region of the lung. Some of these studies suggest the presence of irreversible flow, which would significantly influence particle deposition. However, none of these models incorporated all significant features: non-symmetric, three dimensional, expanding geometry. Therefore, flow mechanics, behind particle deposition, in the alveolar region are not well understood. Furthermore, lung disease influences the physiological factors that impact particle deposition. Emphysema physically changes the structure of the alveolar region of the lung. How particle deposition changes with emphysema is not fully understood.

In this work, two different alveolar geometries were examined using Particle Image Velocimetry (PIV). The first model represented a healthy alveolar sac, while the second model represented an emphysematous alveolar sac. The same, realistic flow rate was used for both models, which allowed for the fluid flow to be examined as only a function of geometry. The PIV technique was validated by comparing to CFD results, using a simple balloon geometry. Pathlines were plotted in the models in order to examine the fluid flow with respect to time. The fluid was examined, by use of streamlines and pthalines, at the entrance of the alveolar sacs and in areas of high probability for irreversible flow. It was found that the fluid flow inside both alveolar sac geometries was completely reversible, and therefore no mixing was taking place. The comparison between the healthy and emphysematic alveolar sac models showed that the pathlines in health traveled closer to the alveolar walls. Particle deposition by Brownian Diffusion was estimated for particle diameter range of 0.1 μm to 0.01 μm. For the pathlines that began at the duct entrance, the pathlines came approximately 1.5 times closer to the wall in the healthy case when compared to emphysema. Because the pathline traveled closer to the alveolar walls, the particle diffusion was greater in the healthy then emphysema. In the healthy geometry particles with a diameter less then 0.02 μm were estimated to diffuse to all of the alveolar walls within a 5 second time frame, where in emphysema 7 seconds would be needed. It was also determined that if a particle diffuses off of the original streamline, it will remain in the alveolar sac, therefore allowing it to deposit in later breaths.

Table of Contents

Permission for Duplication……..……….……………………………………………ii

Acknowledgements……..…..………………………………………………………iv

Abstract…………..……………………………………..………………………...v

Table of Contents…….……………………………………………………...….vii

List of Figures……………………………………………………………………....xi

Chapter 1: Introduction and Background Information……………...……………..1

1.1 Structure and Function of the Respiratory Tract………..……..…………...1
    1.1.1 Anatomy……………………………………………..…..………..1
        1.1.1.1 Lung Overview…………………………..………...1
        1.1.1.2 Structure of the Acinus…………………..…..…….…..3
    1.1.2 Mechanics of Breathing………………………………..………..4
        1.1.2.1 Flow Rate…………………………………..………..5
        1.1.2.2 Volumes…………………………………..……..…5
1.2 Emphysema……………………………………………………..…....6
    1.2.1 Changes in Structure of the Acinus……………………..………6
    1.2.2 Changes in Breathing Patterns…………………………..………7
    1.2.3 Changes in Function of Gas Exchange in Acinus………..……..8
1.3 Particle Deposition……………………………………………..……9
    1.3.1 Importance of Studying Particle Deposition……………..…..9
    1.3.2 Diffusion and Particle Deposition in Alveoli……………..……10

Chapter 2: Literature and Preliminary Work Relevant to Mixing……….........…12

2.1 Definition of Mixing………………………………………………….…12
2.2 Literature on Mixing in the Lung……………………………………….12
    2.2.1 Numerical Alveolar Models…………………………………....12
        2.2.1.1 Fluid Flow Characteristics…………………………...13
        2.2.1.2 Particle Deposition……………………………………...14
    2.2.2 Physical Alveolar Mixing Experiments…………………………..19
    2.2.3 Animal Experiments………………………………………...…23
    2.2.4 Human Experiments……………………………………………24
        2.2.4.1 Findings in Health……………………………………...26
        2.2.4.2 Findings in Emphysema………………………………..28
2.3 Preliminary Research Relevant to Alveolar Mixing………………….…29
2.4 Gaps in Alveolar Particle Deposition Research…………………………31
    2.4.1 Geometry………………………………………………………….31
    2.4.2 Flow Rates……………………………………………...……32
    2.4.3 Disease Presence…………………………………………….....33
    2.4.4 Fluid Mixing Influence on Particle Deposition………………..…33

2.4.5 Alveolar Wall Structure and Material Properties…..……………34
2.5 Thesis Work Statement……………………………………….…………34

Chapter 3: Model Geometry…………………………………………….…………..35
3.1 CAD Design……………………………………………………………...35
3.1.1 Balloon Model Geometry……………………………………......35
3.1.2 Healthy Alveolar Sac Model Geometry……………………………36
3.1.3 Emphysemic Alveolar Sac Model Geometry……………………...39
3.2 Manufacturing Procedure and Material…………………………………40
3.2.1 Male Aluminum Mold……………………………………………..40
3.2.2 Compliant Hollow Cast…………………………………………....41
3.3 Measurement Analysis…………………………………………………..44
3.3.1 Effective Airway Diameter Analysis………………………………44
3.3.2 Depth to Mouth Diameter Analysis………………………………46
3.3.3 Comparison between Large Scale CAD Model and Aluminum Cast………………………………………………….……..49

Chapter 4: Model Fluid Dynamics……………………………………………..…...51
4.1 Scaling up the Flow Parameters……………………………….………....51
4.1.1 Theory……………………………………………………….…….…51
4.1.2 In Vivo Reynolds and Womersley Numbers……………….……..55
4.1.3 Possible Experimental Parameters………………………………...56
4.1.3.1 Influence of Index Matching Fluid……………..……….…...57
4.1.3.2 Influence of Cycle Time……………………………………..58
4.1.3.3 Final Experimental Flow Parameters……………..…….……59
4.2 Obtaining the Breathing Curve……………………………………….……62
4.2.1 Spirometer Measurement…………………………………………63
4.2.2 Noise Smoothing……………………………………………………64
4.2.3 Inlet Flow Condition for Each Model……………………………66
4.2.4 Validation of Curve…………………………………………………69
4.3 Experimental Reynolds and Womersley Numbers……………….…..……70

Chapter 5: Experimental Setup……………………………………………….…..….73
5.1 Test Rig and Data Acquisition……………………………………….…...73
5.1.1 New Setup Procedure for the Test Rig……………………………74
5.1.2 Pressure Sensor for Flow Measurement…………………………..77
5.1.3 Syringe Pump……………………………………………………...81
5.1.4 Labview Interface…………………………………………………81
5.2 PIV System………………………………………………………………...84
5.2.1Overall Experimental Setup……………………………………...84
5.2.2 High Speed Camera………………………………………………..85
5.2.2.1 Frame Rate Analysis…………………………………………...88
5.2.3 Laser………………………………………………………………..89
5.2.4 Fluid………………………………………………………………..90
5.2.5 Particles………………………………………………………….…91
5.2.5.1 Particle Buoyancy……………………………………………...91

5.2.5.2 Particle Size……………………………………………...……92
5.2.5.3 Particle Mixing Ratio……………………….……………95

Chapter 6: PIV Analysis Techniques………………………………………………97

6.1 Vector Analysis………………………………………….…………97
6.1.1 Cross Correlation Theory………………………………………97
6.1.2 Image Analysis Error……………………………………...100
6.1.3 Analysis Software……………………………………………103
6.2 Experiment Specific Image Analysis Parameters………………………103
6.3 Vector Validation and Post Processing………………………………….105
6.4 Frame and Time Alignment…………………………………………..106
6.5 Calculation of Streamlines and Pathlines………………………………109

Chapter 7: Experimental Validation…………………………………………………110

7.1 CFD Model………………………………………………………………110
7.1.1 Boundary Conditions and Fluid/Material Properties…………….110
7.1.2 Mesh and Tolerance Convergence Analysis……………………..112
7.2 Model Deformation Analysis……………………………………………116
7.3 Fluid Flow Results………………………………………………………122
7.3.1 Velocity Profile Plots…………………………………………..122
7.3.2 Pathlines………………………………………………………..126
7.4 Conclusion………………………………………………….....…132

Chapter 8: Alveolar Sac PIV Results………………………………………………...133

8.1 Results of Healthy Alveolar Sac………………………………………133
8.1.1 Pathlines Beginning at Duct Entrance……………………………135
8.1.1.1 Time Resolution Analysis………………………………135
8.1.1.2 Pathline Location at End of Inhale……………………...137
8.1.1.3 Irreversible Flow Analysis………………………………139
8.1.2 Pathlines and Streamlines Inside Top Two Alveoli………………142
8.1.2.1 Irreversible Flow Analysis………………………………143
8.1.2.2 Pathline Location at End of Inhale………………………149
8.1.3 Pathlines at the Bottom of the Alveolar Sac……………………...150
8.2 Pathline Results of Emphysema Alveolar Sac…………………………153
8.2.1 Pathlines Beginning at the Duct Entrance………………………..154
8.2.2 Pathlines Inside Top Two Alveoli………………………………..157
8.2.2.1 Irreversible Flow Analysis………………………………158
8.2.2.2 Pathline Location at End of Inhale………………………159
8.3 Particle Diffusion………………………………………………………160
8.3.1 Diffusion in Healthy Alveolar Sac………………………………..162
8.3.2 Diffusion in Emphysematic Alveolar Sac………………………...166
8.4 Comparison Between Healthy and Emphysema Alveolar Sacs………..169

Chapter 9: Discussion………………………………………………………………173

9.1 Comparison to Literature………………………………………………173
9.2 Limitations of Work……………………………………………………175
9.3 Future Work……………………………………………………………180

9.4 Summary and Conclusion……………………………………………181

References…………………………………………………………………….184

Appendix……………………………………………………………………….187
Appendix A: Emphysema Report……………………………………………………188
Appendix B: Matlab Program: Image Recognition and Definition……………….206

Figures

Figure 1.1: Lung Lobe Location (Marieb and Hoehn, 2007)…………………….………2

Figure 1.2: Lung Generation Definitions (Weibel, 1965)……………………..……….2

Figure 1.3: Respiratory Bronchioles, Alveolar Duct, Alveolar Sac and Alveoli Definitions (Marieb and Hoehn, 2007)………..…………… ………………………………..…3

Figure 1.4: Scanning Elector Microscope image of the alveolar duct. A is an alveolus, S is the alveolar septa, D is the alveolar duct and PA is a small pulmonary artery (Weibel, 1998)………………………………………………………………………………4

Figure 1.5: Example of Flow Rate Curve (Levitzky, 2003)…………………………....5

Figure 1.6: Lung Volume (Beachey, 1998)……………………………………………5

Figure 1.7: Acinus Region of the healthy lung (A) and a lung with emphysema (B) (Grippi, 1995)……………………………………………………………………….6

Figure 1.8: Excised Emphysema Lung (Greaves and Colebatch, 1980)………………….7

Figure 1.9: TLC as a Function of Elastic Recoil Pressure in Normal and Emphysema (Grippe, 1995)………………………………………………………………………..8

Figure 1.10: Aerosol Definition Based on Particle Size (Hinds, 1999)…………………..9

Figure 2.1: Flow through a Three Dimensional, Axial Symmetric, Alveolar Model at a Flow Rate Ratio of 0.008 (A), 0.016 (B) and 0.15 (C) (Tsuda et al.,1995)……………...13

Figure 2.2: Flow Through a Three Dimensional, Axial Symmetric Model based on the Half Angle of 60 degrees (A), 75 degrees (B) and 90 degrees (C) (Tsuda et al., 1995)...14

Figure 2.3: Stationary, Three Dimensional, Alveolar Model Subject to Different Sized Particles (Tsuda et al., 1994)…………………………………………………………15

Figure 2.4: Particle Concentration Results as a Function of Acinus Generation for Moving and Rigid Walls (Haber et al., 2003)…………………………………………15

Figure 2.5: Particle Deposition Based on Particle Size, Deposition Forces, Tidal Volumes and Flow Rate at the Trachea (Choi and Kim, 2007)……………………………………16

Figure 2.6: Fluid, Structure, Interaction Numerical Model Created by Dailey and Ghadiali (2007)………………………………………………………………………………….17

Figure 2.7: Particle Impaction Time for Diffusion and Sedimentation for Different Sized Particles (Dailey and Ghadiali, 2007)…………………………………………………18

Figure 2.8: Percent of Particle Deposition Based on Different Sized Particles for Normal and Emphysematous Lungs (Strum and Hofmann, 2004)……………………………….19

Figure 2.9: Tsuda et al. (1999). Tracer die in T-shaped model with Tidal volume to duct volume of 2. Swirls become more complex as cycle number increases………………..20

Figure 2.10: Streamlines in Stationary Alveolar Duct, with Depth to Mouth Diameter Ratios of 0.5 (A) and 0.67 (B) (Karl et al., 2004)……………………………………..21

Figure 2.11: Prediction of Alveolar Recirculation for Different Flow Rates (Tippe and Tsuda, 1999)………………………………………………………………………..22

Figure 2.12: Fluid Pattern in Cast Rat Lung (Tsuda et al., 2002)………………………..23

Figure 2.13: Mode shift for Aerosol Bolus Experimentation (Brand et al., 1997)……...25

Figure 2.14: Streamlines at the End of Inhale for a Change in Alveolus Volume of 1.48e-8 ml……………………………………………………………………………………29

Figure 2.15: Irreversible Pathlines for a Change in Alveolus Volume of 1.48e-8 ml…...30

Figure 3.1: Balloon Model CAD Dimensions…………………………………….....36

Figure 3.2: Definition of Alveolar Duct Diameter and Alveolar Sac Length…………....36

Figure 3.3: Alveolus Depth, Radius and Mouth Diameter Definitions………………….…37

Figure 3.4: Healthy Alveolar Sac CAD Model…………………………………..……38

Figure 3.5: Emphysemic Alveolar Sac CAD Model………………………………..……39

Figure 3.6: Schematic of the Manufacturing Process (Senior Design, 2006 – 2007)…...40

Figure 3.7 Healthy Alveolar Sac Aluminum Cast…………………………………....40

Figure 3.8: Emphysemic Alveolar Sac Aluminum Cast…………………………………41

Figure 3.9: Alveolar Sac Aluminum Cast (Areas of potential material build up are outlined……………………………………………………………………………..43

Figure 3.10: Healthy Alveolar Sac PIV Images with Problems Due to Material Build Up Highlighted………………………………………………………………………44

Figure 3.11: Different Ways to Measure Effective Airway Diameter……….……….45

Figure 3.12: Healthy Alveolar Sac CAD Model. A). Alveolus Depth (D) to Mouth Diameter (MD) Locations. B). Row Location………………………………………..46

Figure 3.13: Emphysematic Alveolar Sac CAD Model. A). Alveoli Depth (D) to Mouth Diameter (MD) Locations. B). Row Location………………………………………...47

Figure 3.14: Depth to Mouth Diameter Analysis. Comparison between Alveolar Sac CAD and Published Values…...……………………………………………………49

Figure 4.1: Example How Time and Duct Diameter was Read off Graph. Figure shown is for a Womersley number of 0.039…………………………………………………59

Figure 4.2: Reynolds Number as a Function of Time and Duct Diameter………………61

Figure 4.3: Womersley Number as a Function of Time and Duct Diameter…………….61

Figure 4.4: Flow Rate as a Function of Time and Duct Diameter……………………….62

Figure 4.5: Flow Rate Curve from Spirometer Obtained in the Current Work's Laboratory……………………………………………………………………………….63

Figure 4.6: Flow Rate versus Time Step Data Defined from Matlab Program…….……63

Figure 4.7: Non-Dimensional Inhale with Curve Fit……………………………………64

Figure 4.8: Non-Dimensional Exhale with Curve Fit……………………………………65

Figure 4.9: Volume versus Time for Balloon Model…………………………………….67

Figure 4.10: Volume versus Time for PIV Experimental Healthy Alveolar Sac………..67

Figure 4.10: Volume versus Time for PIV Experimental Healthy Alveolar Sac………..67

Figure 4.12: Flow Rate versus Time for Balloon Model………………………………..68

Figure 4.13: Flow Rate versus Time for PIV Experimental Healthy Alveolar Sac……..68

Figure 4.14: Flow Rate versus Time for PIV Experimental Emphysema Alveolar Sac…69

Figure 4.15: In Vivo Sized Flow Rate Curve Used for Validation of Inhale and Exhale Time Ratio……………………………………………………………………………….70

Figure 4.15: Unsteady Reynolds Number for Experimental Balloon Model……………71

Figure 4.16: Unsteady Reynolds Number for Experimental Healthy Alveolar Sac Model...71

Figure 4.17: Unsteady Reynolds Number for Experimental Emphysemic Alveolar Sac Model…………………………………………………………………………………71

Figure 5.1: Test Rig………………………….…………………………………………..74

Figure 5.2: Model Attachment…………………………………………………………..75

Figure 5.3: Housing Chamber……………………………………………………………76

Figure 5.4: Pressure Sensor………………………………………………………………77

Figure 5.5: Pressure Sensor Graph Used for Calibration………………………………..78

Figure 5.6: Labview Block Diagram: Pressure Sensor Calibration Location……………78

Figure 5.7: Linear Change in Volume Graph with Pause. Input and Pressure Sensor Output is Presented. Graph used for Pressure Sensor Analysis…………………………79

Figure 5.8: Realistic Volume Curve, With Pauses. Used for Comparison between Input and Output for Pressure Sensor Analysis………………………………………………..80

Figure 5.9: Realistic Volume Curve, Without Pauses. Used for Comparison between Input and Output for Pressure Sensor Analysis…………………………………………80

Figure 5.10: Labview Block Diagram: Pump Calibration………………………………81

Figure 5.11: Labview User Interface……………………………………………………82

Figure 5.12: Wave Form Definition Section of the Labview Interface…………………82

Figure 5.13: Specific Model Parameter Section of the Labview Interface……………...83

Figure 5.14: Measurement Output Section of the Labview Interface…………………...84

Figure 5.15: Experimental Setup………………………………………………………..85

Figure 5.16: Camera Setup………………………………………………………………87

Figure 5.17: Optical Chopper Image…………………………………………………….89

Figure 5.18: Picture of the LSG…………………………………………………………90

Figure 5.19: Forces Acting on a Fluid Particle………………………………………..91

Figure 5.20: Relationship for Diameter of Particle on Image and Magnification……….94

Figure 5.21: Particles on Image…………………………………………………….94

Figure 6.1: Diagram of Two Images Segmented into Interrogation Regions……………98

Figure 6.2: Definition of Coordinate System and Light Intensity for Interrogation Regions Separated by a Known Δt………………………………………………………..98

Figure 6.3: Example of Cross Correlation Plane. S_D is the displacement vector (Keane and Adrian (1992)……………………………………………………………….99

Figure 6.4: Implementation of cross-correlation using FFT (Raffel et al., 1998)……..100

Figure 6.5: Bias Error Diagram Due to Peak Locking (Raffel et al., 1998)………….....101

Figure 6.6: RMS Error for Particle Displacements as a Function of the Particle Diameter (Raffel et al., 1998)…………………………………………………………..102

Figure 6.7: Definition of Processing Mask Dotted Line. Healthy Alveolar Sac Model, Light Intensity at Top of Model……………………………………………………...103

Figure 6.8: Example of the Output Voltage versus Time Graph for the Camera………104

Figure 6.9: Example of Change in Volume Versus Time Graph Outputted from Labview. Figure Used in Location of Cycle Begin Time…………………………………………108

Figure 6.10: Streamline and Pathline Example………………………………………109

Figure 7.1: Fluid, Material (A), and Boundary Condition (B) Locations on CFD Balloon Model…………………………………………………………..…………………111

Figure 7.2: Mesh (A) and Location of Velocity Profile (B) of CFD Balloon Model…113

Figure 7.3: Mesh Size Convergence for CFD Balloon Model……………….………..114

Figure 7.4: Mesh Size Convergence for CFD Balloon Model: Focused on High Speed Area……………………………………………………………………………………114

Figure 7.5: Absolute Tolerance Convergence for CFD Balloon Model………………115

Figure 7.6: Absolute Tolerance Convergence for CFD Balloon Model: Focused on High Speed Areas……………………………………………………………………………116

Figure 7.7: PIV Image (A) and CFD (B) Dimension Locations. All dimensions are in mm…………………………………………………………………………………...117

Figure 7.8: Model Deformation Measurement Locations………………………………118

Figure 7.9: 3 Pixel Errors in Hollow Cast Measurement Technique…………………...119

Figure 7.10: Model Deformation Analysis between CFD and PIV for Measurements 1, 2 and 3……………………………………………………………………………………120

Figure 7.11: Model Deformation Analysis between CFD and PIV for Measurements 5 and 6……………………………………………………………………………………120

Figure 7.12: Model Deformation Analysis between CFD and PIV for Measurement 4.121

Figure 7.13: Comparison of Fillet Area of Hollow Cast (A) and CFD Model (B)…….121

Figure 7.14: Balloon Velocity Profile Plot for Maximum Velocity Magnitude at Inhale…………………………………………………………………………………124

Figure 7.15: Balloon Velocity Profile Plot for High Acceleration at Inhale…………...125

Figure 7.16: Balloon Velocity Profile Plot for Maximum Velocity at Exhale…………125

Figure 7.17: Balloon Velocity Profile Plot for Maximum Velocity at Exhale…………126

Figure 7.18: Location of Each Time Step for Balloon Pathline Analysis……………..127

Figure 7.19: Pathlines in PIV Balloon Model for 1st Breathing Cycle………………...129

Figure 7.20: Pathlines in PIV Balloon Model for 2nd Breathing Cycle………………...129

Figure 7.21: Pathlines in PIV Balloon Model for 3rd Breathing Cycle…………………130

Figure 7.22: CFD Pathlines Results…………………………………………………….130

Figure 8.1: Coordinates of Areas of Interest in the Healthy Alveolar Sac. All dimensions are in mm……………………………………………………………………………….134

Figure 8.3: Healthy Alveolar Sac Time Step. Areas highlighted where a separation time of 0.1 seconds was used. All other areas a time separation of 0.2 seconds was used…136

Figure 8.4: Pathlines for Healthy Alveolar Sac for 1st Breathing Cycle……………….138

Figure 8.5: Pathlines for Healthy Alveolar Sac for 2nd Breathing Cycle……………...138

Figure 8.6: Pathlines for Healthy Alveolar Sac for 3rd Breathing Cycle…………….139

Figure 8.7: Pathlines Beginning at Exhale at a position of -31.97 mm, -1 mm from the Average Distance Traveled by the Pathline at the End of Exhale……………………141

Figure 8.8: Pathlines Beginning at Exhale at a position of -31.97 mm, +1 mm from the Average Distance Traveled by the Pathline at the End of Exhale…………………….142

Figure 8.9: Streamlines of Healthy Alveolar Sac at 1.2 Seconds……………………..143

Figure 8.10: Pathlines for Three Iterations of the First Cycle in the Healthy Alveolar Sac for the Left Alveolus (A) and the Right Alveolus (B)………………………………...144

Figure 8.11: Pathline of Neutrally Buoyant Particle Tracked with Image J over a Breathing Cycle…………………………………………………………………..145

Figure 8.12: Pathline Tracked Using PIV Vector Analysis Technique over a Breathing Cycle…………………………………………………………………………………146

Figure 8.13: Pathlines in Healthy Left Alveolus for First Cycle (A), Second Cycle (B) and Third Cycle (C)……………………………………………………………….149

Figure 8.14: Pathlines in Healthy Right Alveolus for First Cycle (A), Second Cycle (B) and Third Cycle (C)……………………………………………………………….150

Figure 8.15: Pathlines in the Bottom Section of the Healthy Alveolar Sac……………151

Figure 8.16: Pathline of Neutrally Buoyant Particle Tracked with Particle Tracking Technique Using Image J (A) and Pathline using PIV Vector Analysis Technique (B)……………………………………………………………………………………152

Figure 8.17: Coordinates of Emphysema Alveolar Sac. All dimensions are in mm…..153

Figure 8.18: Pathlines for Emphysematic Alveolar Sac for 1st Breathing Cycle……….155

Figure 8.19: Pathlines for Emphysematic Alveolar Sac for 2nd Breathing Cycle……..156

Figure 8.20: Pathlines for Emphysematic Alveolar Sac for 3rd Breathing Cycle……...154

Figure 8.21: Pathlines of Three Cycles in the Emphysematic Alveolar Sac for the Left Alveolus (A) and the Right Alveolus (B)……………………………………………158

Figure 8.22: Pathlines in Emphysematic Left Alveolus for First Cycle (A), Second Cycle (B) and Third Cycle (C)…………………………………………………………..159

Figure 8.23: Pathlines in Emphysematic Right Alveolus for First Cycle (A), Second Cycle (B) and Third Cycle (C)……………………………………………………….159

Figure 8.24: Healthy Alveolar Sac Diffusion Time Using Distance from Pathlines Location at the End of Inhale to the Closest Radial Alveolar Wall for Pathlines Beginning at Alveolar Duct……………………………………………………………..165

Figure 8.25: Healthy Alveolar Sac Diffusion Time Using Distance from Pathlines Location at the End of Inhale to the Closest Radial Alveolar Wall for Pathlines Beginning Inside Top Two Alveoli………………………………………………………...165

Figure 8.26: Emphysematic Alveolar Sac Diffusion Time to Closest Alveolar Wall for Top Pathlines………………………………………………………………..168

Figure 8.27: Emphysematic Alveolar Sac Diffusion Time to Closest Alveolar Wall for Pathlines Inside Top Alveoli……………………………………………………...168

Figure 8.28: Theoretical Brownian Diffusion Distance for Particle Size and Time……172

Chapter 1

Introduction and Background Information

1.1 Structure and Function of the Respiratory Tract

The respiratory system consists of the lungs, chest wall, and the nervous system that controls the muscles for respiration. The diaphragm, the intercostals muscles, the abdominal muscles, and the rib cage are all a part of the chest wall (Levitzky, 2003). There are several functions of the respiratory system, which includes the following; gas exchange, acid-base balance, pulmonary defense and metabolism, the management of bioactive materials, and phonation (Levitzky, 2003).

1.1.1 Anatomy

1.1.1.1 Lung Overview

The main function of the lung is to provide gas exchange. The gas exchange occurs because the blood that is pumped through the body becomes deoxygenated and carbon dioxide rich. The venous blood is pumped into the pulmonary capillaries by the right ventricle. Oxygen, which is within the air that is breathed in, exchanges with the carbon dioxide inside the blood. The oxygen rich blood then flows through the body and supplies the various tissues with oxygen. The carbon dioxide rich air is exhaled out of the body.

The human body contains two lungs. The left lung consist of two lobes and the right side consists of three. Figure 1.1 shows the overall location of the different lobes in the lung. Both lungs are connected to the trachea by the bronchi. The lungs can be separated into two categories, the conducting zones and the transitional and respiratory zones. The conducting zones are responsible for transmitting the air that is breathed in down to the respiratory zone. The respiratory zone is the where the gas exchange takes place.

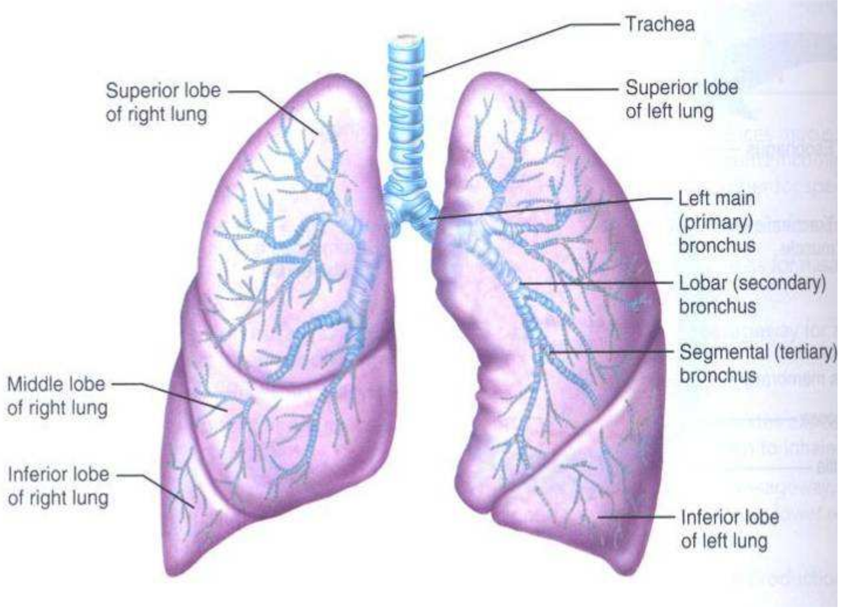

Figure 1.1: Lung Lobe Location (Marieb and Hoehn, 2007).

The lung is described based on generations. The lung consists of twenty three generations; beginning with the trachea and ending with the alveolar sac, as shown Figure 1.2.

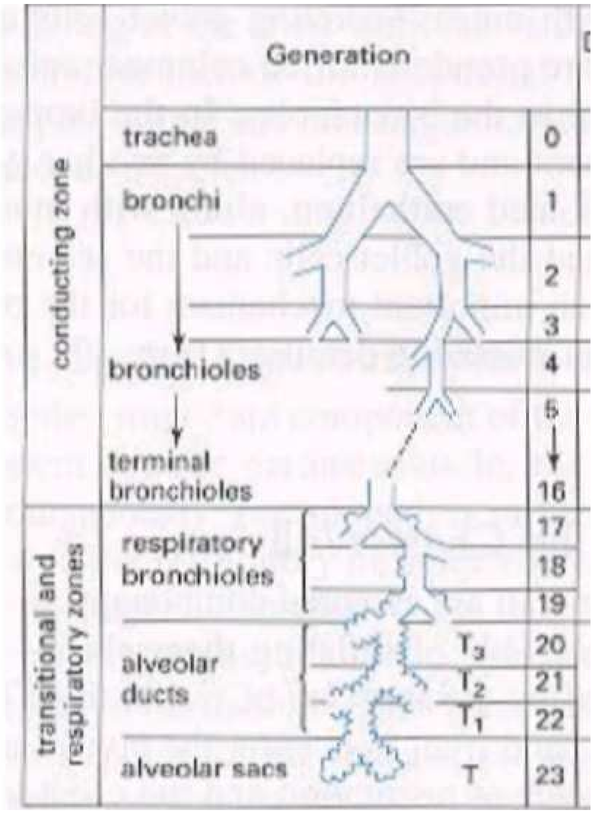

Figure 1.2: Lung Generation Definitions (Weibel, 1965).

At the end of each generation there is a bifurcation, which leads into two different airways of the proceeding generation. The first sixteen generations consist of the conducting zone. The respiratory zone, or the acinus region, is defined as generations 17 through 23.

1.1.1.2 Structure of the Acinus

Gas exchange occurs in the pulmonary capillary, which are within the alveolar walls in the respiratory zone, or acinus of the lung. The respiratory zone, or the acinus, contains the respiratory bronchioles, alveolar ducts and the alveolar sacs, as shown in Figure 1.3. An alveolus is the bud like sphere that first begins appearing on the respiratory bronchioles. When the bronchioles are covered completely by alveoli, the plural term for alveolus, they are considered to be alveolar ducts. The end of the alveolar duct is the alveolar sac, where alveoli cover all three sides of the lumen. The tissue of the acinus region of the lung is called the septa. Figure 1.4 shows a Scanning Electron Microscope image the alveolar duct, surrounded by alveoli.

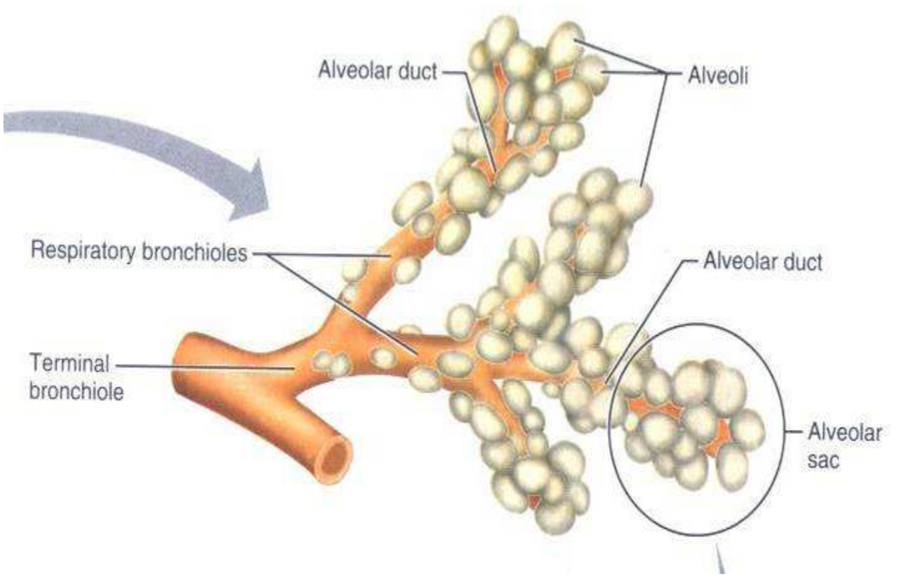

Figure 1.3: Respiratory Bronchioles, Alveolar Duct, Alveolar Sac and Alveoli Definitions (Marieb and Hoehn, 2007).

1.1.2 Mechanics of Breathing

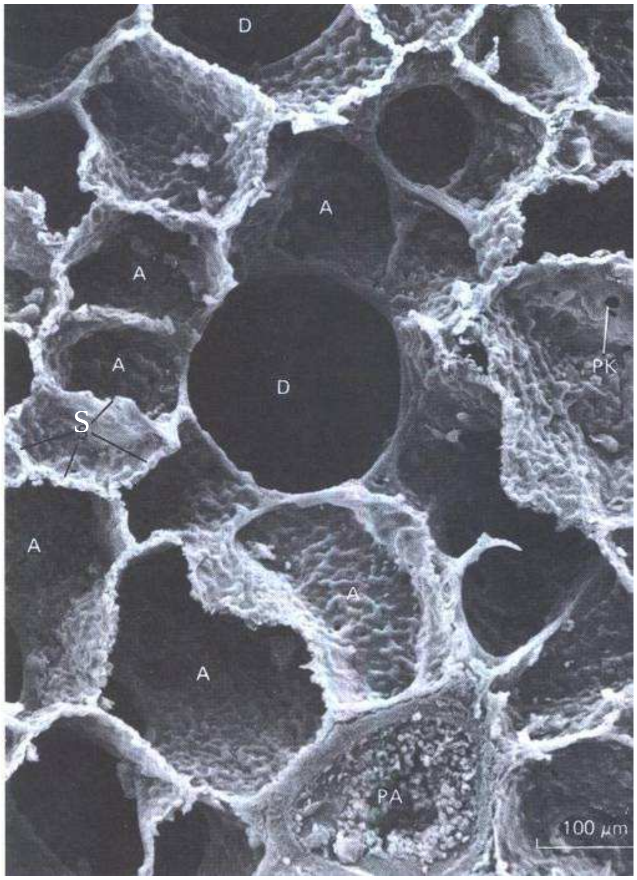

Figure 1.4: Scanning Elector Microscope image of the alveolar duct. A is an alveolus, S is the alveolar septa, D is the alveolar duct and PA is a small pulmonary artery (Levitzky, 2003).

Breathing is induced by a pressure gradient within the alveolar region of the lung, caused by the increase of the thoracic cavity, the cavity between the lung and the chest wall. Inspiration is controlled by muscles and therefore it is a triggered response due to a need for oxygen. During inspiration, the thoracic cavity causes a negative pressure inside the alveolar region, relative to the atmospheric pressure. Because the alveolar tissue is elastic, the alveoli increase in volume due to the pressure gradient. The negative pressure draws air into the lungs, until the pressure within the alveolar region is equal to the atmospheric pressure. Expiration is a passive reaction due to elastic recoil of the lung. Expiration occurs when the muscles that caused inspiration relax. During expiration the thoracic cavity’s volume decreases, which cause the alveoli to contract. The air within the lung is exhaled until the pressure within the alveolar region of the lung becomes equal to atmospheric.

1.1.2.1 Flow Rate

The flow rate at the mouth, is unsteady; it varies with time. Figure 1.5 is an example of the flow rate measured at the mouth, with respect to time. The figure is only an example, and therefore is only an approximation of the flow rate. Typically, the inhale portion of the curve is shorter then the exhale portion of the curve.

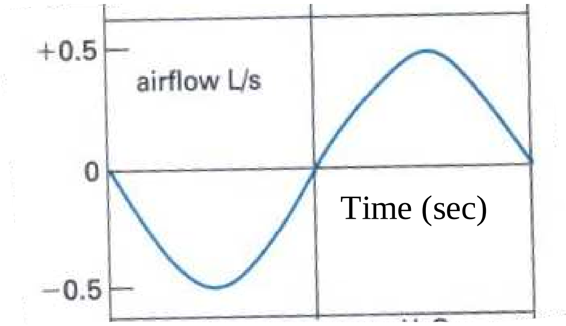

Figure 1.5: Example of Flow Rate Curve (Levitzky, 2003).

1.1.2.2 Volumes

An understanding of lung volumes is needed in order to understand the lung mechanics. Figure 16 shows the different lung volumes. The total lung capacity (TLC) is the maximum volume that the lung can hold. The residual volume is the amount of air left in the lung after maximum exhalation. The volume of air within the lung, before a normal breath, is considered the functional residual capacity (FRC). The amount of air that is breathed in, during rest, is considered the resting tidal volume (TV). The lung volumes in the human vary based on the

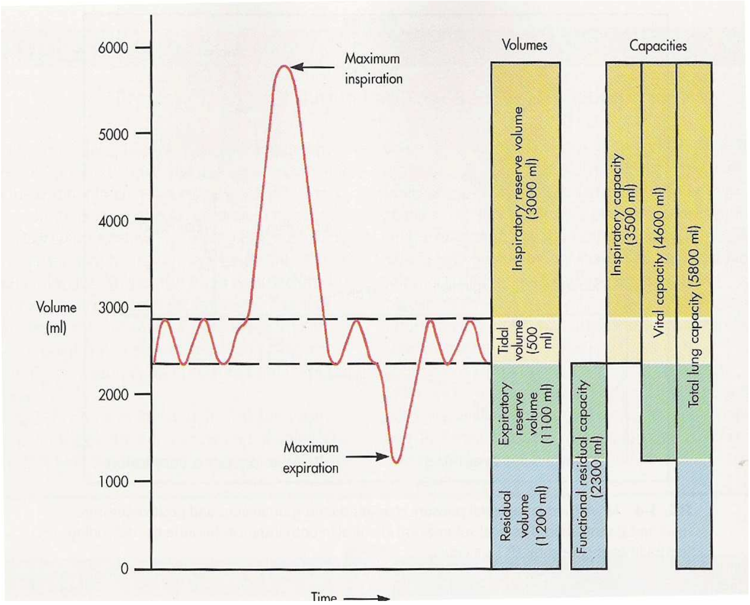

Figure 1.6: Lung Volume (Beachey, 1998)

gender, size and disease presence.

1.2 Emphysema

Emphysema is a disease that occurs in the acinus region of the lung. There are two types of emphysema, Centrilobular and Panacinar emphysema. Cigarette smoking causes Centrilobular emphysema. Centrilobular emphysema influences the proximal portion of the terminal bronchioles. Patients with α_1-antiprotease deficiency, as well as some elderly patients, contain Panacinar emphysema. Panacinar emphysema influences the entire respiratory bronchiole (Grippe, 1995). There are varying degrees of emphysema and it can become worse due to age or continuing to inhale toxic particles. There is no cure for emphysema and therefore it is irreversible. A literature report, which was completed by the author as a partial requirement of the BioMaterial course at RIT, is included in Appendix A. The report gives a detailed summary of emphysema and the changes that occur during the disease.

1.2.1 Changes in Structure of the Acinus

With Emphysema the elastic properties of the respiratory zone are damaged. The damaged tissue loses structure and therefore causes the individual alveoli to merge and expand. The new alveoli then have an increased volume, but decreased surface area in which

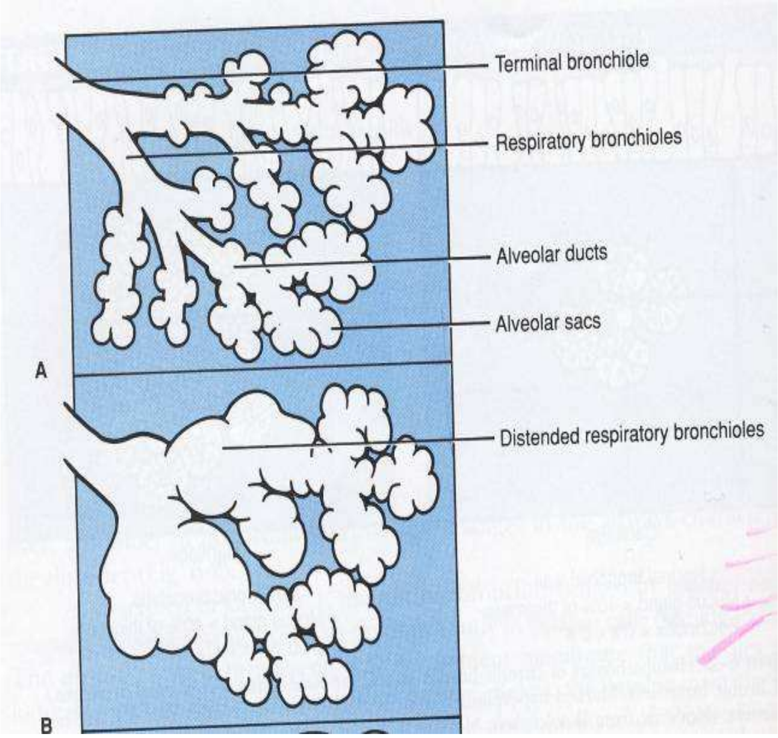

Figure 1.7: Acinus Region of the healthy lung (A) and a lung with Centrilobular emphysema (B) (Grippi, 1995).

oxygen can diffuse (Grippi, 1995). The elastic recoil is decreased, much like an overstretched rubber band. An emphysematous lung acts much like an overstretched rubber band, the tissue is damaged and overtime the damaged tissue loses its original elastic properties. The individual alveoli do not return to their original shape, and therefore remain in an expanded state. Figure 1.7 shows the difference between a healthy acinus, Figure 1.7A, and an acinus with emphysema, Figure 1.7B. It can be noticed from the picture, that the alveoli have become expanded and merged. Figure 1.8 shows an example of an emphysematous section of a lung that has significant tissue damage. The section of the lung is open to atmosphere and therefore should be completely deflated. As it can be seen from Figure 1.8, the alveoli on the left side of the sectioned lung do not appear to be deflated, for their elastic properties have been damaged due to the tissue damage that occurs with emphysema, and therefore do not hold their original shape (Greaves and Colebatch, 1980).

Figure 1.8: Excised Emphysema Lung
(Greaves and Colebatch, 1980)

1.2.2 Changes in Breathing Patterns

In emphysema the alveolar walls lose their elasticity and expand. Because of the tissue damage, the breathing pattern changes. The overall lung volume increases with emphysema. The elastic recoil pressure, the pressure induced when the lung is expanding, decreases.

Figure 1.9 shows the relationship between percent TLC and the elastic recoil pressure. The emphysema patient must use extra effort during expiration, because the elastic recoil is not driving all of the air out of the alveolar space. The expiration phase of breathing takes a longer amount of time in emphysema patients. Due to the extended mount of time, the alveoli do not empty and the air becomes trapped (Grippe, 1995).

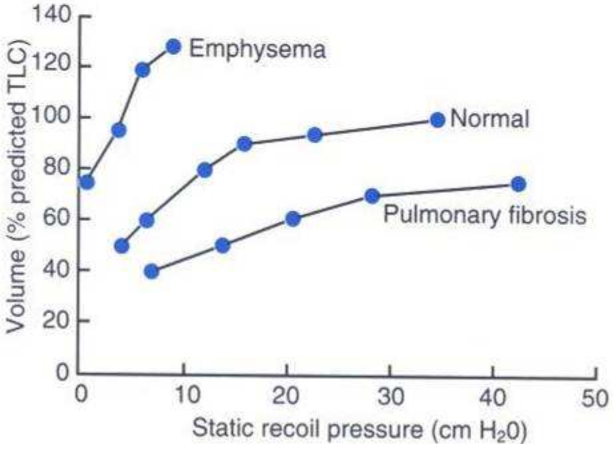

Figure 1.9: TLC as a Function of Static Recoil Pressure in Normal and Emphysema (Grippe, 1995).

1.2.3 Changes in Function of Gas Exchange in the Acinus

The change in the lung structure and breathing pattern, in emphysema patients influences their gas exchange ability. The trapped air inside the alveoli becomes dead space; it does not leave the alveoli and therefore those alveoli do not participate in gas exchange. Also, there is less area for gas exchange to occur because the acinus region of the lung lose surface area when the alveoli expand and merge. The combination of alveolar dead space and loss in alveolar surface area, causes the emphysema patients to have difficulty in the oxygen and carbon dioxide gas exchange. It can become difficult, especially during exercise, for patients to supply the body with sufficient amount of oxygen (Grippe, 1995).

1.3 Particle Deposition

There are many different types of particles, some of which can be harmful, while others carry small amounts of medication. An aerosol is a collection of particles suspended within a gaseous medium (Hinds, 1999). Figure 1.10 classifies aerosols based on their size.

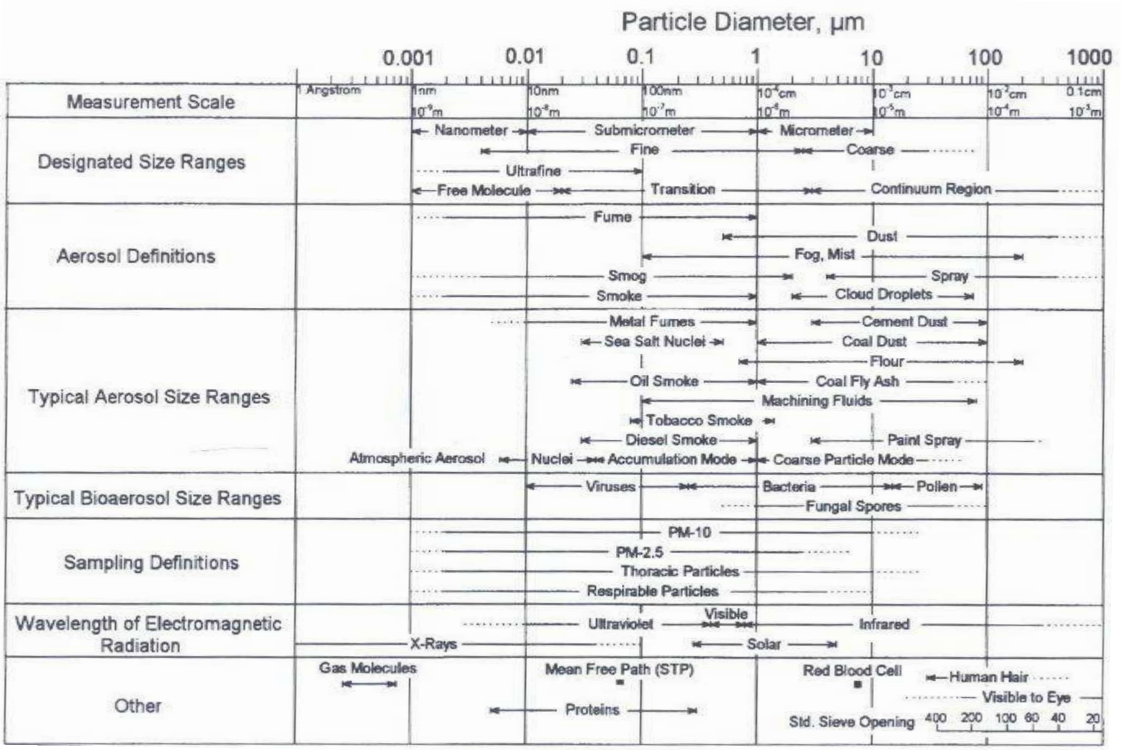

Figure 1.10: Aerosol Definition Based on Particle Size (Hinds, 1999).

1.3.1 Importance of Studying Particle Deposition

Studying particle deposition is important because particles that are breathed in have the potential of depositing on the lung walls. There are three different mechanisms for particle deposition: sedimentation, impaction, and diffusion. Sedimentation and impaction forces mainly influence larger sized particles, while diffusion impacts smaller particles. A particle will deposit on the lung wall due to sedimentation forces when the particle drifts in the direction of gravity due to its weight. Impaction occurs if particle momentum causes the particle to not follow the fluid around a bend, and therefore hit a wall. Diffusion occurs when particles move from a high particle concentration to a lower particle concentration. Because particles will deposit, due to these three forces, and because it known that toxic particles do cause harm, such as in emphysema, it is important to study what influences particle deposition within the lung. Also, understanding what mechanisms impact particle deposition may aid in aerosol medication development.

1.3.2 Diffusion and Particle Deposition in Alveoli

Small sized particles have a high likelihood to travel deep into the lung, because of their small potential to deposit by sedimentation or impaction. These small particles have a high probability to deposit due to diffusion. Diffusion occurs because of a concentration gradient, particles will migrate, due to Brownian diffusion forces, from a high concentration to a low concentration. Deposition due to diffusion is dependent on the size of the particle, the distance the particle must travel and the amount of time that is allowed for the deposition. If particle deposition occurs in the alveolar region of the lung, then the particles have a chance to migrate into the bloodstream.

There is some controversy in the literature, as to whether small sized particles reach the alveolar region of the lung. The tidal volume, volume breathed in during a breath, is a small portion of the air already inside the lung, residual air. There are two mechanisms that may allow for particles that are contained within the tidal volume, to reach the alveolar region of the lung. The first mechanism is by axial diffusion. The tidal volume is of high particle concentration, and therefore the particles may diffuse into the lung because of the low particle concentration gradient in the alveolar region. The second mechanism may be due to fluid mixing between the tidal air and the residual air of the lung. Particles with low diffusion may not have enough time to diffuse to the alveolar region of the lung, but if the tidal and residual air mixes, the particles may become trapped in the low concentration area. If particles are able to stay in the lung, and not be exhaled, there may be enough time for the particles to diffuse to the alveolar walls. However, smaller particles in the nano size range have very large diffusion rates, and therefore some studies suggest that these particles may deposit in the upper airways (Risa Robinson Dr., Mechanical Engineering, RIT).

Chapter 2
Literature and Preliminary Work Relevant to Mixing

2.1 Definition of Mixing

Mixing is an irreversible phenomenon that occurs when a system undergoes a process that cannot be returned to its original state by exactly reversing the process. Tsuda et al. (1995) theorized that in order to have irreversible flow in a Stokes flow regime, where inertia forces are not present; the system must be three dimensional. The three dimensions can be a combination of a two dimensional, time dependent flow or be geometrically three dimensional. In the lung, mixing refers to the different transport mechanisms, except Brownian diffusion, that irreversibly transfers air that is breathed, into the air that is already present in the lung (Darquenne and Prisk, 2005). There is controversy in the literature, as to whether mixing occurs in the acinus region of the lung, and if it does, what factors influence it. Many studies, including numerical, physical experimental models, animal and human, have been performed in trying determine if there is mixing and how mixing may impact particle deposition.

2.2 Literature on Mixing in the Lung

2.2.1 Numerical Alveolar Models

There are several numerical alveolar models in literature. Numerical models use computational methods to solve physical equations. Many of the numerical models simulate different fluid flow characteristics based on geometry, expansion, and flow rate. Particle deposition percentage and estimation, based on fluid flow characteristics, is estimated by many of the models.

2.2.1.1 Fluid Flow Characteristics

Several numerical models have examined how flow rate, expansion, and geometry influence the fluid flow in the acinus region of the lung.

Tsuda et al. (1995) examined the influence of expanding walls and geometry on fluid flow in the alveolar region of the lung. The three dimensional, axial symmetric, model consisted of a duct with toruses, which represented alveoli. Both the duct and alveoli walls rhythmically expanded and contracted due to a sinusoidal function. A flow rate ratio was developed, in order to determine the influence of expansion. The flow rate ratio is the ratio between the flow rate inside the alveolus and the flow rate inside the duct. Figure 2.1 shows the results of the expanding alveolus at different flow rate ratios. Figure 2.1A is for a flow rate ratio of 0.008, Figure 2.1B is for a flow rate ratio of 0.016 and Figure 2.1C is for a flow rate ratio of 0.15. From the figure, it can be determined that circulation was present for the low flow rate ratios. For the flow rate ratio of 0.15, Figure 2.1C, there was no circulation. The authors showed that when circulation is present there is irreversible flow; therefore for a flow rate ratio of 0.15, the flow is reversible. It was concluded,

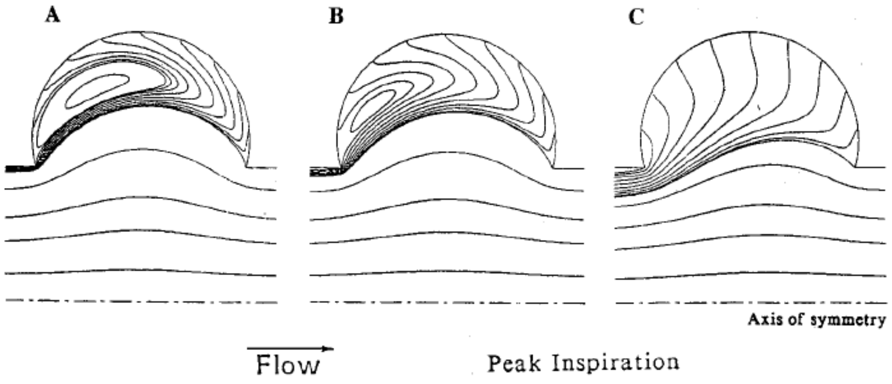

Figure 2.1: Flow through a Three Dimensional, Axial Symmetric, Alveolar Model at a Flow Rate Ratio of 0.008 (A), 0.016 (B) and 0.15 (C) (Tsuda et al.,1995).

by the authors, that a higher flow ratio would represent the most distal areas of the lung, the alveolar ducts and sacs, and therefore the flow is reversible in those areas of the lung.

It was also shown, by Tsuda et al. (1995), that the flow characteristics were also dependent on the alveolar geometry. The alveolar geometry was altered by changing the radius of the mouth of the alveolus and depth of the alveolus. The geometry was altered by a half angle, which is a function of the depth and radius of the mouth of the alveolus. Figure 2.2 shows the fluid flow varying degrees of the half angle. Figure 2.2A is for a half angle of 60 degrees and a flow rate ratio of 0.01, Figure 2.2B is for a half angle of 75 degrees and a flow rate ratio of 0.008, and Figure 2.2C is for a half angle of 90 degrees and a flow rate ratio of 0.006. The analysis showed that circulation, and therefore irreversible flow, occurs for smaller half angles. Circulation did not occur for the half angle of 90 degrees.

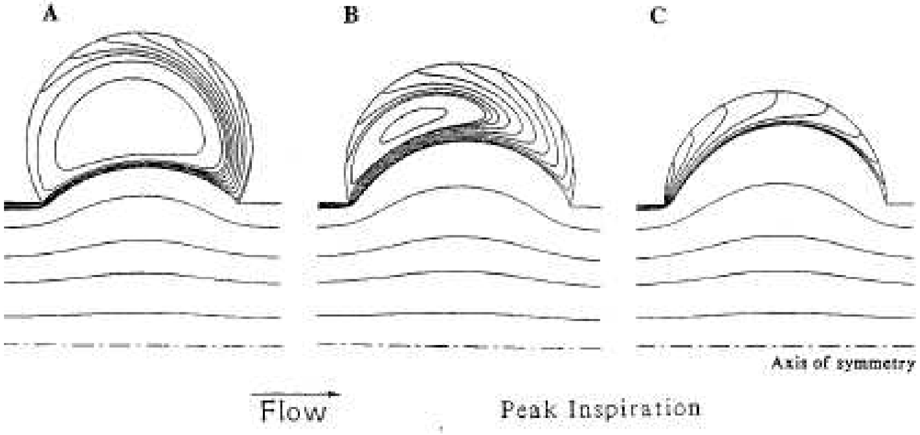

Figure 2.2: Flow Through a Three Dimensional, Axial Symmetric Model based on the Half Angle of 60 degrees (A), 75 degrees (B) and 90 degrees (C) (Tsuda et al., 1995).

2.2.1.2 Particle Deposition

An analysis was performed by Tsuda et al. (1994), where the goal was to determine particle deposition due to gravitational and diffusive forces in different geometries. Two different, stationary, geometries were used in the numerical model. The first model was a duct, with no alveoli. The second model was a three dimensional, axial symmetric torus, where the torus structures represented alveoli. Particles between 0.01 μm and 10 μm were subjected to gravitational and diffusive forces. Figure 2.3 shows the results of particle within the alveoli model. The model determined that there was more particle deposition in the simple duct model, which did not contain alveoli. It was also shown that the larger sized particles were subject to gravitational forces and the smaller particles were influenced by diffusion.

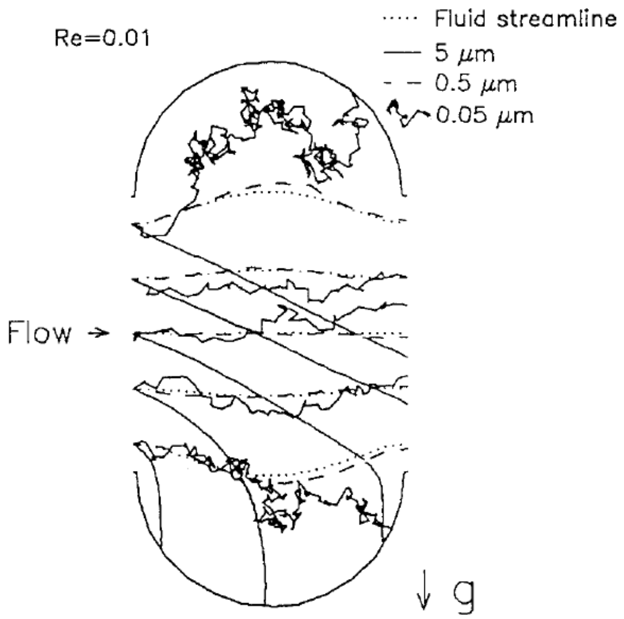

Figure 2.3: Stationary, Three Dimensional, Alveolar Model Subject to Different Sized Particles (Tsuda et al., 1994)

A particle deposition comparison, based on the percent expansion of the alveolus, was presented by Haber et al. (2003). The article examined a single alveolus, which was subject to a fluid flow over top of it. A ratio was developed in order to explain the fluid flow; the ratio between the amplitude of the shear and the expansion flow. A large ratio represented the proximal end of the acinus, where a small ratio

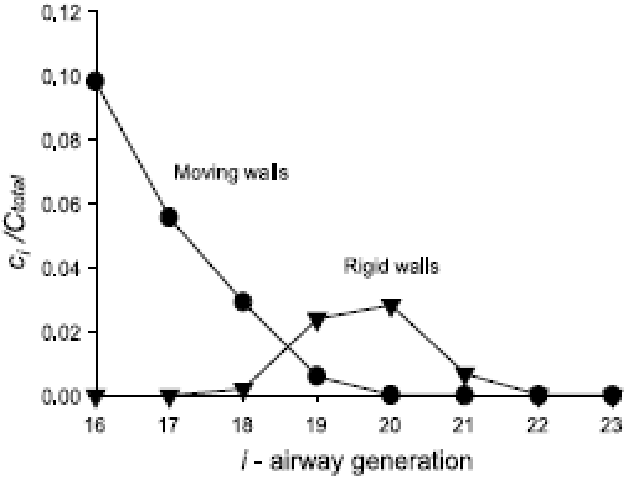

Figure 2.4: Particle Concentration Results as a Function of Acinus Generation for Moving and Rigid Walls (Haber et al., 2003).

represented the distal end of the acinus; the alveolar ducts and sacs. Particles with a diameter of 0.5 μm were injected into the fluid flow. Figure 2.4 shows the aerosol concentration at each generation, which is normalized, based on the concentration of particles entering the alveolus. The article determined that particle deposition is influenced by the expansion and contraction of the alveolus, and therefore particle deposition cannot be correctly estimated by stationary models. Also, more particles entered the alveolus, and deposited, for the deeper areas of the acinus.

Choi and Kim (2007) developed a mathematical analytical model that simulated particle deposition based off of the Trumpet model. The trumpet model is a mathematical model of the lung that estimates particle deposition. The original geometry of the Trumpet model was expanded on; more realistic alveoli were used. Different tidal volumes and trachea flow rates were simulated in order to determine their influence on particle deposition. Figure 2.5 shows the particle deposition for the different volumes and flow rates. Three forces acted on the particle

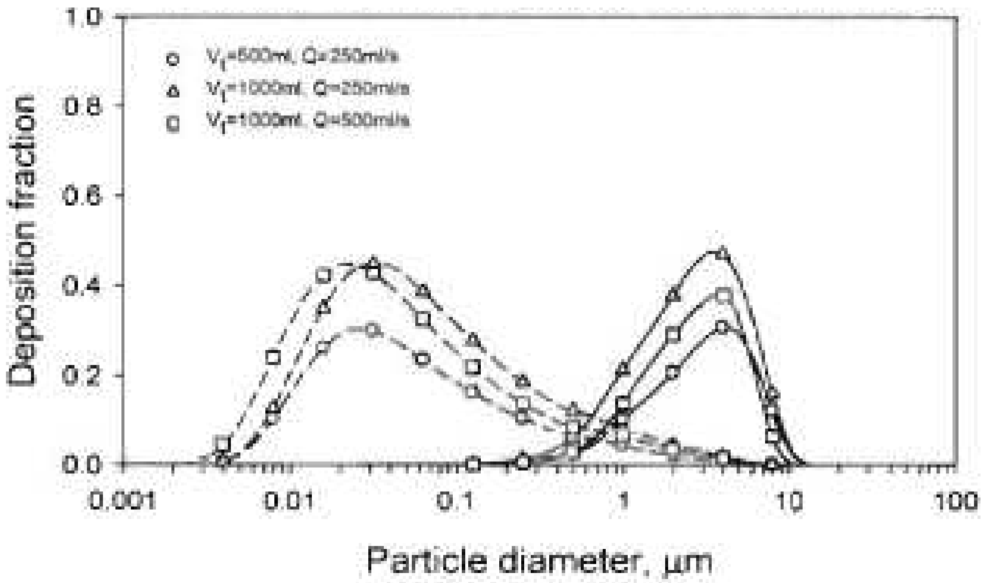

Figure 2.5: Particle Deposition Based on Particle Size, Deposition Forces, Tidal Volumes and Flow Rate at the Trachea (Choi and Kim, 2007).

deposition; sedimentation, impaction and diffusion. Choi and Kim (2007) concluded that particles with a diameter less then 0.2 µm will deposit mainly due to diffusive forces. Also, the article determined that, there was a higher percent deposition for a larger flow rate and tidal volume.

A fluid, structure, interaction model was developed by Dailey and Ghadiali (2007). The model is shown in Figure 2.6. An oscillating pressure was induced, which created the expansion and contraction of the alveolar model. Particle deposition was studied for particles between 0.1 and 5 µm in diameter. Two deposition forces were examined, sedimentation and diffusion. Figure 2.7 shows the amount of time for particle deposition, based on the size of the particle and the deposition forces present. The article determined that particles less then 1 µm will deposit, due to diffusion, in less then 15 seconds. It was also shown, that sedimentation only influences larger sized particles, particles greater then 0.5 µm.

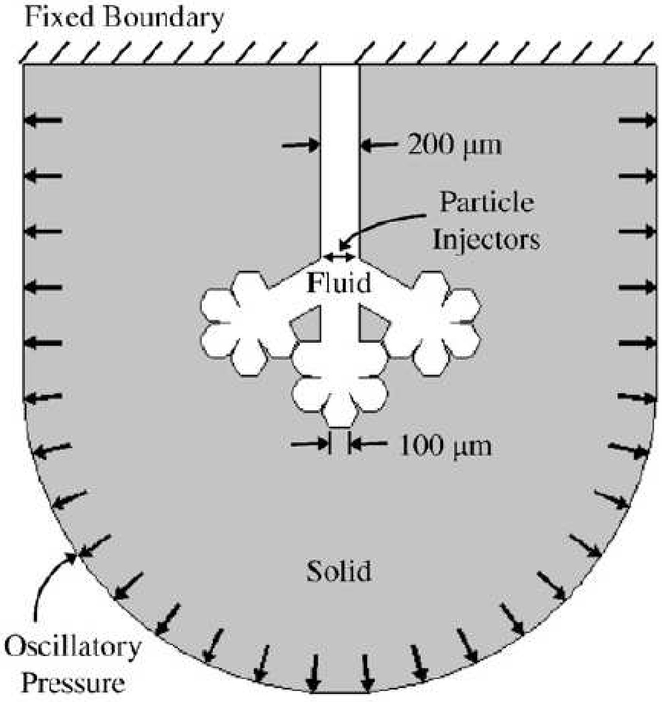

Figure 2.6: Fluid, Structure, Interaction Numerical Model Created by Dailey and Ghadiali (2007).

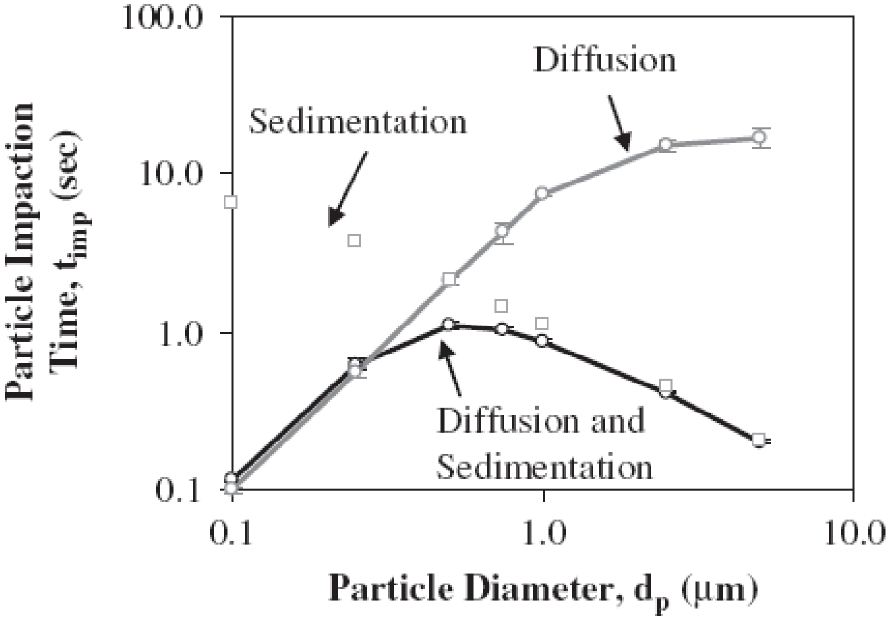

Figure 2.7: Particle Impaction Time for Diffusion and Sedimentation for Different Sized Particles (Dailey and Ghadiali, 2007).

Strum and Hofmann (2004) examined particle deposition, due to diffusive and sedimentation forces, in a Monte Carlo Simulation of the alveolar duct and sac region of the lung. Four different models were created, which represented four different geometries, three of which represented different diseased states due to emphysema. In order to determine the influence of mixing, three different mixing ratios were used, 0, 0.25 and 1.0. A mixing ratio is the ratio of mixing to no mixing, therefore a mixing ratio of 1.0 represents complete mixing. Figure 2.8 shows the particle deposition percentage based on particle size, disease, and mixing ratio. The article concluded that mixing does not influence particle deposition greatly, when it did influence particle deposition, it had the greatest impaction on particles of 0.1 μm in size. It was also concluded that there is significantly less particle deposition in the diseased lungs.

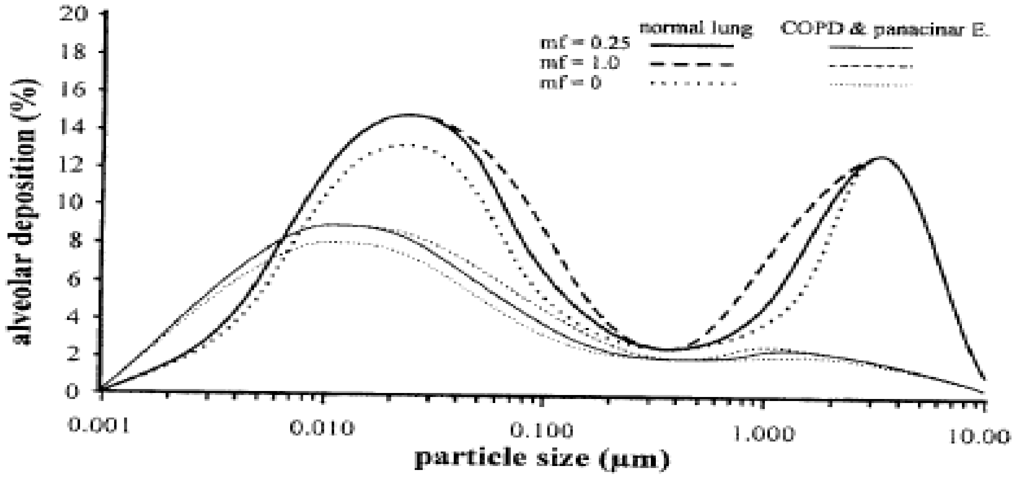

Figure 2.8: Percent of Particle Deposition Based on Different Sized Particles for Normal and Emphysematous Lungs (Strum and Hofmann, 2004).

2.2.2 Physical Alveolar Mixing Experiments

Physical alveolar models are models which simulate and visualize fluid flow in the alveolar region of the lung in a laboratory setting. The models are constructed at a large size, using fluid scaling techniques, which are used to link the results to what is occurring in the body. The fluid can be visualized two different ways; the first is when the alveolar region is modeled using fluid of two different colors and therefore the interaction of fluid can be examined. The second way to visualize the fluid flow is the use of particle image velocitmetry (PIV). PIV not only allows for the fluid to be visualized, but has the ability to quantify velocity fields.

A physical alveolar model that examined the fluid flow by different color dies was presented by Tsuda et al. (1999). The article used a three dimensional T-shaped model in order to demonstrate that asynchrony can lead to fluid irreversibility. The model was in the shape of a T. The fluid flow was simulated by pushing and pulling created by two pistons connected on both sides of the T shaped model. Colored die was introduced to the system in order to physically determine if mixing will take place with geometric hysteresis. Miki et al. (1993) determined that there is geometric hysteresis present during normal breathing in the lung. In order to determine of this geometric hysteresis is one of the factors of mixing Tsuda et al. (1999) moved the pistons at different phase angles in order to mimic in vivo conditions. The angle that Miki et al. (1993) found was approximately 10 degrees, and therefore the experiment with the T-shaped model was performed at 0, 5, 10, and 20 degrees. It was found that at 0 degrees the tracer die did not mix with the fluid even after ten cycles, indicating that the model itself did not create mixing. Figure 2.9 shows the fluid patterns for angles of 5, 10 and 20 degrees. It was shown that even with a small geometric hysteresis, phase angle of 5 degrees, irreversible flow occurred. Irreversible flow was concluded because as the number of cycles increased the complexity of the swirls also increased.

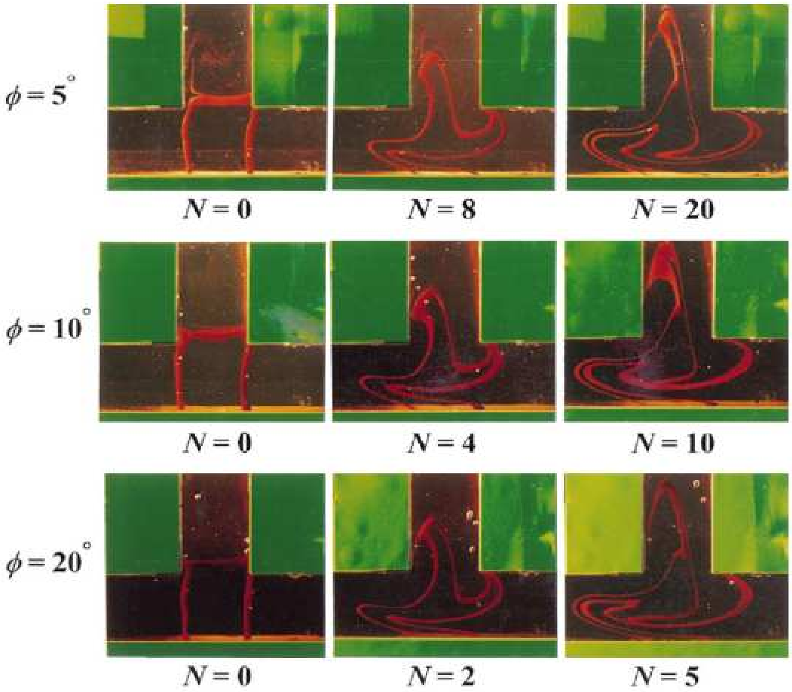

Figure 2.9: Tsuda et al. (1999). Tracer die in T-shaped model with Tidal volume to duct volume of 2. Swirls become more complex as cycle number increases.

Karl et al. (2004) created a physical model in order to understand fluid flow in an alveolated duct. The stationary geometry consisted of a duct with square shaped alveoli. The alveolar depth to mouth diameter was altered in order to determine the changes in the shape of the alveolus on the fluid flow. The fluid flowed over top of the alveoli. Glass particles were submerged in the uniform profile fluid. Streamlines were captured by illuminating the glass particles with a laser light and capturing their location with a high speed camera. Figure 2.10 shows the streamlines for different alveolar depth to mouth diameter ratios, where Figure 2.10A is for a ratio of 0.5 and Figure 2.10B is for a ratio of 0.67. When Ra was less than 0.5, Figure 2.10A, there were two recirculation flows in the corners of the cavities, and the recirculation flows increased in size as Ra increased. When Ra was between 0.5 and 0.67, Figure 2.10B, there were still two recirculation areas, but a streamline goes across the opening of the cavity, which separates the flow. The article concluded that the fluid flow pattern does change with alveolar geometry.

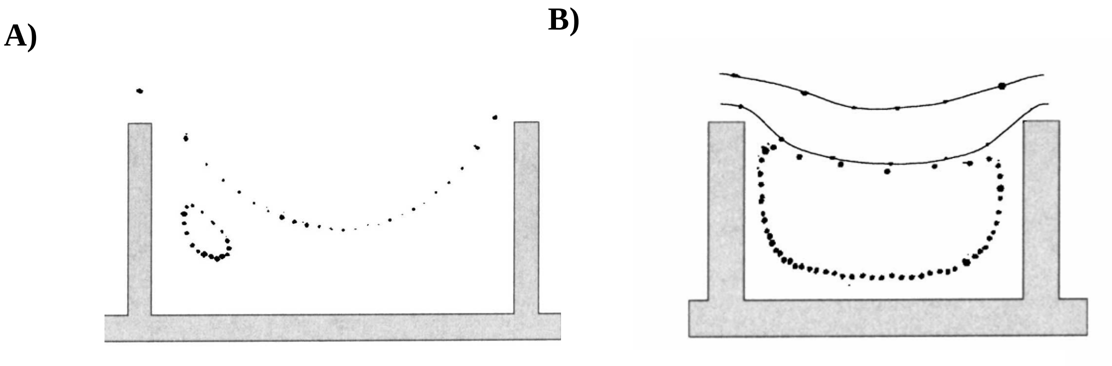

Figure 2.10: Streamlines in Stationary Alveolar Duct, with Depth to Mouth Diameter Ratios of 0.5 (A) and 0.67 (B) (Karl et al., 2004).

A three dimensional, axial symmetric, PIV model, was developed by Tippe and Tsuda (1999). The sinusoidal expanding model contained toruses on a tube, which represented alveoli on a duct. Fluid traveled over the alveoli. Three different trachea flow rates were used in the analysis, 0.8L/s, 1.6 L/s and 3.2 L/s. The flow rate ratio, the ratio of the flow rate inside the alveolus and flow rate through the duct, were examined. The fluid flow patterns were examined based on the flow rate at the trachea and the flow rate ratio. Figure 2.11 shows the relationship between the flow rate ratio and the fluid flow rate at the trachea. The article concluded that there is no alveolar recirculation for a flow rate ratio of greater then 0.06. Also, the article predicted that a larger flow rate ratio represents alveolar ducts and sacs, and therefore alveolar recirculation in the distal areas of the lung only occurs for large trachea flow rates.

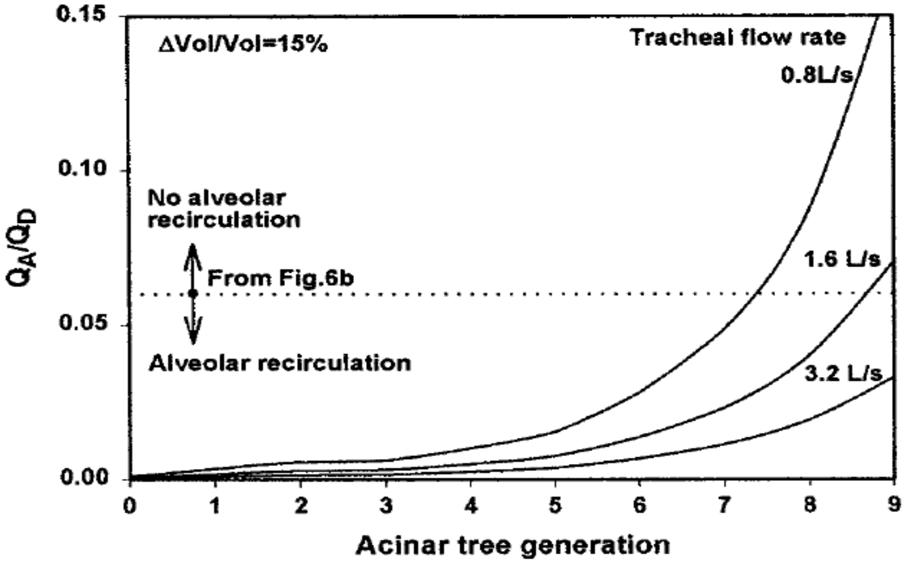

Figure 2.11: Prediction of Alveolar Recirculation for Different Flow Rates (Tippe and Tsuda, 1999).

2.2.3 Animal Experiments

Animals are often used in invasive experiments. Results obtained allow for a more graphic understanding of mixing and particle deposition. Tsuda et al (2002) studied the flow in the acinar regions of several excised rat lungs. The reasoning behind this study was to determine if there is mixing in the acinar region of a lung. Excised rat lungs were filled with a white fluid to a volume of 60% TLC, then filled with a the same fluid, but blue, for a tidal volume of 20% TLC. Breathing cycles were performed on the excited rat lungs to see how the white and blue fluid interacted with each other. The fluid was then allowed to solidify. The cast was sliced at different lung generations in order to determine the patterns of the blue and white fluids at different generations and cycle number. The finished cast part was sliced into several sections, depending on the airway generation that was being studied and was examined with a light microscopy. It was found that in all generations, previous to the 12^{th} generation in the rat lung, contained fractal patterns with a fractal

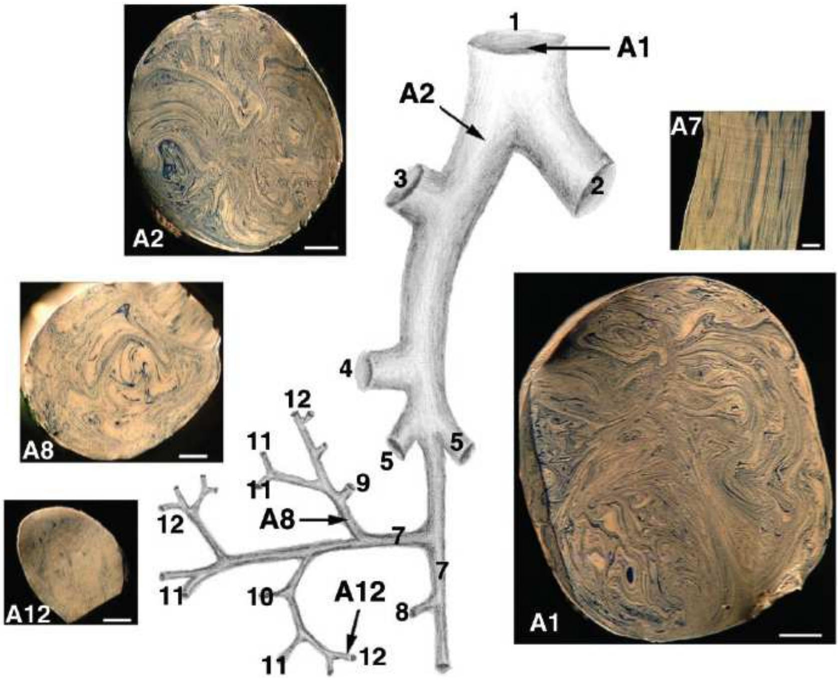

Figure 2.12: Fluid Pattern in Cast Rat Lung (Tsuda et al., 2002).

dimension of approximately 1.1. The article concluded that the consistency in the fractal patterns suggested that the reason behind the spiral shaped flow was due to irreversible flow in the acinar regions. If mixing was occurring in the upper airways then the fractal dimension would change in the first 12 airways. Figure 2.12 shows the fluid patterns at the different airway generations of the cast rat lung. Tsuda et al. (2002) was successful in determining mixing occurs in the acinus of the lung.

Zeltner et al. (1991) looked at the deposition of 0.9 μm aerosol particles in eighteen hamsters. The study compared the difference between rest and exercise, based on the volumetric flow rate of the hamster's breathing, in order to determine if flow rate influences particle deposition. The article also determined how long the particles remained in the lungs, by examining the lungs at different time periods, 10 min, 24 hours and 7 days after exposure. Each section of the lung was analyzed in order to determine where the particles deposited. It was determined that flow rates impacted particle deposition in the upper respiratory tract, but did not significantly change particle deposition in the peripheral region of the lung. It was also noted that after one day some of the particles in the alveolar ducts moved to the alveoli. Most of the particles left the upper airways after seven days after exposure, but most of the particles remained in the peripheral region even after several days. This article concluded that flow rate does not influence particle deposition in the peripheral region of the lung. Also, if particles do make it to the alveolar region of the lung, the particles will become trapped and remain in the peripheral region of the lung.

2.2.4 Human Experiments

Because of the controversy behind whether mixing actually occurs in the acinus region of the lung, studies have been performed in order to prove its existence. Aerosol experiments are a non-invasive way to determine specific characteristics of the lung. An aerosol experiment is performed by inhaling an aerosol bolus at different lung penetration depths. The aerosol bolus is defined as a volume of gas which contains aerosol particles. The particle concentration of the aerosol bolus is measured at inhalation and exhalation. The bolus half width is a means of measuring the width of the bolus between two points of one half the maximum concentration (Heyder et al, 1988), and is used to classify aerosol bolus.

Three different properties, which are important in determining mixing, can be found with an aerosol experiment, dispersion, particle deposition, and mode shift. Dispersion is the measurement of how much the half width of the particle changed from inhalation and exhalation. Convective mixing can influence dispersion, for when there is more mixing there will be a greater dispersion. Mixing in the acinus can be determined by using particles that have a low diffusivity, and examining how much they have dispersed. Deposition is measured by the difference in number of particles present in the inhaled and exhaled bolus. The mode, M, of the bolus is the volume at which the exhaled bolus is at maximum concentration. If breathing was

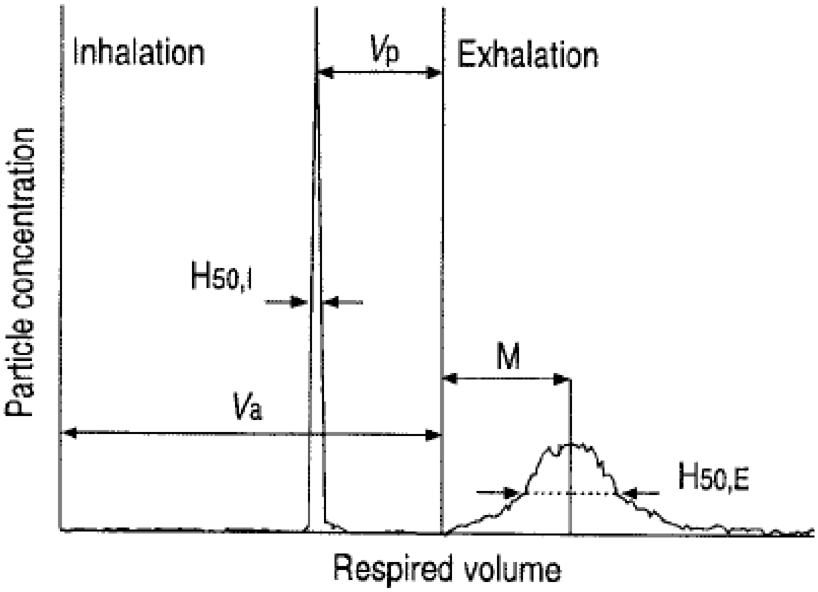

Figure 2.13: Mode shift for Aerosol Bolus Experimentation (Brand et al., 1997).

symmetrical the mode would be equal to the volumetric lung depth, Vp. Figure 2.13 shows the mode shift, which measures the difference between the mode and the volumetric lung depth (Brand et al., 1997).

2.2.4.1 Findings in Health

Heyder et al. (1988) performed an aerosol bolus experiment in order to determine how lung depth influences aerosol bolus behavior. Particles that were approximately 1µm in diameter were used. The reason behind choosing these small particles was because diffusion and gravitational settling should be very low and therefore if there is not mixing, the particles would be confided to the inspired air. The patients used a flow meter that monitored when the aerosol was inhaled and the particle concentration of the inspired and expired air. The atmospheric air following the inhaled bolus varied between 100 and 800 cm^3 in order to allow for the aerosol to penetrate to different depths in the lung. It was found that the deeper into the lung the particles were able to penetrate, the more disperse the exhaled particles were, even in the peripheral region of the lung. It was also found that the relationship between the expired dispersion of the bolus was linearly related to how deep the aerosol traveled into the lung.

Brand et al. (1997) studied aerosol bolus dispersion in 79 healthy subjects in order to determine factors which contribute to aerosol bolus dispersion and deposition. The subjects inhaled a specified volume of aerosol bolus at different lung depths and flow rates. Different volumetric lung depths were used to determine how lung depth influences particle deposition; 200, 400, 600, and 800 cm^3, and flow rates of 100 – 700 $cm^3\ s^{-1}$. It was determined that there was a significantly higher aerosol deposition with a slower air flow rate; signaling that the longer the aerosol particles remain in the lung, the higher the chance of them depositing. It was also observed that the half width bolus dispersion increased with the square root of the volumetric lung depth, indicating that convective forces are present in the peripheral region of the lung. The lung inflation and the particle size, 0.5 – 2 μm, did not impact particle deposition.

Heyder et al. (1988) and Brand et al. (1997) were able to draw the same conclusions, aerosol bolus becomes more dispersed the deeper into the lung the aerosol particles penetrate. The articles concluded that inn order for this to be the case, convective mixing must occur, for the flow was shown to be irreversible. The relationship of dispersion based on volumetric lung depth was different between Heyder et al. (1988) and Brand et al. (1997) Heyder et al. (1988) determined that the increase in bolus half width increased linearly with volumetric lung depth, while Brand et al. (1997) determined it increased to the square root of volumetric lung depth.

Darquenne and Prisk (2005) tested the theory of stretching and folding, and the influence of gravity on particle deposition, by studying aerosol bolus dispersion in eight healthy subjects. In the case of gravitational effects, the subjects were tested in a normal environment. For the experiments where it was assumed gravity was negligible, the experiments were performed in the Aeronautics and Space Administration Microgravity Research Aircraft.. In order to determine whether stretching and folding occurs in the lung, and therefore mixing, flow reversals were used. After the bolus was inhaled at a specific lung depth, the subject would perform a specified amount of flow reversals. A flow reversal allows for small breaths of inhalation and exhalation, which do not change the final volume of the lung. These small breaths allowed for the alveoli to expand and contract with the aerosol bolus still being contained inside of the airspace. Particle dispersion was measured at exhalation at different amounts of flow reversals. Aerosol bolus of 0.5 μm diameter were inhaled at penetration volumes of 300 ml and 1200 ml; acinar entrance and in the periphery of the acinus respectively. It was determined that an increase in flow reversal did not show an increase in dispersion, for both gravity cases; which may be because the stretching and folding did not occur in the number of flow reversals performed or the stretching and folding phenomenon occurred in the first breath. It was also determined that dispersion at 300 ml volumetric penetration depth did not change due to the influence of gravity. Contrastingly it was found that the aerosol became more dispersed in gravity at the 1200 ml penetration depth. The article suggested that the influence of gravity on particle dispersion signifies that there are ventilatory inhomogeneities in the acinus region of the lung and therefore these homogeneities impact convective mixing. Theoretically, in a gravitational environment the lung distorts under its own weight and therefore the alveoli at the bottom of the lung are less expanded, which indicates there is a greater amount of ventilation in the bottom of the lung. It was found that there was a greater deposition of the particles when subjects were placed in a gravitational environment for both 300 ml and 1200 penetration volume. This signifies that gravity plays a role in particle deposition.

2.2.4.2 Findings in Emphysema

Kohlhaufl et al. (1997) compared aerosol bolus dispersion and mode shift in 29 patients with pulmonary emphysema to the 79 healthy subjects performed by Brand et al. (1997). The patients in the study showed signs of advanced emphysema. Aerosol boluses of 0.9 μm diameter were inhaled at lung depths of 200, 400, 600, and 800 cm^3. It was determined that in emphysema the bolus dispersion increased as the lung depth increased, as was also found in the healthy subjects. The average dispersion for each of the lung volumes was greater in the patients with emphysema. The increase in bolus dispersion indicates there is an increase in ventilation asymmetry. It was also noticed that there was a significant difference between the mode and the volumetric lung depth, the mode shift. It was hypothesized, by the authors that the reason why the bolus was more dispersed in emphysema, and there was a high mode shift, was because the disease does not influence all the alveoli the same, therefore some of the alveoli can be healthy while an alveolus next to it can be severely damaged. The gas may mix different in each of the alveoli and therefore fluid flow would not be as symmetrical, as it may be assumed to be in the healthy lung. Another hypothesis would be there may be airway obstructions in a patient with emphysema and therefore the gas would have to take different airway paths then it would take if the lung was healthy.

2.3 Preliminary Research Relevant to Mixing

Research was completed by this author, and presented at the American Association for Aerosol Research conference in November, 2007. A three dimensional, expanding, alveolar model was created. The model contained an alveolus on a duct,

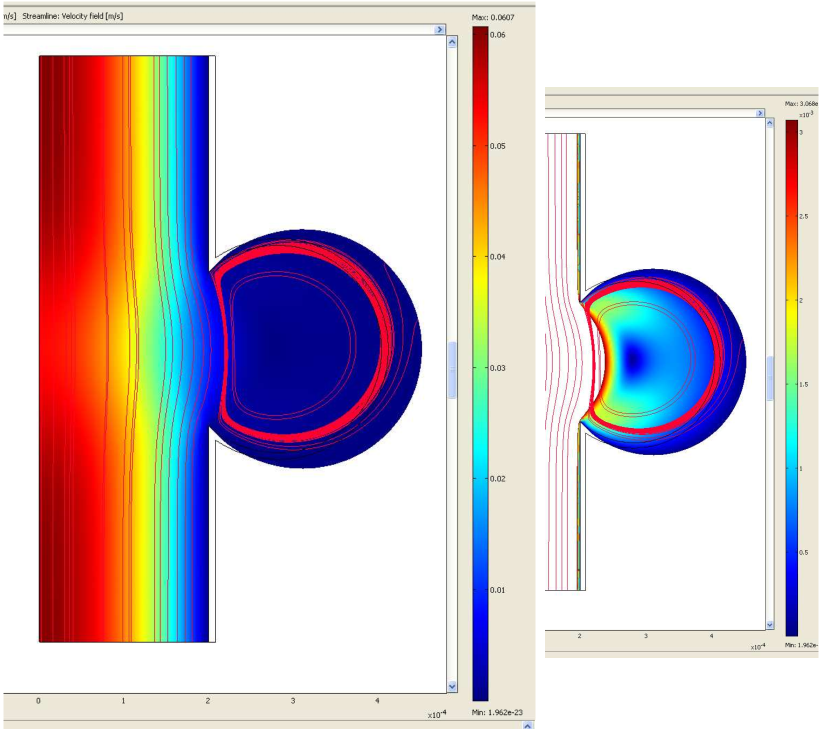

Figure 2.14: Streamlines at the End of Inhale for a Change in Alveolus Volume of 1.48e-8 ml.

which represented the 17th generation. The model was solved using fluid, structure interaction, finite element techniques, in COMSOL, Multiphysics. The expansion and contraction of the alveoli was imposed by a pressure force, which allowed the alveoli to expand, with respect to time. Four different expansions were used; a maximum change in volume of 0 ml, 1.48e-8 ml, 2.89 e-8 ml and 4.33e-8 ml. The model was imposed to five breathing cycles. Fluid flow rate, with respect to time, was specified at the inlet, and fluid exited the model through the outlet. The model showed that there was recirculation in the alveolus, and the recirculation led to irreversible flow. Figure 2.14 shows the streamlines, at the end of inhale, for the maximum change in volume of 1.48e-8 ml. It can be noticed that the streamlines separated from the main fluid flow, in the duct, and created a circulation pattern. Figure 2.15 shows a pathline, which expresses irreversible flow within the alveolus. From the model, it was determined that irreversible flow does occur in the 17th lung generation. Further study was performed in order to determine the irreversible flow's impact on particle deposition.

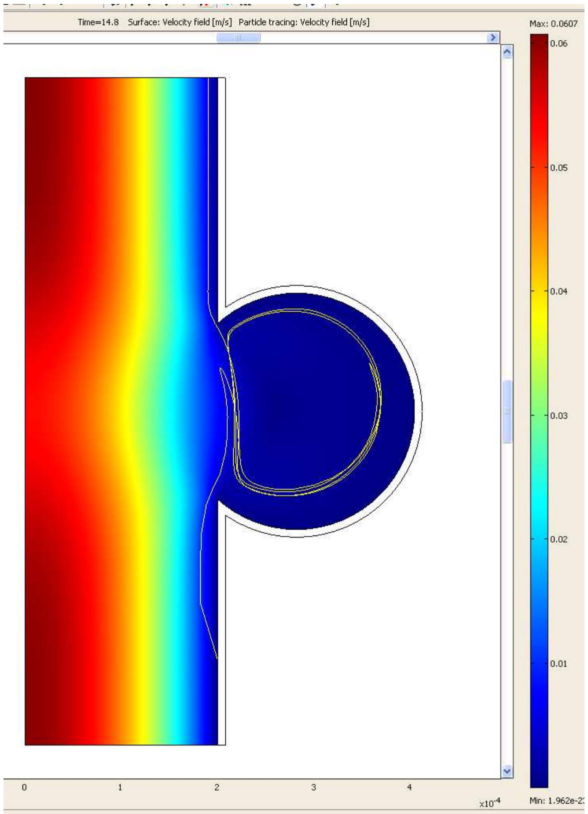

Figure 2.15: Irreversible Pathlines for a Change in Alveolus Volume of 1.48e-8 ml.

Additional analysis was completed in order to determine the influence of the expanding walls on particle diffusion. Particles, with a diameter size range of 0.01 μm and 0.1 μm, were released at the inlet of the model. The concentration of particles at the outlet of the model was examined. For a particle with a diameter of 0.1 μm, a particle with long diffusive time, the particle concentration at the outlet decreased with time. It was also shown, that that the amount the alveolus expanded had an influence on particle concentration at the outlet. The particle concentration at the outlet decreased for a higher alveolus change in volume. It was shown that for a maximum change in volume of 4.33e-8 ml, there was a 15 percent difference in the outlet concentration of 0.1 μm, when compared to the model that did not expand. It was concluded, that he expansion of the alveolus allowed for particles to travel inside the alveolus, and become trapped, allowing them to not be exhaled. This phenomenon may allow for particles with high diffusive times, more time to diffuse to the alveolar wall.

2.4 Gaps in Alveolar Particle Deposition Research

2.4.1 Geometry

There has been some research directed towards determining the influence of geometry on fluid flow pattern and particle deposition in the acinus of the lung. Tsuda et al. (1995) and Karl et al. (2004) examined how the alveolar depth to alveolar mouth opening radius ratio influenced fluid patterns. The articles showed that the fluid flow irreversibility differed significantly based on the ratio. The geometry used for the analysis was a simple torus model, which represented alveoli on a duct. The article’s conclusions may differ for a more realistic alveolar geometry.

There has not been any research completed that examined different shapes of alveoli. Most alveolar research has been completed have been on spherical alveoli. Dailey and Ghadiali (2007) did examine fluid flow in hexagonal shaped alveoli, but the article did not compare the results to the simple spherical models. Alveoli in the body are not perfect spheres, and therefore understanding how the different geometry may influence fluid flow and particle deposition may be crucial.

Currently, there have not been any articles that have researched a three dimensional, expanding, non-symmetric alveolar model. There have been models that examine fluid flow in symmetric three dimensional models (Tippe and Tsuda, 1999 and Karl et al., 2004). Modeling the fluid flow in a non-symmetric, realistic, alveolar model would aid in the understanding on what influences mixing and particle deposition.

2.4.2 Flow Rates

Fluid flow examinations in the published alveolar models have all used either a steady flow rate, or a sinusoidal flow rate curve. There have not been any models that have imposed a realistic flow rate. There is controversy as to whether flow rate does influence fluid flow, and particle deposition (Dailey and Ghadiali, 2007, Brand et al., 1997, and Zeltner et al., 1991). Fluid flow and particle deposition changes have not been examined for different flow rates that occur with disease, such as with emphysema. A complete understanding of how tidal volume, time to complete a breathing cycle, breathe hold, and flow rate shape, changes the fluid flow and particle deposition is needed in order to accurately predict particle deposition percentages.

2.4.3 Disease Presence

It is not fully understood the difference in the fluid flow pattern in the alveolar region, and particle deposition, in emphysema compared to a healthy person. There has not been any work completed on visualizing fluid streamlines or pathlines in an emphysema model. Strum and Hofmann (2004) examined only particle deposition in an emphysema model, but their model was only two-dimensional and did not take into consideration expanding alveolar walls. There has not been any work completed that have imposed the changes in the alveolar material properties that occurs with emphysema. Different tissues are changed more then others, and therefore the damaged area may cause non-uniform expansion during a breathing period. It has been shown that non-homogeneities do influence fluid mixing (Tsuda et al., 1999). There is controversy as to whether there is more or less particle deposition with emphysema (Strum and Hofmann, 2004 and Kohlhaufl, 1997); therefore more studies need to be completed in order to fully understand the changes.

2.4.4 Fluid Mixing Influence on Particle Deposition

The influence of mixing on particle deposition is not fully understood and there have not been any conclusions drawn that answers the questions as to after what breathing cycle number does particle deposition becomes influenced. Darquenne and Prisk (2004) predicted it only takes one cycle in their human experiments. Butler and Tsuda (2005) and Tsuda et al. (1999) showed that flow becomes more mixed with increasing cycle number, but not how this impacts particle deposition. A complete understanding of mixing and particle deposition will aid in the particle deposition percentage prediction.

2.4.5 Alveolar Wall Structure and Material Properties

Understanding the material properties and alveolar wall structure may be crucial in understanding fluid flow pattern, and particle deposition, in the alveolar region of the lung. There has not been research completed on non-uniform expansion of healthy alveoli. Dailey and Ghadiali (2007) looked at realistic material properties, but the material expanded uniform to itself. Also, research has not been conducted that looks at the influence of interdigitization of alveoli on the relative amount of expansion with respect to alveolar location. The understanding of non-uniform expansion and how alveoli interact with each other will aid in the development of fluid flow understanding.

2.5 Thesis Work Statement

The scope of this thesis was to determine if irreversible flow occurs in healthy and emphysema alveolar sac geometries, and how the fluid flow pattern influences particle deposition by diffusion. An experimental technique, Particle Image Velocitmetry (PIV), was used for examination of the fluid flow. Validation was performed by comparing numerical and PIV results using a simple balloon geometry model. Three dimensional, expanding, alveolar sac geometries were used in order to represent a healthy and emphysematic alveolar sac. A realistic flow rate was defined and implemented to simulate the breathing of the alveolar sacs. The differences in the fluid flow between the healthy and emphysematic alveolar sacs were examined. Particle deposition by Brownian diffusion was estimated based on the fluid flow, and a comparison was made between the healthy and emphysematic alveolar sacs.

Chapter 3
Model Geometry

Chapter 3 describes the three different geometries that were used for the experimentation; a balloon model and two alveolar sac geometries; one representing a healthy alveolar sac and one representing an emphysematic alveolar sac. In this work the balloon model was used for both PIV and CFD analysis and the alveolar sac models were used only for PIV analysis. The design of the geometries, how the PIV models were manufactured and a comparison of the geometry to that found in literature, is given in this chapter.

3.1 CAD Design

The three models CAD designs are given in the following section. The alveolar sac models were designed based off geometry found in literature. There were two different sized models designed, for the alveolar sac models, a small scale model representing in vivo geometry and a large scale model, used for the PIV experimentation. In this section all dimensions for the alveolar sac models are for the small scale model.

3.1.1 Balloon Model Geometry

The balloon model was created for verification of technique, and therefore was used for both PIV and CFD analysis. The model's geometry was based off of a 50ml boiling flask. The boiling flask was a sufficient general representation of the more complicated geometry of the alveolar sac. The volume of the balloon model is similar to the volume of the alveolar sacs and therefore the same non-dimensional fluid scaling technique, were able to be applied

(Section 4.1.3.3). The dimensions of the balloon model are shown in Figure 3.1. The duct radius of the balloon model was measured directly from the boiling flask. The bulb radius and the fillet radius were measured from the PIV photographed image. The thickness of the model was determined based on the average thickness of the PIV model (Section 7.2).

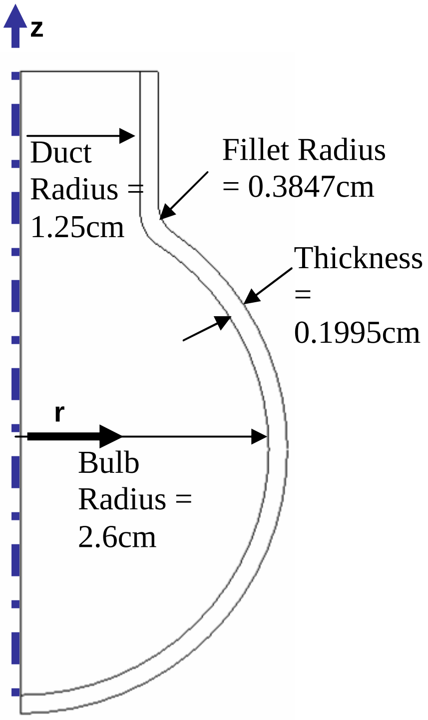

Figure 3.1: Balloon Model CAD Dimensions.

3.1.2 Healthy Alveolar Sac Model Geometry

The alveolar sac models were derived from idealized geometry from the literature. The creation of the geometry was a combined effort of the Alveolar Sac Senior Design Teams 2005 – 2006 (P06215) and 2006 – 2007 (P07021). Two different articles were originally used in order to determine the overall size and shape of the alveolar sac. Both articles report the dimensions of lung castings, representing the airspace within the lung. Weibel (1964) determined the geometry based on five healthy lung castings, of various ages and gender, fixed at an approximate 75 percent Total Lung Capacity (TLC). The article defined the radius of an alveolus, the depth of an alveolus, and the average number of alveoli on an alveolar sac. The overall

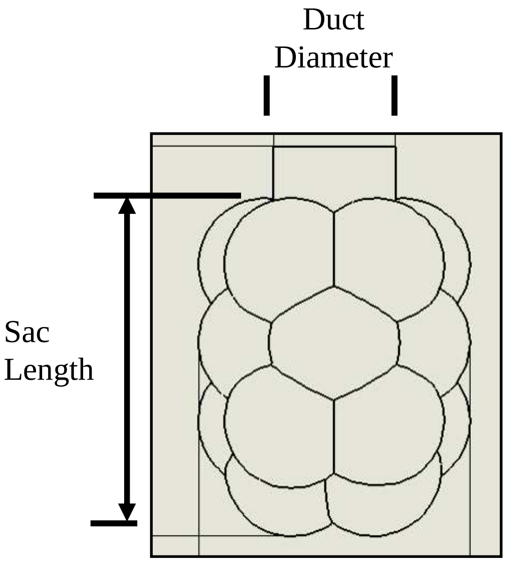

Figure 3.2: Definition of Alveolar Duct Diameter and Alveolar Sac Length.

alveolar sac length and the radius of the alveolar duct were given in Haefeli-Bleuer & Weibel (1988). In this article, the geometry was derived from lung castings of the upper lobes of two cadavers, at approximately 90 to 100 percent TLC. The exact inflation of the lungs was unknown. Figure 3.2 shows the duct diameter and sac length definitions and Figure 3.3 shows the alveolus depth, radius and mouth diameter definitions.

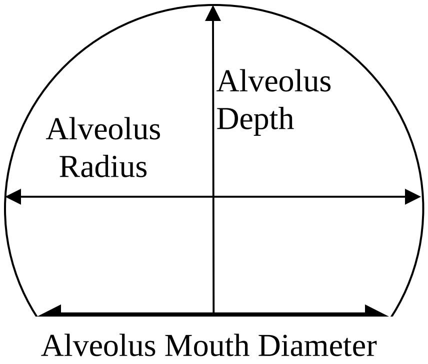

Figure 3.3: Alveolus Depth, Radius and Mouth Diameter Definitions.

It was assumed that the approximate volume of the lung at the beginning of inhale, Functional Residual Capacity (FRC), of a healthy lung is 50% TLC. In order to scale down each alveolus to the FRC volume (V_{FRC}), the following equation was used on each alveolus on the healthy alveolar sac model (Weibel and Gomex, 1962)

$$\frac{d_{Vm}}{d_{FRC}} = \left(\frac{V_m}{V_{FRC}}\right)^{1/3} \tag{3.1}$$

where the volume measured, V_m, is the volume at which the article measured the lung at, 75% TLC. An average TLC is 6000 mL (reference), therefore 75% TLC is 4500 mL. The FRC was assumed to be 50 percent of 6000 mL, 3000 mL. The diameter of the each alveolus, measured at 75%TLC (d_{Vm}) was 0.28 mm (Weibel, 1964). The FRC diameter, d_{FRC}, was determined to be 0.24 mm, Equa. 3.1.

After observing the original geometry, based off Weibel (1964) and Haefeli-Bleuer & Weibel (1988), it was noted that the resulting effective airway diameter, the average diameter of the alveolar sac, was over twice that given by Haefeli-Bleuer & Weibel (1988). The effective airway diameter was almost as large as an emphysematic alverolar sac (Kohlhaufl et al., 1988). Further investigation showed that the alveoli depth to mouth diameter ratio was too large when compared to literature (Klingele and Staub, 1970 and Mercer et al., 1987). In order to incorporate the findings from literature, the number of alveoli was reduced from 17 to 13, which reduced the effective airway diameter and increased the depth to mouth diameter ratio. The original geometry given by Weibel (1964) and Haefeli-Bleuer & Weibel (1988) was used for the emphysema model. A more detailed comparison is given in Sections 3.3.1 and 3.3.2. The final healthy alveolar sac CAD model is shown in Figure 3.4, for the top and side view. A summary of each dimension, as well as the emphysema dimensions, is given in Table 3.1

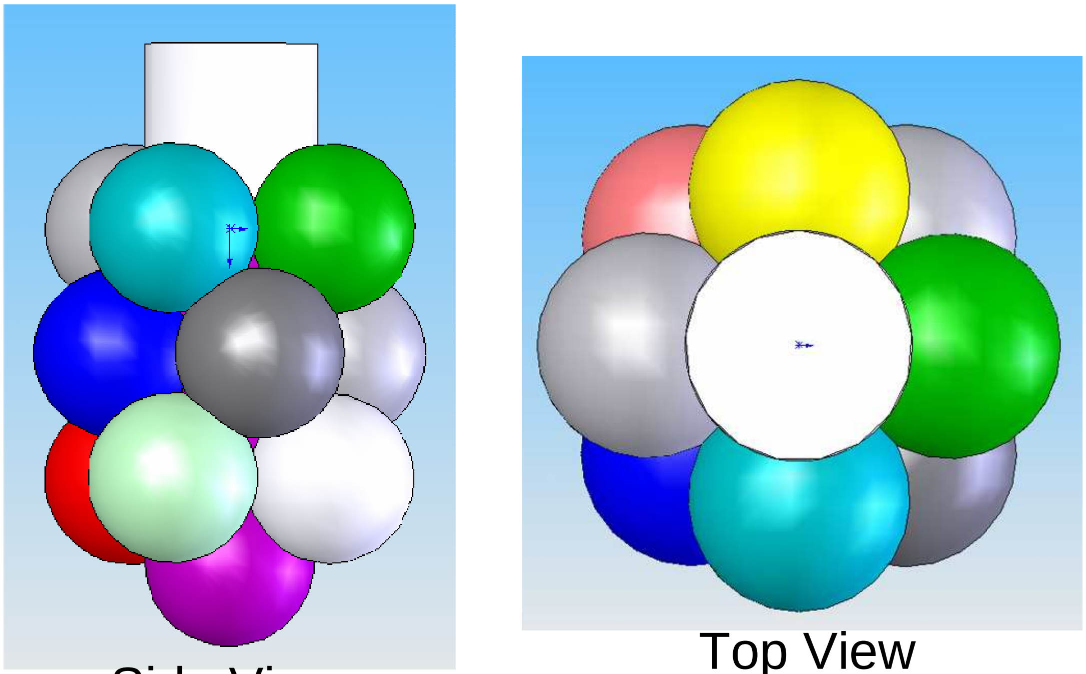

Side View

Top View

Figure 3.4: Healthy Alveolar Sac CAD Model.

Table 3.1: Alveolar Sac CAD Dimensions

	Article Dimension	Article	Healthy CAD Dimension	Emphysematic CAD Dimension
Duct Diameter (mm)	0.25	Haefeli-Bleuer & Weibel (1988)	0.25	0.25
Alveolus Radius (mm)	0.14	Weibel (1964)	0.122	0.14
Alveolus Depth (mm)	0.23	Weibel (1964)	0.165	0.108
Sac Length (mm)	0.75	Haefeli-Bleuer & Weibel (1988)	0.748	0.748
Number of Alveoli	17	Weibel (1964)	13	17
Depth to Mouth Diameter Ratio	0.82 – 1.16	Klingele and Staub (1970) & Mercer et al. (1987)	0.64 – 0.87	0.34 – 0.45
Effective Airway Diameter (mm) – Healthy	0.25	Haefeli-Bleuer & Weibel (1988)	0.3116 - 0.554	
Effective Airway Diameter (mm) - Healthy	0.39	Kohlhaufl et al. (1988)	0.3116 - 0.554	
Effective Airway Diameter (mm) - Emphysema	0.63	Kohlhaufl etal. (1988)		0.553 - 0.589

3.1.3 Emphysemic Alveolar Sac Model Geometry

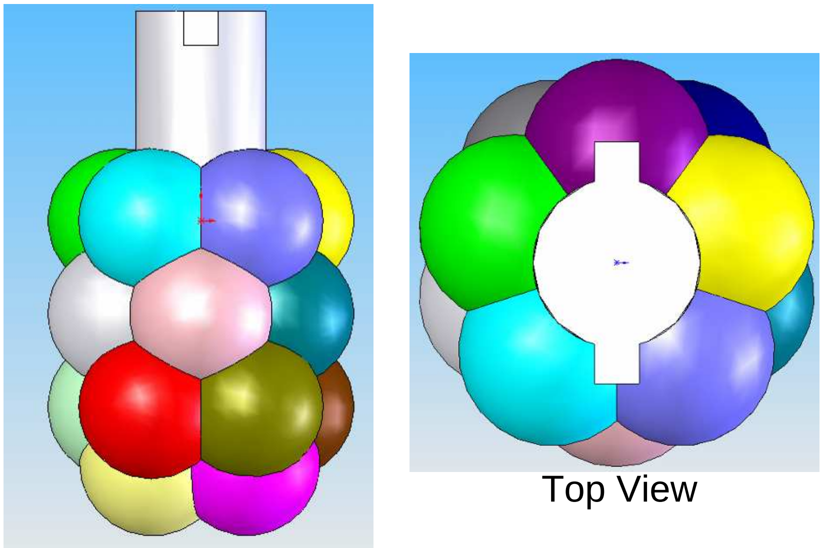

Side View

Top View

Figure 3.5: Emphysemic Alveolar Sac CAD Model

The emphysema model had the same duct diameter and length as the healthy model. Figure 3.5 shows the emphysema alveolar sac CAD model for the side and top views. The depth to mouth diameter ratio, effective airway diameter, number of alveoli, alveoli radius and the volume of the alveolar sac was larger then the healthy alveolar sac. The dimensions of the emphysema alveolar sac CAD model are shown in Table 3.1.

3.2 Manufacturing Procedure and Material

The manufacturing technique was first developed by the Alveolar Sac Senior Design Team 2006-2007. The process involved making a male cast and using the male cast to construct the female hollow cast. The hollow cast was what is used in the PIV experimentation. A schematic of the overall process of making the final model, used for PIV, is shown in Figure 3.6.

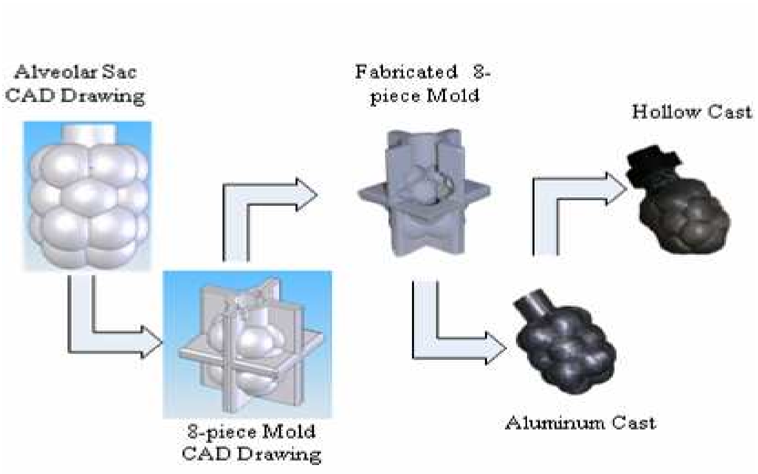

Figure 3.6: Schematic of the Manufacturing Process (Senior Design, 2006 – 2007).

3.2.1 Male Aluminum Mold

The male cast part must be made out of a metal or glass in order to work with the female casting material. The hollow casting material reacts with ceramic and plastic materials. The male cast for


Side View
Top View

Figure 3.7 Healthy Alveolar Sac Aluminum Cast.

the balloon model was the glass boiling flask. The alveolar sac large scale CAD models were 75 times the small scale size. The large scale models were scaled based on the non-dimensional fluid scaling parameters (Section 4.1). The process in making the male cast was as follows; design an eight piece female mold based on the CAD model, fabricate the female mold with Rapid Prototyping (Mechanical Engineering Technology Department, RIT) and cast the male mold out of aluminum. The alveolar sac casts were made in the School for American Crafts at RIT. The healthy aluminum cast lost some model definition during the aluminum casting process. In order to re-define each alveolus a Dremel was used, to define the areas in between each alveolus. Figure 3.7 shows the final aluminum cast for the healthy alveolar sac, and Figure 3.8 shows the final aluminum cast for the emphysema alveolar sac.


Side View

Top View

Figure 3.8: Emphysemic Alveolar Sac Aluminum Cast

3.2.2 Compliant Hollow Cast

The female hallow cast is made out of Ultraflex from Douglas and Sturgess Inc. The material's index of refraction, after shaped into the hollow cast, was 1.481+/- 0.002 (Nelsy Carcamo, Department of Science and Mathematics, NTID, RIT). The index of refraction of the material needed to be similar to the index of refraction of the fluid, in order to do the PIV analysis. The material was chosen based on its high compliance and index of refraction.

Each time a new hollow cast was needed, the following process needed to be completed. The material is a thermoplastic elastomer; therefore it melts and turns into a liquid when heat is applied. Because the hollow cast must be clear for the PIV analysis, it was important not to burn the material during the heating process. First, the solid Ultraflex material needed to be cut into pieces approximately $1cm^3$. The small cubes allowed for an increased surface area to volume ratio, which made it easier and quicker to melt. The small cubes were melted by placing a small amount of the $1cm^3$ pieces must be put in a beaker that was heated by a heat source that provided at least 400ºC of heat. Small amounts of the material were added when the cubes already in the beaker were molten. Particular attention was made in making sure that the molten material was continuously stirred; the material had a potential to burn and yellow. When there was enough material to make a mold, it was decided on as to how thick the final model must be, since the thickness of the model could be altered by the temperature of the material. The viscosity of the material depended on the temperature of the material; the viscosity decreased as the temperature increased. If the model needed to be very thin, then the model itself could be heated using a heat gun. Heating the model allowed for the material to still remain hot as the model was dipped, which kept the viscosity low and the model material thin.

After the material was at the correct temperature and viscosity, the male mold was dipped into the molten Ultraflex material. The balloon male mold was a 50 ml boiling flask and the alveolar sac male molds were the aluminum casts. Care was taken in making sure the casts did not touch the beaker walls, for if the casts bumped the breaker walls, it would ruin the hollow cast model. The Ultraflex dripped as the model was pulled out of the beaker. It was undesirable to get the drip on the hollow cast, for it would create non-uniform thickness in that area, therefore care was taken in controlling the drip. Once the model was out of the molten Ultraflex, it was rotated until all material was dry, approximately 1 minute, in order to minimize the thickness variation. The Ultraflex material had be completely cool, solidified, before the hollow cast could be removed from the male aluminum cast. To speed up the cooling process, cold water was run over the hollow cast.

The model was prone to tearing and bubbles, therefore the manufacturing process could become tricky. It was determined, that the balloon hollow cast needed to be made with thicker walls, because of the amount of experimentation and learning that was conducted on it. Thinner walls were needed, because of the complex geometry, for the healthy and emphysema hollow casts. Material would build up in the defined areas of the hollow cast. Figure 3.9 shows a potential area for material build up. The areas of the material build up would show up in the PIV photographed image, as shown in Figure 3.10. Errors would occur, only in the blurry areas of the image, during the PIV vector analysis. It was not fully understood why the blurry spots appeared on the photographed image. Possible reasons may be as follows; the difference in the index or

Figure 3.9: Alveolar Sac Aluminum Cast (Areas of potential material build up are outlined.

refraction between the glycerin and the material, the material build up areas are reflecting light, or the built up areas are not allowing light to pass through them. Reducing the blurry areas by making the material thinner, as well as avoiding the blurry area during the PIV vector analysis, aided in assuring that the blurry areas did not influence the final PIV results.

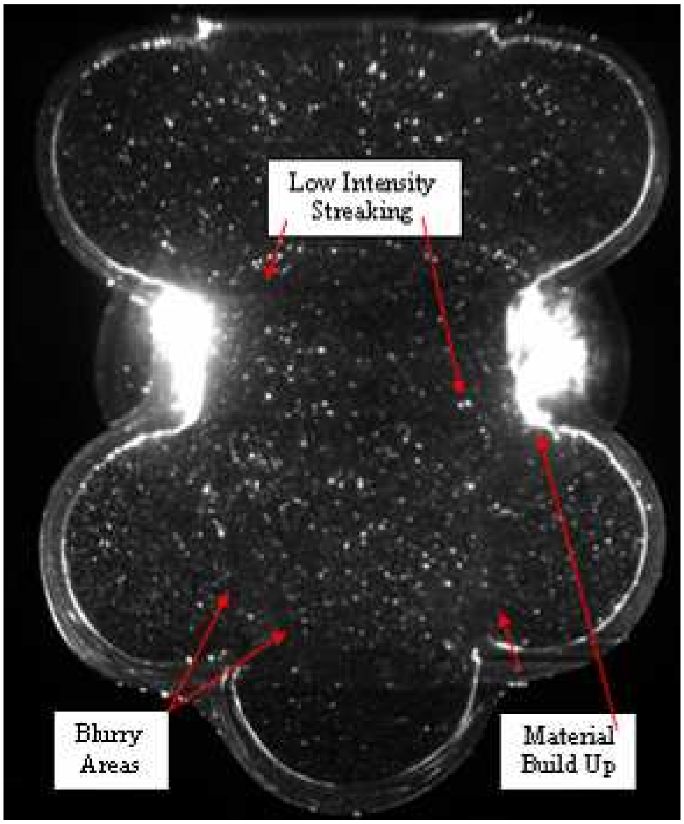

Figure 3.10: Healthy Alveolar Sac PIV Images with Problems Due to Material Build Up Highlighted

3.3 Measurement Analysis

A measurement analysis was performed on the alveolar sac models in order to validate the geometry of the models. The CAD small scale models were compared to alveolar sac and alveoli dimensions found in literature. The geometry was validated two ways; by the effective airway diameter and performing a depth, to mouth diameter analysis. The CAD alveolar sac large scale model and the aluminum cast for both the healthy and emphysematic alveolar sacs were compared to each other. The analysis allowed for validation of geometry for the aluminum cast manufacturing procedure.

3.3.1 Effective Airway Diameter Analysis

Kohlhaufl et al (1988) compared the effective airway diameter of healthy and emphysematic lungs. The effective airway diameter is the average diameter of the alveolar sac. In order to obtain the range of possible effective airway diameters in the models, the effective airway diameter was measured two different ways. Figure 3.11 shows the two ways the effective airway diameter was measured. The first measurement measured the smallest possible effect airway diameter and the second measurement measured the largest effective airway diameter. The measurements were taken parallel to the top of the model. Table 3.2 expresses the effective airway diameter for the small scale healthy and emphysemic alveolar sacs compared to the article. The effective airway diameter of the CAD models is within the range reported by Kohlhaufl et al. (1988). The effective airway diameter reported by Haefeli-Bleuer & Weibel (1988) is much lower, as mentioned in Section 3.1.2, and was inconsistent with articles that reported the effective airway diameter of alveolar sacs.

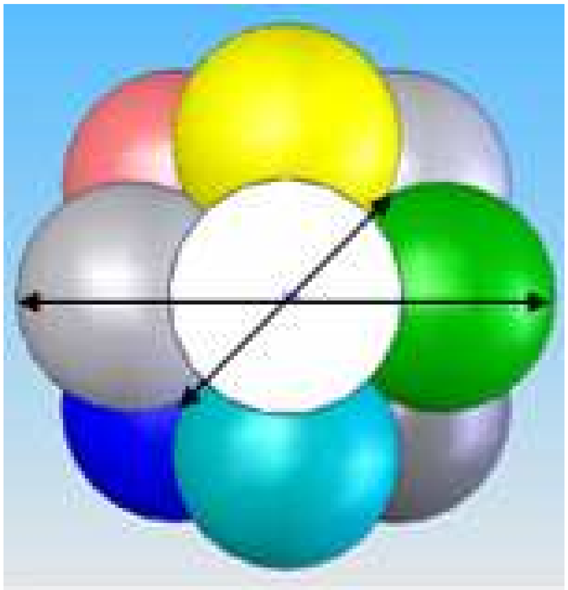

Figure 3.11: Different Ways to Measure Effective Airway Diameter

Table 3.2: Effective Airway Diameter Comparison			
	Kohlhaufl et al (1988)	Haefeli-Bleuer & Weibel (1988)	CAD Model
Healthy Alveolar Sac (mm)	0.39	0.25	0.3116 - 0.554
Emphysemic Alveolar Sac (mm)	0.63	N/A	0.553 - 0.589

3.3.2 Depth to Mouth Diameter Analysis

An alveolus shape analysis was performed on the healthy and emphysema CAD models and compared to findings from literature (Klingele and Staub, 1970 and Mercer et al., 1987). Mercer et al (1987) measured the depth and mouth diameter of rat alveolar tissue from excised rat lungs at various lung inflations. The alveoli measurements from Kingele and Staub (1970) were performed on excised cat lungs at different lung inflations. Both articles measured the depth to mouth diameter ratio during inflation and deflation. The articles did not specify exactly where the dimensions were taken.

Because of the various methods of measuring the depth to mouth diameter of an alveolus, three different methods were used on the alveolar sac CAD models. Table 3.3 expresses the measurements for both the healthy and emphysematic alveolar sacs at FRC, 50% TLC, initial breathing volume of the lung. Figure 3.14 compares the depth to mouth diameter ratio for the alveolar sac

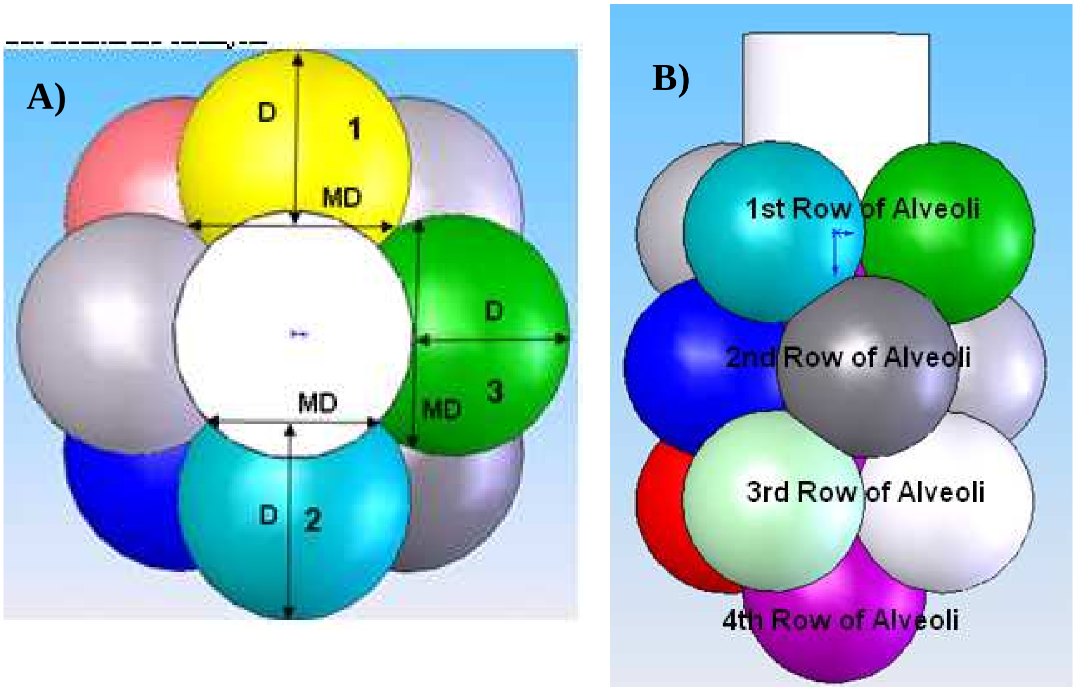

Figure 3.12: Healthy Alveolar Sac CAD Model. A). Alveolus Depth (D) to Mouth Diameter (MD) Locations. B). Row Location.

CAD models to the articles. Figure 3.12A and Figure 3.13A show the location of each of the methods used for measuring the depth to mouth diameter ratio for the healthy and emphysema alveolar sacs, respectively. Method 1 was measured three different times for each alveolus on each row. Figure 3.12B and Figure 3.13B show the different rows for the healthy and emphysema alveolar sac, respectively. Method 1 was taken three times, for each row, because of the variation in the mouth diameter and depth based on where the measurement was taken. On some areas of the model the alveoli are merged, where other parts they are not. The second row of alveoli was touching both the first row and the third row, therefore the alveolus depth was smaller then the other rows. For method 1, the largest, smallest and medium depth to mouth diameter measurements were taken, and the average was computed. Method 2 and 3 were only applied to row 1, for the measurement would be the same for all of the rows. From the analysis, it was determined that the healthy alveolar sac model is comparable to the depth to

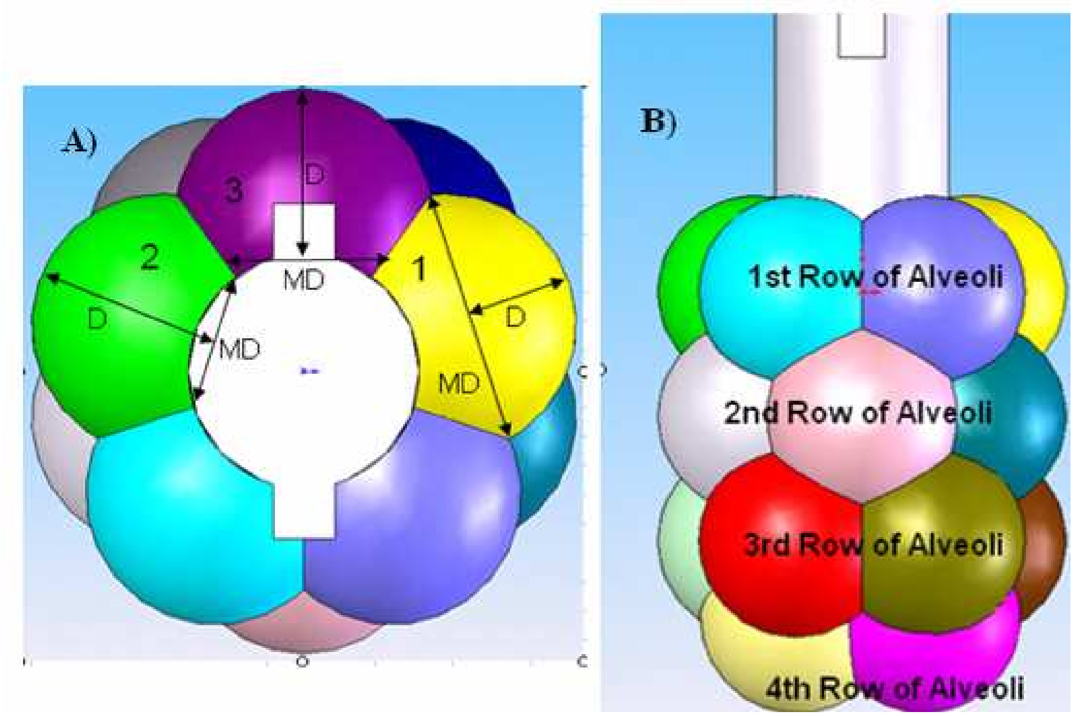

Figure 3.13: Emphysematic Alveolar Sac CAD Model. A). Alveoli Depth (D) to Mouth Diameter (MD) Locations. B). Row Location.

mouth diameter reported in the articles. The method that best represents the depth to mouth diameter ratio, method 1, is very similar to Kingele and Staub (1970), especially for rows 3 and 4. Method 1 for the emphysematic model depth to mouth diameter ratio is much smaller compared to the healthy, which is consistent with this disease. In emphysematic lungs the alveoli become less defined and begin to merge, which would make the mouth diameter larger, and the alveolus depth smaller, therefore the ratios are considered to be physiologically realistic. Method 2 for the healthy alveolar sac CAD model falls between Kingele and Staub (1970) and Mercer et al (1987) data. Method 3 is similar to method 1 and is within the range of Kingele and Staub (1970). Method 2 and 3 for the emphysematic alveolar sac CAD model has a much larger ratio then method 1. The two methods are not accurate representation of the emphysematic lung. As shown in Figure 3.13 A, method 2 and 3 are for areas of the alveolus where the tissue is not meeting, therefore method 2 and 3 were not a good representation of the actual depth to mouth diameter in emphysema. From the depth to mouth diameter analysis, it was concluded that the healthy depth to mouth diameter ratio was comparable to the ratio reported in the articles. The emphysema depth to mouth diameter is larger then the emphysema, for method 1, which is consistent with the disease.

Table 3.3: Alveolar Sac CAD Model Dimensions

	Healthy			Emphysematic		
	Average Mouth Diameter (MD)	Average Depth (D)	D/MD	Average Mouth Diameter (MD)	Average Depth (D)	D/MD
	mm			mm		
Measurement 1 - Row 1	0.23	0.16	0.72	0.28	0.12	0.45
Measurement 1 - Row 2	0.23	0.15	0.64	0.25	0.09	0.34
Measurement 1 - Row 3	0.21	0.18	0.87	0.27	0.11	0.40
Measurement 1 - Row 4	0.21	0.17	0.81	0.27	0.11	0.41
Measurement 2	0.18	0.20	1.14	0.15	0.20	1.36
Measurement 3	0.23	0.16	0.71	0.18	0.18	1.00

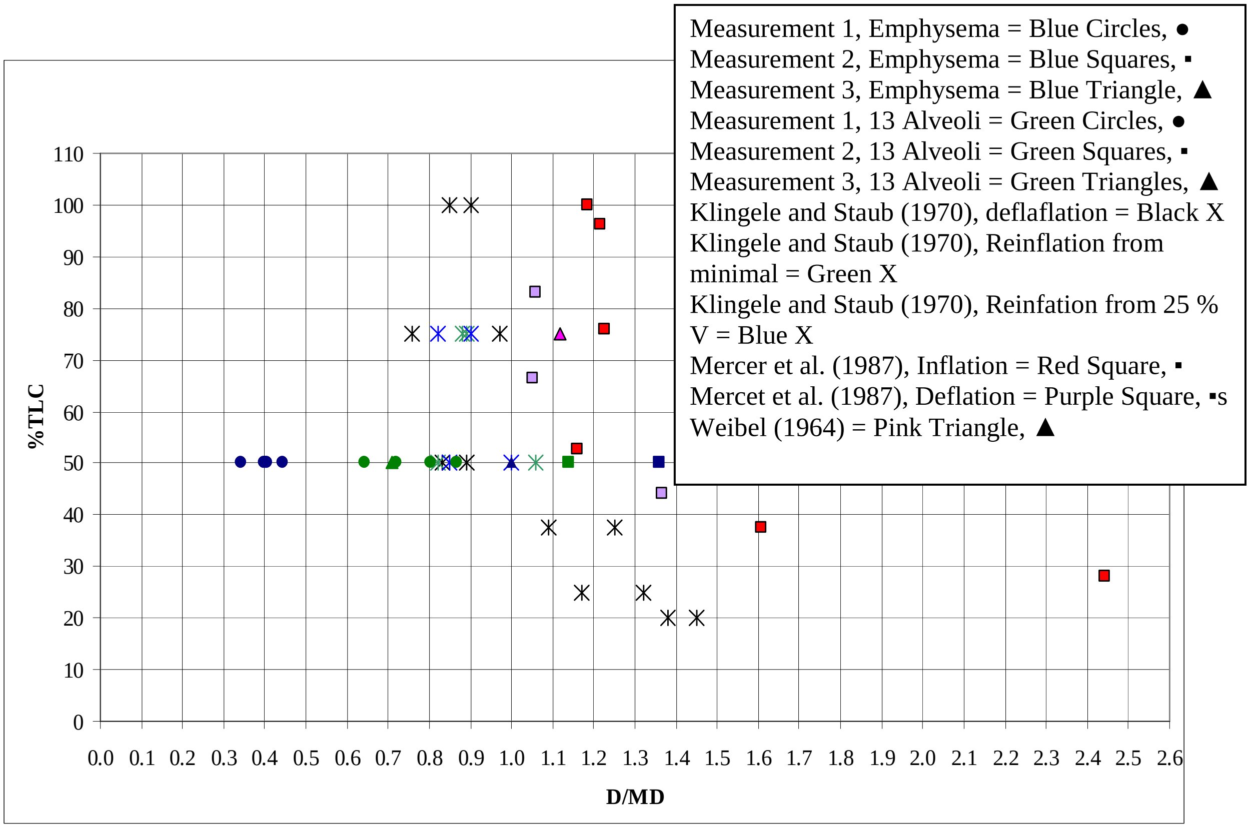

Figure 3.14: Depth to Mouth Diameter Analysis. Comparison between Alveolar Sac CAD and Published Values.

3.3.3 Comparison between Large Scale CAD Model and Aluminum Cast

A comparison was made between the large scale CAD model and the aluminum cast models for the alveolar sacs, which is shown in Table 3.4. The aluminum cast model's dimensions where taken with a caliper, which had an accuracy of 0.025 mm. There were some differences between the aluminum cast model and the CAD model. The duct diameter of the aluminum cast model differed from the CAD model. In order to account for this difference, the fixture to which the alveolar sac model attaches to contains an inner diameter that matched exactly to the large scale CAD model. The diameter matching was crucial, for the fluid scaling was based off of the duct diameter. The aluminum cast alveolus radius, for the healthy alveolar sac, differed from the CAD dimension. The radius varied on the aluminum cast model by almost 1 mm. The variation was due to the aluminum casting process and the

Dremel work completed on the model. The depth to mouth diameter ratio also changed in the aluminum cast of the healthy alveolar sac. By observation, it was concluded that the depth to mouth diameter ratios were increased when the alveoli were made more defined with the Dremel tool. It was determined that the aluminum cast models were good a representation of the large scale alveolar sac CAD models, and therefore good representation of in vivo healthy and emphysema alveolar sacs.

Table 3.4: Large Scale Alveolar Sac Dimensions

	Healthy Alveolar Sac		Emphysematic Alveolar Sac	
	CAD Model	Aluminum Cast Model	CAD Model	Aluminum Cast Model
Duct Diameter (mm)	18.75	18.54	18.75	19.05
Alveolus Radius (mm)	9.15	8.38 - 9.34	10.5	10.5
Sac Length (mm)	56.1	54.2	56.1	56.6
Effective Airway Diameter (mm)	23.37 - 41.55	29.8 - 41.86	41.475 – 44.175	40.94 - 44.45

Chapter 4
Model Fluid Dynamics

In order to represent the fluid dynamics within the body, the fluid flow dynamics needed to be considered. Two steps were taken in order to make sure the flow represented what is occurring in the body; fluid scaling from the small scale in vivo size to the large scale experimental size, and defining the flow curve at the inlet of each model.

4.1 Scaling up the Flow Parameters

In order to scale in vivo geometry to experimental size, the fluid needed to be scaled. The majority of the scaling theory was completed by the author as a part of the Alveolar Sac Team Responsibility in Senior Design 2006 - 2007. Fluid scaling defines what parts of the governing equation controls the behavior of the fluid. In order to properly represent what is occurring in the body, the same forces of the governing equation must dominate the fluid flow in the experimentation.

4.2.1 Theory

Fluid flow is governed by the incompressible, constant viscosity, Navier-Stokes partial differential equation

$$\rho\left[\frac{\partial \vec{u}}{\partial t} + \vec{u} * \nabla \vec{u}\right] = -\nabla P + \mu \nabla^2 \vec{u} + \rho \vec{g} \qquad (4.1)$$

where ρ is the density of the fluid, $\vec{u}$ is the velocity vector, t is time, P is the pressure, μ is the dynamic viscosity and g is the gravitational vector. The gradient is defined as,

$$\nabla = \frac{\partial}{\partial x}\hat{i} + \frac{\partial}{\partial y}\hat{j} + k\frac{\partial}{\partial z}\hat{k} \tag{4.2}$$

The Navier-Stokes equation is simply a force balance; the first term is the inertia forces, the second term is the pressure forces, the third term is the viscous forces and the fourth term is the gravitational forces. The conservation of mass is quantified by the continuity equation

$$\nabla \bullet \vec{u} = 0 \tag{4.3}$$

A well-posed system of equations to solve for the alveolar sac motion and associated fluid dynamics requires boundary conditions to be specified. The effective of the gravitational term is to adjust the shape of the alveolar sac through the balance of forces across the alveolar membrane. Apart from this, gravity does not impart motion to the liquid, by introduction of stream functions into the set of general equations. Thus we can neglect the gravitational term in what follows.

Scaling reveals the dominant terms in the Navier-Stokes. The velocity, u, is defined on the order of U,

$$u \approx U \tag{4.4}$$

where U is the average velocity at the entrance to the sac. The time scale is defined based on the oscillating nature of the expanding and contracting system

$$t \approx \frac{1}{\omega} \tag{4.5}$$

where $\omega=2\pi f$ and f is the frequency (Hz). The length scale is based on the diameter, D, of the system,

$$\nabla \approx \frac{1}{D} \tag{4.6}$$

The pressure scale is unknown, and is therefore left arbitrary at this point in the scaling process as,

$$P \approx P_s \tag{4.7}$$

Each variable in Equa. 4.1 can be defined as a non-dimensional parameter based on the scales defined in Equa. 4.4 – 4.7. The variables are defined as

$$u = u^{*}U \tag{4.8}$$

$$\nabla = \frac{\nabla^{*}}{D} \tag{4.9}$$

$$P_0 = P^{*}P_s \tag{4.10}$$

$$t = \frac{t^{*}}{\omega} \tag{4.11}$$

where the * denotes the non-dimensional parameter. Substituting and rearranging Equa. 4.8 - 4.11 into Equa. 4.1, gives the non-dimensional form of the Navier-Stokes equation.

$$\left[\frac{\rho\omega D^{2}}{\mu}\right]\frac{\partial u^{*}}{\partial t^{*}} + \left[\frac{\rho DU}{\mu}\right]\left[u^{*}\nabla^{*}u^{*}\right] = -\left[\frac{P_s D}{\mu * U}\right]\nabla^{*}P^{*} + \nabla^{*2}u^{*} \tag{4.12}$$

Three important dimensionless parameters are found in this non-dimensional equation. Reynolds number is defined by

$$\mathrm{Re} = \frac{\rho DU}{\mu} \tag{4.13}$$

which determines the role of the steady inertia forces relative to viscous forces. The second non-dimensional parameter,

$$B = \frac{\omega\rho D^{2}}{\mu} \tag{4.14}$$

which determines the role of the non-steady inertia forces. The non-dimensional parameter B is related to the Womersley number as,

$$Wo = \frac{D}{2}\sqrt{\frac{2\pi f}{\nu}} \tag{4.15}$$

(Womersley, 1955) . Substituting Equa. 4.14 into 4.15 gives the second non-dimensional parameter as

$$B = 4Wo^2 \tag{4.16}$$

The third non-dimensional parameter is

$$C = \frac{P_s D}{\mu U} \tag{4.17}$$

which determines the determines the scale Ps, once it is balanced against the other dominant terms in the Navier-Stokes equations.

In the in vivo analysis of the dimensionless parameters (Section 4.1.2), it was found that both the Reynolds number and the Womersley number are very small, such C=1 in Eq. 4.12 which defines the pressure scale as,

$$P_s = \frac{\mu U}{D} \tag{4.18}$$

In this limit, the Navier-Stokes equation reduces to

$$-\nabla^* P^* + \nabla^{*2} u^* = 0 \tag{4.19}$$

which when coupled with the continuity equation (Eq.4.3) yields Stokes' description for steady flow.

In order to have the Stokes Equation govern the fluid flow for the scaled up PIV experiment the non-dimensional parameters, Reynolds number and Womersley number, must be less then one. With this theory, the pressure and viscous forces will govern the fluid behavior.

4.1.2 In Vivo Reynolds and Womersley Numbers

The flow in and out of an in vivo alveolar sac is driven by the expansion and contraction of the sac. Reynolds number (Equa. 4.13) and Womersley number (Equa. 4.15) can be defined based on the expansion and contraction of the sac.

The average velocity is defined as

$$u_z = \frac{\overline{Q}}{A} \tag{4.20}$$

where $\overline{Q}$ is the average flow rate during a breathing cycle. A, the cross sectional area of the duct, is given by

$$A = \frac{\pi D^2}{4} \tag{4.21}$$

The final volume, V_f, after expansion, is defined as

$$V_f = (1+E)V_i \tag{4.22}$$

where E is the fraction expanded and V_i is the initial volume. The total average time to complete the expansion is

$$t = \frac{V_f - V_i}{\overline{Q}} \tag{4.23}$$

and frequency is defined as

$$f = \frac{1}{2t\pi} \tag{4.24}$$

Substituting Equa. 4.16, 4.17, 4.18, 4.23 and 4.24 into 4.12 gives Reynolds number as a function of the breathing variables for in vivo conditions

$$\mathrm{Re} = \frac{8EV_i f}{D\nu} \tag{4.25}$$

The Womersley number is already in terms of breathing variables, Equa. 4.15. The variables used to compute the Reynolds and Womersley number for in vivo conditions and the non-dimensional parameters are shown in Table 4.1. The expansion, E, was estimated based on a 3000 ml FRC with a tidal volume (TV) of 900 ml. For normal breathing conditions a typical TV is 750 ml. The 900 ml was used for the worst case, such as a smoker volume or intake for medical inhalation. As shown in Table 4.1, the Reynolds and Womersley numbers are much less then one, therefore the scaling theory developed in Section 4.1 applies. In order to have the large scale experimental conditions represent the in vivo flow, the Reynolds and Womersley numbers were kept less then one, Section 4.3.

Table 4.1: Estimated In Vivo Alveolar Sac Conditions

Initial Sac Volume, V_i(Haefeli-Bleuer and Weibel, 1988)	0.037	mm^3
Airway Diameter, D (Haefeli-Bleuer and Weibel, 1988)	0.25	mm
Kinematic viscosity, ν (Air at Body Temperature)	17.10	mm^2/s
Breathing Frequency, - Light Exertion (Reference)	14	breaths/min
Expansion, E*100	30	Percentage
Reynolds Number, Equa. (4.25)	4.85E-03	
Womersley Number, Equa. (4.15)	0.037	

4.1.3 Possible Experimental Parameters

An investigation was performed in order to determine the range of experimental parameters that would be able to simulate the in vivo flow field in the experimental scaled up geometry. Three parameters were able to be adjusted; the fluid, the size of the model and the time to complete the breathing cycle.

4.1.3.1 Influence of Index Matching Fluid

The non-dimensional parameters vary based the kinematic viscosity of the fluid. Both Reynolds number (Equa. 4.13) and Womersley number (Equa. 4.15) decrease as the kinematic viscosity of the fluid is increased. It was decided a glycerin and water mixture would be used in order to alter the viscosity of the fluid. Table 4.2 shows how the viscosity of the glycerin and water mixture change based on the mixture ratio. For PIV it is very important that the index of refraction of a curved model matches that of the fluid surrounding the model. Because of the constraint of the index of refraction, the fluid's index of refraction needed to match the hollow cast. The index of refraction of the hollow cast was measured to be 1.487 +/- 0.002 (Nelsy Cacamo, Department of Science and Mathematics, NTID). Based on the index of refraction constriction, it was decided that the fluid needed to be one hundred percent glycerin.

Table 4.2: Glycerin and Water Mixture Properties for Different Ratios of Glycerin and Water

Percentage of Glycerin	Density (kg/cm^3)	Viscosity (kg/cm*s)	Kinematic Viscosity (cm^2/s)	Index of Refraction
0.1	1.02E-03	1.43E-03	1.40	1.348
0.2	1.05E-03	2.85E-03	2.71	1.364
0.3	1.08E-03	4.27E-03	3.96	1.379
0.4	1.10E-03	5.69E-03	5.15	1.395
0.5	1.13E-03	7.11E-03	6.29	1.410
0.6	1.16E-03	8.52E-03	7.38	1.425
0.7	1.18E-03	9.94E-03	8.41	1.441
0.8	1.21E-03	1.14E-02	9.40	1.456
0.9	1.23E-03	1.28E-02	10.35	1.472
1	1.26E-03	1.42E-02	11.26	1.487

4.1.3.2 Influence of Cycle Time

The flow rate, as a function of Womersley numbers, was calculated by substituting Equa. 4.21 and 4.18 into 4.14,

$$\overline{Q} = \frac{4Wo^2 E V_i \nu}{D^2} \tag{4.26}$$

where 0.3 was used for the expansion, E, 11.3 cm^2/second for the kinematic viscosity, ν. The volume and duct size varied. The volume was determined based on the initial volume of the healthy alveolar sac model, and varied from a volume of 1.05e-4 cm^3, with a duct diameter of 0.025 cm, to a volume of 105 cm^3, with a duct diameter of 2.5 cm. Twenty one different sizes were used for the calculations. The flow rate was calculated for different values of Womersley number, 0.039, 0.1, 0.215, 0.3 and 0.39.

Substituting Equa. 4.22, 4.23 into 4.25 gives time as a function of the breathing parameters,

$$t = \frac{V_i E}{\overline{Q}} \tag{4.27}$$

for the different flow rates for the range of Womersley numbers solved for using Equa. 4.26.

The flow rate (Equa. 4.26) as a function of the time (Equa. 4.27) and model size, based on the duct diameter. Separate graphs were created for the Womersley number of 0.039, 0.1, 0.215, 0.3 and 0.39. Figure 4.1 shows the graph for a Womersley number of 0.039. The duct diameter was read off of Figure 4.1 for breathing cycle times of 5, 10, 15, 20 seconds. The same procedure was completed for all of the Womersely number graphs. For example, at a time of 5 seconds, the duct diameter was read to be 0.23 cm for the Womersley number of 0.039. The cycle time range was determined based on the limitations of the syringe pump, which is restricted based on the amount of volume it can displace with time. The limitations of the pump restricted what size model could be used.

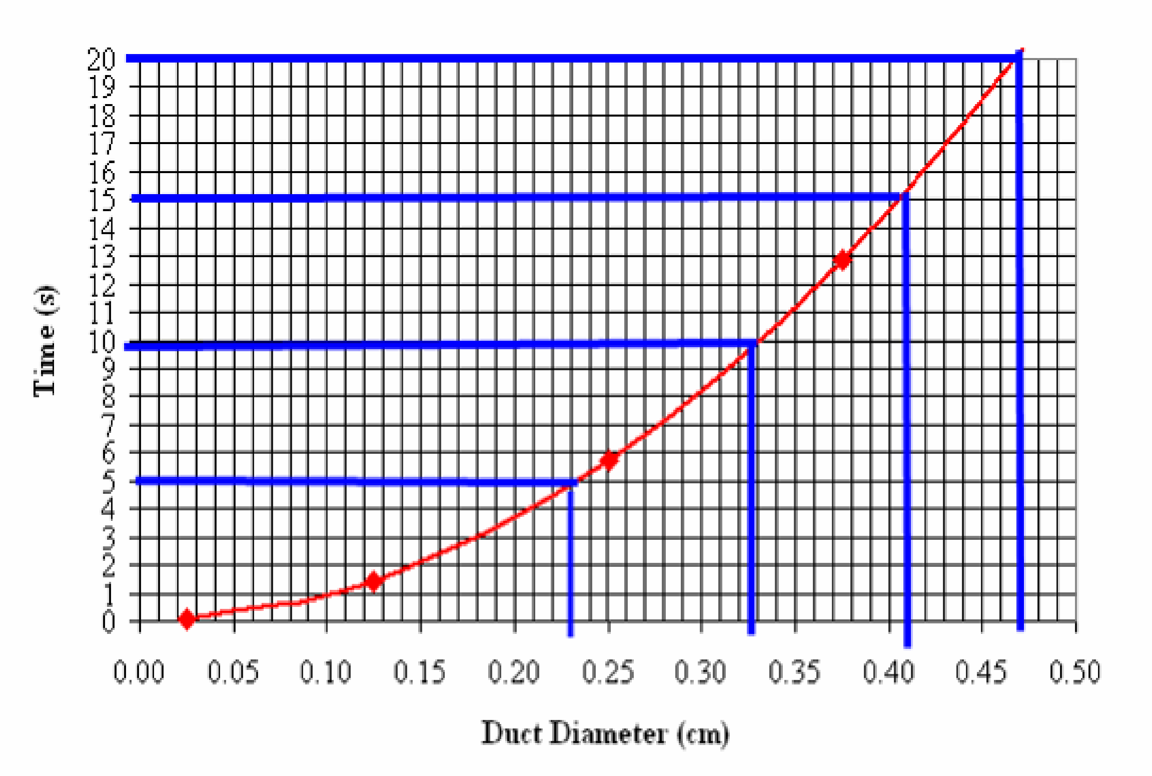

Figure 4.1: Example How Time and Duct Diameter was Read off Graph. Figure shown is for a Womersley number of 0.039.

4.1.3.3 Final Experimental Flow Parameters

The duct diameter and time read off Figure 5.1, for each Womersley number, was used to compute the flow rate for each case. The average flow rate was determined from rearranging Equa. 4.27,

$$\overline{Q} = \frac{V_i E}{t} \tag{4.28}$$

where the initial volume was determined based off the duct diameter and the volume of the healthy alveolar sac model. The Reynolds number, as a function of the flow parameters, was computed by substituting Equa. 4.20 and 4.21 into Equa. 4.13.

$$\mathrm{Re} = \frac{4\overline{Q}}{\nu \pi D} \tag{4.29}$$

Graphs for Reynolds number, Figure 4.2, Womersley number, Figure 4.3 and flow rate, Figure 4.4 were created. The figures were used in determining the range of duct diameter, based on the time, that could be used for the experimentation. It was decided that a model with a duct diameter of 1.875 cm would be used for a time of 8 seconds, for the healthy alveolar sac model. The reason why the model size was chosen was so it would fit in the test rig (Section 5.1), without any alterations. Other sized models could be used, but the model attachment fixture would have to be re-designed. The Reynolds number was approximated to be 0.25, the Womersley number was approximated to be 0.25, and the average flow rate was approximated to be 4 ml/sec. The graphs were also used in approximating the experimental parameters for the emphysema model.

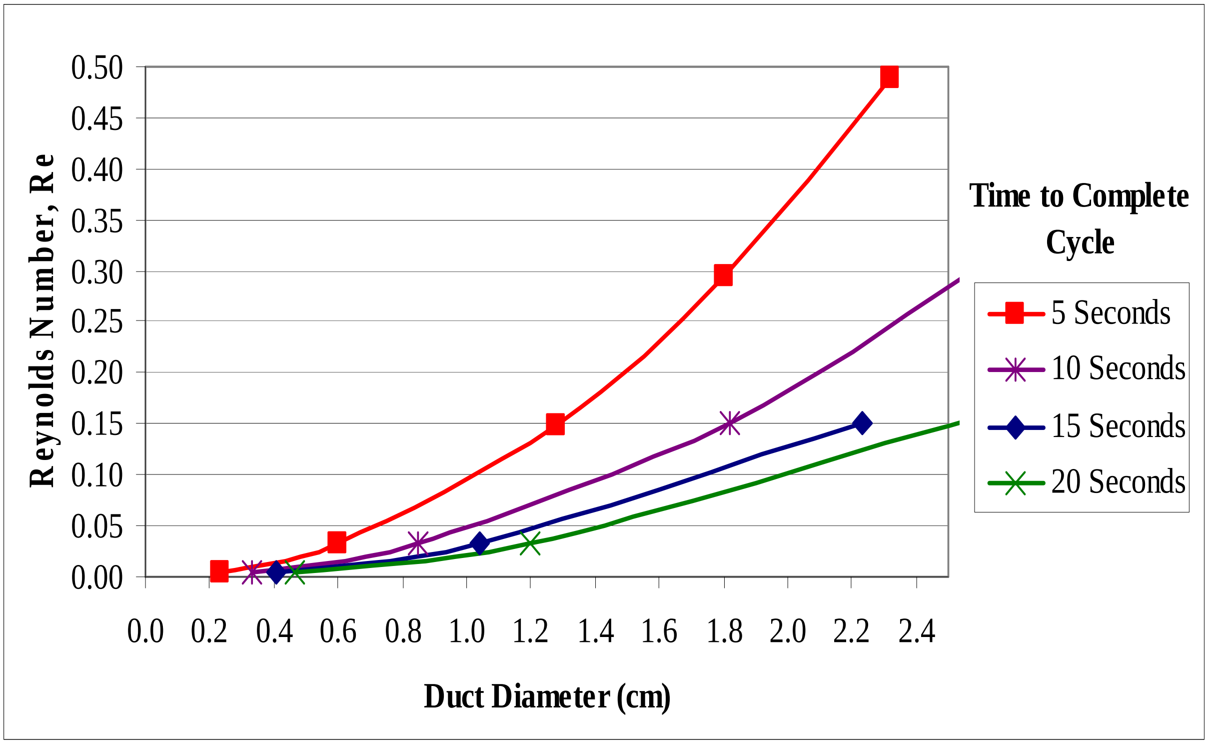

Figure 4.2: Reynolds Number as a Function of Time and Duct Diameter.

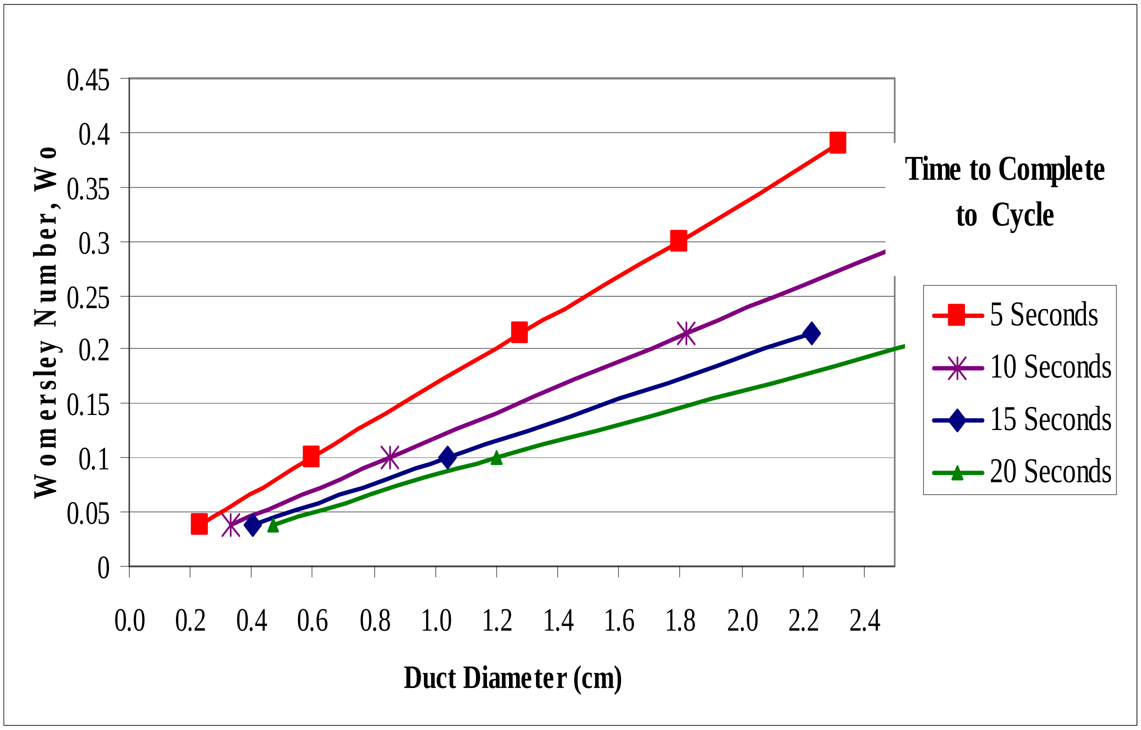

Figure 4.3: Womersley Number as a Function of Time and Duct Diameter.

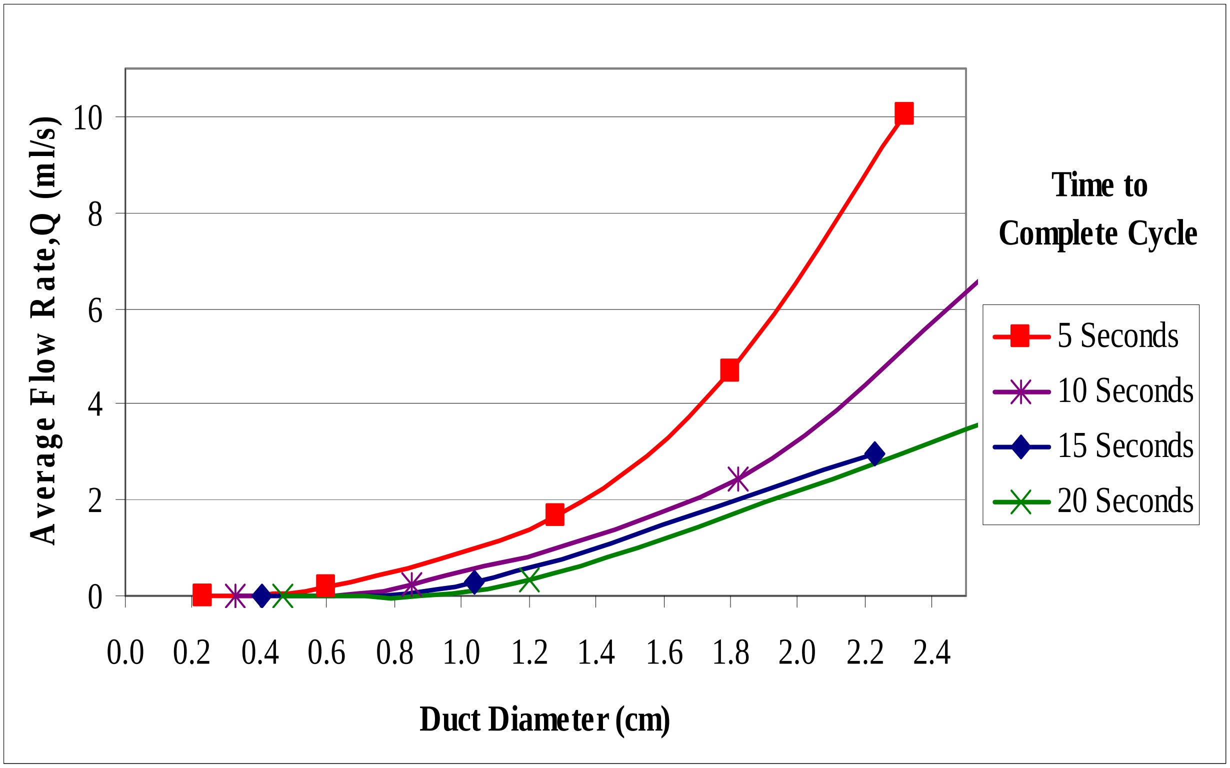

Figure 4.4: Flow Rate as a Function of Time and Duct Diameter.

4.2 Obtaining the Breathing Curve

A realistic, unsteady, breathing curve was used for the PIV and CFD analysis. The flow was measured directly in vivo and scaled to the specific volume of the lung being analyzed. A good, average and defined flow rate curve was not found in literature. Images were found from, but these images were not defined mathematically, making it difficult to apply to the models. Important characteristics from these flow rate curves were noted; the peak at inhale and the exponential decrease in flow rate at the tail end of exhale. These features were used in the determination process of what flow rate curve to use. The overall process in defining the flow rate curve is as follows; in-vivo experimentation using a spirometer, converting the flow rate image into a data file, removing the noise by smoothing the data, scaling the flow rate for the specific experimentation, and importing the flow rate data file into the PIV and CFD experimentation.

4.2.1 Spirometer Measurement

The breathing curve was acquired in the laboratory by use of a spirometer. The spirometer used was Cadio Perfect Spirometer from Welch Allyn. The spirometer captures the flow rate of a person, during breath, by a pivot tube inside the spirometer. While acquiring the flow rate curve, the subject paid particular attention to making sure a full breath was taken; being careful to exhale fully in order to acquire the very slow flow rate that occurs at the end of exhale. Several flow rates were acquired, the flow curve that was a good representation of the flow characteristics was used. The image used for the analysis is shown in Figure 4.5. The magnitude for the

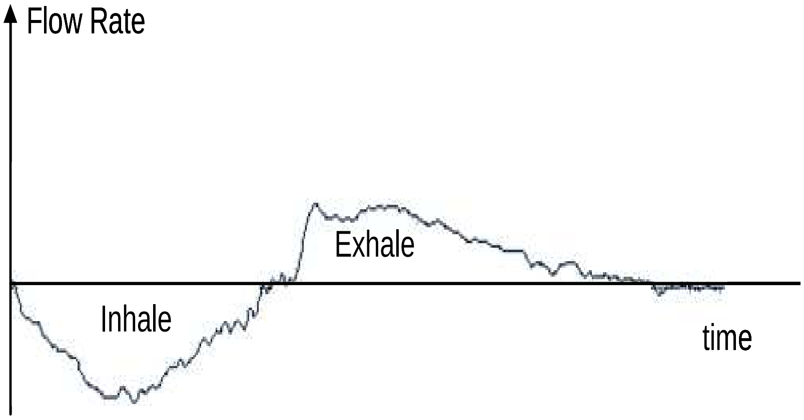

Figure 4.5: Flow Rate Curve from Spirometer Obtained in the Current Work's Laboratory

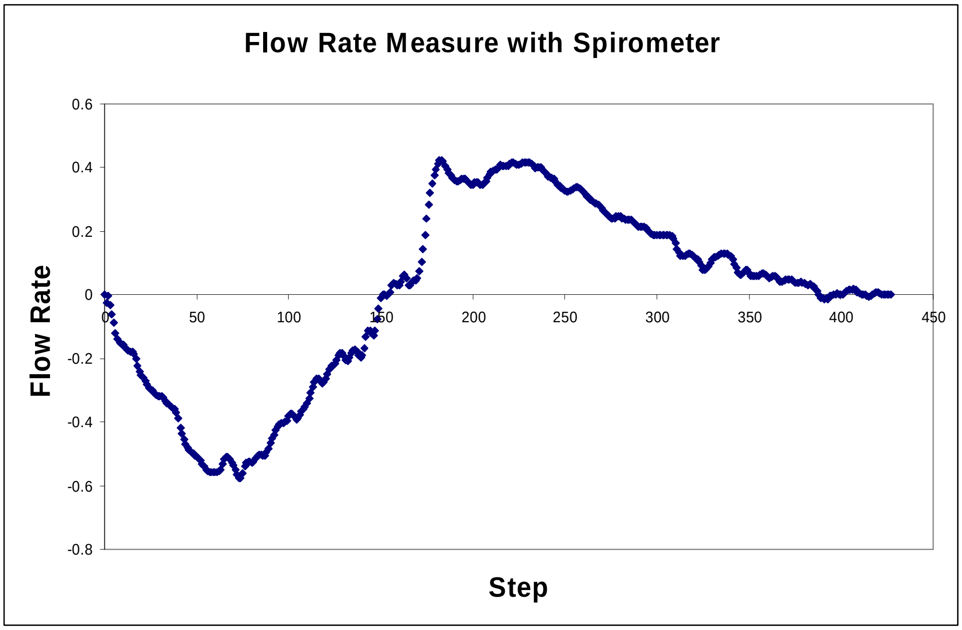

Figure 4.6: Flow Rate versus Time Step Data Defined from Matlab Program.

flow rate at the mouth and time to complete a breath was given with the spirometer, but the measurements were for the subject's specific parameters. Because the curve's magnitude would be altered later for the specific model being analyzed, the magnitude of the flow rate and time were omitted.

A Matlab program developed by Matthew Waldron (Electrical Engineering Department, RIT) was used to convert the image file into data. Figure 4.6 shows the data file outputted from Matlab. The program is included in Appendix B. The Matlab program defined the magnitude of the flow rate and the step size. The values were normalized in a future step for the magnitude for each model.

4.2.2 Noise Smoothing

The data from the spirometer is noisy and therefore it is not ideal to use the noisy data directly for the experimentations. Fitting a curve to the data allowed for removal of the noise. Two curves, one to inhale and one to exhale, was fitted to the data using the least squares method in an Excel program developed by Dr. Steven

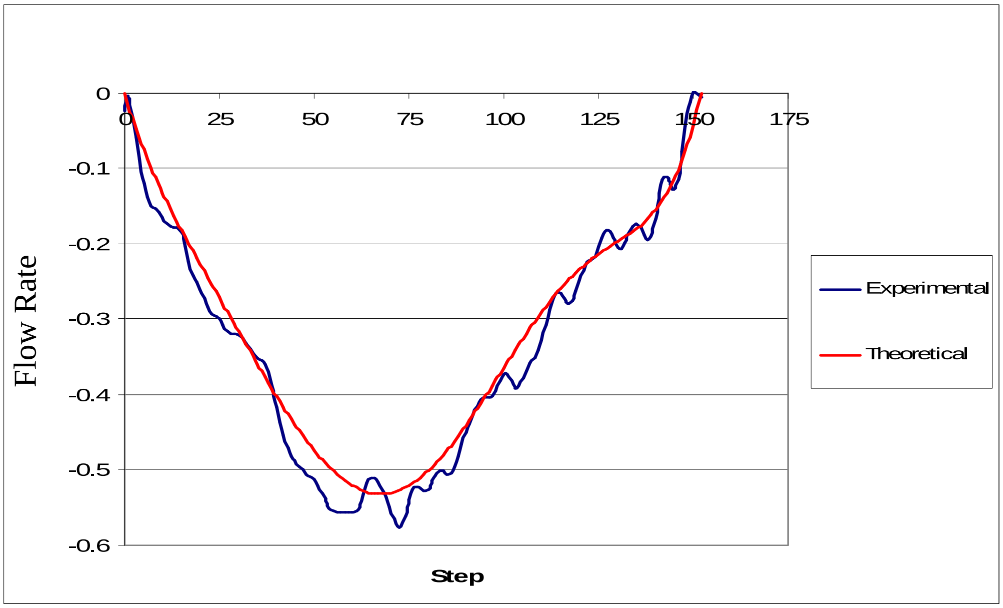

Figure 4.7: Non-Dimensional Inhale with Curve Fit

Weinstein (Mechanical Engineering Department, RIT). The Excel solver function was used in order to adjust coefficients of a polynomial until a best fit was determined. Figure 4.7 shows the curve fit for inhalation and Figure 4.8 shows the curve fit for exhalation. The exhale portion of the flow rate curve was a combination of a polynomial and an exponential curve, which allowed for the exponential characteristic at the end of the exhale curve. It was important that the change in volume was conserved because the experiment model must return to its original volume at the end of exhale. An equal change in volume for inhale and exhale was not achieved by the spirometer measurements. Importance rankings can be set in the Excel solver program, based on different desired line characteristics. Two areas of high importance was specified for the end of exhalation; the first specification was making sure

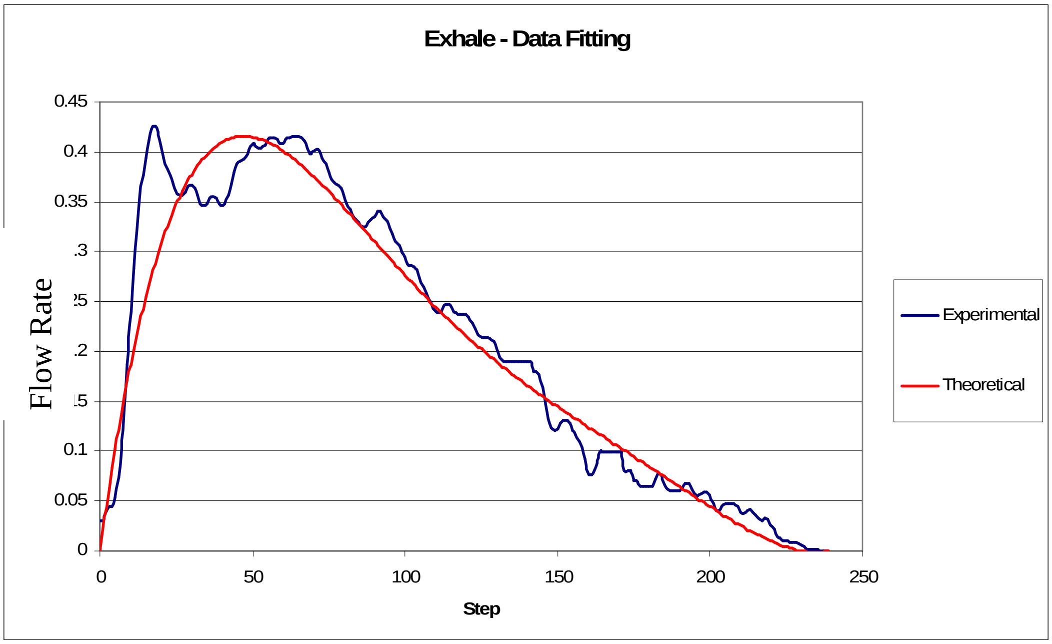

Figure 4.8: Non-Dimensional Exhale with Curve Fit.

the flow rate returned to zero at the end of exhalation. The second importance specification was for the integral of the inhalation and exhalation to be the same, such that the change in volume was conserved. The final data graphs were used to specify the inlet flow rate conditions for each model.

4.2.3 Inlet Flow Conditions for Each Model

The non-dimensional flow rate graphs needed to be converted, to actual flow rate and time values, such that they would represent the inlet flow rate for each of the models. The first step in obtaining the specific model graphs for flow rate was converting the flow rate into change in volume, by taking the integral. This was completed because the change in volume for each experimental model is known, based on the initial volume and the percent expansion, which can be used to give actual values to the normalized data. The volume data was normalized, such that the ranges of values were between zero and one. The normalized volume data was multiplied by the maximum change in volume of the model. The maximum change in volume for the balloon was 21.48 ml, 13.29 ml for the healthy alveolar sac and 18.15 ml for the emphysema alveolar sac. The time portion of the graph was normalized, from zero to one, and then multiplied by the total time to complete a cycle. The time for the balloon was 12 seconds, 8 seconds for the healthy alveolar sac and 11 seconds for the emphysema alveolar sac. The time was determined based on the fluid analysis (Section 4.1.3.3) and the pump limitations. The change in volume and time could also be altered, and specified for different cases, in the Labview user interface (Section 5.1.3). Figure 4.9 shows the change in volume curve, with respect to time, for the balloon model. The PIV experimental healthy alveolar sac change in volume curve versus time is shown in Figure 4.10. Figure 4.11 shows the change in volume curve, with respect to time, for the PIV experimental emphysema alveolar sac.

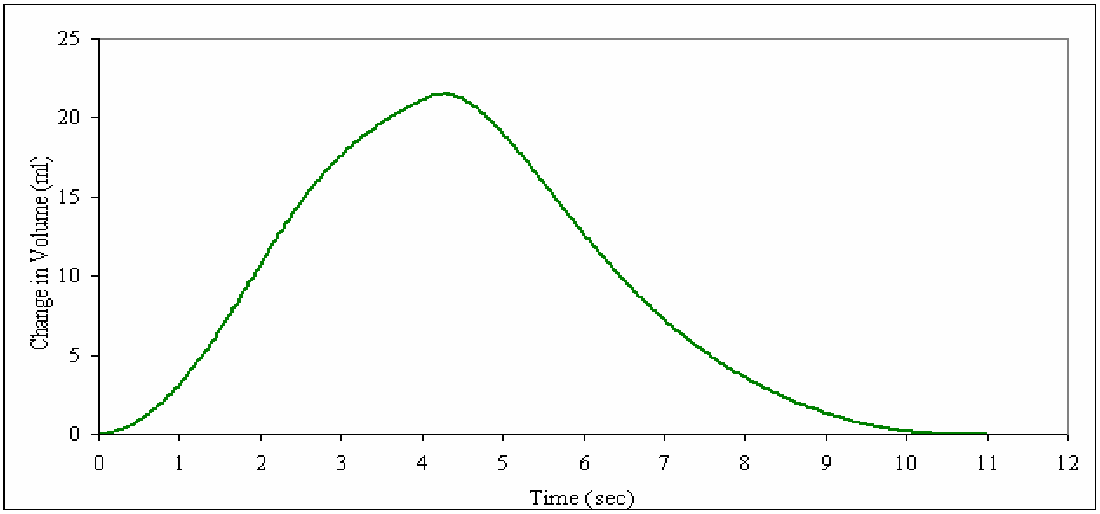

Figure 4.9: Volume versus Time for Balloon Model.

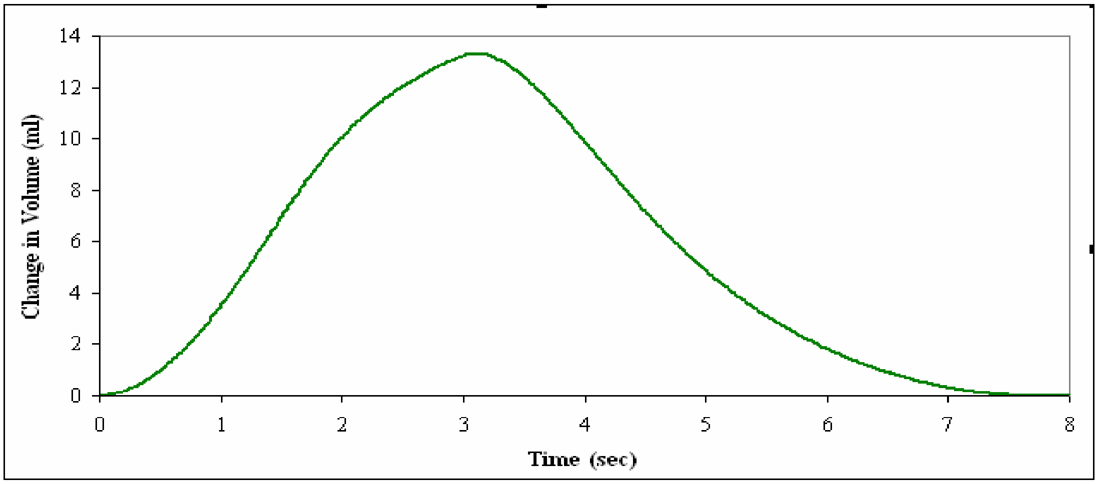

Figure 4.10: Volume versus Time for PIV Experimental Healthy Alveolar Sac.

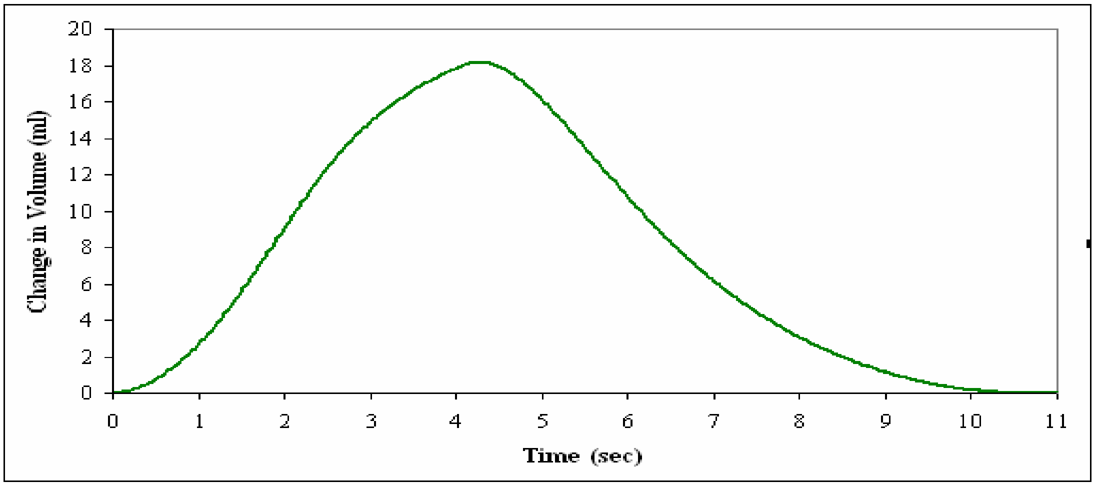

Figure 4.10: Volume versus Time for PIV Experimental Healthy Alveolar Sac.

The flow rate graph was then obtained by taking the derivative of the volume curve for each experimental model. Figure 4.12 shows the flow rate curve, with respect to time, for the balloon model. The PIV experimental healthy alveolar sac flow rate curve versus time is shown in Figure 4.13. Figure 4.14 shows the flow rate curve, with respect to time, for the PIV experimental emphysema alveolar sac.

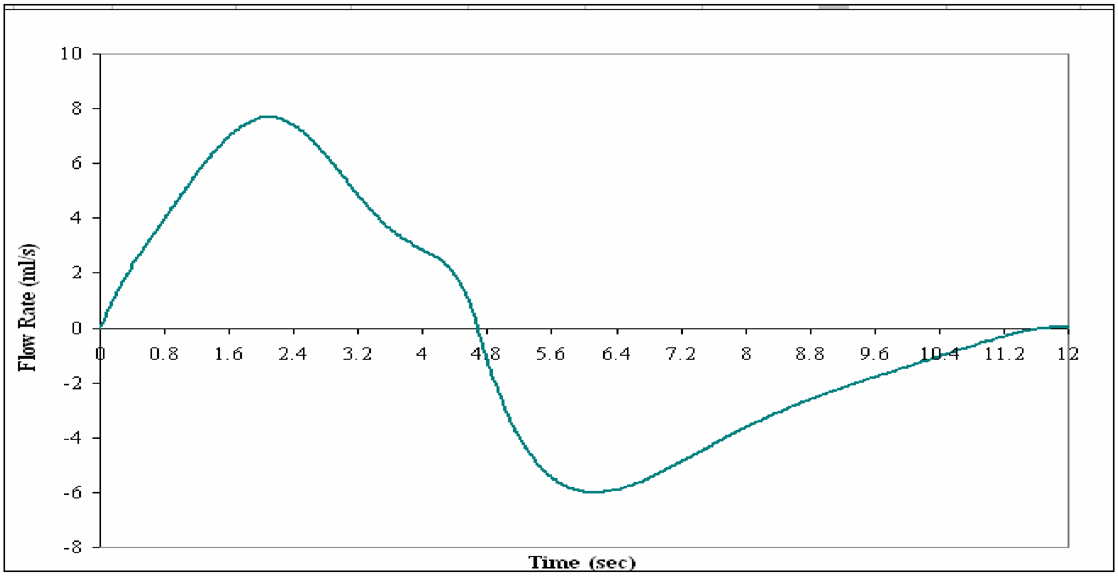

Figure 4.12: Flow Rate versus Time for Balloon Model

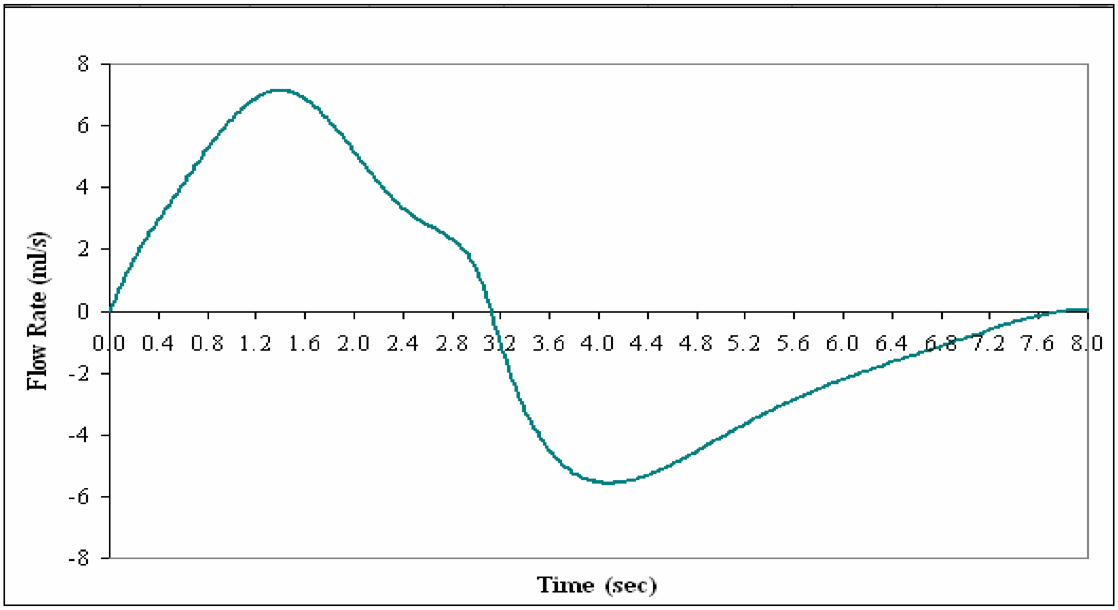

Figure 4.13: Flow Rate versus Time for PIV Experimental Healthy Alveolar Sac.

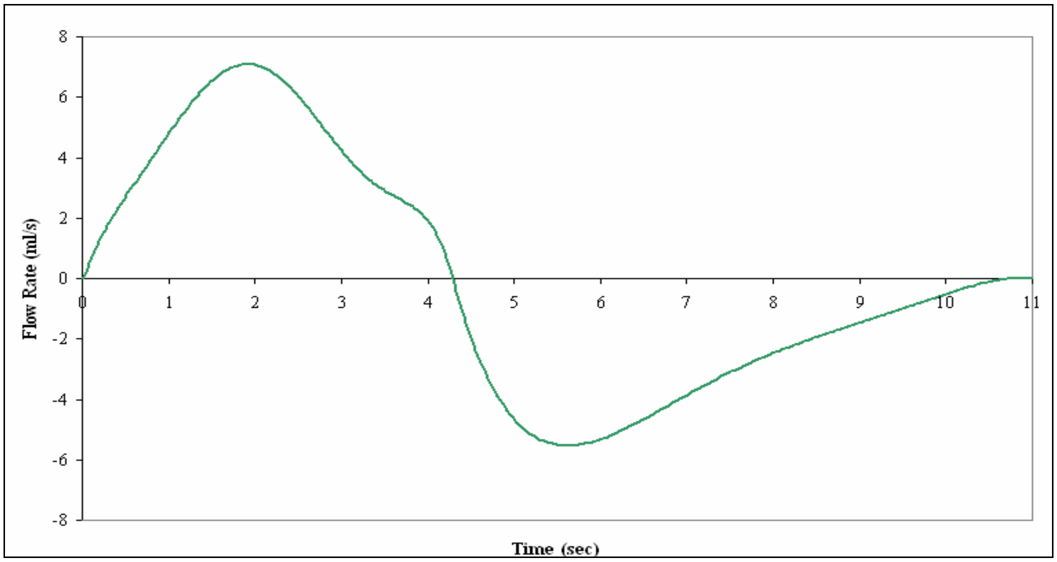

Figure 4.14: Flow Rate versus Time for PIV Experimental Emphysema Alveolar Sac.

4.2.4 Validation of Curve

In order to assess the accuracy of the curve, the magnitude of the experimental PIV flow rate curve was converted for the in vivo healthy alveolar sac model of in vivo size and compared to published values. The in vivo flow rate curve was determined by dividing the PIV experimental change in volume curve by 75^3, where 75 is the scale of the model, and then taking the derivative to obtain the flow rate curve. The total in vivo time for a breath, without pause, is an average of 3.9 seconds (Risa Robinson, Mechanical Engineering, RIT). The time portion of the graph was converted to a total breathing time of 3.9 seconds, by normalizing the time and multiplying by the total time of 3.9 seconds. Figure 4.15 shows the resulting in vivo flow rate curve. The article, (Risa Robinson, Mechanical Engineering, RIT) gave the inhale and exhale portions of the breath, 1.53 seconds for inhale and 2.3 seconds for exhale, for a inhale to exhale time ratio of 0.67. The flow rate ratio for the flow rate determined by this work, was 0.64. It was concluded that the inhale to exhale flow rate ratio is a good representation, based on the published values.

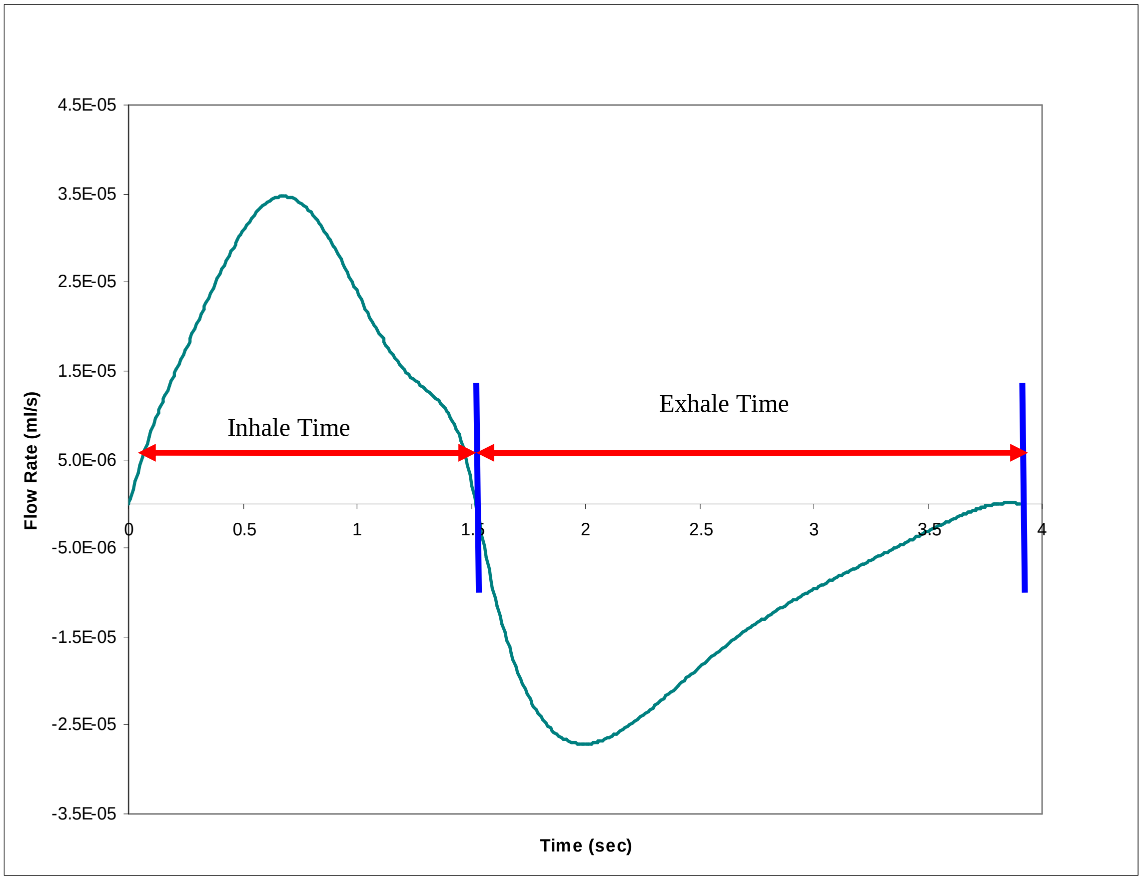

Figure 4.15: In Vivo Sized Flow Rate Curve Used for Validation of Inhale and Exhale Time Ratio.

4.3 Experimental Reynolds and Womersley Numbers

The Reynolds number and Womersley numbers calculated in Section 4.1.3.3 were only for an average flow rate and for the healthy alveolar sac; therefore these numbers only estimated the dimensionless parameters. The experimental specific Reynolds numbers were calculated from Equa. 4.36, where the duct diameter was specific for each model (Section 3.3.3), the kinematic viscosity was for pure glycerin and the flow rate varied based on Figures 4.12, 4.13 and 4.14, for the balloon, healthy alveolar sac and emphysema alveolar sac, respectively. Figure 4.15 shows the experimental Reynolds number for the balloon model, Figure 4.16 shows experimental Reynolds number for the healthy alveolar sac, and Figure 4.17 shows the experimental Reynolds number for the emphysema alveolar sac.

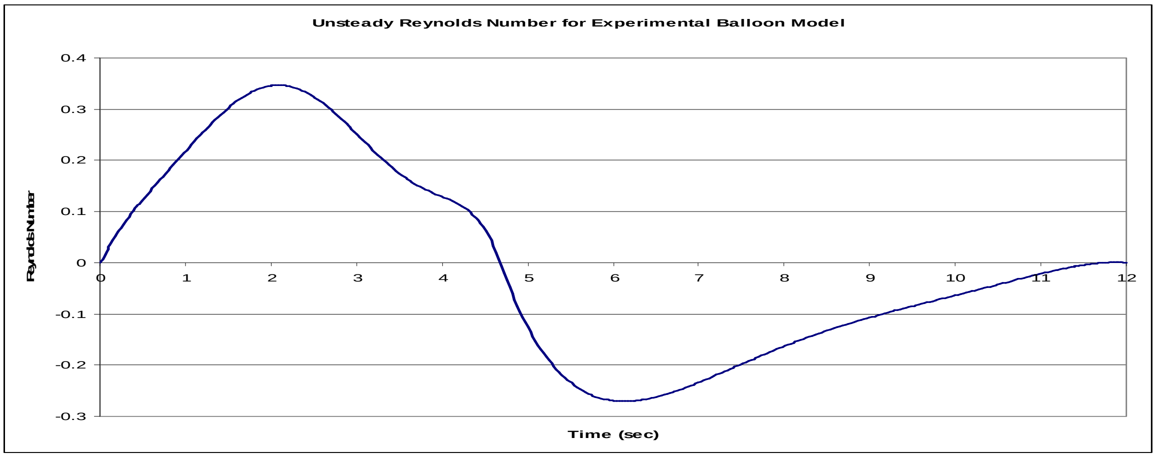

Figure 4.15: Unsteady Reynolds Number for Experimental Balloon Model.

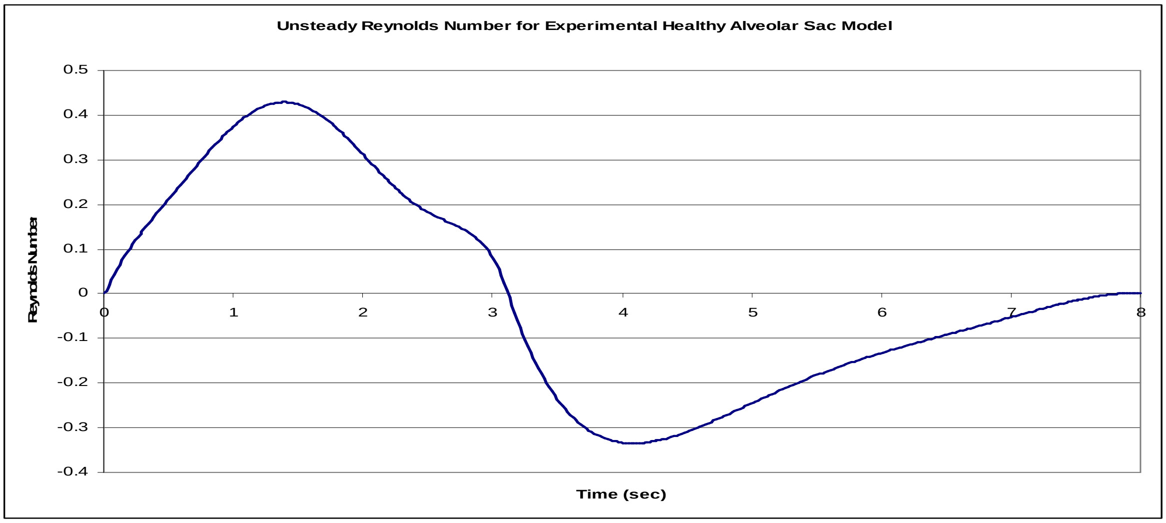

Figure 4.16: Unsteady Reynolds Number for Experimental Healthy Alveolar Sac Model.

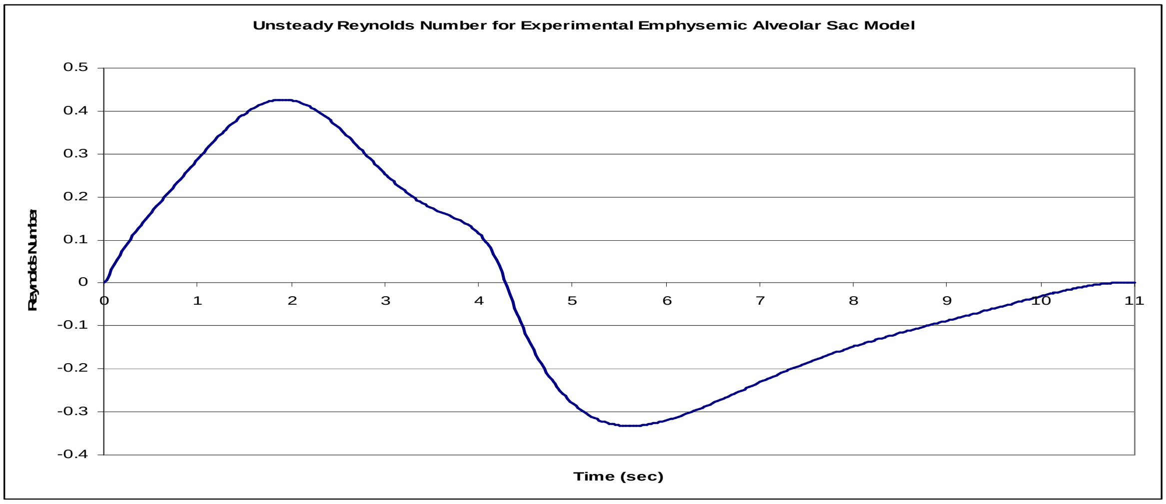

Figure 4.17: Unsteady Reynolds Number for Experimental Emphysemic Alveolar Sac Model.

The Womersley Number is not a function of time and therefore can be calculated directly. Equa. 4.15 was used to calculate the Womersley number for the experimental conditions. Table 4.3 shows the experimental conditions for each model.

Table 4.3: Experimental Womersley Number for PIV Experimental Large Scale Model

	Duct Radius (cm)	Time to Complete Cycle (second)	Womersley (Wo) Number
Balloon Model	1.25	12	0.27
Healthy Alveolar Sac	0.94	8	0.25
Emphysema Alveolar Sac	0.94	11	0.21

Chapter 5
Experimental Setup

In order to correctly model the fluid flow, the experimental setup needed to be able to correctly simulate and capture the fluid flow. The test rig controls and monitors the breathing pattern. The illumination and capturing of the flow fluid is accomplished through the PIV setup. Care was taken in creating the experimental setup in order to reduce experimental errors.

5.1 Test Rig and Data Acquisition

The design and construction of the test rig was completed in Senior Design 2006 – 2007, as shown in Figure 5.1. The rig housed the model and controlled the breathing cycle. The test rig also contained sensors which monitor the fluid flow. The control of the pump and the data acquisition from the sensors was completed with the use of a Labview program.

The breathing pattern was controlled by the syringe pump. The pump was located on the side of the test rig. The expansion and contraction of the pump created the positive and negative volume displacement that controls the expansion and contraction of the model. Fluid entered and exited the model through the volume chamber at the top of the test rig.

Two static pressure sensors monitored the fluid flow. The first sensor was connected to the volume chamber and measured the height of fluid. The pressure was converted, in Labview, to volume and flow rate, Section 5.1.2. The output of the pressure sensor was crucial in determining if the system was working properly and was used in the post processing analysis. The second sensor, located on the side of the chamber of the test rig, measured the static pressure within the house chamber. The measurement from the pressure sensor was not used in the current experimentation, but may be used in future work, particularly, to verify the pressure required to expand and contract the model for a structural finite element analysis comparison.

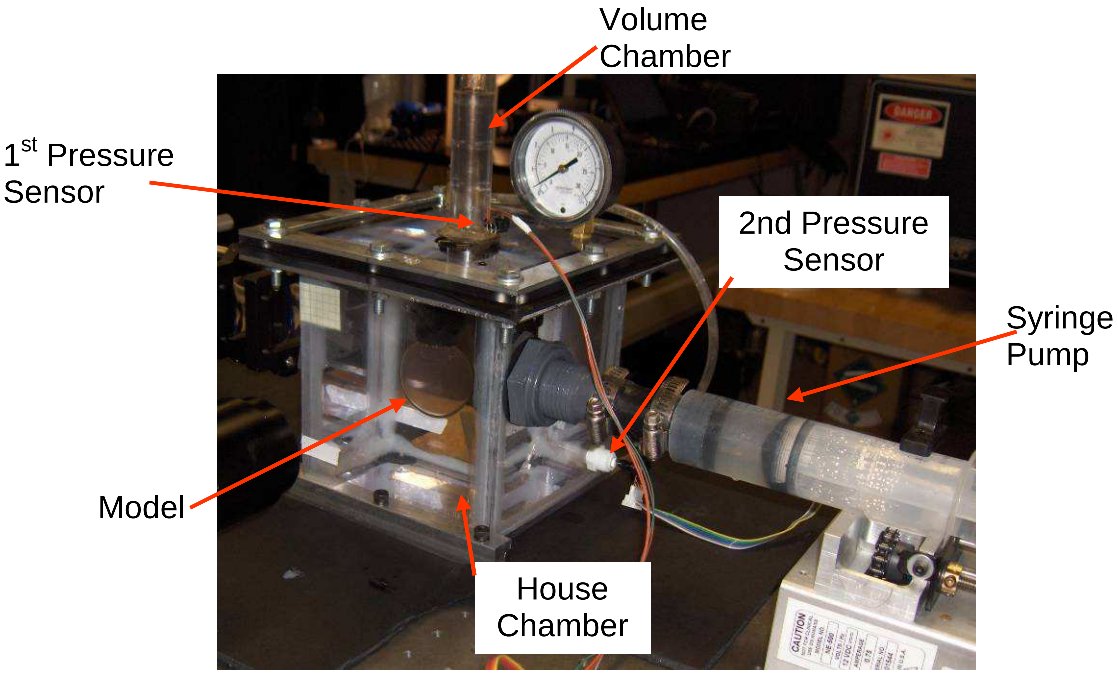

Figure 5.1: Test Rig

5.1.1 New Setup Procedure for the Test Rig

Each time a new model needed to be replaced, or fresh fluid needed to be added to the model, the test rig had to be dismantled and re-setup. The process in replacing the model was important, and care was taken in order to correctly complete the task. The first step was to remove the cover of the test rig. The test rig cover was attached by eight bolts, as shown in Figure 5.3. After the bolts were taken off, the cover needed to be carefully lifted. If there was difficulty in removing the cover, which may be caused by a tight seal caused by the gasket, a lever was used to remove the cover. When the top of the cover was lifted, the weight of the model had to be supported. The model was full of glycerin and it had a high potential to tear under the weight of the glycerin. The old glycerin was dumped into a holding container until it could be disposed properly. If the model needed to be cleaned and re-used, the excess glycerin was cleaned out with a combination of paint thinner and water.

A new model may be attached to the fitting, as shown in Figure 5.2. The new model needed to be removed from the aluminum casting, which could be accomplished by simply stretching the hollow cast over the aluminum cast. The duct of the model needed to be attached to the fitting connected to the chamber. Two different sized fittings were made, one for the balloon model and one for the alveolar sac models. The inside diameter of the fittings matched the diameter of the duct leading into the model. When attaching the new model, care was taken in making sure the model was aligned correctly. The model could be fixed to the fitting with super glue. Epoxy could not be used, for it would deteriorate the plastic of the model. To assure an airtight seal, tape needed to be wrapped around the duct. Any tape

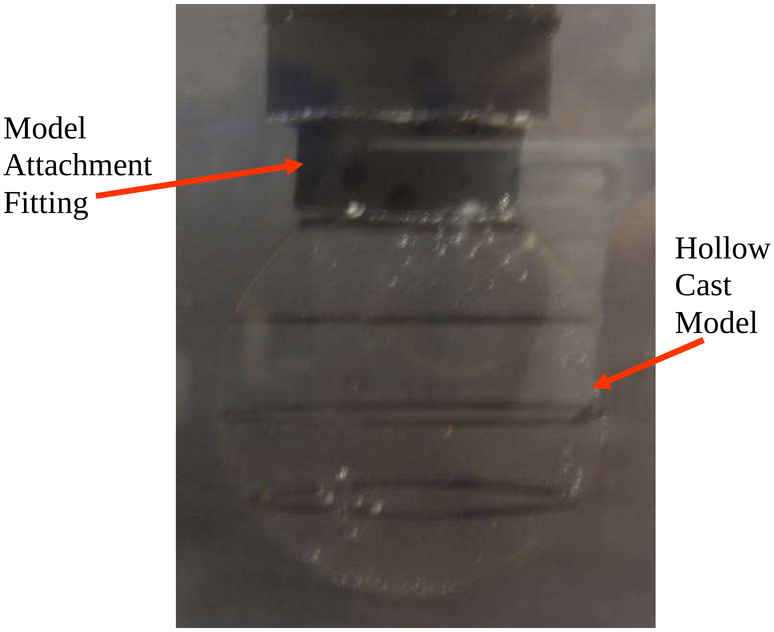

Figure 5.2: Model Attachment

that may leave a residue, particularly duct tape, could be used, for it would discolor the hollow cast model.

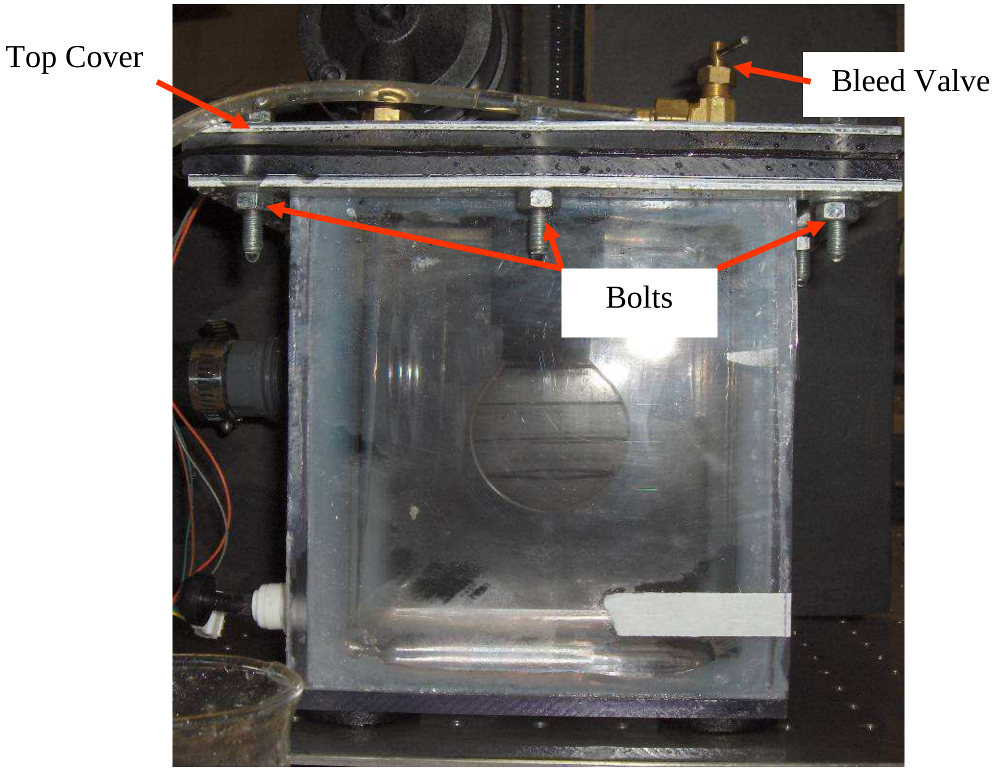

Figure 5.3: Housing Chamber

The new fluid needed to be added to the model before it was inserted into the test rig. The amount of fluid added to the model, before inserting the model, had to be about equal to the volume of the model. Before the top is reattached to the house chamber, the pump had to be completely expanded and glycerin needed to be added to the chamber in order to replace glycerin that dripped when removing the top. Once the chamber is ready, the top was replaced and the bolts fastened tightly. Large bubbles were removed from the chamber with use of the bleed valve. If the chamber was too full of fluid, excess glycerin was removed through the bleed valve. More glycerin had to be added to the volume chamber, in order to have enough fluid to perform the experimentation. The last step in the test rig setup procedure was to add a small amount of oil to the top of the volume chamber. Glycerin could not be exposed to air for long periods of time, for it would absorb water molecules from the air. The oil prevented the glycerin from being exposed to air

5.1.2 Pressure Sensor for Flow Measurement

An integrated silicon pressure sensor, part number MPXV5004GP, was used. The sensor is shown in Figure 5.4. The sensor was placed in the volume chamber and was used to determine change in volume and flow rate of the model. The pressure sensor read the height of the fluid in the volume chamber and converts the height of the fluid into change in volume. The volume chamber contained both glycerin and motor oil, because glycerin could not be exposed to air. Motor oil and glycerin have different densities and therefore the pressure may change based on the ratio of glycerin to motor oil. Each time an experimentation was performed the pressure sensor had to be calibrated, in order to correct for the variation of ratio between glycerin and oil. During the calibration procedure six readings were performed, which allowed for an accurate calibration. The voltage was read using the program, Measurement Instrumentation, and the height of the fluid inside the volume chamber was read directly from the volume chamber. The slope of volume versus amplitude graph was used for the calibration, as shown in Figure 5.5. The slope of the curve was imported into the Labview block diagram, as shown in Figure 5.6.

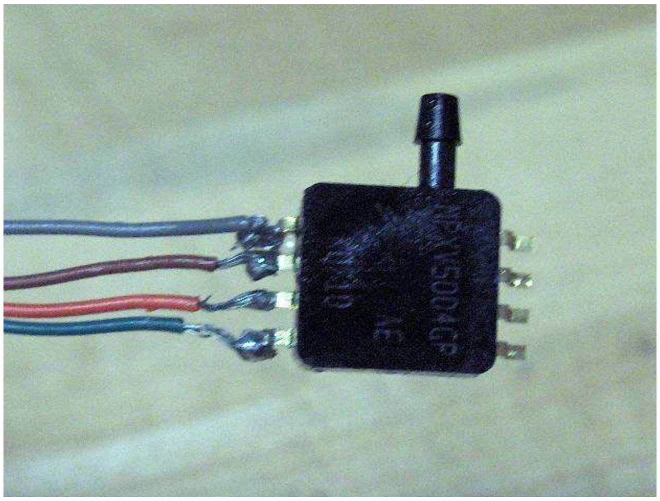

Figure 5.4: Pressure Sensor

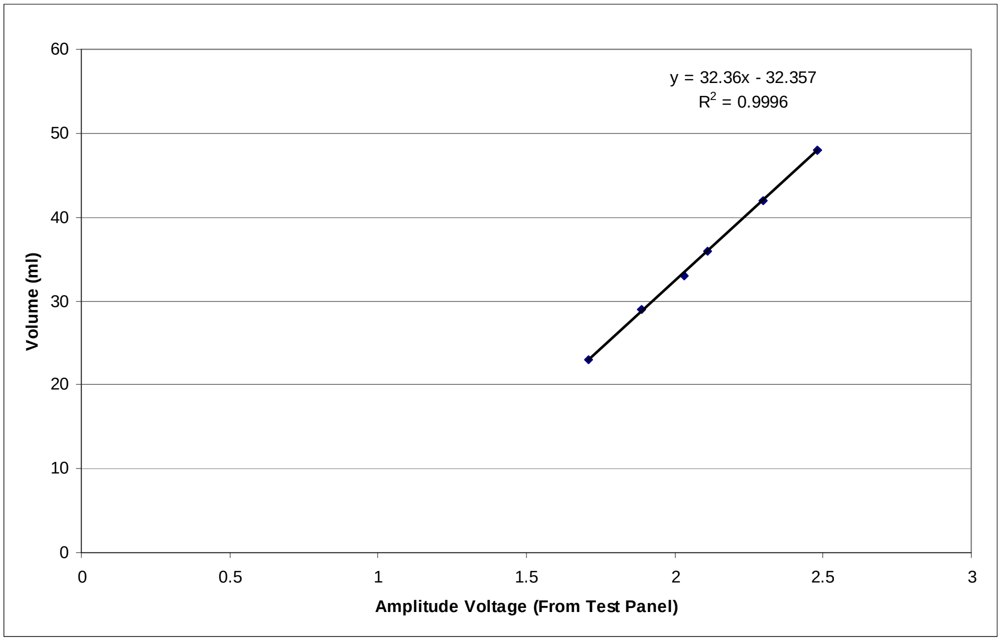

Figure 5.5: Pressure Sensor Graph Used for Calibration.

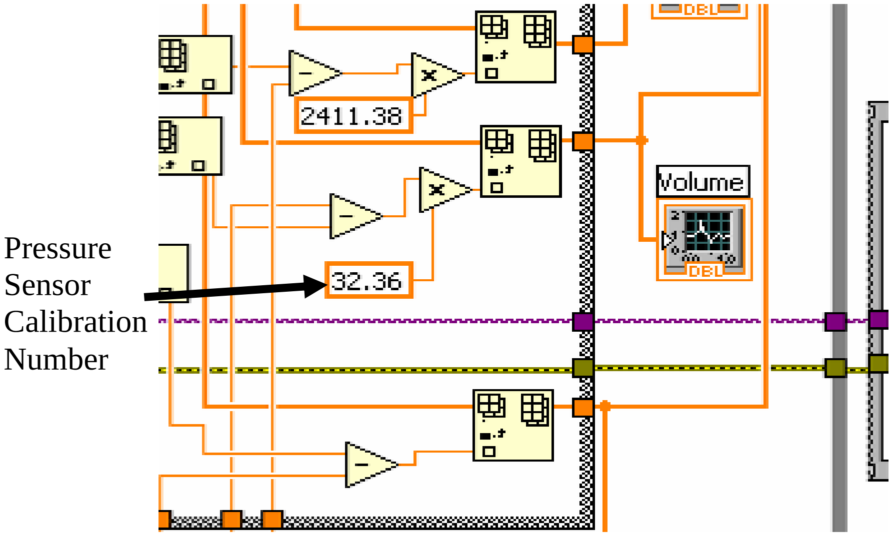

Figure 5.6: Labview Block Diagram: Pressure Sensor Calibration Location.

During experimentation it was noticed that the change in volume graph outputted from Labview contained some error. In order to determine that the error was in the pressure sensor reading, an analysis was completed. The analysis was performed by reading a linear change in volume with respect to time curve, into the pump, which is the input line on Figure 5.7. The simulation was run three times, in order to obtain a range of data. The output of the pressure sensor, for each run, is shown in Figure 5.7. In addition to the pressure sensor, the change in volume was read by eye from the volume chamber. The pressure sensor error was approximated by examining the maximum change in volume for the input and the output. From the analysis, it was determined that the pressure sensor contained an error of approximately 1 ml, which was also seen when reading the measurement directly from the volume chamber. The same analysis was performed with the realistic volume curve, with and without pauses. Figure 5.8 shows the input and output results for curve with a pause, and Figure 5.9 shows the result without a pause. Again, it was shown that the error of approximately 1 ml was present, which was determined based on the differences between the maximum output curve height and the input signal. The 1 ml error in the pressure sensor was unable to be reduced.

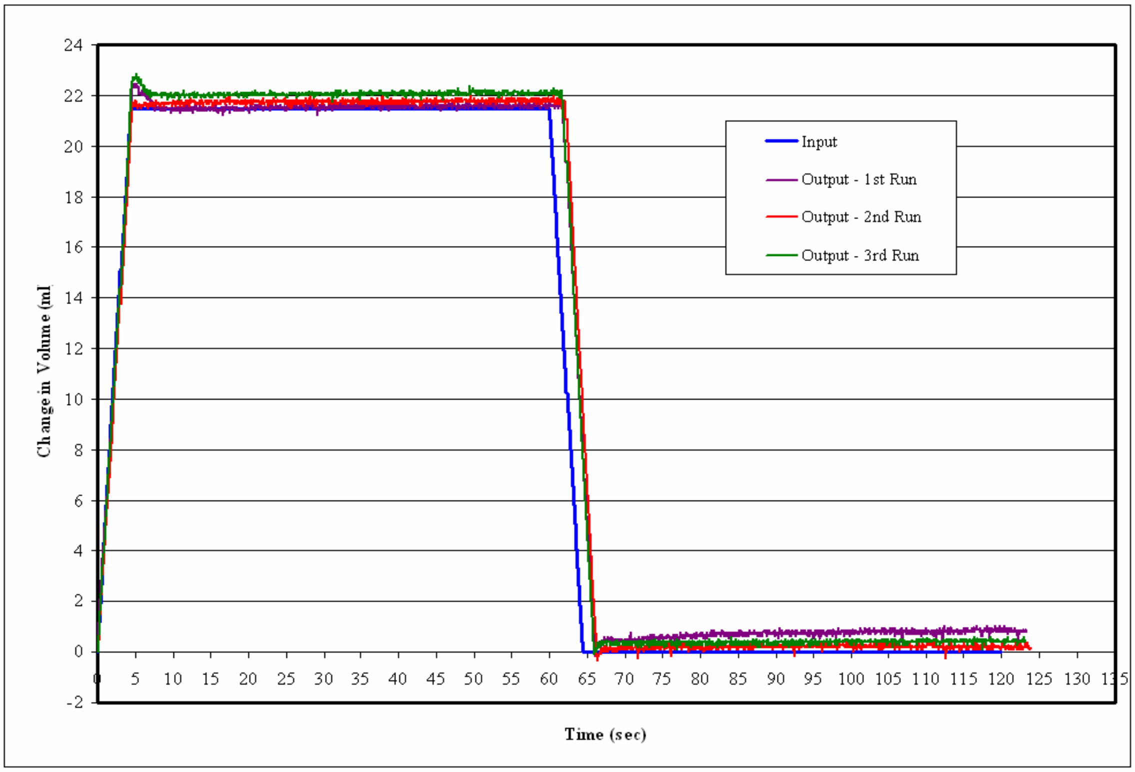

Figure 5.7: Linear Change in Volume Graph with Pause. Input and Pressure Sensor Output is Presented. Graph used for Pressure Sensor Analysis.

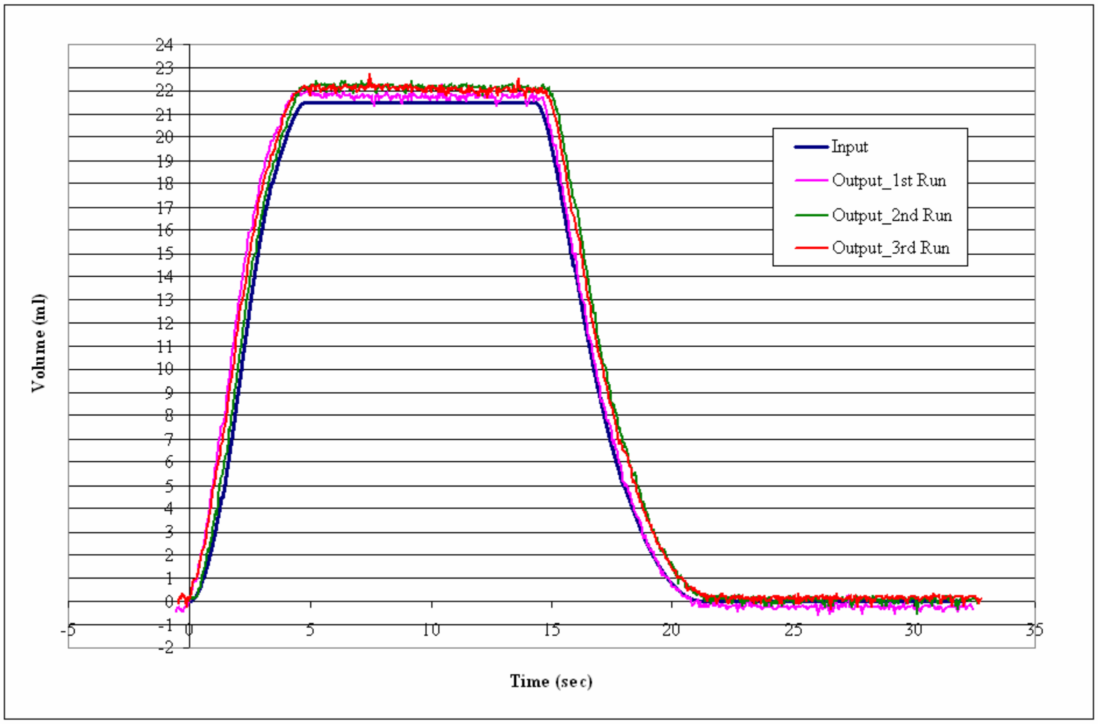

Figure 5.8: Realistic Volume Curve, With Pauses. Used for Comparison between Input and Output for Pressure Sensor Analysis.

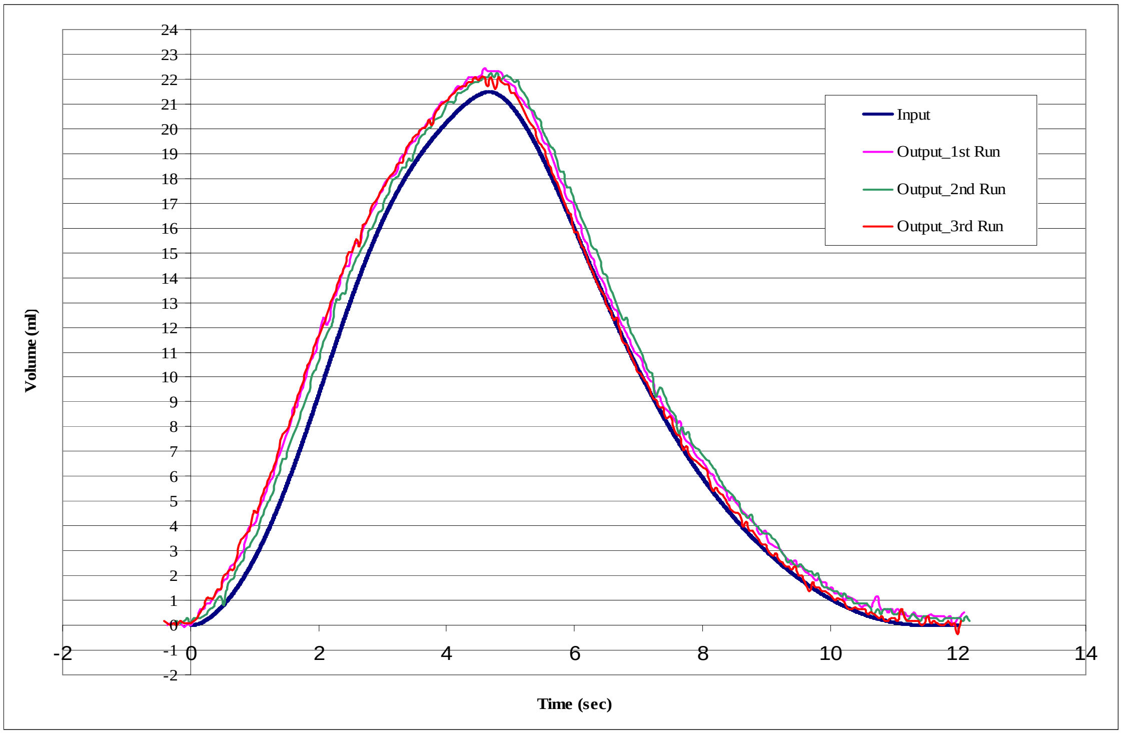

Figure 5.9: Realistic Volume Curve, Without Pauses. Used for Comparison between Input and Output for Pressure Sensor Analysis.

5.1.3 Syringe Pump

The syringe pump controls the pressure force which expands and contracts the model to simulate breathing conditions. In order to assure the pump is displacing the correct amount of volume, it must be calibrated. The pump was calibrated once during the experimentation time period. The calibration procedure was completed using the step linear volume graph, Figure 5.7. The calibration number was altered, until the pump was displacing the correct volume. The calibration number is inserted into the Labview Block diagram, Figure 5.10. From Figure 5.7, it can be seen that there was some delay in time between the pause and contraction. The number of breathing cycles that was able to be performed was limited, because the pump would begin to skip and displace the wrong amount of volume. A pump controller would be able to better control the pump and correct the pump if it began to skip.

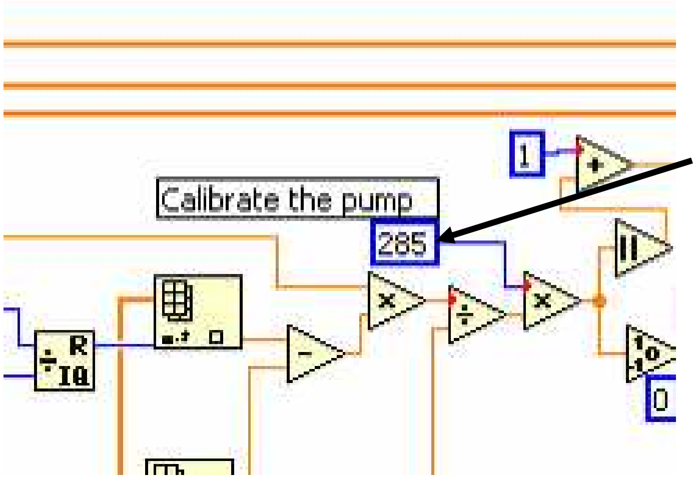

Pump Calibration Number

Figure 5.10: Labview Block Diagram: Pump Calibration

5.1.4 Labview Interface

The Labview Interface was developed in Senior Design 2006 -2007, as shown in Figure 5.11. The interface allowed the user to input the desired experimental parameters and visualize the output from the sensors.

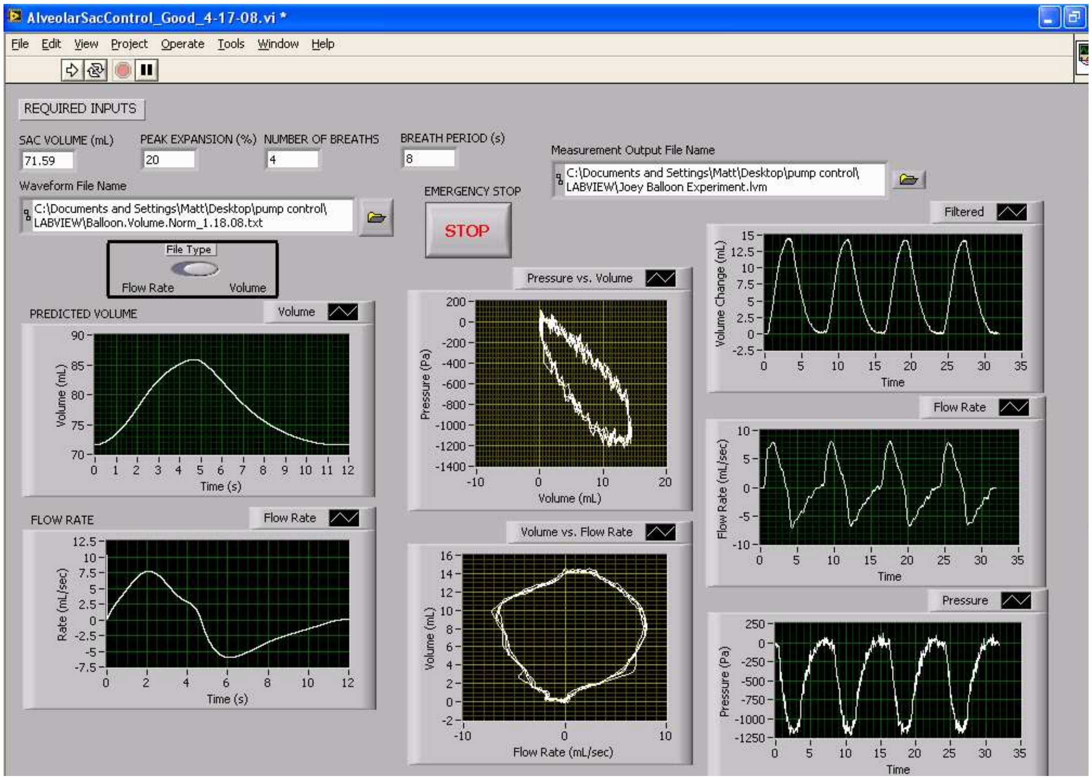

SAC VOLUME (mL) 71.59
PEAK EXPANSION (%) 20
NUMBER OF BREATHS 4
BREATH PERIOD (s) 8
Waveform File Name C:\Documents and Settings\Matt\Desktop\pump control\LABVIEW\Balloon.Volume.Norm_1.18.08.txt
Measurement Output File Name C:\Documents and Settings\Matt\Desktop\pump control\LABVIEW\Joey Balloon Experiment.lvm

Figure 5.11: Labview User Interface

The first step in using the interface was to define a breathing curve wave form, as shown in Figure 5.12. A text data file was be loaded into the interface by specifying a waveform file name. Either a volume or flow rate curve could be used; the user would need to specify what file type was used under the File Type section. The flow rate or volume curve that was inputted into Labview, had to be normalized, such that the range was between -1 and 1. A central difference differential scheme was used in Labview to convert from change in volume to flow rate curve.

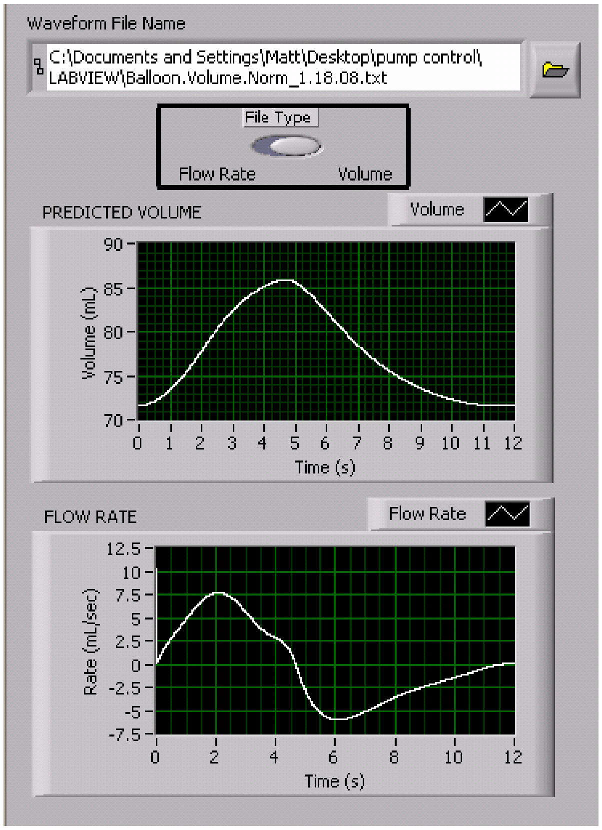

Waveform File Name C:\Documents and Settings\Matt\Desktop\pump control\LABVIEW\Balloon.Volume.Norm_1.18.08.txt

Figure 5.12: Wave Form Definition Section of the Labview Interface

In order to specify the range of the wave form curve, the specific parameters for each model needed to be defined, as shown in Figure 5.13. These parameters were used to convert the wave form’s amplitude and time for the specific experimentation. The specific experimental parameters used in this work is presented in Table 5.1.

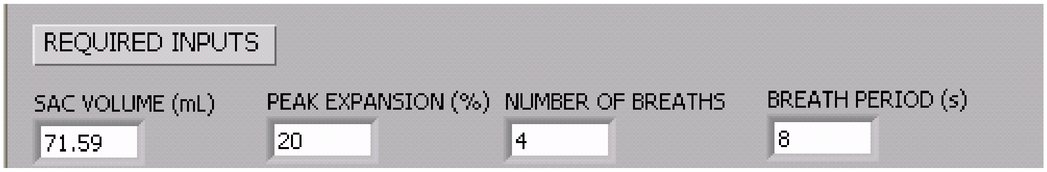

SAC VOLUME (mL) 71.59
PEAK EXPANSION (%) 20
NUMBER OF BREATHS 4
BREATH PERIOD (s) 8

Figure 5.13: Specific Model Parameter Section of the Labview Interface

Table 5.1: Experimental Parameters

	Healthy Alveolar Sac	Balloon Model	Emphysema Alveolar Sac
Initial Volume (ml)	44.31	71.59	60.51
Expansion (%)	30	30	30
Total Change in Volume (ml)	13.29	21.48	18.15
Total Time (sec)	8	12	11

The output from the sensors were shown in the measurement output section, as shown in Figure 5.14. The volume and flow rate curves were generated from the pressure sensor that measured flow rate, and the pressure curve was generated from the pressure sensor located at the side of the housing chamber. The pressure versus volume curve and a volume versus flow rate curve were also generated, which can be used in future experiments to show diseased states. A data file was also created and outputted from Labview, which contained the pressure, volume, flow rate, and when the camera turned on.

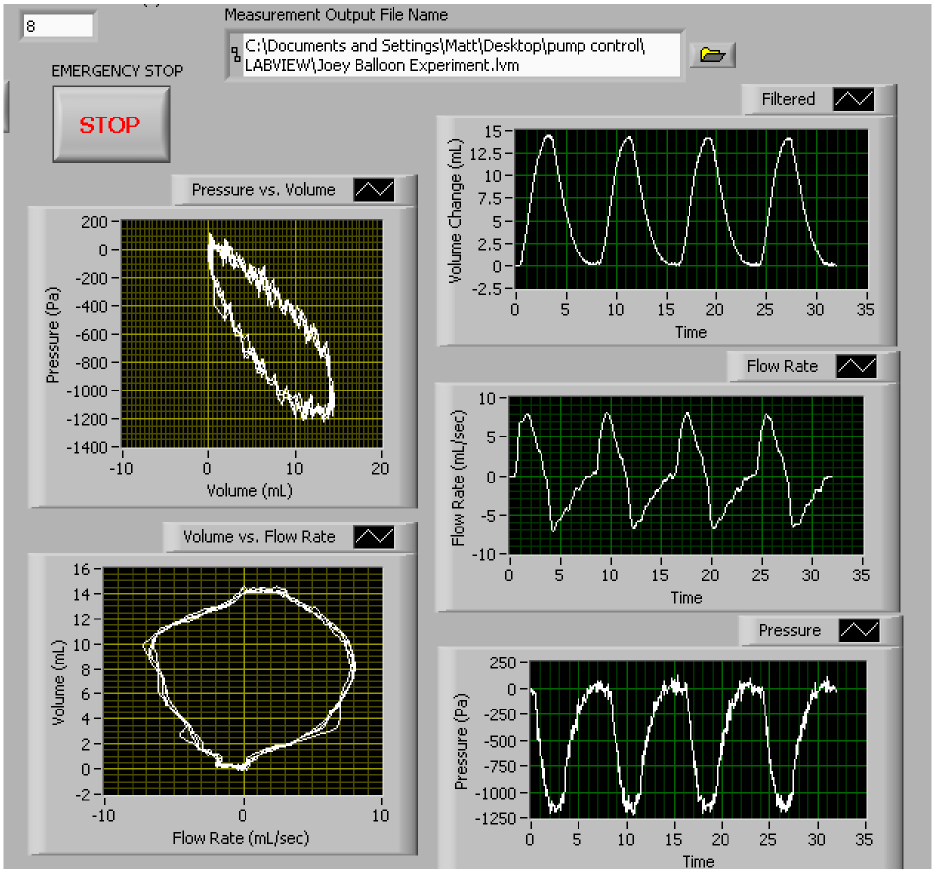

8

Measurement Output File Name

C:\Documents and Settings\Matt\Desktop\pump control\LABVIEW\Joey Balloon Experiment.lvm

Figure 5.14: Measurement Output Section of the Labview Interface.

5.2 PIV System

5.2.1 Overall Experimental Setup

The overall PIV system consisted of the laser system, camera, and the test rig, as shown in Figure 5.15. The Laser Sheet Generator (LSG), camera and test rig must be aligned and perpendicular to each other, such that the images may be taken in the correct plane. In order to assure each system is aligned, an alignment fixture was made. The fixture, which remained stationary, allowed the test rig to be posited flush it its surface. The camera and the LSG were positioned exactly perpendicular to the test rig.

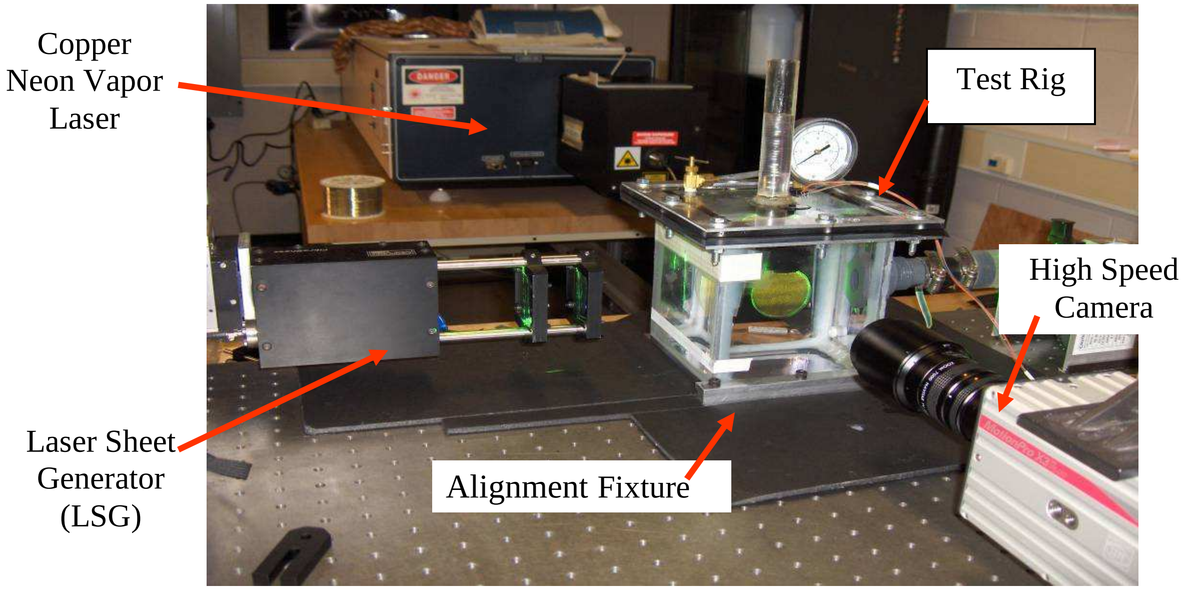

Figure 5.15: Experimental Setup.

5.2.2 High Speed Camera

The camera used for the PIV measurements was a monochromatic MotionPro X3 Plus from Redlake. The camera had a 1280 x 1024 pixel resolution, for a frame rate up to 2000 fps. Each pixel on the array is 12 μm in length and width, p_L. An image is defined as the picture on the array in the camera. The magnification, M, between the physical object and the image is defined by

$$M = \frac{z}{Z} \tag{5.1}$$

where Z is the distance from the lens to the physical object, 136.525 mm, and z is the distance from the lens to the array. The distance from the lens to the array is calculated by

$$z = \frac{1}{{}^{1}\!/_{F} - {}^{1}\!/_{Z}} \tag{5.2}$$

where F is the focal length,

$$F = \frac{p_L * Z}{p_{PL}} \tag{5.3}$$

where p_{PL} is the length and width of a pixel, which was determined during the calibration procedure for each experiment. The Magnification for each experiment is shown in Table 5.2. From the table it can be noticed that the magnification for each experiment are very similar.

Table 5.2: Optical Parameters for Each Experiment

Pixel Size on Array (µm), p_L	12	Distance From Lens to Physical Object (mm), Z	136.525
	Balloon	Healthy	Emphysema
Pixel Physical Length (mm), p_{PL}	0.0639	0.0643	0.0635
Focal Length (mm), F	25.451	25.292	25.611
Distance from Lens to Array, z	31.335	31.096	31.579
Magnification, M	0.231	0.229	0.233

The lens used for the experimentation was a Navitar TV Zoom 7000 camera lens. The aperture diameter of the lens is 15.875 mm for when the shutter is completely open (Russell Barkley, Imaging Science Department, RIT). The f# of the lens is 1.28 (Russell Barkley, Imaging Science, RIT), which was used in the particle calculations, Section #. A complete description of the lens may be found elsewhere (Pryune, 2004). The camera was mounted on two optical stages, as shown in Figure 5.16. The stages allowed the camera to be moved parallel to the image plane. The stages and mounting brackets also allowed for the camera to be horizontal.

The MotionScope PCI High Speed Digital Imaging System software, a Redlake product, was used to acquire the images. This software allowed for the specification of the frame rate and shutter speed of the camera used for the experimentation. Specific instructions on the use of the software can be found in the manual (Instructions, Redlake Imaging, 2007).

The frame rate and shutter speed depended on the amount of light needed to achieve a good image, as well as the speed of the fluid being analyzed. The frame rate, defined in frames per seconds, specified the number of photos taken per second. The time separating the images is the reciprocal of the frame rate. The shutter speed defined how long the shutter was open while an image was being taken, therefore the shutter speed must be less then the frame rate. If the shutter speed was too long, particle streaking may occur. Particle streaking occurs when a particle moves significantly when the shutter is open.

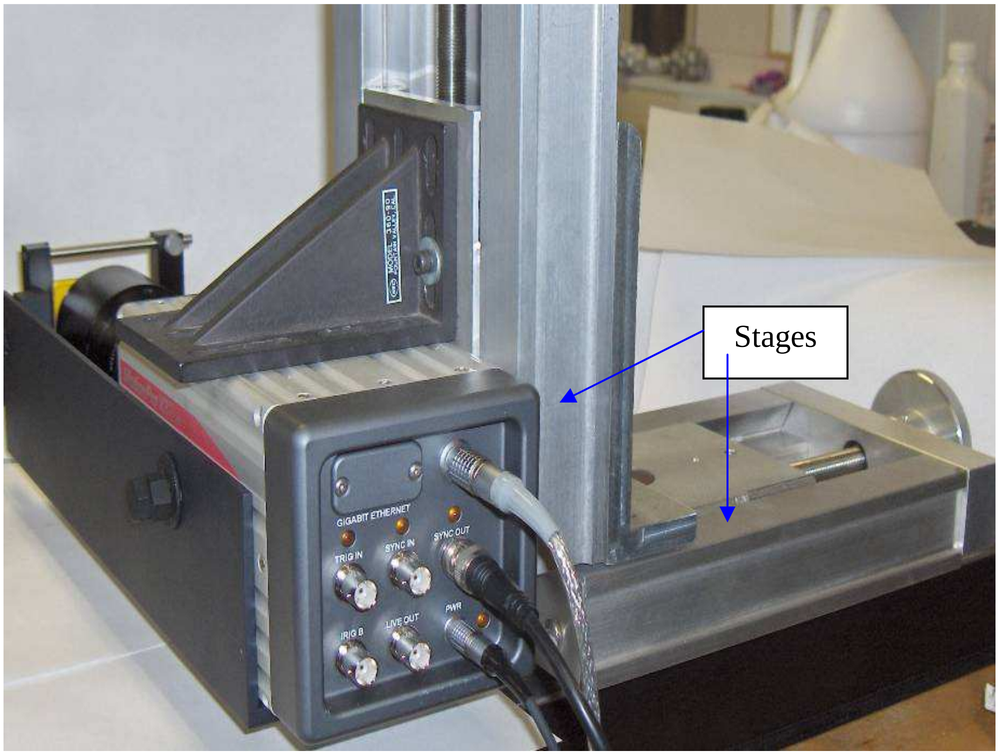

Figure 5.16: Camera Setup

When streaking occurs, the particle no longer appears as a small bright dot on the image, instead there is a line, indicating the path the particle took. Significant particle streaking was undesirable, for it may lead to error in the cross correlation. The length or shape of the streak pattern may change from one image to the next, making it difficult to find a correlation between the two images. It was important to use a shutter speed long enough to get enough light to the lens, but small enough to streaking did not occur.

In order to determine the best frame rate needed for experimentation, knowledge of how the images will be analyzed must be known first. As described in Section 6.1.1, during the cross-correlation analysis an image is broken into interrogation areas. The size of the desired interrogation areas needs to be determined before the experimentation. The particles must remain in the interrogation area during sequential images; therefore the frame rate cannot be too slow such that particles travel too far.

5.2.2.1 Frame Rate Analysis

An analysis was performed in order to determine the accuracy of the frame rate of the camera. A precise optical chopper, model number MC1000A, was used for the analysis. The optical chopper contains a microprocessor control and a crystal stabilized phase-locked loop, which allowed for stability and for drift free performance. The optical chopper was calibrated for an RMS error of 0.2 degrees at 1 kHz (Instructions, Laser Lab Instruments). For the analysis, a frame rate of 50 Hz was used for the camera. The optical chopper was set to 25 Hz. The definition of the rate of the chopper is the number of times a window passes a spot, therefore for the 25 Hz a window passes a spot 25 times per second. The chopper contains 10 windows, therefore in 1 second the optical chopper will turn 2.5 times, or 900 degrees. Because the camera's frame rate was 50 Hz the optical chopper rotated 18 degrees between each camera frame. A small piece of white tape had been applied to the optical chopper. The tape allowed for the movement of the optical chopper to be distinguishable, as shown in Figure 5.17. A low shutter speed was used, such that streaking did not occur.

The program, Image J, was used for the analysis. In order to reduce error in the measurement technique, 50 frames were analyzed and the average angle was determined. The average angle was measured to be 18.012 degrees, which was only 0.07 percent different from the predicted 18 degrees. The small error may have been introduced by the measurement technique of Image J or by the RMS error of the optical chopper. It was concluded that the camera frame rate was highly accurate and was not a source of error in the PIV measurements.

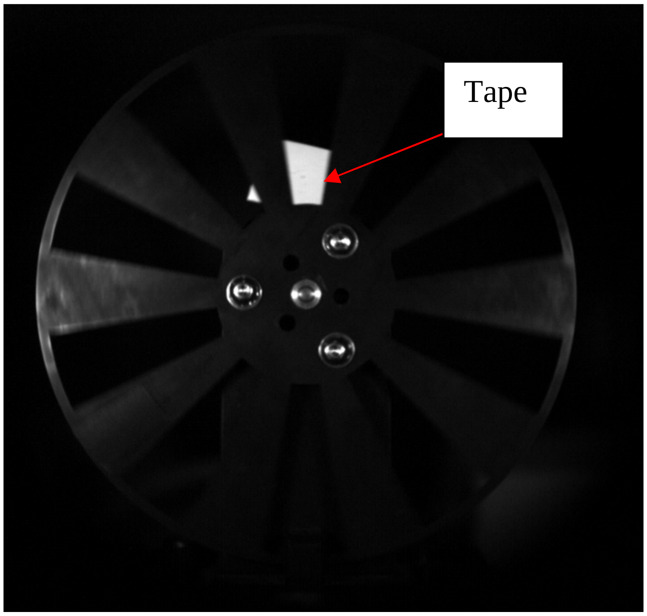

Figure 5.17: Optical Chopper Image

5.2.3 Laser

The laser used for the experiment was a 20 W, copper vapor laser. The laser produced two wavelengths, 510.6 nm and 578.2 nm. The PIV light sheet was generated by a set of mirrors in the Laser Sheet Generator (LSG), as shown in Figure 5.18. The light sheet is 1 mm thick and 48 mm wide at the throw distance of 155 mm. The throw distance is the distance to the belt, or the distance to where the light sheet becomes 1 mm thick and 48 mm wide. The LSG was mounted on two adjustable stages, which allowed for the LSG to be moved parallel to the model apparatus. A level was used in order to make sure the light sheet exited the LSG at the correct angle.

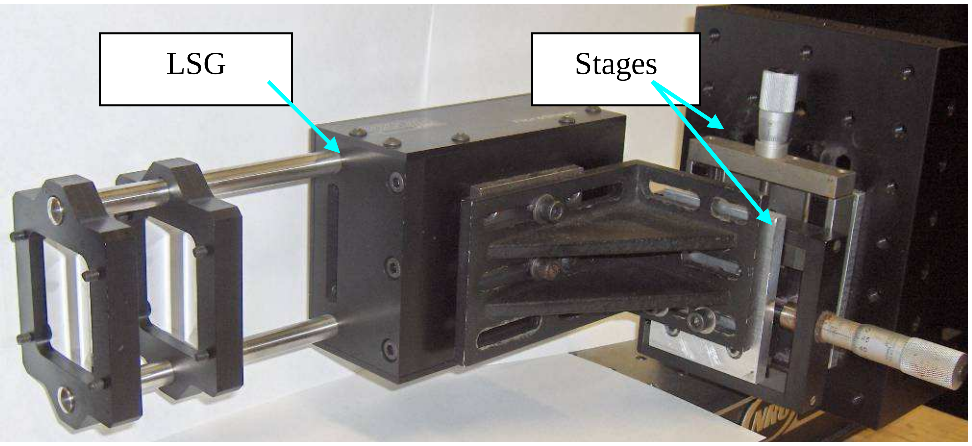

Figure 5.18: Picture of the LSG

5.2.4 Fluid

Pure glycerin was used for the experimentation. The one hundred percent glycerin was used in order to be similar to the index of refraction of the material of the model. Because the model’s geometry is complex the index of refraction between the fluid and the model was important, such that the camera can focus on the laser light sheet. Two measurements were taken on the index of refraction of the glycerin. The first measurement analyzed new glycerin, which was 1.4728. The second measurement analyzed the glycerin inside the housing chamber, because the gylcerin had been in there for a long period of time. The index of refraction of the older glycerin was measured to be 1.4717. The reason why this measurement was taken was to assure that index of refraction of the glycerin did not change after being used. The index of refraction of the molded hollow cast material was measured to be 1.4811. All index of refraction measurements had an error of +/- 0.002 and were measured by Nelsy Carcamo (Nelsy Cacamo, Department of Science and Mathematics, NTID, RIT).

5.2.5 Particles

Seeding particles were chosen such that they were neutrally buoyant, and travel with the fluid. If the particles travel with the fluid then it could be inferred that the speed of the fluid was the same as the speed of the particles. The particles were illuminated with the laser light and were captured by the high speed camera. Some of the errors related to the PIV analysis can be directly related to the size, number of particles in the image, and the buoyancy of the particles relative to the fluid, therefore particles were a very important part of the PIV setup.

Red, Fluorescent, Polymer Microspheres were used for the PIV experiment; properties of the particles are shown in Table 5.3. The particles were purchased from Duke Scientific. Fluorescent particle were used in the experiment in order to have the wavelength of the particle emission differ from the wavelength of the laser emission. An optical filter is used to omit some of the laser light, while still allowing for maximum light from the particles to reach the camera image. The optical filter removed some of the laser light reflection. A detailed explanation of the fluorescence and laser wavelength is found elsewhere (Pryune, 2004).

Table 5.3: Particle Properties

Particle Diameter	8	μm
Particle Density	1.05	g/cm^3
Particle Volume	85.3	μm^3

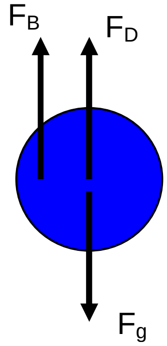

Figure 5.19: Forces Acting on a Fluid Particle.

5.2.5.1 Particle Buoyancy

In order to assure that the particles were neutrally buoyant, in the time frame of the experiment; a force balance was performed. Figure 5.19 shows the forces acting on the particle, where F_B is the buoyancy force, F_D is the drag force and F_g is the gravity force.

The force balance is performed by

$$\Sigma F_y = 0 = F_D + F_B - F_g \tag{5.4}$$

where the buoyancy force is calculated by

$$F_B = V_p * g * \rho_f \tag{5.5}$$

where V_p is the volume of the particle, 85.3 μm^3, g is gravity, 980 cm/s^2, and ρ_f is the density of the fluid, 1.261 g/cm^3. The force due to drag is

$$F_D = 3 * \pi * d_p * u_{rel} \tag{5.6}$$

where d_p is the diameter of the particle, 8 μm and u_{rel} is the relative velocity, or the velocity difference between the particle and the fluid. The force due to gravity is

$$F_g = V_p * g * \rho_p \tag{5.7}$$

where ρ_p is the density of the particle, 1.05 g/cm^3. The equations were solved for the relative velocity. The particle raises 5.3e-7 cm/s. For a 12 second time period, the total time for the simple balloon model's complete cycle, a particle will only rise 0.063μm. Since the maximum frame separation was 0.02 seconds, for a frame rate of 50 Hz, a particle will only raise 1.06e-4μm during this time frame. From the analysis, it was determined that the particles were neutrally buoyant for the time period of the experimentation.

5.2.5.2 Particle Size

The particle image diameter size, dτ, the size of the particle on the camera image array, was calculated. The reason why this analysis was completed was to determine if the particles were within the range, which as been shown to have the least amount of PIV analysis error (Section 6.1.1). The particle image diameter was calculated by

$$d\tau = \sqrt{(M * d_p)^2 + d_{diff}^2} \tag{5.8}$$

where λ is the scattering wavelength of the particles, 542 nm, and d_{dif} is the minimal particle diameter solved by

$$d_{diff} = 2.44 * f\#*(M+1)*\lambda \tag{5.9}$$

where f# is 1.28 and M is the magnification, which is shown in Table 5.2. The equations for the particle image diameter size were from Adrian (1991) and were defined for particles in air. Because the particles used in this experimentation were in glycerin, the equations only give an estimate of the particle image size. The particle image diameter was calculated to be about 0.23 pixels. Figure 5.20 shows how the particle image diameter changes based on the magnification of the camera. In order to have the desired pixel size of 2 – 3 pixels, the magnification of the camera needed to be over 3. The large magnification was not ideal for the experiment because the entire model would not fit in the image. In order to have this high of a magnification a smaller model would need to be used. Figure 5.21 shows a typical section of a PIV photographed image taken during the experimentation. It can be noticed that the particles on the image are within the 2 – 3 pixel range. Some of the particles are larger then 3 pixels. There are a few possible reasons why the particles are larger then the calculated. First, the particle diameter calculations were for air. Particle scattering changes based on the medium, and therefore the particle scattering may be larger in glycerin. There may also be particle clumping, where a few particles stick together. The particle clumping may be a reason why there are a few spots on the image that are larger then the 2 – 3 pixels. The larger spots may also be small air bubbles in the glycerin. The final reason may be due to image blurring. The photograph may be slightly blurred, which would make the particles appear larger. It was determined that because most of the particles on the image were within the desired 2 – 3 pixel range, the particle size was sufficient for PIV.

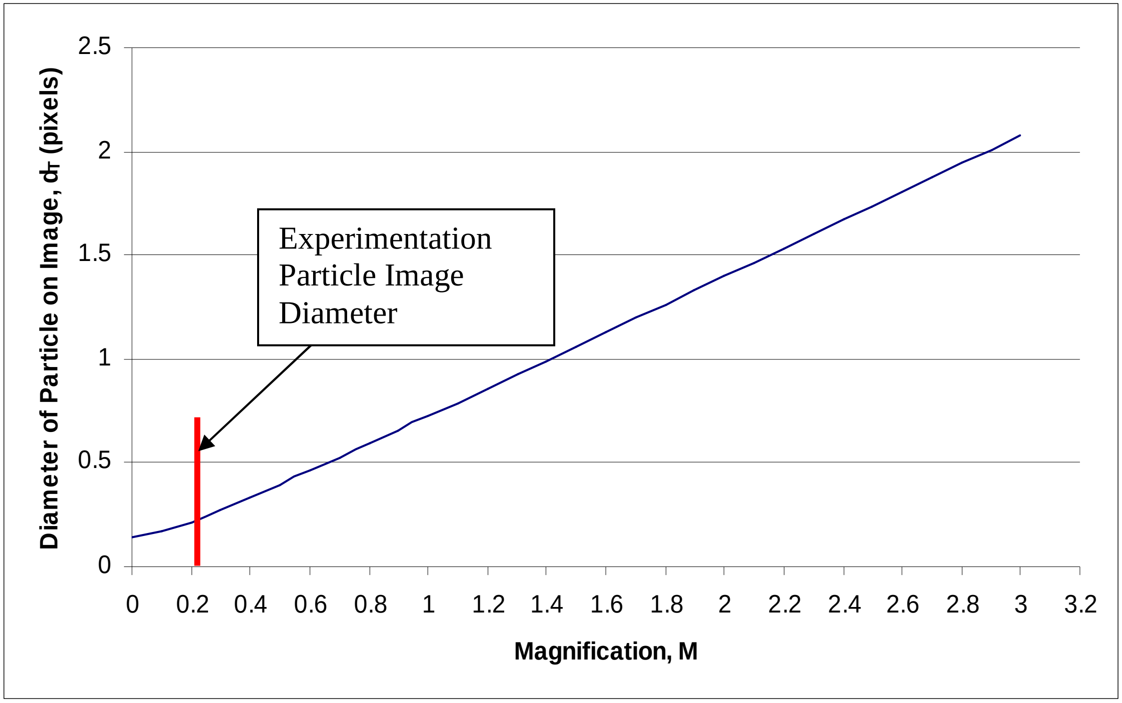

Figure 5.20: Relationship for Diameter of Particle on Image and Magnification.

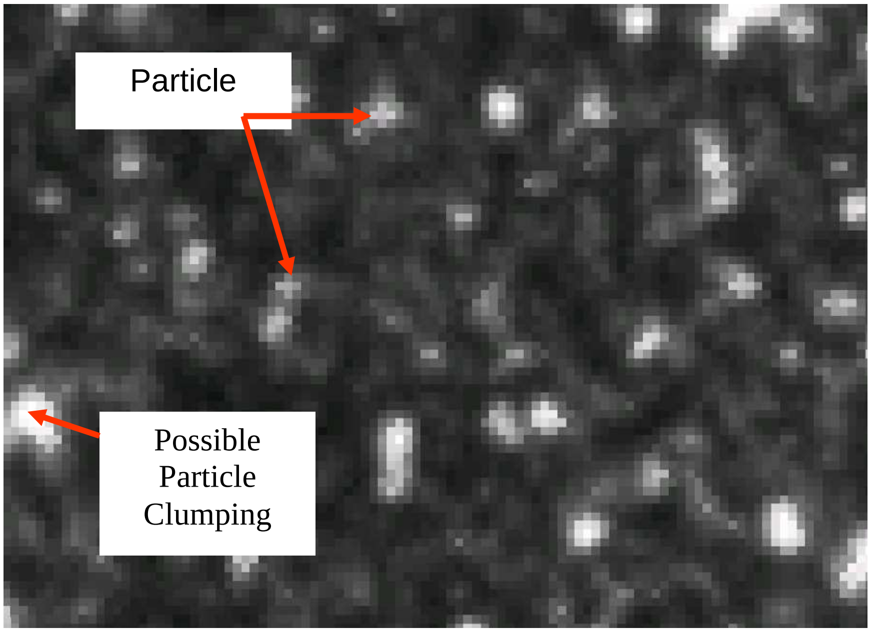

Figure 5.21: Particles on Image.

5.2.5.3 Particle Mixing Ratio

The number of particles in an image was also important as discussed in the error Section, Section 6.1.2. An understanding of how the image would be analyzed needed to be known, before the number of particles could be determined. In the post processing analysis, the image was sectioned into areas of 32 pixels^2 (Section 6.2). Each interrogation region needed approximately 32 particles to have the least amount of error (Section 6.1.2). The number of interrogation regions, IR, was determined by

$$IR = \frac{V_s}{V_{\text{int}}} \tag{5.10}$$

where the physical volume of each interrogation region, V_{int}, was determined based on the magnification, 0.0087 ml. For 150 mL, V_s, solution there are 17241 interrogation regions, IR. The number of particles, NP, needed was determined by

$$NP = 32 * IR \tag{5.11}$$

It was determined 551724 particles were needed. In order to calculate the number of particles to add to the solution, the mass of the particles, M_{ps}, must be known

$$M_p = \rho_p * V_p * NP \tag{5.12}$$

The volume of the particles (V_p) was determined by

$$V_P = 4/3 * \pi * \left(\frac{d\tau}{2} \right)^2 \tag{5.13}$$

where an average particle diameter, d_τ, of 2 pixels, 0.024e-3 m, was used. The particle to solution mixture ratio was determined to be 0.0042 g, M_p, to 150 mL of solution. In order to account for particle loss and clumping, a factor of 1.5 was used; therefore the final mixture ratio was 0.0063 g to 150 mL of solution.

The particles were mixed in the solution using a magnetic mixer. In order to get a good mixture, the solution was mixed in increments of 75 mL. During the mixing process, particles that clumped together needed to be broken apart. The mixing caused bubbles in the solution; therefore the solution could not be directly used for the PIV analysis. It was found that it was best to let the particle and glycerin solution sit for approximately 12 hours, which allowed enough time for the bubbles to rise. It was not desirable to put the mixture into the model directly after mixing, and then wait the 12 hours, because the particles would rise approximately 0.023 cm during the 12 hour time frame.

Chapter 6
PIV Analysis Techniques

6.1 Vector Analysis

Conversion of a set of images, acquired using the single exposure, double frame technique, into data files was completed through PIV cross correlation. The following section includes the theory behind cross correlation, the source of error, the measures that can be enforced for error reduction, and the analysis software used to compute the velocity vectors.

6.1.1 Cross Correlation Theory

Converting a set of images into displacement data is a process that involves the light intensity of the image created by the illuminated particles. The images produced are grey scale images, which contain dark and bright areas of various light intensities. The neutrally buoyant particles within the fluid produce the bright intensity regions.

In double frame, single exposure PIV, there are two images analyzed during the cross correlation process. The images are separated by a known time, Δt. Each image was broken into many small interrogation regions, Figure 6.1. In Figure 6.1, the dark and light areas are inverted for illustration purposes only.

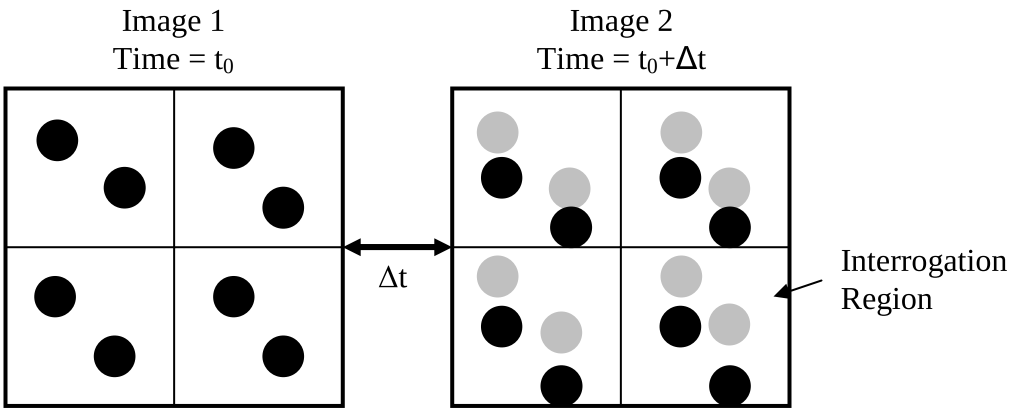

Figure 6.1: Diagram of Two Images Segmented into Interrogation Regions.

The light intensity, as a function of location, is determined for each interrogation region in both images. The distance traveled, within each interrogation region, is determined based on the cross correlation function, for digital discrete functions, R(x,y) (Raffel et al., 1998)

$$R(x,y) = \sum_{i=-K}^{K} \sum_{j=-L}^{L} I(i,j) I'(i+x, j+y) \tag{6.1}$$

where I(i,j) is the intensity in an interrogation region in image 1 and I`(i,j) is the intensity of an interrogation region in image 2, Figure 6.2.

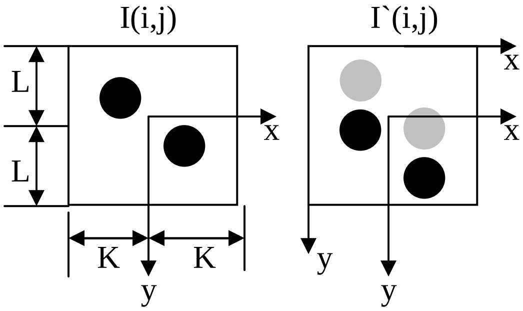

Figure 6.2: Definition of Coordinate System and Light Intensity for Interrogation Regions Separated by a Known Δt.

The cross correlation is calculated for different shifts in the x and y direction. The best correlation occurs where the cross correlation function is at the maximum. The displacement vector is determined based on the location of the maximum correlation, where the displacement vector is

$$s = x\hat{i} + y\hat{j} \tag{6.2}$$

The final cross correlation function is made up of three components

$$R(s) = R_c(s) + R_D(s) + R_F(s) \tag{6.3}$$

where R_D is the displacement vector, R_F is the noise and R_C is the convolution of the mean intensities (Keane and Adrian, 1992). The cross correlation graph is shown in Figure 6.3.

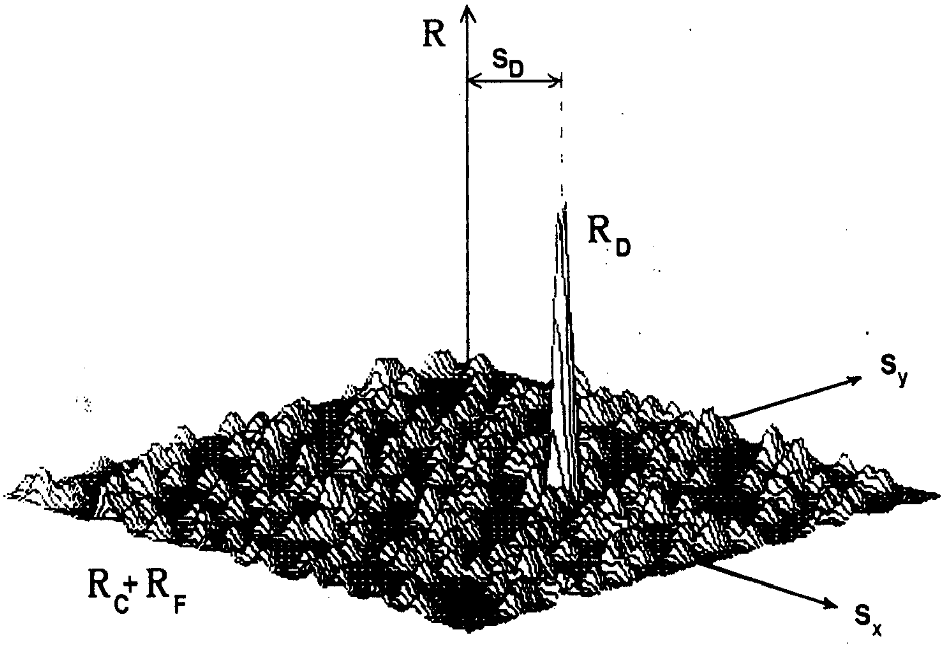

Figure 6.3: Example of Cross Correlation Plane. S_D is the displacement vector (Keane and Adrian (1992).

It is possible to have the displacement vector described to subpixel accuracy. The process of defining the displacement was completed by fitting a curve to three points in both the x and y direction, the correlation at either side of the maximum correlation was used for the three point fit.

The time separating the images is used to calculate the velocity. The displacement vector, and therefore the velocity vector, is determined for each interrogation region and therefore the resolution of the data file is dependent on the interrogation region size. The size of the interrogation regions must be 2^n, where n is a positive integer, pixels in length and width in order to implement Fast Fourier Transforms.

Fast Fourier Transforms (FFT) are used in the calculation of the cross correlation because solving Equa. 6.1 can be computationally intensive. The correlation theorem states that the the cross correlation is equal to the complex conjugate multiplication of their Fourier transforms (PIV: A Practical Guide). The use of FFT allows for the cross correlation to be computed in the frequency domain instead of the spatial domain. FFT significantly speeds up the computational time of determining the cross correlation (Huang et al., 1997). Figure 6.4 graphically expresses the use of the FFT in obtaining the cross correlation.

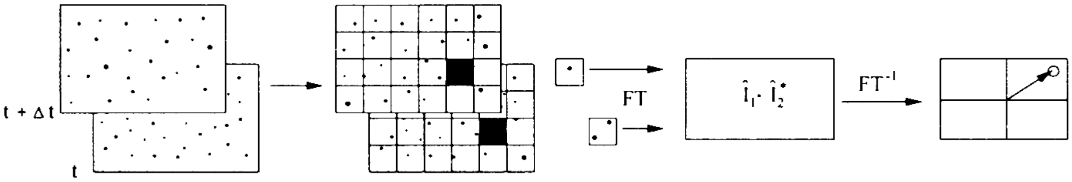

Figure 6.4: Implementation of cross-correlation using FFT (Raffel et al., 1998).

6.1.2 Image Analysis Error

There are several potential areas for error in PIV experimentation. The errors explained in this section are due to error in the image analysis only. There are three types of errors, outliers due to a poor cross correlation, mean-bias errors and root-mean-square (RMS) errors (Huang et al., 1997).

Outliers may be due to a poor image, especially if the image is blurry or does not contain many particles. Outliers may not pass the peak to peak intensity ratio, which is the ratio between the highest correlation peak and the second highest correlation peak, and therefore be dismissed, from the vector field. If they are not dismissed, the outliers can be easily detected, because of their strong deviation from the average, and they can either be removed from the vector field manually or not used in the actual analysis.

The mean-bias error is the difference in the actual displacement and the displacement determined by the processing algorithm. Mean-bias errors occur due to an over or under estimation of the displacement vector (Raffel et al., 1998). Bias error becomes important if peak locking occurs; when a particle image is too small to fit a curve to the cross correlation function. Figure 6.5 shows the relationship between the bias error and the particle image size. It was predicted that bias error due to particle diameter was minimal for this experimentation, based on Figure 6.5, for the particle images were greater then 2 pixels.

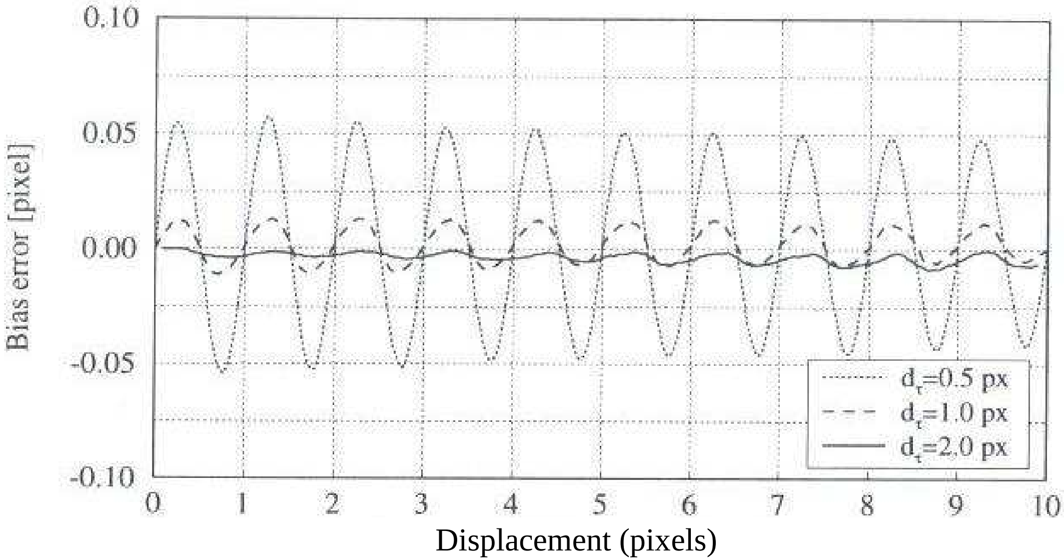

Figure 6.5: Bias Error Diagram Due to Peak Locking (Raffel et al., 1998).

An additional source of bias error is when there is in-plane loss of particle image pairs during the cross correlation process (Raffel et al., 1988). In-plane loss occurs when the particles travel outside of interrogation region on the second frame, which may lead to not being able to obtain a vector which accurately represents the flow field. The in-plane loss of image pairs can be reduced by picking a sufficient interrogation spot size or using a Recursive Nyquist Grid (Section 6.2).

RMS error is the measurement uncertainty or random error (Raffel et al., 1998). Potential sources of RMS error are as follows; poor particle seeding density, strong velocity gradients, three-dimensional flow, non-uniformity in particle illumination and noise that may be induced by the capturing of the images (Huang et al., 1997).

RMS error is at a maximum if the displacement vector is in-between two integers, 0.5 pixels, as shown in Figure 6.6 (Raffel et al., 1998). The reason why the error is at a maximum at this location is because the displacement is furthest from a pixel, and therefore there is more guessing in determining the displacement vector. The error can be reduced by using the Recursive Nyquist Grid. It was also shown, in Raffel et al. (1998), that the RMS is at a minimum for a large number of particle images within an interrogation window, specifically 32 particle/interrogation window.

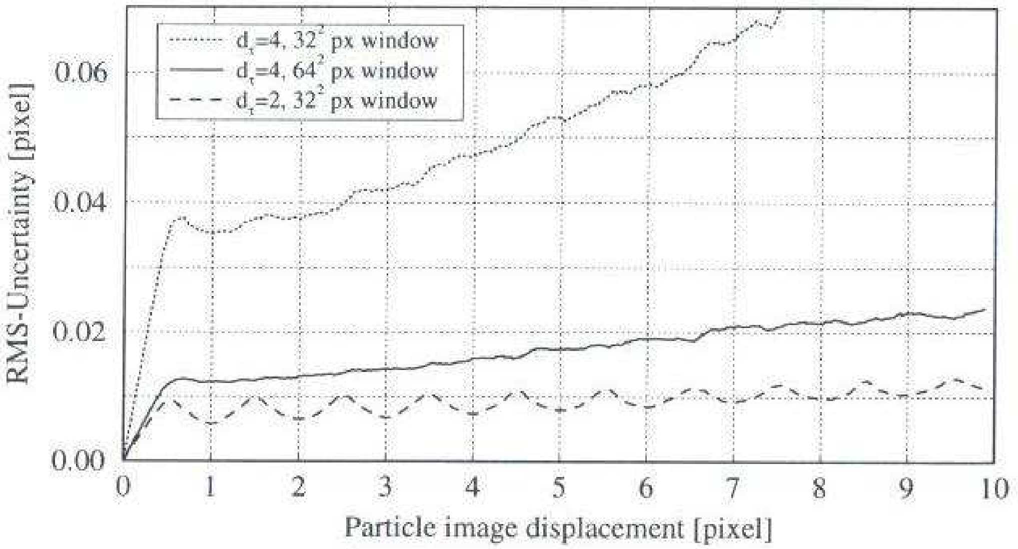

Figure 6.6: RMS Error for Particle Displacements as a Function of the Particle Diameter (Raffel et al., 1998).

For cross-correlation, the bias error and RMS error are additive. The order of magnitude of the error is approximately 0.1 pixels (Huang et al., 1997). The order of magnitude of potential error was taken into consideration during the vector analysis performed.

6.1.3 Analysis Software

The software used for the processing of the PIV images was Insight 3G, which is a TSI product. The processing software performed the cross correlation of the set of images. The velocity vectors were displayed and analyzed using TecPlot. TecPlot contains a module which allowed for easy importation of the vector file that was outputted from Insight. The calculation of the streamline and pathlines were completed in TecPlot (Section 6.5).

6.2 Experiment Specific Image Analysis Parameters

The process in determining the velocity vector is as follows; define the area of the image being analyzed, break image into interrogation regions, compute the displacement vector by cross correlation, perform vector validation and replacement, and convert the displacement vector into velocity by a known delta time.

The processing mask is the area of the image that is being analyzed. For each experiment the processing mask is defined. The location of the processing mask was defined as the edge of the model. Because the model expanded and contracted, the image with the largest deformation, at maximum inspiration, was used for defining the processing mask. The size of the model and the size of the light sheet required that two sets of photographed images be acquired for the healthy and emphysematic alveolar sac models, one with the light

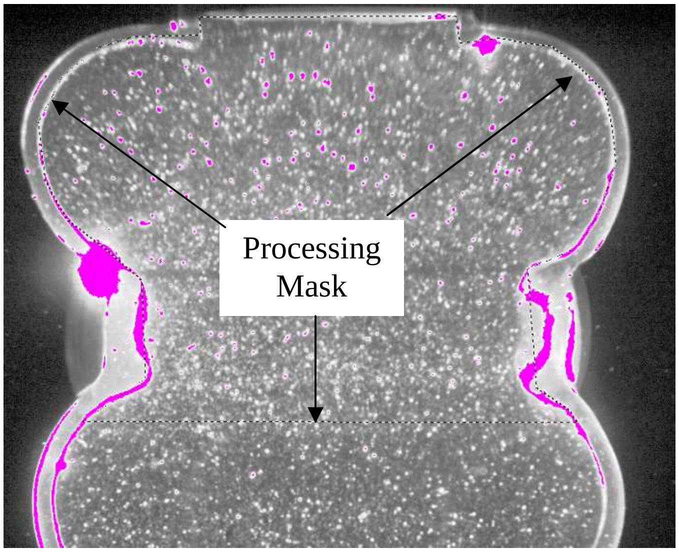

Figure 6.7: Definition of Processing Mask Dotted Line. Healthy Alveolar Sac Model, Light Intensity at Top of Model.

sheet focused at the top of the model and one with the light sheet focused at the bottom of the model. The processing mask for each set was defined only where the light sheet illuminated the fluid, as shown in Figure 6.7.

The light intensity of the image was normalized before cross correlation. The image was normalized using the minimum and maximum intensity in the image (Instruction, Insight 3G, 2007). It was found that by normalizing the image intensity, there were a greater number of vectors that were able to be determined by the cross correlation.

The processing mask area needed to be segmented into interrogation regions. With large displacements it is possible for many of the particles to leave the interrogation region, which may make it difficult to find the best correlation; therefore a Recursive Nyquist Grid was used. A Nyquist Grid offsets the spot window of the first image 50 percent in the horizontal and vertical directions on the second image. The overlap allows for a reduction in in-plane loss of particle pairs. With the Recursive Grid, the cross correlation starts with a large interrogation region and determines the displacement vector for that region. It then breaks up the large interrogation region into smaller regions and uses the displacement vector to determine the spot window offset for the seconds pass. The process allows for an easier detection of the vector for the smaller region (Instruction, Insight 3G, 2007). For all three experiments, balloon, healthy and emphysematic alveolar sac, the large interrogation region was set to 2^6 pixels^2, 64 pixels^2. The Recursive Nyquist Grid was set for only two iterations; therefore the smallest interrogation region was 2^5 pixels^2, 32 pixels^2.

Different types of curves could be fitted to the maximum cross correlation (Section 6.1.1). For all three experimentations a Gaussian curve fit was used, because it can determine the displacement with accuracy of 0.1 pixels. The use of the Gaussian function allowed for the greatest amount of accuracy of defining the displacement vector to the subpixel accuracy (Instruction, Insight 3G, 2007).

The velocity vectors were computed based on the displacement vector and the time separating the frames being analyzed. There are two different time definitions used in the analysis of the photographed images. First, the delta time, Δt, is the time separating the frames used for the cross correlation, as shown in Figure 6.1. Because the flow is unsteady, the velocity was determined at specific times in the flow rate curve. The delta time and velocity data file time separation were specific for each model and the location of the model being analyzed.

6.3 Vector Validation and Post Processing

Displacement vectors were validated based on the difference of the maximum cross correlation and the second highest maximum cross correlation, or the difference between the highest peak and the second highest peak, which is the peak to peak noise. The peak to peak noise was vector processing set to 2, which meant that the highest peak was twice the size of the second highest peak. If the peak to peak noise criterion was not met, the vector was removed from the data file. The holes that were created by removal of bad vectors were replaced by the median of the vectors surrounding the hole.

During the cross correlation processing analysis, there were not many vectors that did not pass the peak to peak noise criteria, in fact most of the vectors had a peak to peak noise ratio much greater then 2. The areas of the model that produced the most error were the areas that contained blurry areas, as shown in Section 3.3.2. The blurry areas were only a problem in the alveolar sac hollow casts. Even though these areas were replaced by the median vector, care was taken in trying to avoid these areas during the pathline analysis.

6.4 Time and Frame Alignment

Because the fluid flow was unsteady, it was imperative to know what time in the flow curve each image frame represented. The camera outputs a voltage when a picture is taken. The camera sync out voltage was acquired through Labview, in the same program which monitored and controlled the expansion and contraction of the models. The Labview program was started before the camera began taking images; therefore the first frame was taken in the middle of the first cycle. The reason why the camera was started in the middle of the cycle, was to determine exactly what time and what frame the camera began taking images. Thousands of images were acquired during the experimentation, and therefore it was crucial to determine what frame represented what time in the breathing curve. The camera remained on, in order to continue to capture photographs for the proceeding cycles. The cycles preceding the first cycle were used for all analysis purposes. An example is presented, to show how the frames were correlated to the breathing curve times. The same correlation

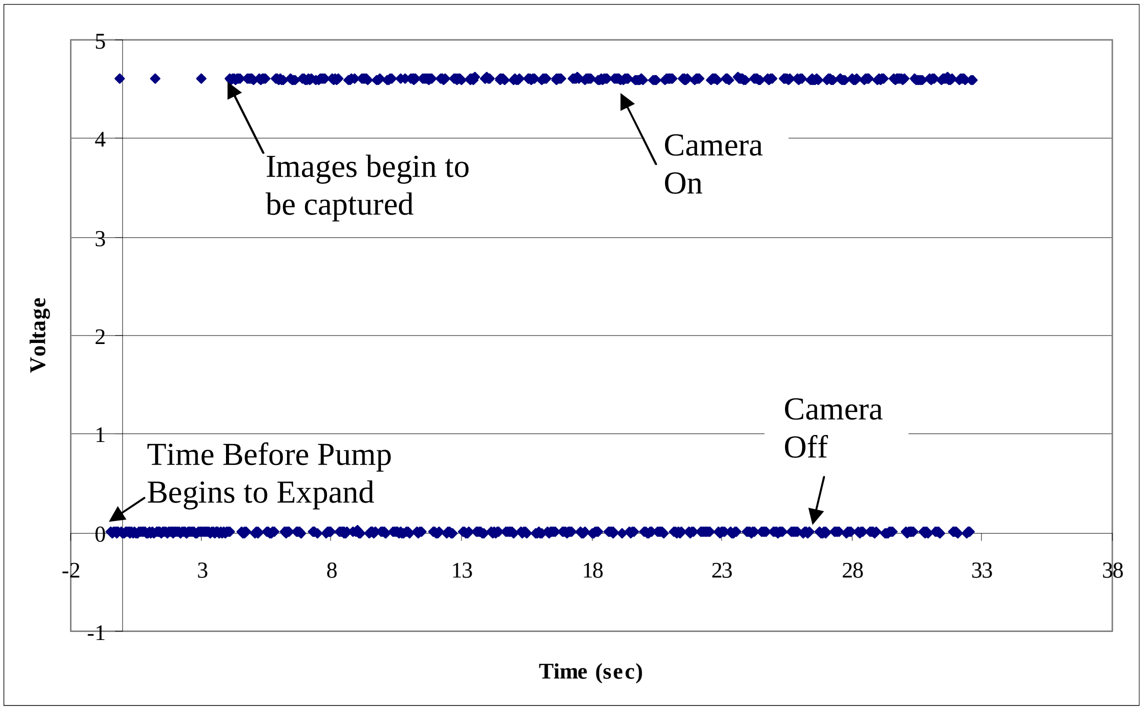

Figure 6.8: Example of the Output Voltage versus Time Graph for the Camera.

concept was applied to all of the experimentations.

The voltage as a function of the time step was outputted from Labview. The time step was normalized, from zero to one, and multiplied by the time to complete the four cycles. There was a small time delay between when the Labview program started and when the pump began to expand, therefore this time was subtracted from the time. Figure 6.8 shows the voltage versus time graph for the camera. The time at which the voltage increased to approximately 4.5 V was when the camera began taking pictures. Because the camera was in a live view mode, which allowed for alignment, there were a few areas where the voltage increased to 4.5 V before the frame acquiring began as shown in Figure 6.8. The step, or time resolution, of the output from the Labview program was every 0.05 seconds; therefore there was an error of 0.05 seconds in the determination of when the camera turned on.

The flow curve from the pressure sensor was outputted from Labview with the same time step as the camera. The change in volume of the model versus time was plotted, as shown in Figure 6.9. The change in volume graph was used, instead of the flow rate graph, because it was a direct measurement taken from the pressure sensor. The flow rate curve was the derivative of the change in volume. The time at which each cycle began was determined from Figure 6.8. It is seen, from Figure 6.8, that it can be difficult to determine exactly what time the cycle began, because of the noise created by the pressure sensor. There was approximately 0.15 second error, which is 7 frames for the balloon model and 15 frames for the healthy and emphysema models, in determining where the cycle begins. To determine what frame the cycle began the following equation was used

$$\text{Frame} = [\text{Time of Cycle Begin} - \text{Time Camera Begins}]*\text{Frame Rate} \tag{6.4}$$

For example, the camera began at a time of 4.081 seconds, as shown in Figure 6.8. The second cycle, or the first full cycle, began at a time of 8.213 seconds. The frame rate was 100 Hz. Using Equa. 6.4, it was determined that the frame at which the first full cycle began was at frame 408.

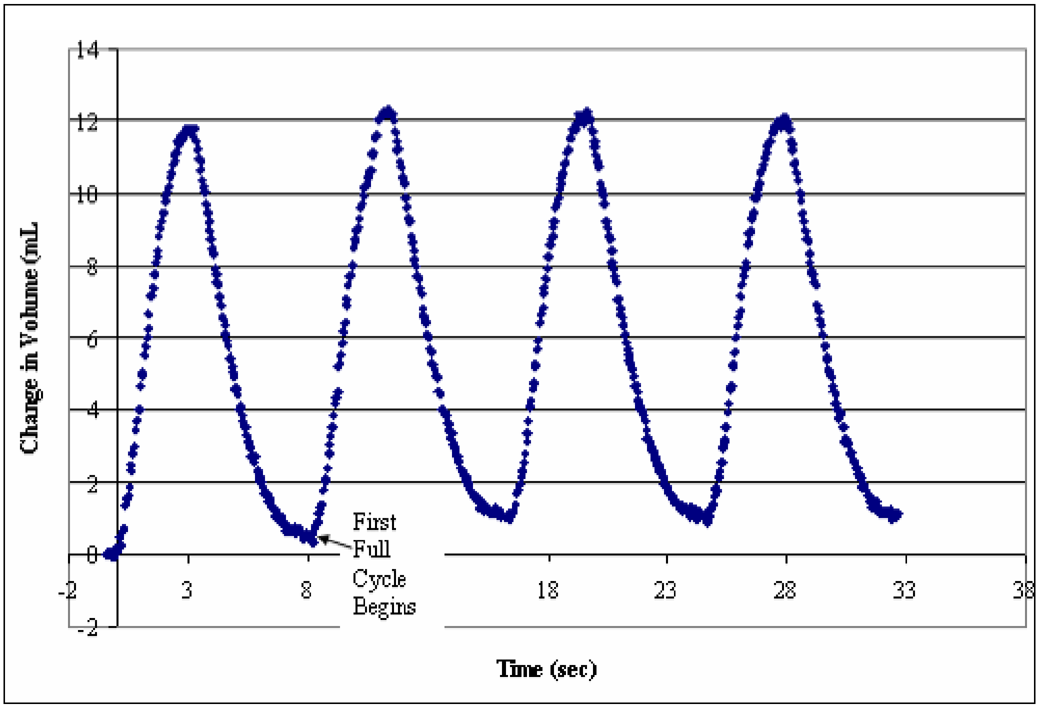

Figure 6.9: Example of Change in Volume Versus Time Graph Outputted from Labview. Figure Used in Location of Cycle Begin Time.

Even though the cycle time was set to a specific time, in this example 8 seconds, the time to complete a cycle varied slightly, by approximately 0.4 seconds more then it should take, due to the acceleration of the pump. In order for the error to not accumulate from cycle to cycle, the frame for where each cycle began was determined. The frame was determined by examining the change in volume curve, Figure 6.9, and determining at what time each cycle began. The frame for each specific time, was determined using Equa. 6.4. For the velocity vector plots in the Balloon model, the frame at which exhale began was also determined in order to be able to accurately align the CFD and the PIV results. From Figure

6.9, it was seen that the volume graph did not return to zero after the second cycle. During the experimentation procedure the change in volume chamber was read, in order to make sure that the pump was displacing the correct volume.

6.5 Calculation of Streamlines and Pathlines

In this work, streamlines and pathlines were used in order to visualize the fluid flow. Streamlines are curves that lie tangent to the velocity vector. Streamlines are not a function of time, only a function of spatial, and therefore are used to examine a steady flow or at a single time period. The pathlines track a fluid, massless, particle through a flow field with time.

The streamlines and pathlines were plotted in Tecplot. The beginning coordinate of the streamline was defined in Tecplot. The velocity vector data files, separated by a known time, were used for the pathline calculation. The time separating the velocity vector data files were defined in Tecplot. To calculate the pathline, numerical time step integration was used. The numerical integration time was defined in Tecplot. The pathlines were calculated over the range of the data files, typically for one breathing cycle. Figure 6.10 shows graphically, how a pathline was created.

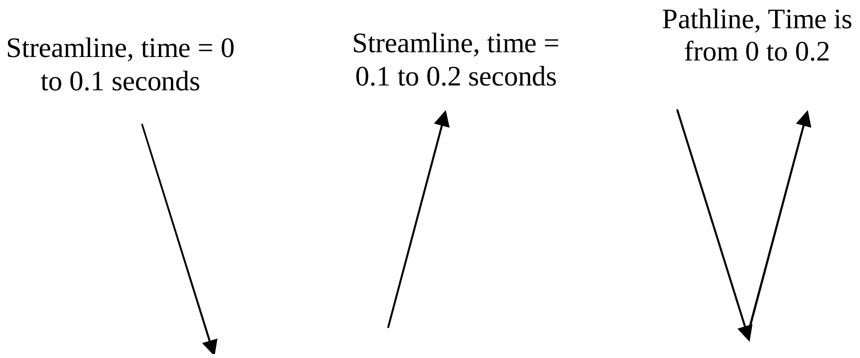

Figure 6.10: Streamline and Pathline Example

Chapter 7
Experimental Validation

7.1 CFD Model

A computational fluid dynamic analysis of the balloon CAD model (Section 3.1.1) was completed. The CFD model was used in the validation procedure of the PIV experimentation. Model material deformation and PIV vector analysis results, for the balloon hollow cast, were compared to the CFD model. The finite element software program, COMSOL, was used for the numerical simulation. The model incorporated non-steady fluid and structure interaction. The structure, as well as the fluid, was modeled because a detailed understanding of how the boundary of the balloon model expanded was unknown. Modeling both the fluid and structure allowed for the model to expand and contract based on an inlet fluid boundary condition. The model was solved for a total of 12 seconds, the length of the un-steady flow rate curve used. The solution was solved for in 0.025 second time increments. In order to assure convergence, a mesh and tolerance analysis was performed.

7.1.1 Boundary Conditions and Fluid/Material Properties

Boundary conditions on the computational model were important, for the boundary conditions controlled the behavior of the system. In this particular model, it was crucial to define the boundary conditions such that the model would behave similarly to the PIV hollow cast model. Figure 7.1B shows the location of the boundary conditions. The flow rate was defined at the inlet of the CFD model. The inlet flow rate boundary condition was defined in Section 4.2.3. Because there was no outlet, the model expanded and contracted in order to account for the fluid entering and exiting through the inlet. The fixed and fluid load boundaries controlled what parts of the model would expand due to the fluid movement and what areas of the model would remain stationary. The model was axially symmetric along the left boundary.

The CFD model needed to incorporate both the fluid and structure properties. Figure 7.1A shows the location of the fluid and the structure. The fluid was modeled as pure glycerin. The material properties of Ultraflex were not fully understood, so material properties had to be estimated. The material was assumed to be isotropic; the material expanded

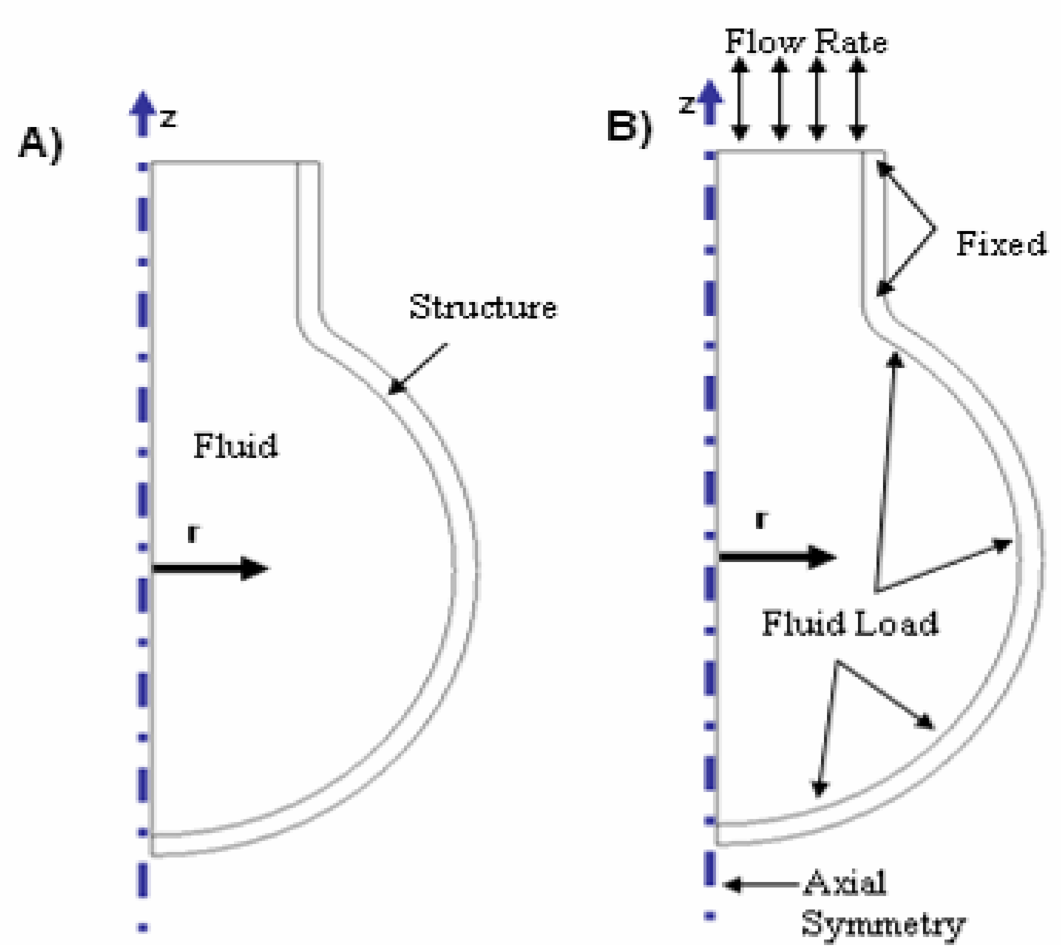

Figure 7.1: Fluid, Material (A), and Boundary Condition (B) Locations on CFD Balloon Model.

uniformly in all directions and Hook's Law could be applied. The elastic modulus was assumed to be 1.2e4 Pa and the Poisson's ratio was 0.49. A test was performed in order to validate the assumption.

The elastic modulus assumption was tested in order to determine how the elastic modulus influences the expansion. Two different elastic moduli were used; 1.2e4 Pa and 1e7 Pa. The balloon's maximum deformation was examined at 4.6 seconds for each elastic modulus. For the elastic modulus of 1.2e4 Pa the maximum deformation was 3.43e-3 m. The maximum deformation for the elastic modulus of 1e7 Pa was 3.37e-3 m. The reason why the maximum deformations were similar, even though very different elastic moduli were used, was because of how the expansion and contraction was defined in the system. The inlet boundary flow rate condition prescribes how much the model must deform in order to account for the fluid entering and exiting the model. Because the pressure force is solved for, and not defined, the pressure force acting on the structural walls would change based on the elastic modulus of the material. The pressure difference between the inlet and the structure remained the same in both models; therefore the fluid flow would behave similarly. Based on the elastic modulus analysis, it was concluded that assuming a physically realistic elastic modulus was acceptable for this particular CFD model. Future work is being completed in understanding the material properties of Ultraflex, in order to create a more realistic model.

7.1.2 Mesh and Tolerance Convergence Analysis

In order to determine the accuracy of the CFD model, a convergence analysis was performed in order to determine if the CFD converged to an accurate solution. The model's accuracy was dependent on two parameters, the mesh and the tolerance criteria. COMSOL defined the default mesh size as Normal, Fine and Finer, indicating the number of mesh elements. Two tolerances were defined in COMSOL, the absolute tolerance, A_{tol}, and the relative tolerance, R_{tol}. The error in the converged solution is determined by

$$|e(i)| \leq R_{tol}\left[|y(i)| + A_{tol}\, y(i)\right] \tag{7.1}$$

where e(i) is the error vector and y(i) is the solution vector (Instruction, COMSOL, 2007).

The dependence of the solution on the mesh size needed to be determined. For the mesh size analysis, the mesh was altered between Normal, Fine and Finer. The relative tolerance was set to 0.01 and the absolute tolerance to 0.000001. The velocity profile was plotted at a location of 0.01325 on the z – axis at time step of 1 second. The location of the analysis was determined to match the location of the velocity profile plot analysis performed in Section 7.3.1. Figure 7.2 shows the location of the velocity profile plot. The velocity profile plots, based on the mesh size are shown in Figures 7.3 and 7.4, for the entire velocity profile and the velocity profile zoomed in to the high speed area. In the very slow regions, close to zero, the maximum percent difference from the Fine to Normal mesh size was 0.44 % and 0.46 % from Fine to Finer. At the area of maximum velocity the Fine

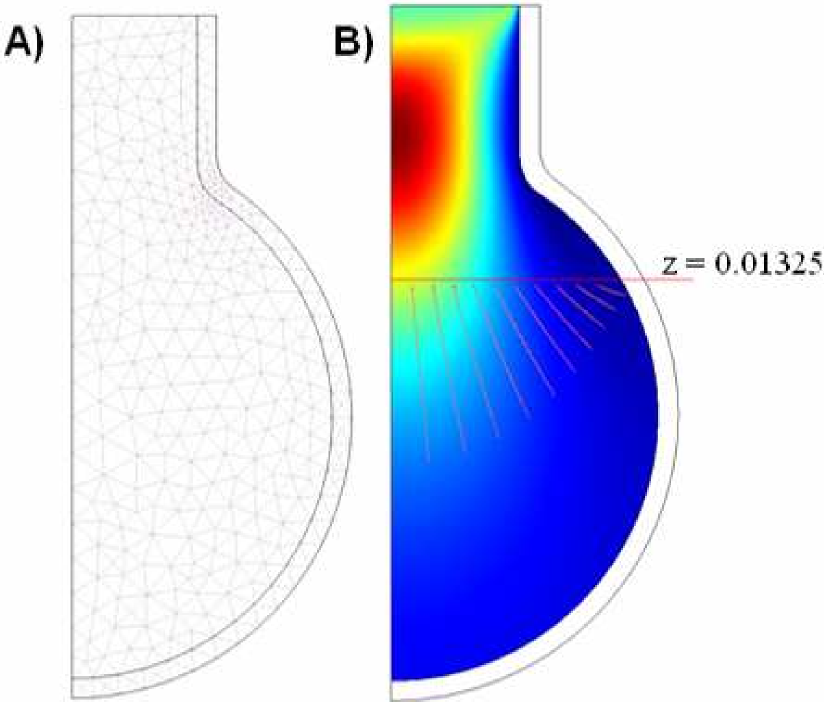

Figure 7.2: Mesh (A) and Location of Velocity Profile (B) of CFD Balloon Model

to Normal mesh size had a percent difference of 0.26 % and the Fine to Finer mesh had a percent difference of 0.21 %. From the analysis it was a mesh size of Fine would be sufficient.

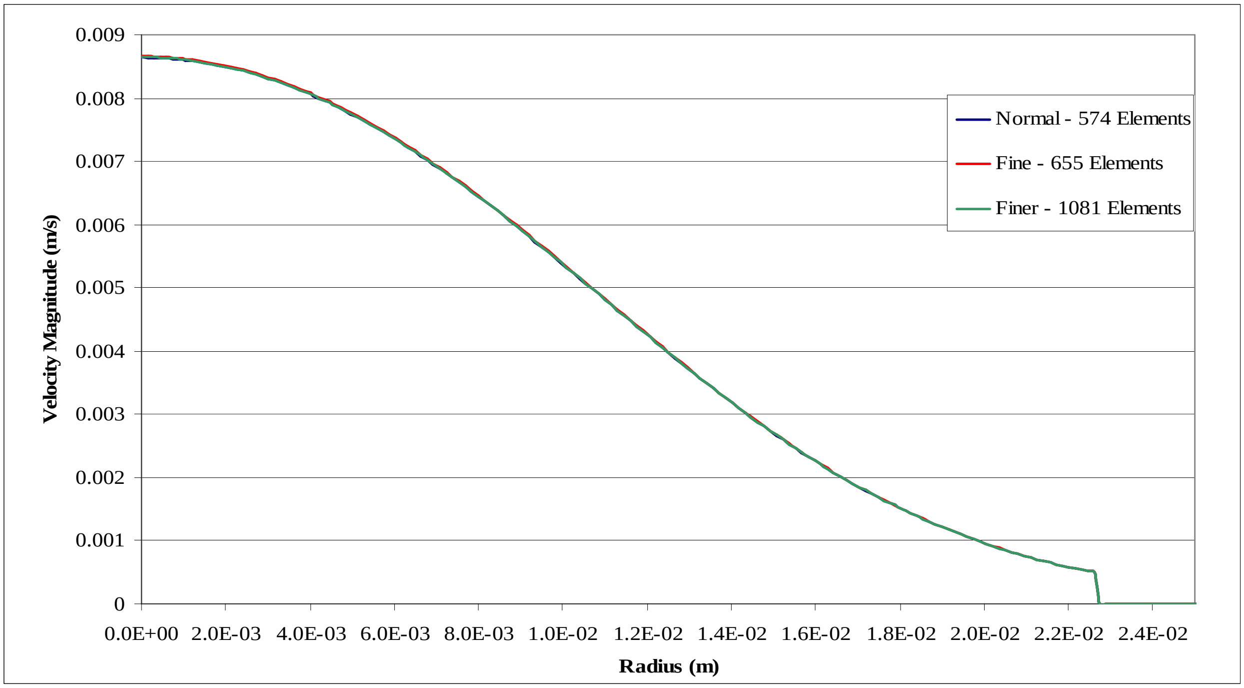

Figure 7.3: Mesh Size Convergence for CFD Balloon Model

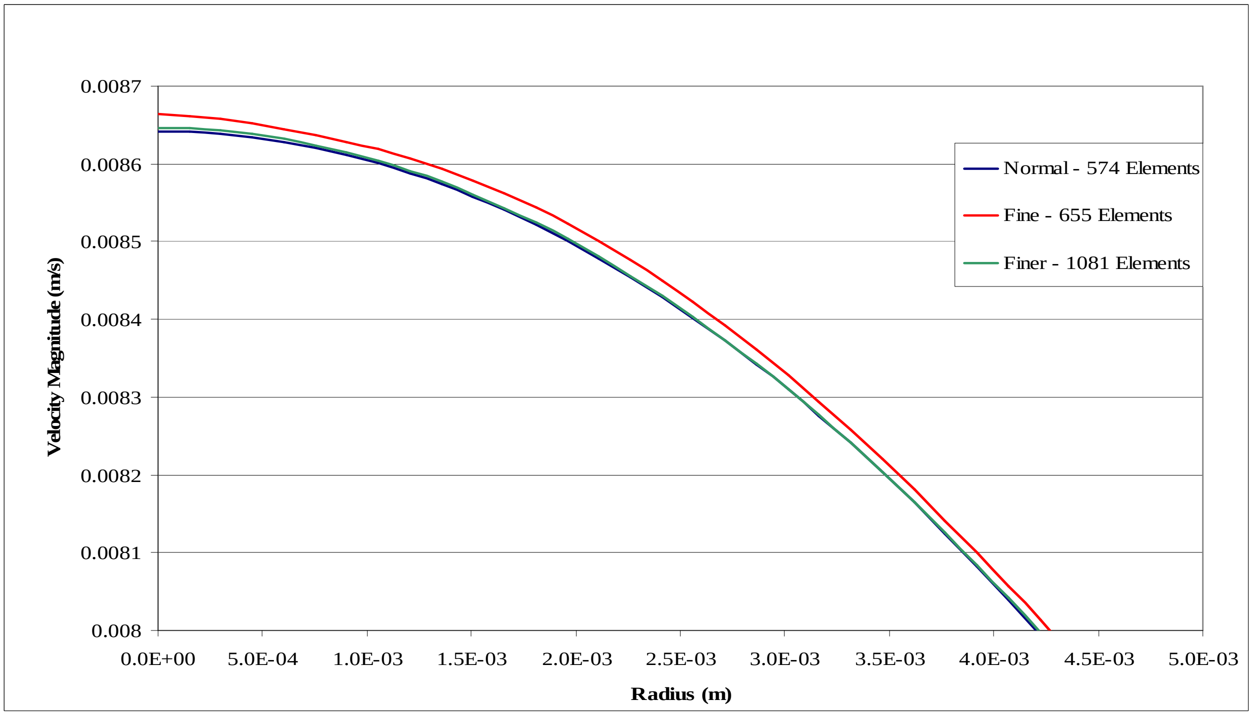

Figure 7.4: Mesh Size Convergence for CFD Balloon Model: Focused on High Speed Area.

A sufficient absolute tolerance needed to be determined for the balloon CFD model. An analysis was performed, where the absolute tolerance was altered between 0.00001, 0.000001 and 0.00000095. The relative tolerance was held at a constant value of 0.01. Figure 7.5 shows the velocity profile plot at 1 second for a z coordinate of 0.01325 m. Figure 7.6 shows the velocity profile plot zoomed into the high speed area. The difference at the very low speed areas of 0.00001 and 0.000001was 0.29% and between 0.000001 and 0.00000095 was 0.34%. At the highest velocity area the difference between 0.00001 and 0.000001 was 0.00044% and between 0.000001 and 0.00000095% was 0.002%. From the analysis it was determined to use an absolute tolerance of 0.000001 and a relative tolerance of 0.01.

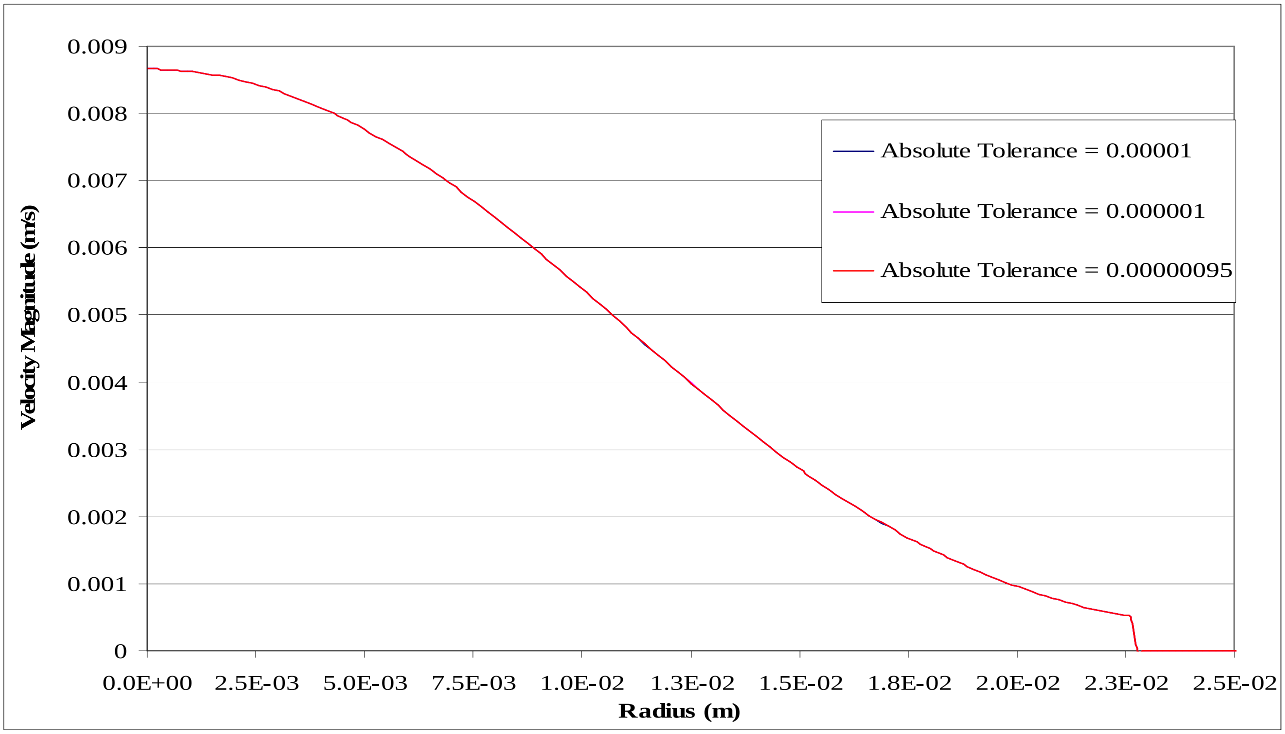

Figure 7.5: Absolute Tolerance Convergence for CFD Balloon Model.

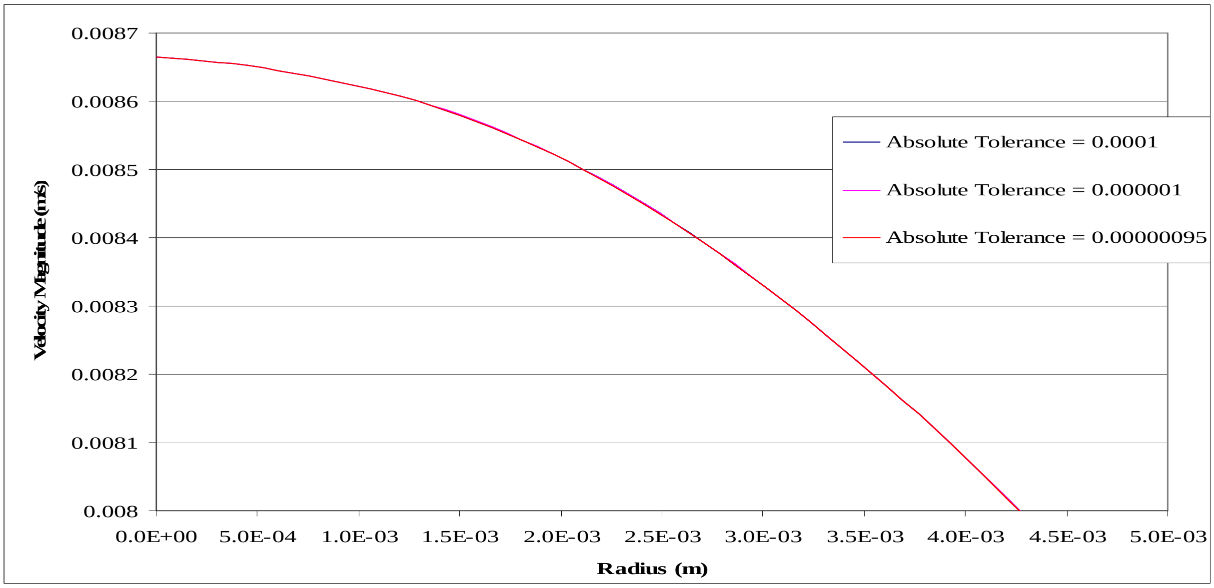

Figure 7.6: Absolute Tolerance Convergence for CFD Balloon Model: Focused on High Speed Areas.

7.2 Model Deformation Analysis

In order to fully understand how the balloon deforms, an analysis was completed on both the hollow cast and the CFD model. The goal of the analysis was to determine if the CFD model and the hollow cast were deforming similarly and if the hollow cast deformed uniformly. There were two reasons why the hollow cast may not deform uniformly. The first was due to a variation in thickness of the hollow cast and the second was the location of the pump. Because of the way the model was made, it was difficult to achieve uniform thickness. The thickness of the model varies from 0.122 mm to 0.269 mm. The pump controlled the expansion and contraction of the hollow cast due to pressure changes. The pump was located on one side of the hollow cast (Section 5.1) and therefore there was potential for there to be a non-uniform pressure distribution inside the chamber, which would cause non-uniform expansion of the hollow cast.

The coordinate system for the PIV and CFD models differed. The coordinate system for the hollow cast PIV analysis is shown in Figure 7.7A, where the origin is at the left bottom corner. Figure 7.7B shows the coordinate system for the CFD mode, where the origin is at the middle of the sphere. Because of the origin differences, care had to be taken in making sure that the coordinate system was converted when analyzing the results. There was approximately 0.2 mm error in determining the location in the PIV experimental model. The PIV and CFD deformation needed to be compared to each other. The hollow cast balloon and the CFD model were measured in several different places. The first three measurements were performed at the widest area of the model. By measuring the radius on either side of the model it could be determined if one side was expanding more then the other side. Measurement 1 was the entire diameter, and for comparison purposes, this measurement was

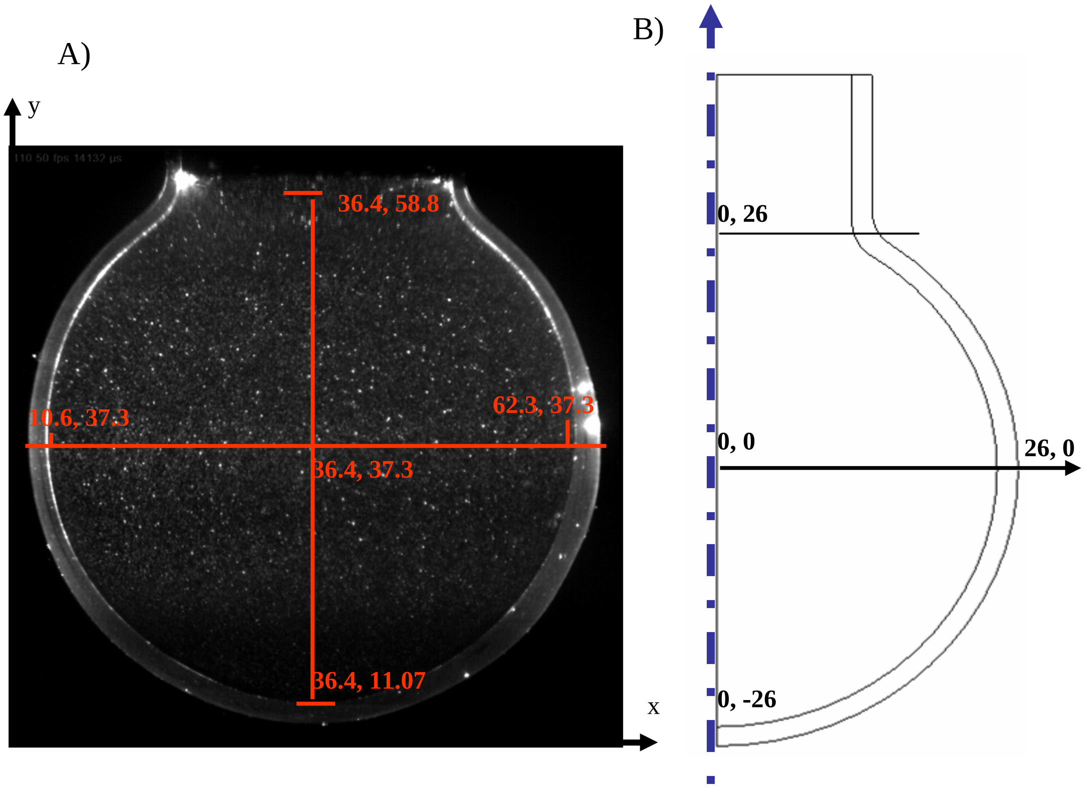

Figure 7.7: PIV Image (A) and CFD (B) Dimension Locations. All dimensions are in mm.

divided by 2 in order to achieve the average radius. Measurement 2 and 3 measured the horizontal radius of the model for the left and right side, respectively. Measurement 5 and 6 allowed for examination of the radius near the fillet for the left and right side, respectively. Measurement 4 was inspected in order to determine how the bottom of the model expanded. Figure 7.8 shows the location of each of the measurements.

The PIV analysis was performed on the images for the first breathing cycle. The measurements were completed in the program, Image J. Care was taken in making sure that only the change in the x direction was measured, in both the hollow cast and CFD model. The deformation was measured at every 0.4 seconds. It was difficult to determine exactly the location of the model because of light reflection and therefore not having a perfectly crisp image Figure 7.9 shows the error, which was approximately 3 pixels, or 0.019cm, error in the measurement from the hollow

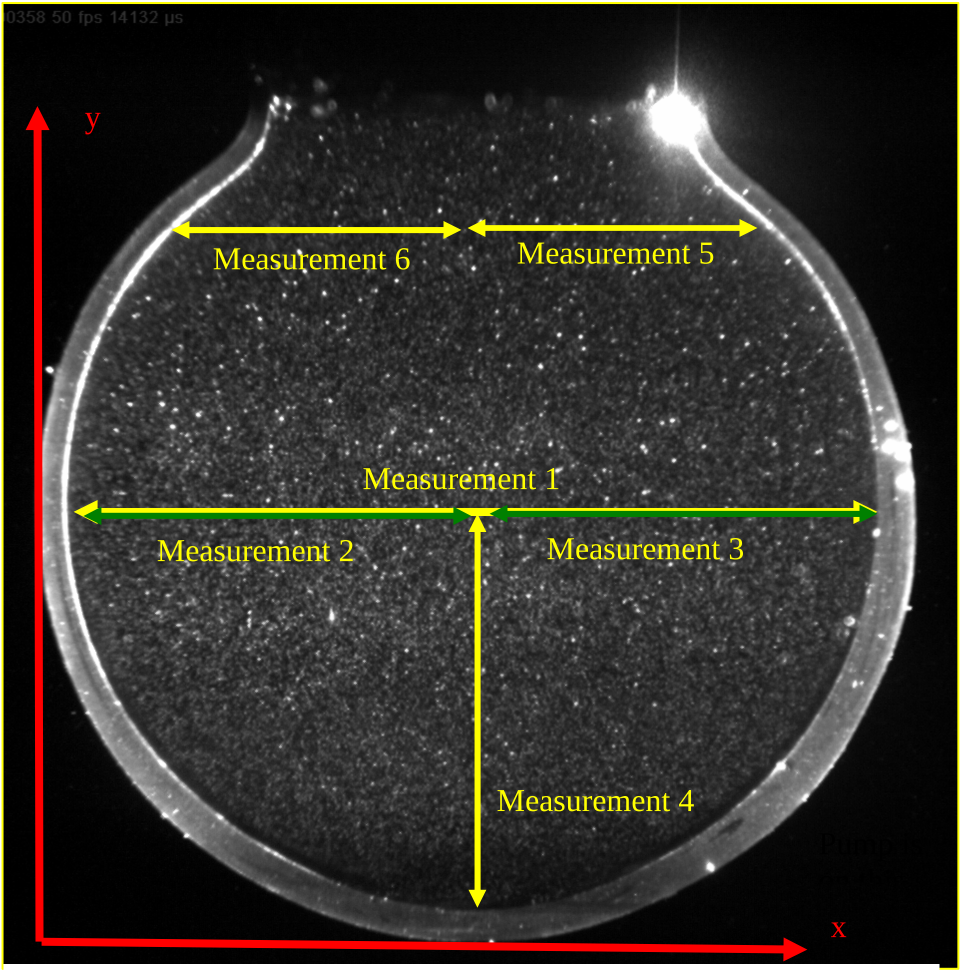

Figure 7.8: Model Deformation Measurement Locations.

cast. Figures 7.10 shows the comparison between the CFD and PIV balloon deformation for measurements 1, 2 and 3. The comparison between CFD and PIV for measurements 5 and 6 is shown in Figure 7.11. Figure 7.12 illustrates the model deformation between the CFD and PIV for measurement 4. Figure 7.10 clearly shows that the model thickness does influence the expansion and contraction of the model. The left side of the hollow cast, measurement 2, the side with the thinner walls expanded more then the side with the thicker wall, measurement 3, Figure 7.8. The pump was on the right side of the hollow cast, which is the side that expanded less. It cannot conclusively be determined whether the pump was pulling the hollow cast, but the side closest to the pump did not expand more then the left side, which would be expected if the pump was pulling the hollow cast. It is shown in Figure 7.12 that the radius, measurement 4, of the bottom of the hollow cast is larger then the CFD model. The hollow cast was made from a boiling flask, not a perfect sphere. The bottom of the boiling flask is approximately 0.025 cm longer then it is wide. The hollow cast expanded more then the CFD model, as shown in Figure 7.11, at the fillet region of the model, measurement 5 and 6. Figure 7.13 shows the PIV and hollow cast completely expanded, where it can be seen that the CFD and PIV model expanded different at the fillet. The knowledge

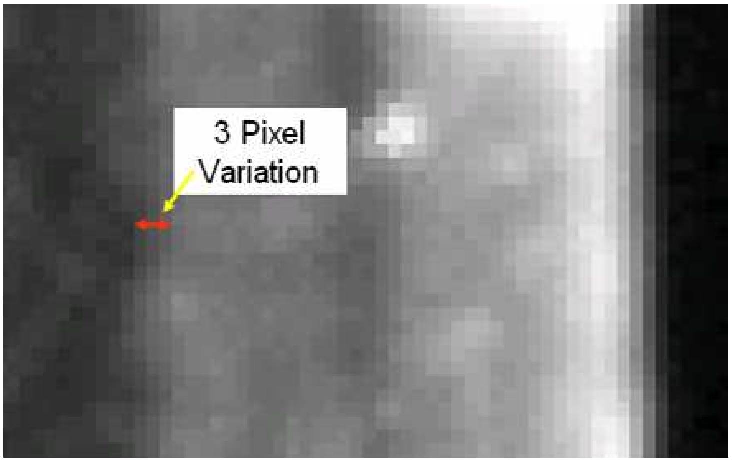

Figure 7.9: 3 Pixel Errors in Hollow Cast Measurement Technique

that the PIV model was expanding more on one side was used in understanding the analysis of the velocity profile plots and the pathlines.

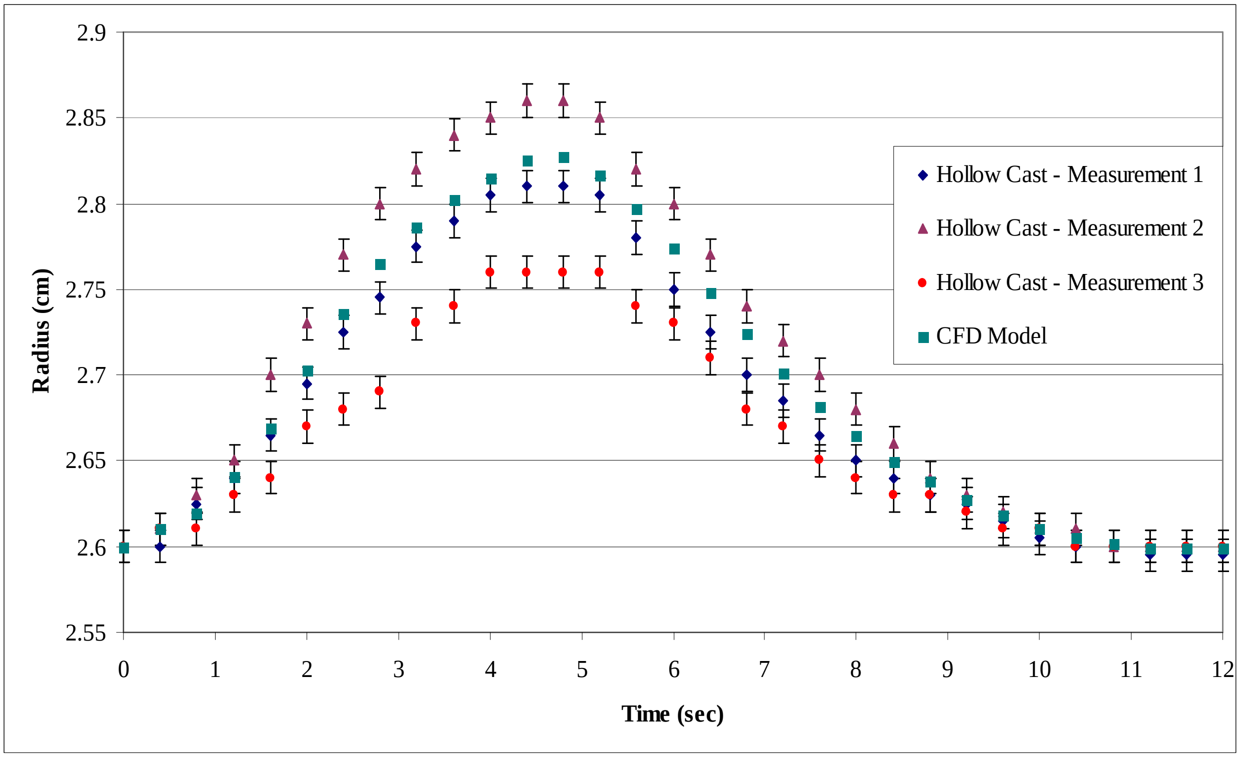

Figure 7.10: Model Deformation Analysis between CFD and PIV for Measurements 1, 2 and 3.

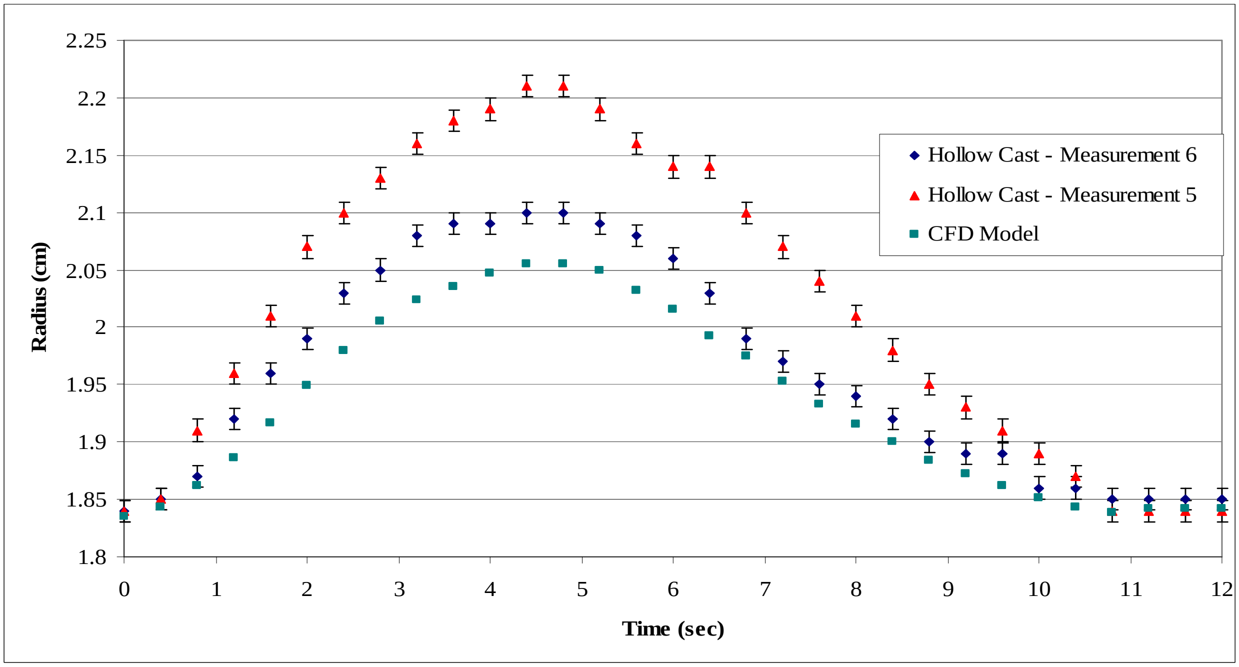

Figure 7.11: Model Deformation Analysis between CFD and PIV for Measurements 5 and 6.

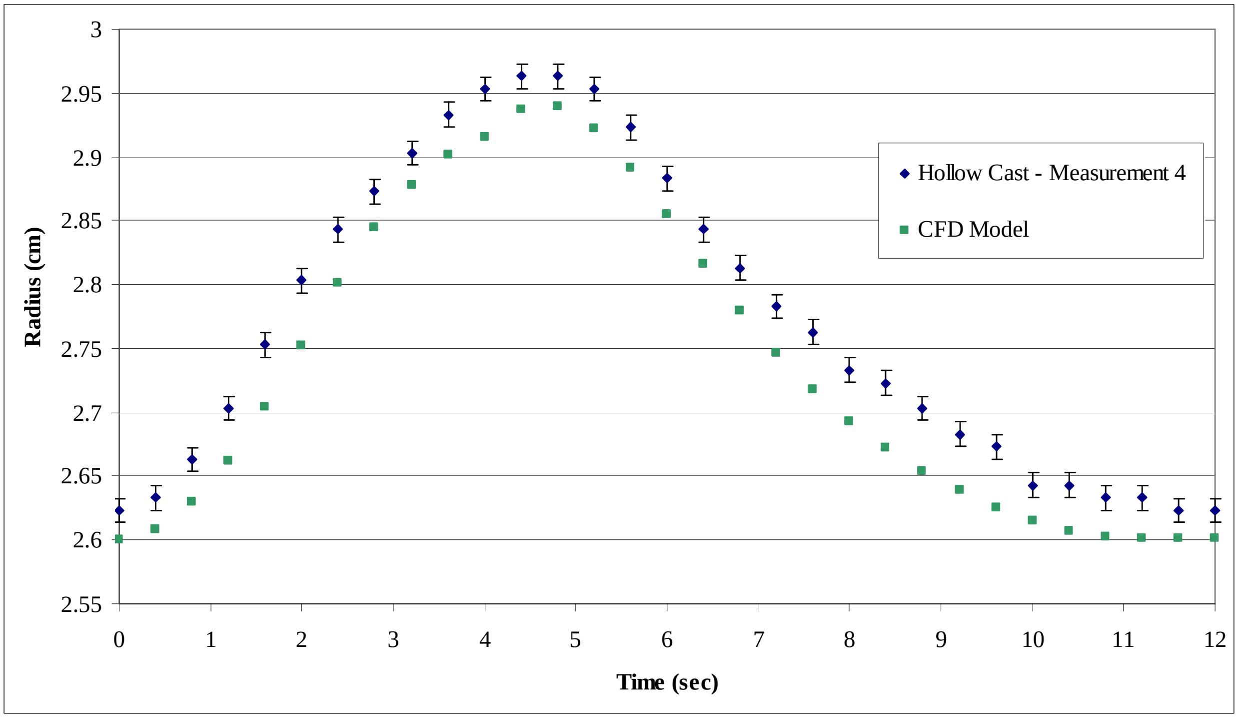

Figure 7.12: Model Deformation Analysis between CFD and PIV for Measurement 4.

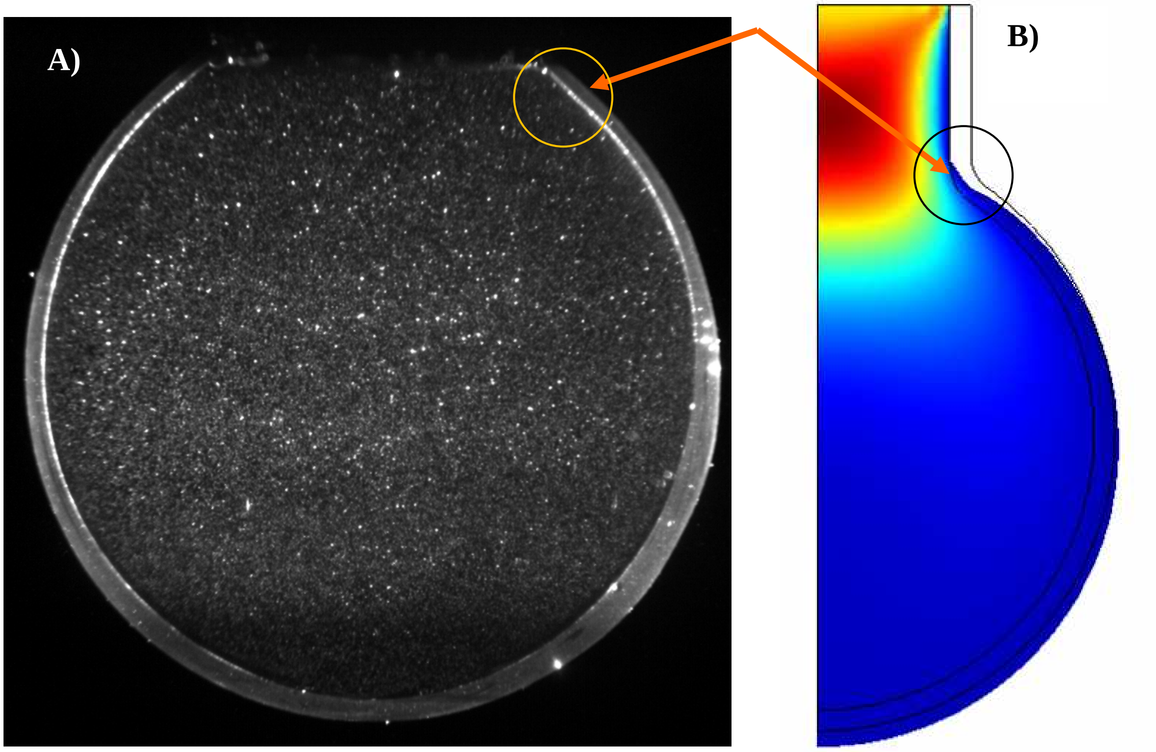

Figure 7.13: Comparison of Fillet Area of Hollow Cast (A) and CFD Model (B).

7.3 Fluid Flow Results

Velocity vectors of the hollow cast and the CFD model were compared two different ways; velocity profile plots and by pathlines.

7.3.1 Velocity Profile Plots

A comparison between CFD and PIV results were made by plotting velocity profile plots for both the CFD and PIV data. Four velocity plots were created representing different times in the flow rate curve, Section 4.2.4. The velocity profile plots that were completed on the Balloon model were at areas of high velocity and acceleration at both inhale and exhale. Table 7.1 shows at what time each plot was at, and the delta time used. At the areas of high velocity were at low acceleration; therefore the velocity did not change quickly. At the areas of high acceleration, the velocity does change quickly, and therefore timing alignment problems are more noticeable. CFD outputs the velocity field at a specific time, therefore the time at which each frame is used for the cross correlation was plotted in the velocity profile plots. For example, the profile plot for high velocity at inhale used frames at times 2.148 seconds and 2.208 seconds for the cross correlation. In the velocity profiles plots, the CFD times were plotted for times 2.148 seconds and 2.208 seconds. The delta time, the time separating the frames for cross correlation, differed between the plots, which depended on what time step was being analyzed. As discussed in Section 6.2, it was important to have a delta time which produced a vector displacement such that errors had a small influence on the vector. The delta time for each time step is also shown in Table 7.1.

Table 7.1: Times Analyzed for Velocity Profile Plots in Balloon Model

	Time of Frame 1 (sec)	Time of Frame 2 (sec)	Average Time (sec)	Delta Time (sec)
High Velocity at Inhale	2.148	2.208	2.18	0.06
High Acceleration at Inhale	1.00	1.06	1.03	0.06
High Velocity at Exhale	6.00	6.06	6.03	0.06
High Acceleration at Exhale	5.40	5.48	5.44	0.08

The velocity profile plots were analyzed at the upper middle of the model. The velocity profile plots could not be taken too close to the duct of the balloon, at y equal to 58.8 mm, for the cross correlation was not strong in that area because of the PIV particles moving in and out of the model. Because the CFD and PIV models expanded slightly different from each other, at the worst near the fillet, the velocity profile plots were taken away from the fillet. The velocity profile plots for the PIV models were all taken at the location of y equal to 47.03 mm which was in-between the middle and top datum planes (Figure 7.7A). The location of the velocity profile plot on the CFD model varied between 13.1 mm and 13.7 mm. The location of the plots were chosen on the CFD model such that the radius at that cross section, for the given expansion amount, matched the radius of the PIV at the same expansion.

Three breathing cycles were performed and analyzed for the velocity profile plots. The analysis of three cycles allowed for an average to be determined. Figure 7.14 shows the comparison between the CFD and PIV at maximum velocity at inhale and Figure 7.15 shows the comparison for high acceleration at inhale. Figure 7.16 shows the comparison between the CFD and PIV at maximum velocity at exhale and Figure 7.17 show the comparison for high acceleration at exhale. The error bars, on the figures, are a combination of the standard deviation between the three cycle as well as an added +/- 0.1 pixel potential error that occurs during PIV analysis (Section 6.1.2). The PIV and CFD velocity profile plots were very similar at the high speed areas, areas of low acceleration, Figures 7.14 and Figure 7.16, for inhale and exhale, respectively. There was more error at the high acceleration areas; the CFD velocity is smaller then the PIV, Figures 7.15 and Figure 7.17, for inhale and exhale, respectively. There was the most standard deviation, between the three PIV cycles, at the plots from exhale, Figure 7.16 and 7.17 for high velocity and high acceleration, respectively. Because the flow is unsteady, the velocity magnitude changes quickly with time. Figure 7.15 shows the velocity magnitude of the CFD plot at 1.0 seconds and 1.06 seconds. From the CFD plots, on Figure 7.15, it can be see that the velocity changes very quickly between 1.0 seconds and 1.06 seconds. The rapid change in velocity indicated that if there was any error in determining what frame, and therefore what time the cycle began, then the velocity profile will reflect that error. It was determined, in Section 6.4, that there is a potential to have 0.2 seconds of error in choosing what frame the cycle begins at. In the low speed area of the velocity profile plot, at the larger radius, the CFD and PIV had a very good correlation for all of the times analyzed. It was determined that there was good agreement between the CFD and PIV, for the velocity profile plots, and if there was any error that does occur it may be due to error in choosing what frame the cycle began at.

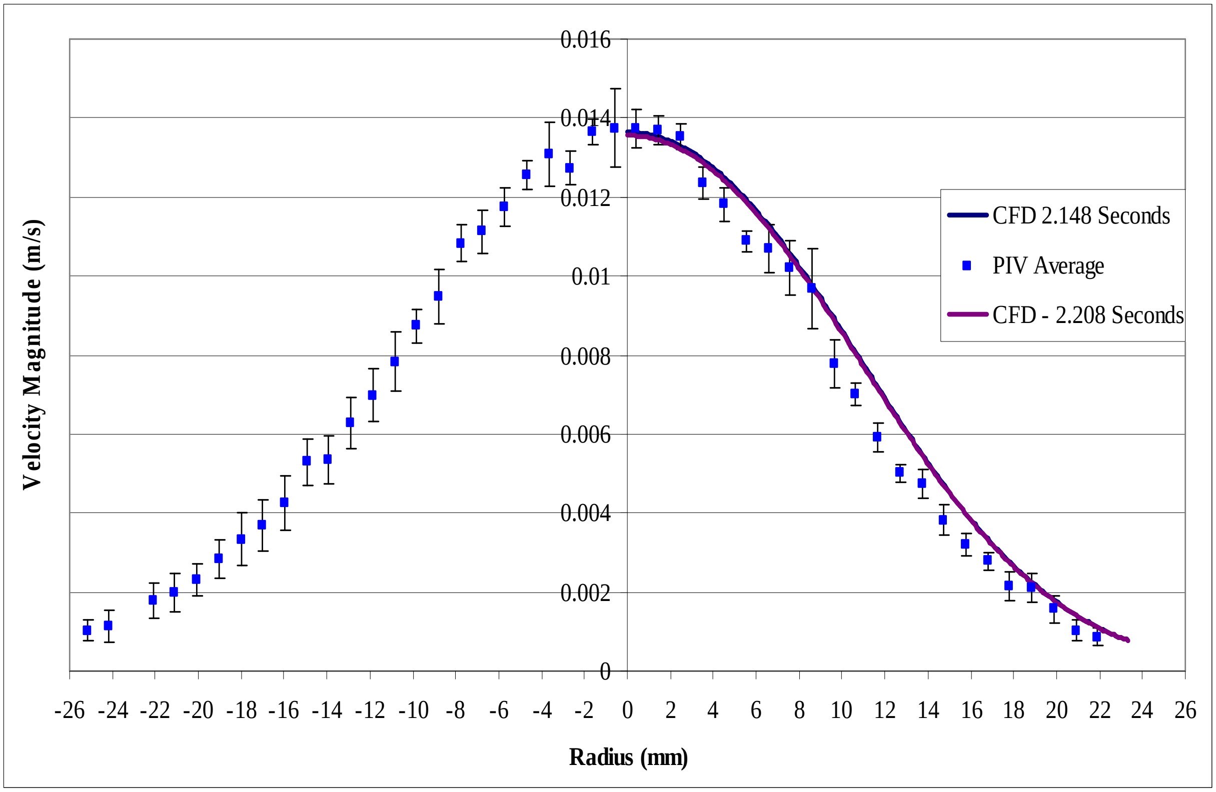

Figure 7.14: Balloon Velocity Profile Plot for Maximum Velocity Magnitude at Inhale.

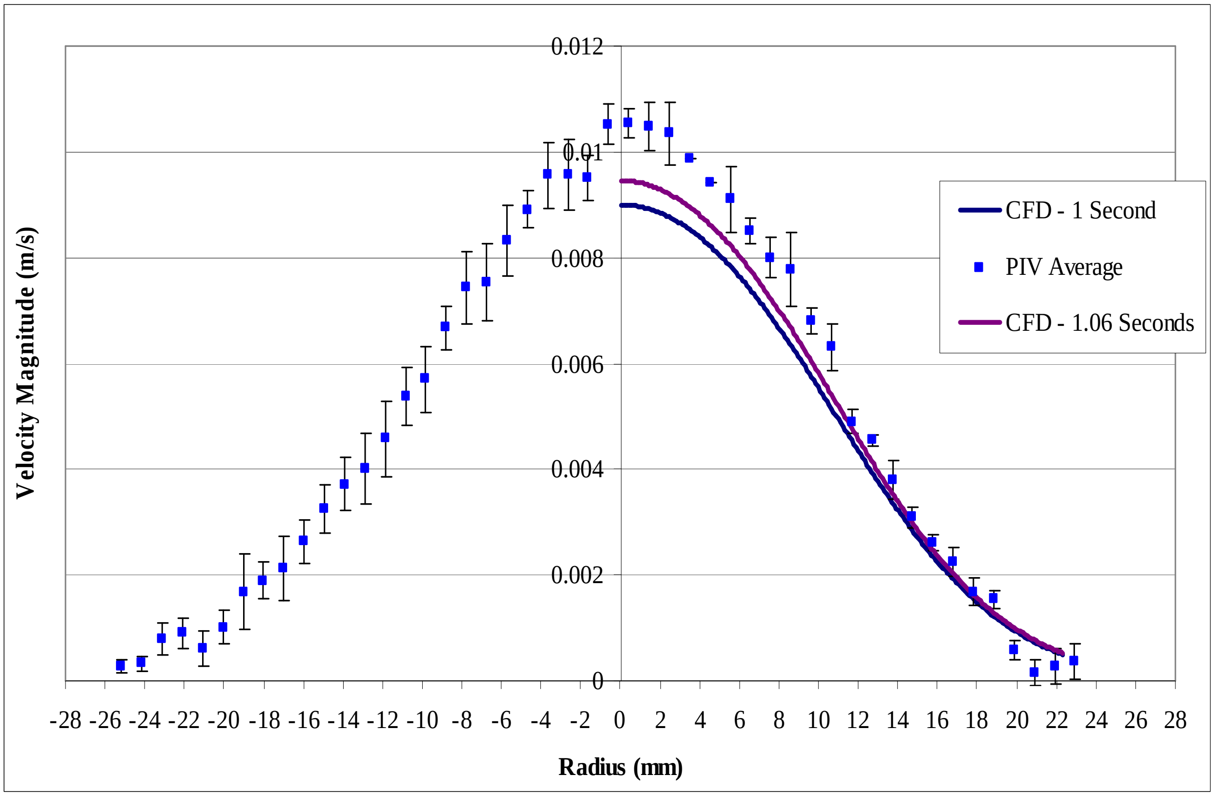

Figure 7.15: Balloon Velocity Profile Plot for High Acceleration at Inhale.

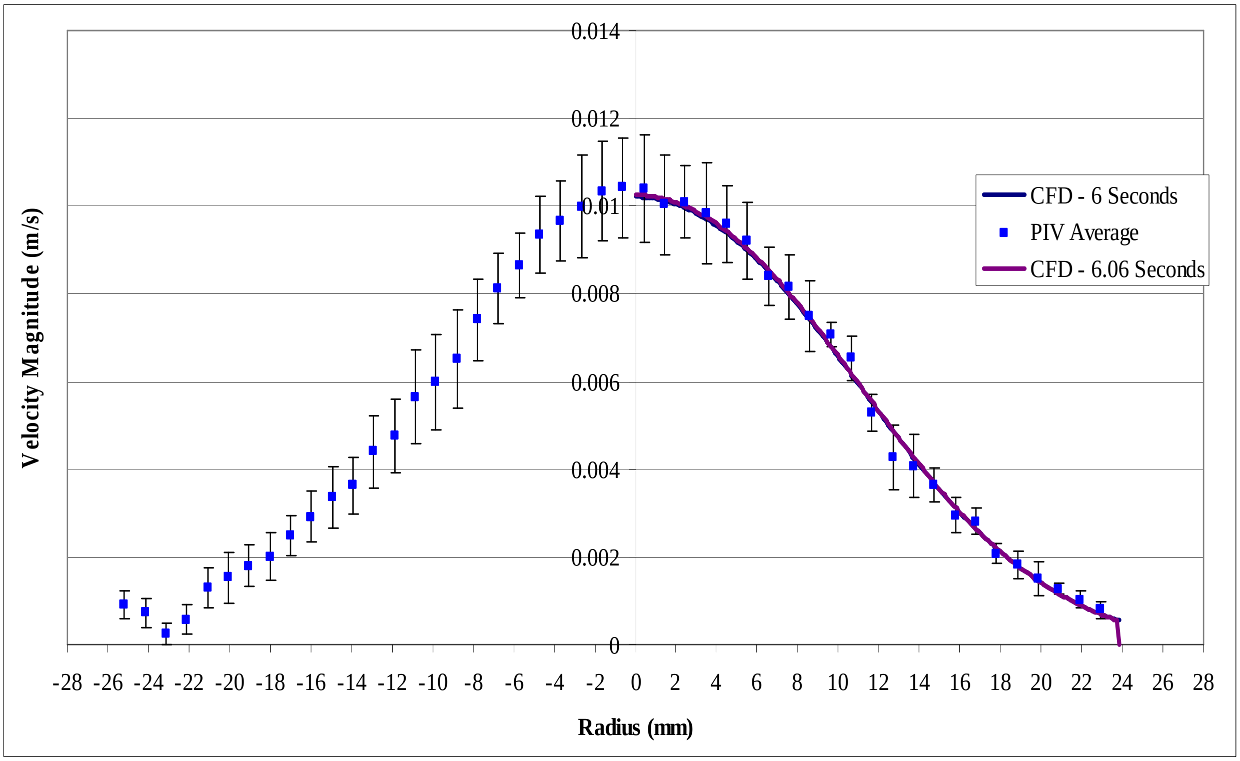

Figure 7.16: Balloon Velocity Profile Plot for Maximum Velocity at Exhale.

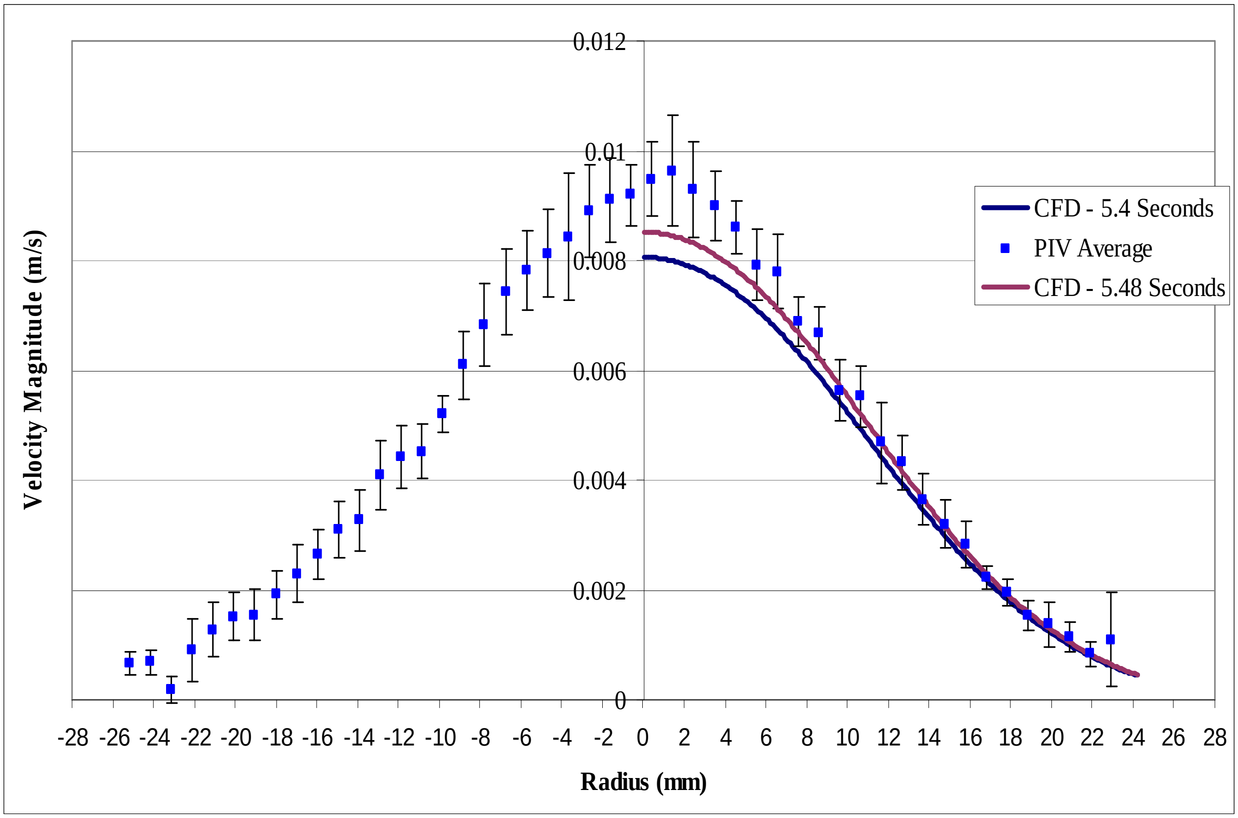

Figure 7.17: Balloon Velocity Profile Plot for Maximum Velocity at Exhale.

7.3.2 Pathlines

Pathlines, which examine the flow field with respect to time, were plotted in both the CFD and PIV balloon models. The velocity vector files that were used in calculating the balloon pathlines were separated by 0.4 seconds. Figure 7.18 shows the time of what each velocity vector was determined. The determination of the delta time, the time separating the frames for cross correlation analysis, for the pathline analysis varied based on the location of the pathline with time. The speed of the fluid decreased the further it traveled into the model and the flow rate increased and decreased with time, depending on what portion of the breathing cycle was being analyzed. In order to determine the best delta time, an iterative time choosing process was developed and followed. For each time step a delta time was chosen and the set of images were analyzed. The data set for all the time steps analyzed \were loaded into TecPlot and the pathlines were calculated. At each time step the location of the pathline was determined. The vector data file from Insight, was then examined and the displacement distance was approximated for the location of the pathline. The delta time was then increased or decreased in order to gain the desired range of displacements in order to reduce the error. The delta time ranged between 0.02 and 0.24 seconds.

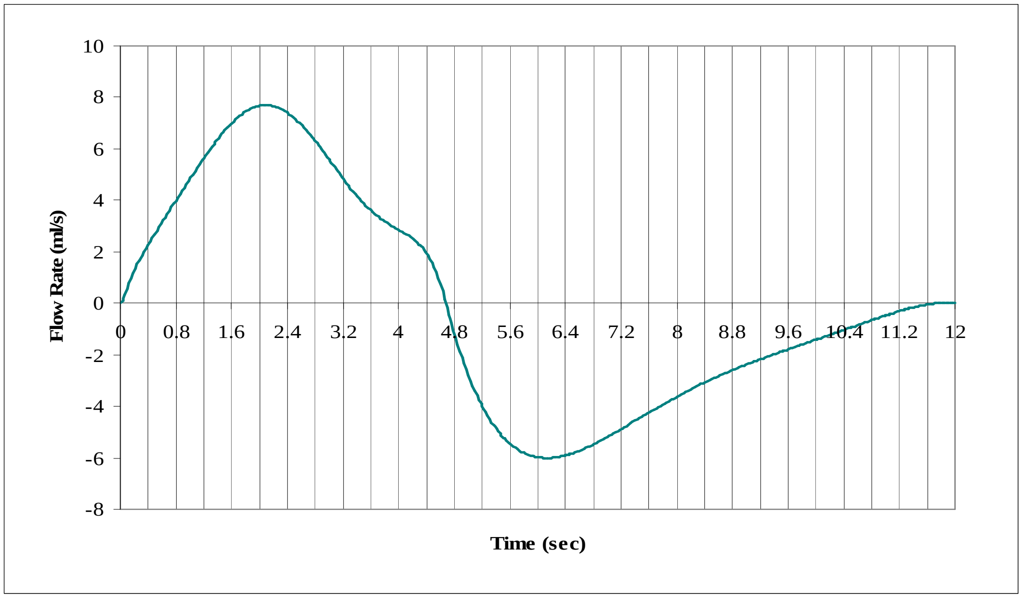

Figure 7.18: Location of Each Time Step for Balloon Pathline Analysis.

The pathline began at the same position in both the CFD and PIV data. The pathlines for the PIV analysis were released at 50 mm and the pathline for the CFD model was at 12.7 mm. The reason why the beginning of inhale position was different for the PIV and CFD models was because the difference in the origin in the coordinate system, as shown in Figure 7.7. The pathlines were spaced 2 mm apart, where the middle pathline was in the middle of the model. The pathlines were plotted in the PIV model separately for all three cycles, in order to obtain an average between the three breathing cycles. Figures 7.19, 7.20 and 7.21 show the pathlines for breathing cycles 1, 2 and 3, respectively. From the PIV figures, it is seen that the pathlines were pulling slightly to the left side, which was consistent with the model deformation analysis, where it was shown that the left side deformed more then the right (Section 7.2). Figure 7.22 shows the pathlines for the CFD analysis.

The distance traveled into the model by each pathline, the difference between the end of inhale location and the beginning of inhale location, was calculated for both the CFD and PIV analysis. The average pathline distance traveled was computed for each PIV cycle and the average was taken. The standard deviation between the three cycles was good, where the worst standard deviation was 0.32 mm for pathline 4; the pathline numbering system is shown in Figure 7.19. The majority of the standard deviation of the pathlines between the three cycles was less then 0.1 mm. The results of the pathline distance traveled for the CFD and PIV is shown in Table 7.2. The difference of the pathline distance traveled between the PIV and CFD is also shown in the table.

It can be seen, that for the pathlines plotted in the slower regions of the model, pathlines 1, 2, 3, 4, 5, 17, 18 and 19, the PIV distance was shorter then the CFD. Another reason why the pathlines between the CFD and PIV did not exactly match, may be because the location of the pathlines may be slightly different. It was determined that there was 0.2 mm error in defining the coordinates in the PIV model, therefore there was 0.2 mm error in determining the start position of the pathlines.

The pathlines closest to the symmetry axis of the CFD model do not return at the end of exhale to their position at the beginning of inhale. The worst pathline, the pathline closest to the axial symmetry line, pathline 11, was 0.4 mm short at the end of exhale, in comparison to the location at the beginning of inhale. Since the center line has highest velocity, this indicates that inertial forces might be present.

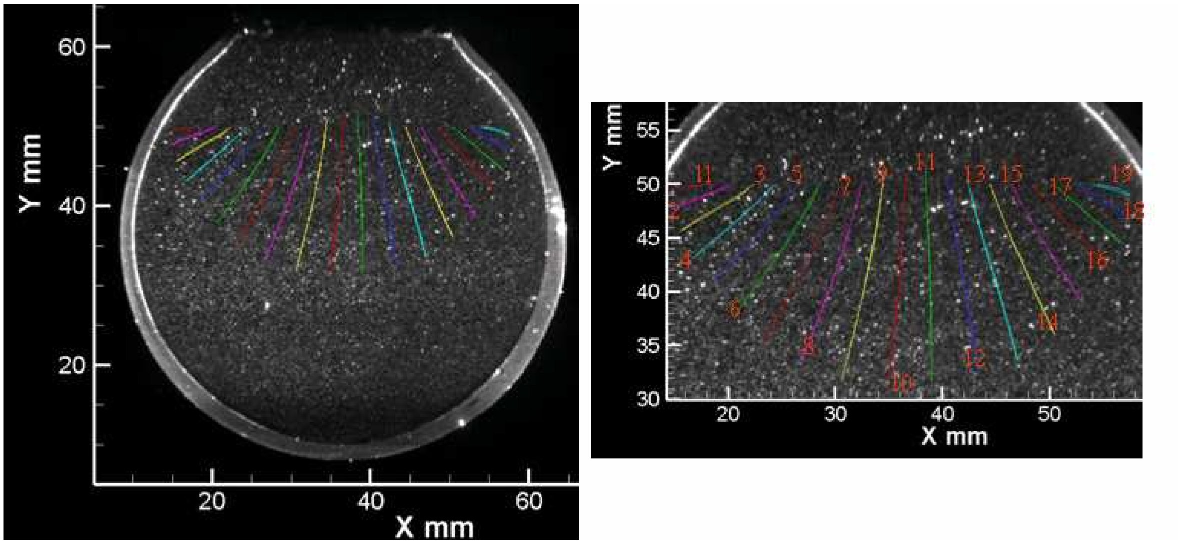

Figure 7.19: Pathlines in PIV Balloon Model for 1st Breathing Cycle.

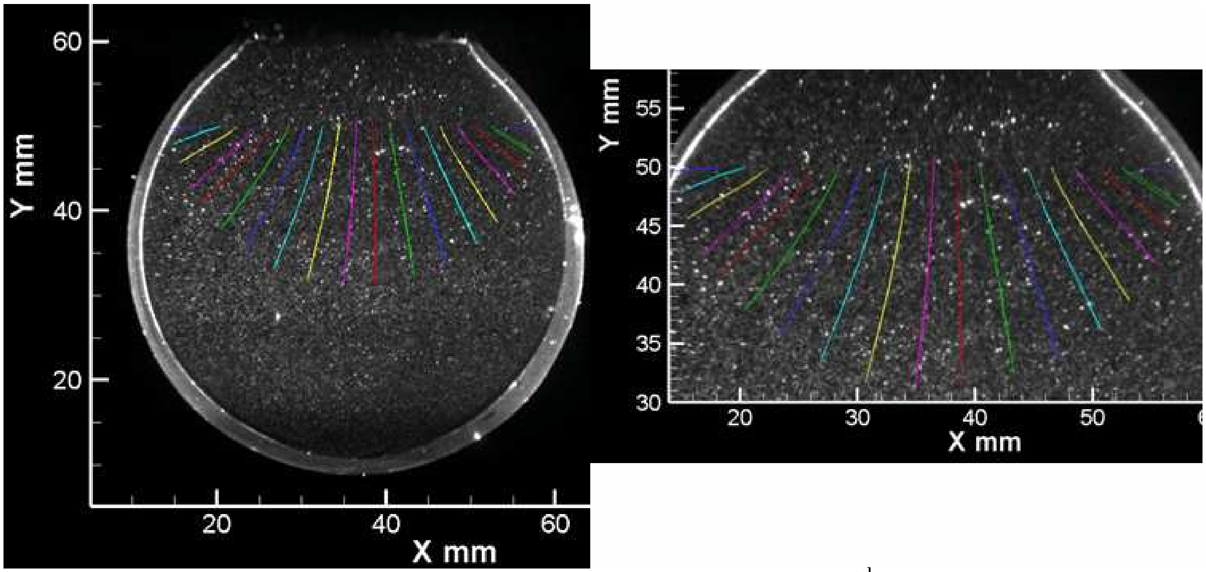

Figure 7.20: Pathlines in PIV Balloon Model for 2nd Breathing Cycle.

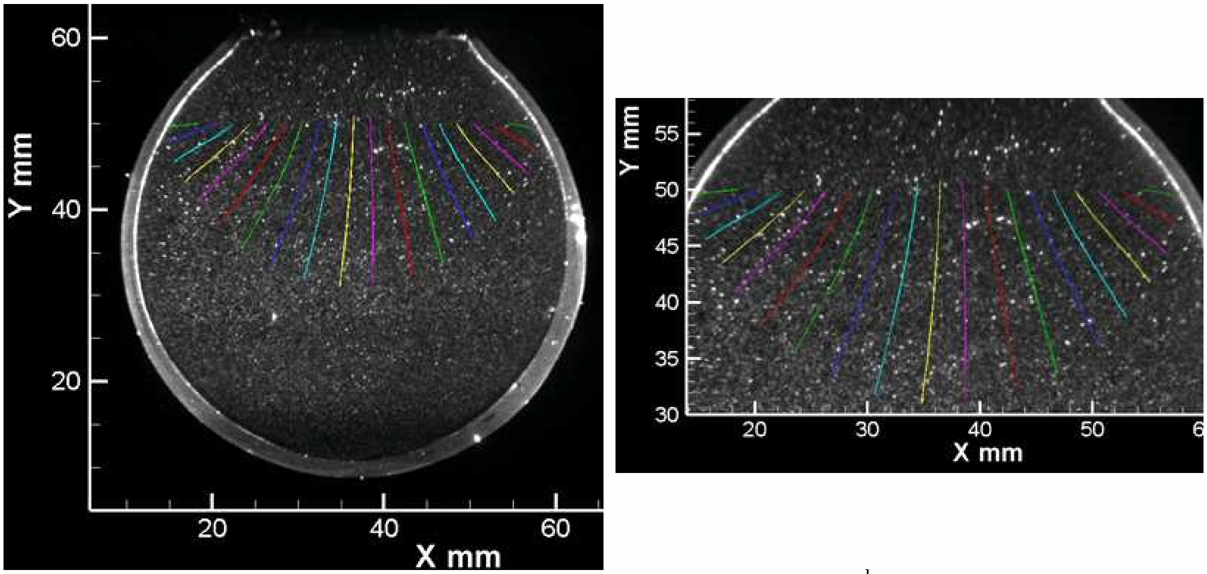

Figure 7.21: Pathlines in PIV Balloon Model for 3rd Breathing Cycle.

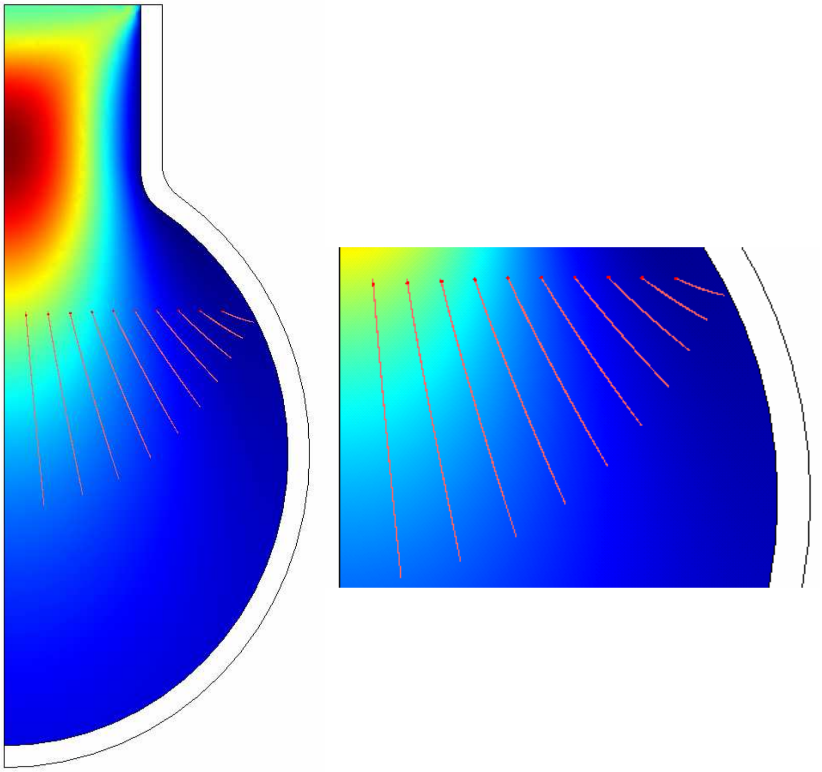

Figure 7.22: CFD Pathlines Results.

Table 7.2: Length of Pathline Between Beginning of Inhale and End of Inhale

		PIV	CFD	Difference Between PIV and CFD
	Pathline	mm	mm	mm
Left Side	1	3.87	4.54	-0.67
	2	6.00	6.37	-0.37
	3	8.20	8.37	-0.17
	4	10.39	10.43	-0.04
	5	12.14	12.41	-0.27
	6	14.41	14.17	0.24
	7	16.24	15.63	0.61
	8	17.68	16.71	0.97
	9	18.68	17.38	1.30
	10	19.07		
Right Side	11	18.80	17.38	1.43
	12	18.03	16.71	1.32
	13	17.00	15.63	1.37
	14	15.21	14.17	1.03
	15	13.20	12.41	0.79
	16	10.59	10.43	0.16
	17	8.34	8.37	-0.04
	18	5.94	6.37	-0.42
	19	3.12	4.54	-1.42

It was theorized, in Section 4.1.1, that because the fluid non-dimensional parameters, Reynolds and Womersley numbers, were much smaller then one, then it could be assumed that there was no inertia forces present. The average Reynolds number for the Balloon model was approximately 0.2 and the Womersley number was 0.27. In order to determine if inertial forces were present, with these low non-dimensional parameters, the CFD simulation was run for a fluid density of zero. The zero density fluid would signify that there were no inertia forces present, and therefore the inertia terms in the Navier-Stokes equation would not be solved for in the numerical analysis. The pathline closest to the axial symmetry line, pathline 11, was analyzed. At the end of exhale, the pathline did return to the position it began at the beginning of inhale. The return of the pathline signifies that there was some momentum present with the Reynolds and Womersley number of 0.2 and 0.27, respectively. Even though inertia was present, the impact on the solution was very small.

7.4 Conclusion

Several conclusions were drawn based on the balloon PIV and CFD analysis. First, an understanding of how the balloon model deformed was gained. It was shown, that the model deformed differently depending on the thickness of the hollow cast walls. Even though thickness variation was undesirable, knowledge of how the balloon model expanded was used in understanding the fluid flow results. Future work could include using different model thicknesses in order to simulate alveoli touching each other or localized diseased states.

It was shown that there was good correlation between the CFD and PIV for the velocity profile plots, especially in areas of low acceleration. Even though the geometry changes between the simple balloon model and the alveolar sac models, it was assumed that if the same analysis techniques were used in the alveolar sac model, the same level of accuracy could be assumed for the alveolar sac models. There was a maximum of 1.4 mm of uncertainty between the CFD and PIV pathline results. The uncertainty of the pathlines was used in the alveolar sac analysis.

The knowledge gained by performing the experiment on the simple balloon model was used for the alveolar sac models. Understanding the experimental setup and the PIV analysis technique was crucial in providing accurate results for the alveolar sac models.

Chapter 8
Alveolar Sac PIV Results

The goal of this work was to compare the fluid flow between healthy and emphysematic alveolar sac geometries and determine the fluid flow's impact on particle diffusion. The fluid flow's behavior was analyzed by use of pathlines. By examination of the pathlines, two flow characteristics could be determined. The first flow feature that was analyzed was whether the flow was irreversible. Irreversibility might increase a particle's residence time within the alveolar sac. The second flow attribute was determination of how far into the model the pathlines penetrated and how close do they travel to the alveolar walls. The behavior of the pathline was used to estimate the amount time was needed for a particle to diffuse to the alveolar walls. Diffusion time was calculated and compared for particles with a diameter range of 0.1 μm to 0.01 μm. It was found that there was a significant difference in pathlines, and therefore diffusion, between the healthy and emphysematic alveolar sac geometries.

8.1 Results of Healthy Alveolar Sac

It was desirable to obtain a good representation of the fluid flow within the alveolar sac and to examine areas where there would be the greatest possibility for irreversible flow. The alveolar sac was photographed at the middle cross-section, which would allow for analysis of the duct and several alveoli. There were two different ways to vertically slice the model in half, one where the middle role of alveoli would be visible in the image, and one where the bottom and top row of alveoli would be visible. There was a greater likelihood for irreversible flow to occur in the top alveoli (Section 2.2.1), therefore it was desired to obtain the top two alveoli in the image. The slice where the top and bottom alveoli were visible was used in this work.

An understanding of the location of the image in the photograph was needed in order to determine where to begin the pathlines. The origin of the image was in the upper left corner. The coordinates of the areas of interest, top, and bottom, and the alveoli, were determined. Figure 8.1 shows the locations of the important areas. If the model was perfectly symmetric and aligned on the fixture connecting it to the housing, then the top and bottom alveoli should have the same x coordinate. The difference is significant in comparison of the error of measurement, which was approximately 0.2 mm. Interestingly, the bottom two alveoli did not have the same y – coordinate, and therefore it could be assumed that the model was slightly pulled to the left. Because the alignment was off, the middle of the model, at the top, did not coincide with the middle of the model at the bottom. The average middle x-coordinate, 37.55 mm, was determined by measuring several points in the model. Even though the misalignment was small, the misalignment was a potential reason for error in the fluid analysis. Because the laser

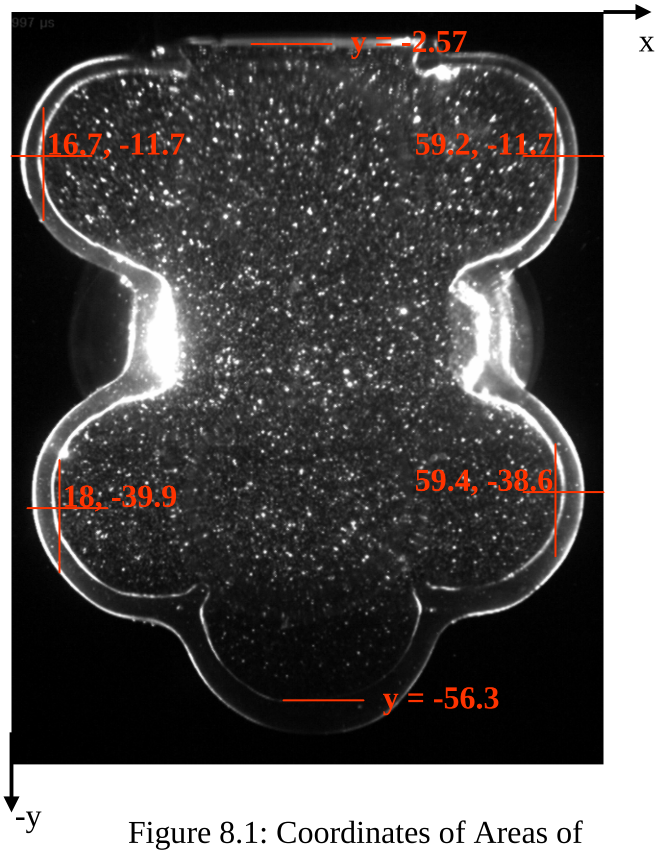

Figure 8.1: Coordinates of Areas of Interest in the Healthy Alveolar Sac. All dimensions are in mm.

light sheet was unable to illuminate the entire image, the experiment was ran twice, once with the light sheet focused near the top and once with the light sheet focused at the bottom.

To determine the fluid behavior in the several areas of the model, pathlines were plotted in the healthy alveolar sac in three different areas, starting at the duct entrance, inside the top two alveoli and at the bottom of the alveolar sac. Pathlines show the path a massless fluid particle would travel with respect to time. The definition of a pathline and how it was created is discussed in detail in Section 6.5.

8.1.1 Pathlines Beginning at Duct Entrance

To determine if there was irreversible flow, and how far the pathlines may travel into the alveolar sac, pathlines were plotted starting at the duct entrance. The pathlines were released from the top of the model at -6 mm, or at -3.43 mm below the top datum. The eleven pathlines for the top half of the model ranged between an x – coordinate of 29.55 mm and 45.55 mm. .

8.1.1.1 Time Resolution Analysis

The best time separation, the time that separates the velocity vector files which were used to create the pathlines, needed to be determined. If too large of a time separation was used, then there may not be enough resolution in the velocity vector files to create pathlines that accurately represented the flow field. The time separating the data files was analyzed two different ways, one with a constant separation of time and one with a finer resolution of time at high acceleration areas. The velocity vector was determined at each point in time and therefore the velocity in between each time was not calculated. At high acceleration areas the velocity was changing quickly, and therefore a finer time resolution may needed to be used in order to predict the fluid flow behavior. The analysis helped determine if the constant time separation was too large of a time resolution to predict the pathline travel distance at areas of high acceleration.

The time resolution was reduced if there was a high possibility of the resolution changing the pathline results. The photographed frames were analyzed at every 0.2 seconds for the constant time separation analysis. For the finer time separation analysis, the separation between times analyzed was reduced to 0.1 seconds in those areas that the pathline was encountering high speeds and was accelerating. The further the pathline traveled into the alveolar sac, the smaller the displacement, for the fluid was moving very slowly. A finer time separation would not influence the travel distance of the pathline if it is moving slowly. Figure 8.3 graphically shows the separation time chosen, where the areas of the smaller time resolution are highlighted. Table 8.1 shows the total distance of the pathline travel, the distance in between the beginning of inhale and the end of inhale, traveled by the 6th pathline, the numbering system is shown in

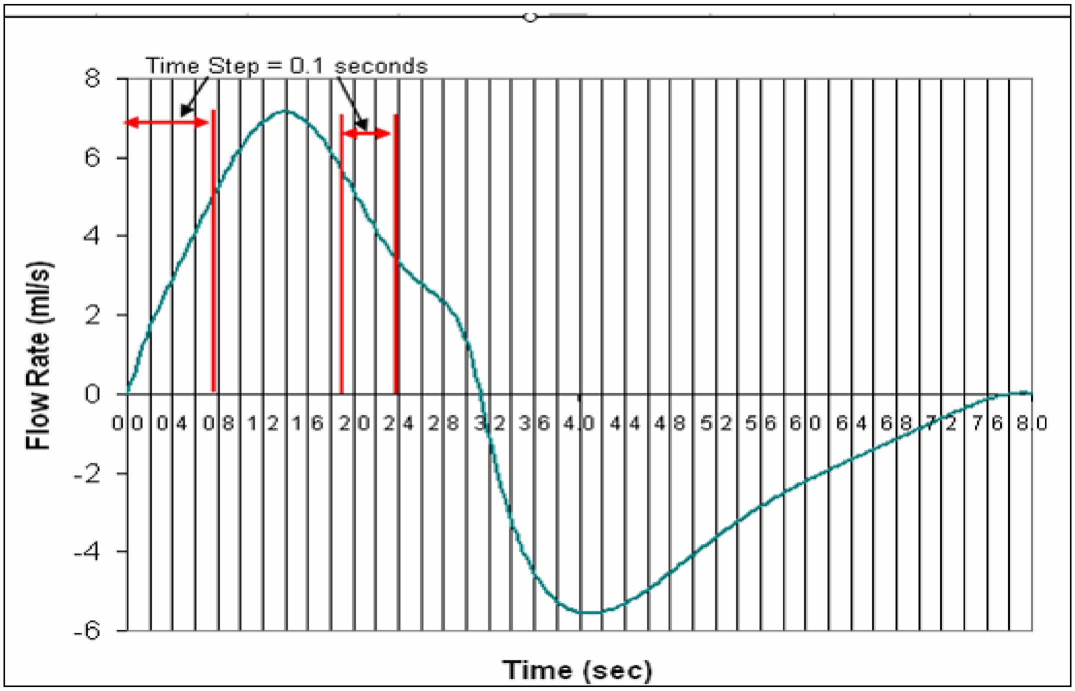

Figure 8.3: Healthy Alveolar Sac Time Step. Areas highlighted where a separation time of 0.1 seconds was used. All other areas a time separation of 0.2 seconds was used.

Figure 8.4, for the two analyses performed. Also, from Table 8.1, it was noticed that for cycles one and three, the distance decreased with the finer resolution, but for cycle two it increased. The difference in the constant and finer time separation for the average distance traveled was only 0.07 mm, Table 8.1. Based on the results, it was determined that it was sufficient to use the constant time separation of 0.2 seconds for all future analyses.

Table 8.1: Comparison of the Distance in Between the Beginning of Inhale and the End of Inhale for Pathline 6 for Time Separation Analysis

	1st Cycle	2nd Cycle	3rd Cycle	Average (mm)
Constant Time Separation, 2 Seconds (mm)	25.07	23.83	26.00	24.97
Finer Time Separation at High Acceleration Areas (mm)	25.03	24.05	25.61	24.89
Average (mm)	25.05	23.94	25.80	24.93
Difference In Distance Between Constant and Finer Time Resolution (mm)	0.05	-0.22	0.40	0.07

8.1.1.2 Pathline Location at End of Inhale

Diffusion was calculated based on the distance between the pathline at the end of inhale and where it would diffuse to, the alveolar wall. In order to calculate diffusion, the distance the pathline traveled into the alveolar sac was needed. The pathlines were plotted for each breathing cycle. Figures 8.4, 8.5 and 8.6 show the pathlines' courses during one complete breathing cycle, for cycles 1, 2 and 3 respectively. The start position of the pathline was at the beginning of inhale, and the end position was at the end of exhale. The pathline colors do not have any significance. The PIV photograph that is behind the pathlines is the healthy alveolar sac at its initial volume. It may seem that some of the pathlines are hitting the alveolar walls, at the end of inhale, but this is not the case, for the alveolar sac is expanded at the end of inhale. Table 8.2 shows the pathline coordinates at the end of inhale for each cycle as well as the average position between the three cycles. The pathline numbering system is shown in Figure 8.4. The average end of inhale coordinates were used in for the particle diffusion analysis in Section 8.3.1.

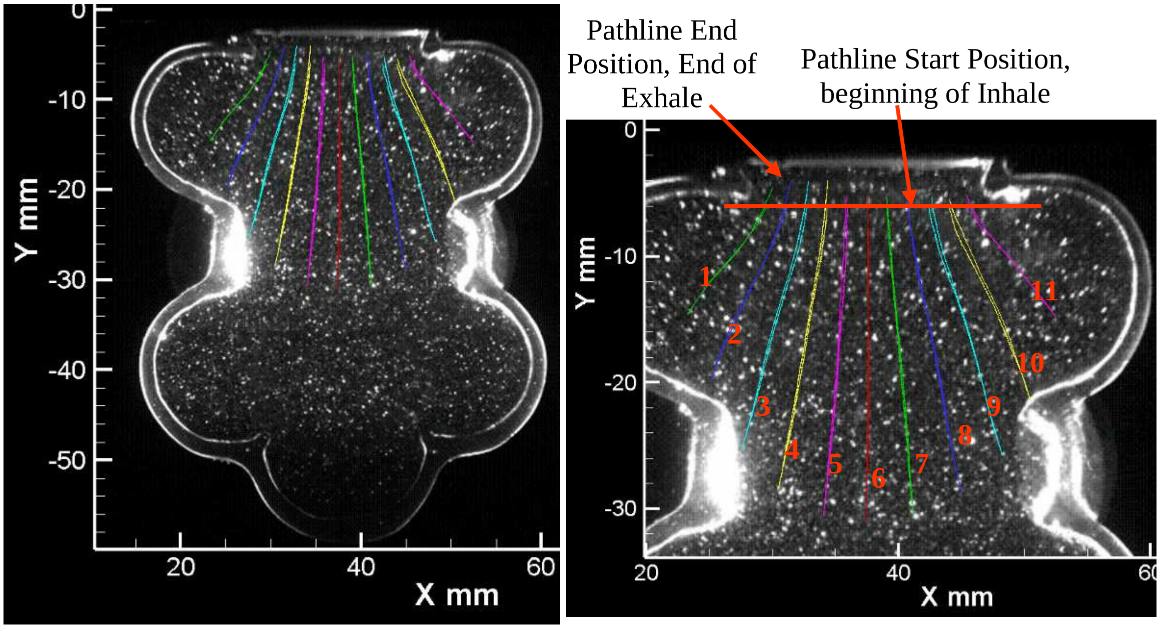
Pathline End Position, End of Exhale

Pathline Start Position, beginning of Inhale

Figure 8.4: Pathlines for Healthy Alveolar Sac for 1st Breathing Cycle.

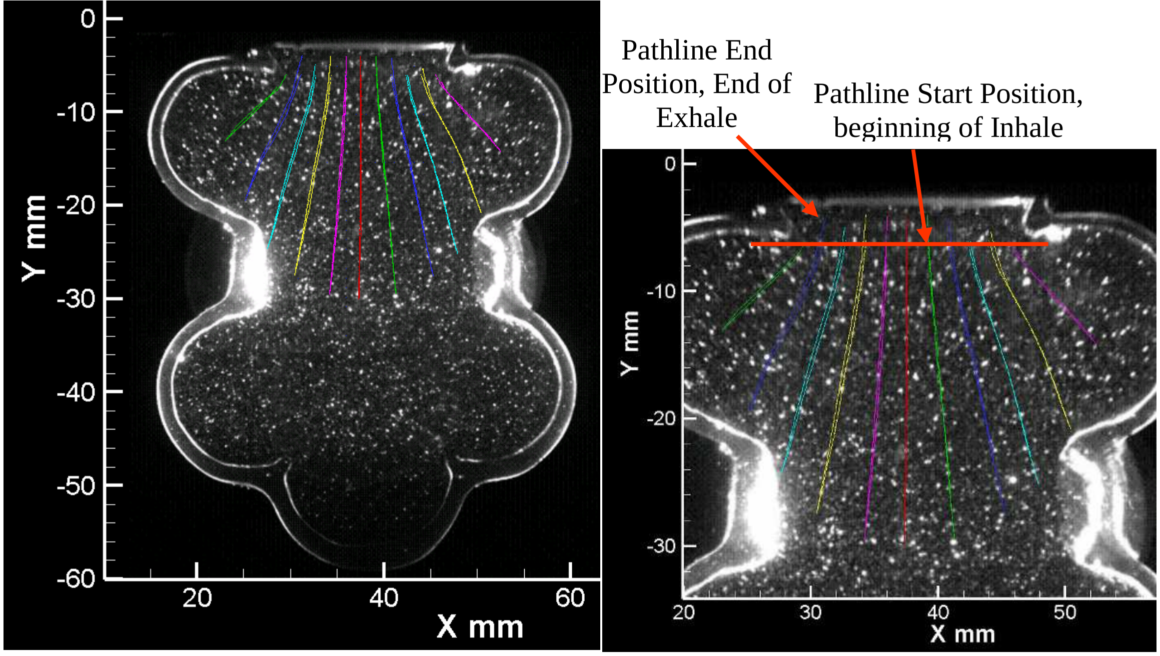
Pathline End Position, End of Exhale

Pathline Start Position, beginning of Inhale

Figure 8.5: Pathlines for Healthy Alveolar Sac for 2nd Breathing Cycle.

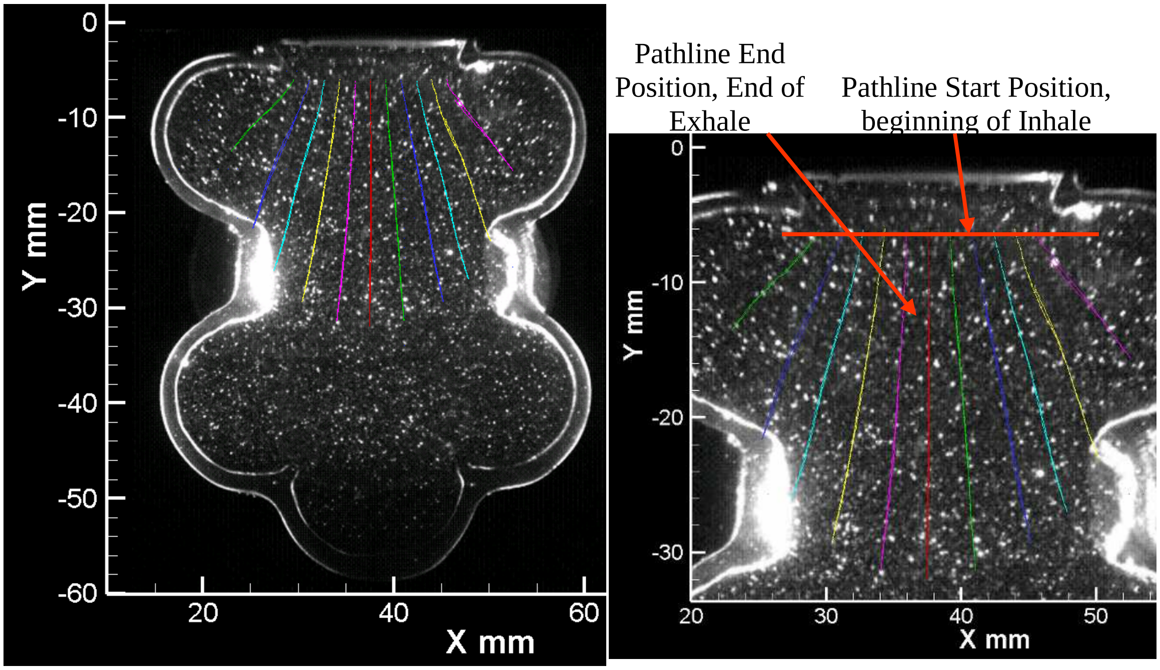

Figure 8.6: Pathlines for Healthy Alveolar Sac for 3rd Breathing Cycle.

Table 8.2: Healthy Pathline End of Inhale Coordinates

	Coordinates (mm)							
	Cycle 1		Cycle 2		Cycle 3		Average	
Pathline	x	y	x	y	x	y	x^*_2	y^*_2
1	23.25	-14.60	23.05	-13.10	23.00	-13.50	23.10	-13.73
2	25.05	-19.95	25.20	-19.45	25.10	-21.70	25.12	-20.37
3	27.50	-25.40	27.50	-24.60	27.40	-26.10	27.47	-25.37
4	30.50	-28.40	30.50	-27.50	30.40	-29.40	30.47	-28.43
5	34.05	-30.60	34.20	-29.55	34.05	-31.50	34.10	-30.55
6	37.50	-31.10	37.35	-30.00	37.50	-32.00	37.45	-31.03
7	41.20	-30.70	41.30	-29.50	41.10	-31.40	41.20	-30.53
8	45.00	-28.75	45.30	-27.65	45.20	-29.40	45.17	-28.60
9	48.25	-25.75	47.90	-25.20	47.90	-27.00	48.02	-25.98
10	50.50	-21.50	50.40	-20.70	50.20	-23.00	50.37	-21.73
11	52.50	-14.80	52.50	-14.25	52.50	-15.60	52.50	-14.88

*x_2 and y_2 were used in Table 8.10.

8.1.1.3 Irreversible Flow Analysis

The pathlines released near the duct of the alveolar sac did not return the beginning of inhale position, as shown in Figures 8.4, 8.5 and 8.6 for cycles 1, 2 and 3, respectively. For the first two cycles the pathlines overlapped and traveled further out of the model then from where they started, by between approximately 0.08 mm and over 2.1 mm, Figure 8.4 and 8.5. It was difficult to estimate how much the particle over traveled, because the pathline left the solution area. In the third cycle the pathline did not return to the starting position at the end of exhale, by a maximum of 5.5 mm, Figure 8.6. Since the pathlines did not return at exhale to the position beginning at inhale, it was possible that irreversible flow was occurring. However, due to PIV error, the irreversible flow may not be present.

During the PIV cross-correlation vector analysis, the algorithm may under or over estimate the velocity vector, which has been described in detail in the error section (Section 6.1.2). If the velocity at any time was over estimated at inhale, and the pathline was calculated from the overestimated velocity, then the pathline may travel more or less than intended. The fluid in the deeper regions of the model was moving very slowly, therefore if a pathline travels into the model more than intended, it would take the massless particle more time to escape the low speed areas. The same concept applied if the velocity was under estimated, and the massless particles did not travel as far into the slower regions. At exhale, the massless particle would leave the slower regions quicker. An investigation was completed in order to demonstrate this concept.

To illustrate the concept that a massless particle may become trapped in the lower speed regions, an analysis was performed. The study would determine how much an error at inhale would have on the position of the pathline at the end of exhale. This experiment was conducted by altering the start position of pathline 6, Figure 8.4, at the beginning of exhale. The start position was altered by 1 mm in the positive and negative directions. The pathline was calculated using the velocity vector data for exhale only. Figure 8.7 shows the pathline travel with a start position of -31.97 mm, -1 mm difference from the average position of the pathline at the end of inhale. Figure 8.8 shows the distance the pathline traveled at exhale for a start position of -29.97 mm, +1 mm difference from the average position of the pathline at the end of inhale. The pathline should return, at exhale, to approximately –6 mm, which is the start position of the pathline at beginning of inhale. For the pathline starting at -1 mm below the average position at the end of inhale, Figure 8.7, the pathline only returns to -9.35 mm, a -3.35 mm difference from the beginning of inhale. The pathline that began at +1 mm from the average position at the beginning of inhale, Figure 8.8, returned to -4.1 mm, a 1.9 mm difference from the beginning of inhale. The analysis showed that there can be a significant amount of error of the pathline at the end of exhale, even when there is a small amount of error in the distance the pathline traveled into the alveolar sac during inhale. From the analysis, it was concluded that the evidence of irreversible flow that was shown in Figures 8.4, 8.5 and 8.6, for cycles 1, 2 and 3, respectively, was only due to

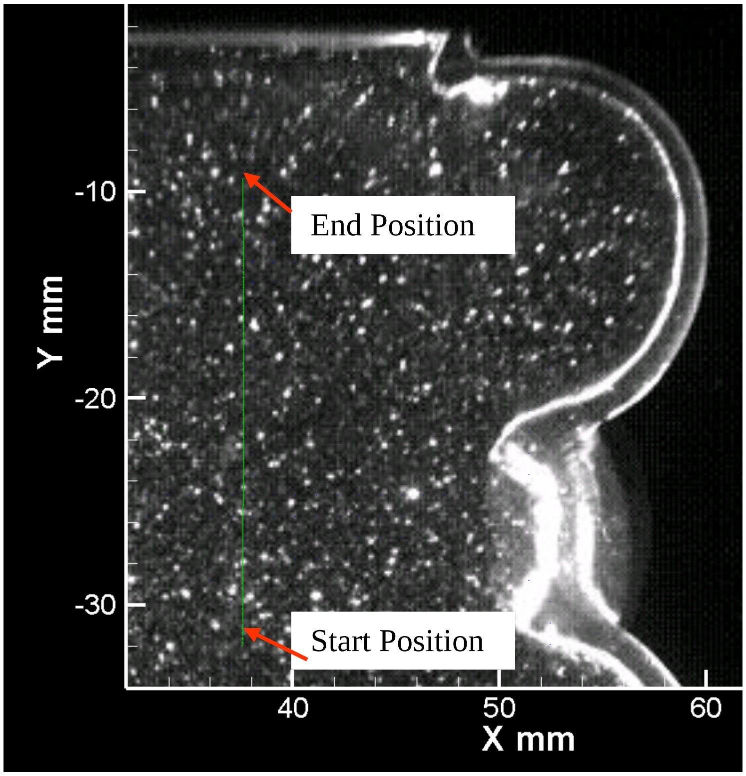

Figure 8.7: Pathlines Beginning at Exhale at a position of -31.97 mm, -1 mm from the Average Distance Traveled by the Pathline at the End of Exhale.

error in the PIV cross correlation velocity vector analysis, and therefore irreversible flow was not actually present in this area of the model.

8.1.2 Pathlines and Streamlines Inside Top Two Alveoli

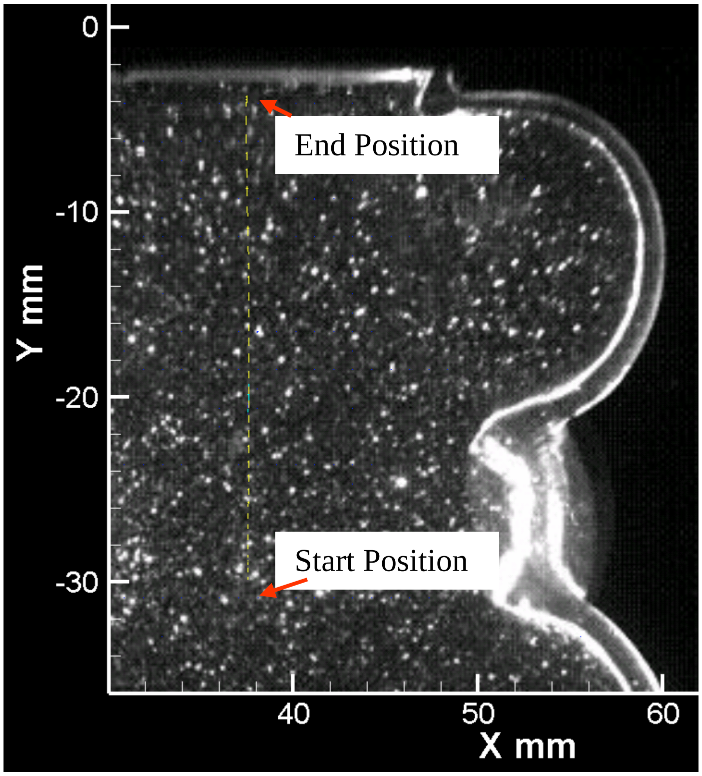

Figure 8.8: Pathlines Beginning at Exhale at a position of -31.97 mm, +1 mm from the Average Distance Traveled by the Pathline at the End of Exhale.

Two analyses were performed; the first examined the behavior of the streamlines and pathlines inside the top two alveoli in order to determine if circulation and irreversible flow was occurring. The second study was to determine the location of the pathline at the end of inhale, which was later used in the diffusion analysis. The pathlines, and streamlines, in the top two alveoli were released at 7.72 mm from the alveolar wall, which were x-coordinates of 24.43 mm and 51.45 mm for the right and left alveolus respectively. Streamlines are lines plotted tangent to the velocity vector, and are not a function of time. Five pathlines and streamlines, were plotted in each alveolus and the first pathline, streamline, started 1.93 mm below the top alveolus wall at -6.75 mm. The spacing between each pathline was 2.57 mm; therefore the last pathline, streamline, began at a y-coordinate of -17.04 mm. The location of the pathlines and streamlines were at sufficient locations in order to gain the information needed.

8.1.2.1 Irreversible Flow Analysis

It has been shown (Tsuda et al., 1995, Karl et al., 2004 and Tippe and Tsuda, 1999) that if circulation and irreversible flow occurs, it is present inside an alveolus. Areas of circulation are a likely place for irreversible flow to occur (Tsuda et al., 1995). The first step in determining irreversible flow was to plot streamlines inside each alveolus. Streamlines were plotted for all solution times. Figure 8.9 shows the streamlines at a solution time of 1.2 seconds. From Figure 8.9 it can be seen there was no evidence of recirculation. Based on the pathline behavior it was determined that if irreversible flow did occur, it was not a result of recirculation. In order to determine if other physical properties were creating irreversible flow, pathlines were plotted and analyzed.

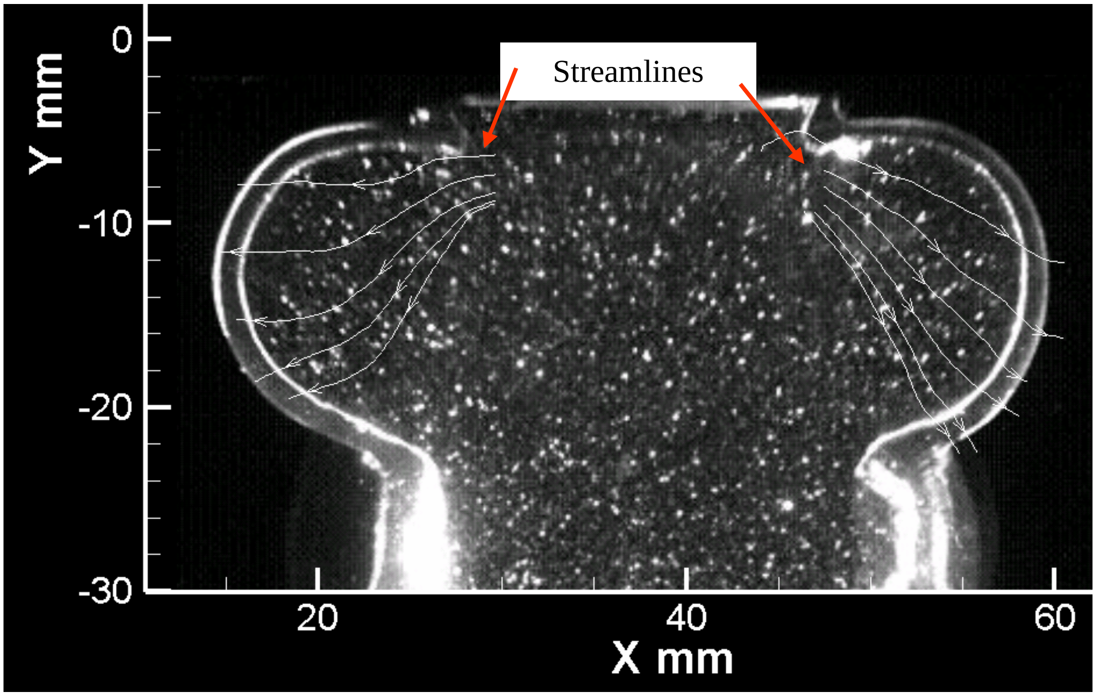

Figure 8.9: Streamlines of Healthy Alveolar Sac at 1.2 Seconds

In order to determine if there was irreversible flow inside the alveoli, and close to the alveolar wall, pathlines were plotted in the top two alveoli. The data set for the first breathing cycle was used in the analysis, because the pathlines for the entire top of the model was the closest to the average. Based on the results from Section 8.1.1.3, it was determined that there should not be a difference in the pathline behavior between the three breathing cycles. Pathlines were plotted for the first cycle over three breathing iterations; the cycle data was used three times consecutively. The first cycle was chosen because the pathlines were closest to the average. Plotting the pathlines over three iterations allowed for irreversible flow to be distinguishable and allow for calculation of increased residence time, if irreversible flow was occurring. The end of exhale position of the pathline after the first cycle was used for the beginning of inhale start position of the pathline for the second cycle. The time separation between velocity vector data files was 0.4 seconds. A larger time separation resolution was appropriate because the fluid was moving much more slowly in the top areas of the model. The time separating the frames analyzed, delta time, Figure 6.1, ranged between 0.02 seconds to 0.2 seconds. For most of the analysis a delta time closer to 0.2 seconds was used, because of the slowly moving flow. Figure 8.10A shows the pathlines in the left alveolus and Figure 8.10B shows the pathlines in the right alveolus. Since the pathlines

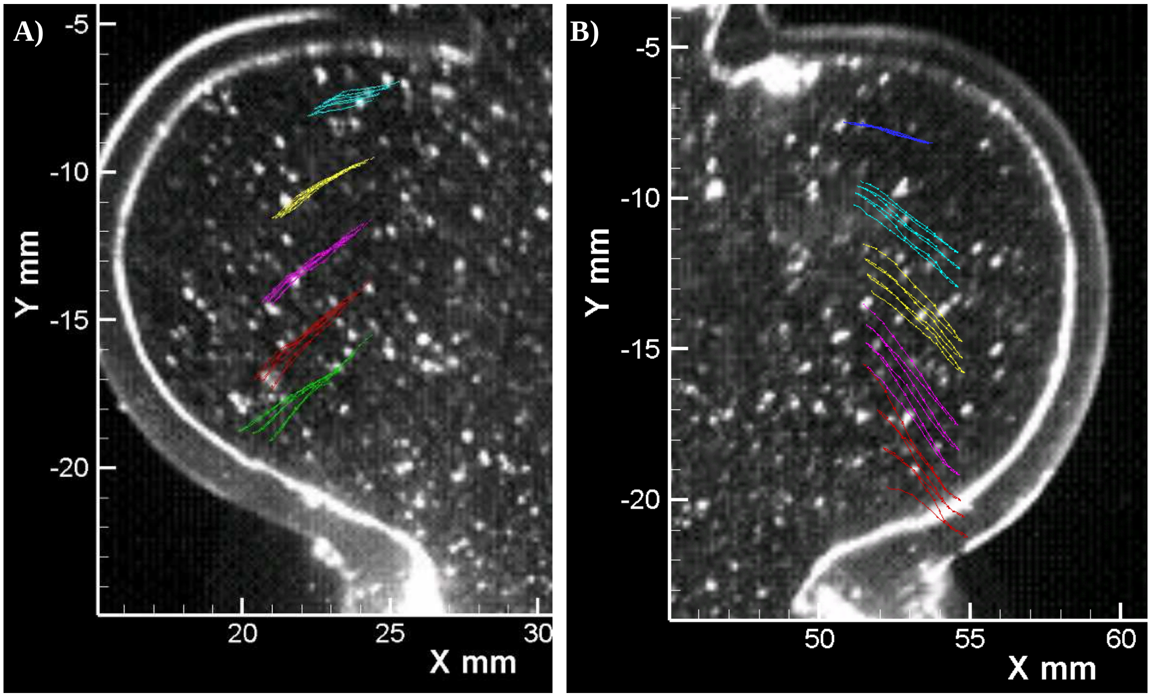

Figure 8.10: Pathlines for Three Iterations of the First Cycle in the Healthy Alveolar Sac for the Left Alveolus (A) and the Right Alveolus (B).

did not return to their original position, it was possible that irreversible flow was present. Because PIV analysis error could be influencing the pathline analysis, it was also possible that irreversible was not accruing. In order to determine if there is irreversible flow, a particle tracking analysis was performed.

Verification needed to be completed in order to determine whether there was irreversible flow present in the top two alveoli. The study was performed by tracking one of the neutrally buoyant PIV particles over one complete breathing cycle. Image J was used for the particle tracking analysis. Because a PIV particle had to be picked in the image, the beginning of inhale coordinates differed slightly from those shown in Figure 8.10. The x-coordinate was at 51.52 mm and the y-coordinate at -14.34 mm. The particle tracking analysis was performed for frames that were separated by 0.4 seconds. The separation time allowed for the same particle to be detectable in all of the images and therefore be visually tracked for the entire cycle. The coordinates of the particle at each frame was

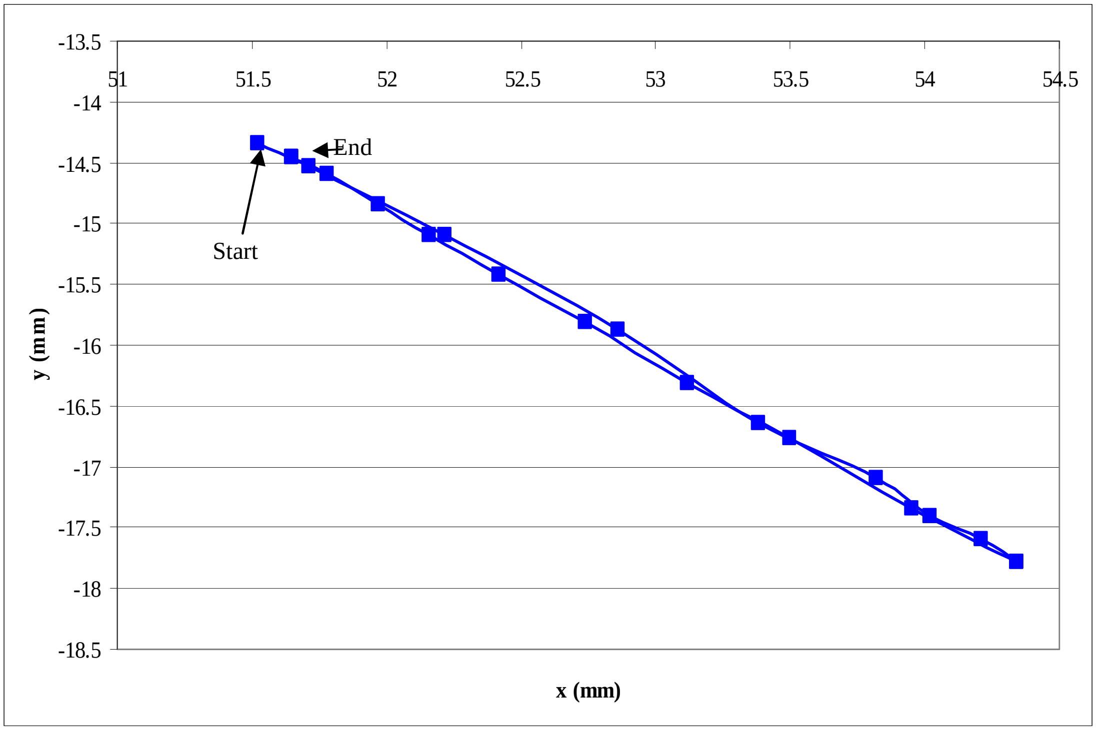

Figure 8.11: Pathline of Neutrally Buoyant Particle Tracked with Image J over a Breathing Cycle.

recorded, Figure 8.11. In order to correlate between Image J and the pathlines from the PIV analysis, a pathline with the same coordinates was plotted over one cycle using the PIV data. Table 8.3 shows the particle coordinates at the beginning of inhale and at the end of exhale for both PIV and the particle tracking analysis. Figure 8.12 shows the pathline for the PIV analysis. From Figure 8.11 and Table 8.3 it can be seen that the pathline of the neutrally buoyant particle tracked using Image J did reverse on itself. The particle did not return to the exact position it started at inhale, but the difference is very small, and may be due to measurement error. There was approximately a 2 pixel, 0.13 mm, error in determining the exact particle position. Because the difference between the start and end position is within measurement error, it was concluded that the pathlines are reversible. The error in PIV may be because there were large particles, or potentially bubbles in the alveoli, a low particle concentration, or that the fluid may be moving in three dimensions. It was noticed, during the analysis, that the particle would begin at inhale with a high light intensity and at the end of inhale it would have a low light intensity. The light intensity would then increase again at the end of exhale. The light intensity observation signifies that the flow is either three dimensional or the laser light sheet is slightly crooked. From the analysis it was concluded that the irreversible

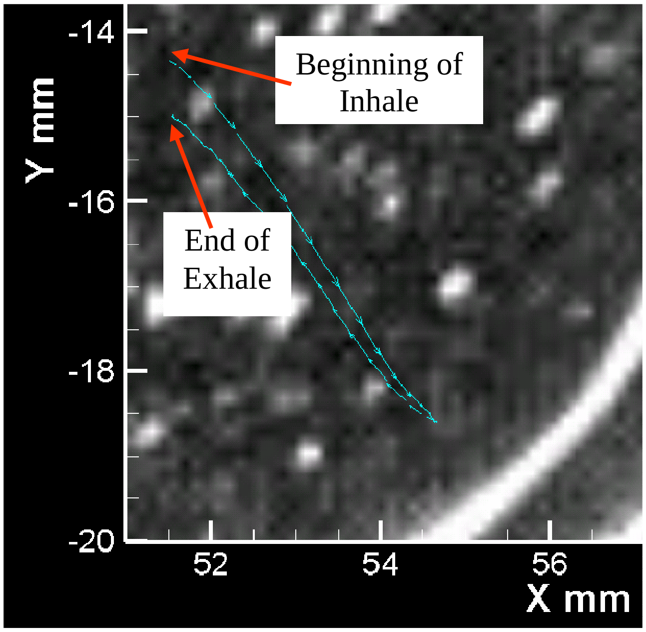

Figure 8.12: Pathline Tracked Using PIV Vector Analysis Technique over a Breathing Cycle.

looking pathlines from the PIV analysis, shown in Figure 8.10, seem to be irreversible only because of error, and therefore they are not actually irreversible.

Table 8.3: Comparison Between Particle Tracking, Using Image J, and PIV Vector Analysis Technique for Pathline at Location of Neutrally Buoyant Particle

	Particle Tracking, Using Image J		PIV Vector Analysis Technique	
	x-coordinate	y-coordinate	x-coordinate	y-coordinate
	mm	mm	mm	mm
Pathline Coordinates at Beginning of Inhale	51.52	-14.34	51.52	-14.34
Pathline Coordinates at End of Exhale	51.65	-14.46	51.55	-14.98
Difference from Pathline Location at End of Exhale to Beginning of Inhale	0.13	-0.12	0.03	-0.64

Further analysis was completed in order to estimate the PIV analysis error. In section 6.1.2 the error due to PIV analysis was estimated to be approximately 0.1 pixels. In order to determine how this error influences the pathlines, an analysis was completed. The distance for each section of the pathline is

$$x_{i+1,j+1} = \sum_{j=1}^{k} \sum_{i=1}^{l} u_j t_{int} + x_{i,j} \tag{8.1}$$

where t_{int} is the integration time, $x_{i,j}$ is the distance traveled for each integration time, i is the integration step, and j is the step between velocity vector solution files, l is the total number of integration steps, or the time separating data files divided by t_{int}, and k is the total number of velocity vector data files. The velocity for each velocity vector solution file is defined as

$$u_j = \frac{d_j + e}{\Delta t_j} \tag{8.2}$$

where d_j is the displacement for the velocity vector solution time, e is the estimated PIV analysis error and Δt is the time separating frames used for the cross correlation. The d and Δt varied for each velocity vector solution file. Substituting 8.2 into 8.1 gives

$$x_{i+1,j+1} = \sum_{j=1}^{k}\sum_{i=1}^{l}\frac{d_j+e}{\Delta t_j}t_{int} + x_{i,j} \tag{8.3}$$

$$x_{i+1,j+1} = \sum_{j=1}^{k}\sum_{i=1}^{l}\frac{d_j}{\Delta t_j}t_{int} + x_{i,j} \tag{8.4}$$

The average displacement, d, was 2.38 pixels, the Δt of 0.13 seconds, a integration time, t_{int} of 0.2 seconds, an error, e, of 0.1 pixels and an initial displacement of 0 pixels. The time separating the velocity vector files is 0.4 seconds, therefore l = 2 time integrations are needed for each velocity vector file. The first integration would be $x_{2,1}$ = 3.79 pixels. The second integration would be $x_{3,1}$ = 3.79 pixels, therefore the total displacement for that velocity vector file, with error, would be 7.57 pixels. Solving Equa. 8.4 without the error, e, the total displacement would be 7.27 pixels. Therefore the difference and the error for each velocity vector data file is 0.3 pixels. Assuming that this error is the worst case, the total error could be estimated by multiplying the error by k = 20, which would result in a total error of 6 pixels. The maximum difference between the pathline beginning of inhale position and the end of inhale position for one cycle, shown in Figure 8.10, is approximately 8 pixels. Because the error estimation is less then the estimated error of 6 pixels, other errors may be present. These errors may be because of reflection of the alveolar sac walls, pump error, where the inhale volume does not match the exhale volume, or PIV particles moving out of the laser light sheet plane. Further analysis would need to be completed in order to fully understand the error.

Subtracting 8.4 from 8.3 results in the error estimation of

$$x_{i+1,j+1} = \sum_{j=1}^{k}\sum_{i=1}^{l}\frac{e}{\Delta t_j}t_{int} \tag{8.5}$$

Therefore the error could be reduced by increasing Δt_j. The Δt does have a limit, for if Δt was too large, the PIV particles may leave the interrogation region, and there would be an increased PIV analysis error.

8.1.2.2 Pathline Location at End of Inhale

In order to determine the diffusion time, and make a comparison between healthy and emphysematic alveolar sacs, for particles that travel inside the alveoli, the location of the pathline at the end of inhale needed to be determined. The pathlines were plotted in each alveolus for each breathing cycle.

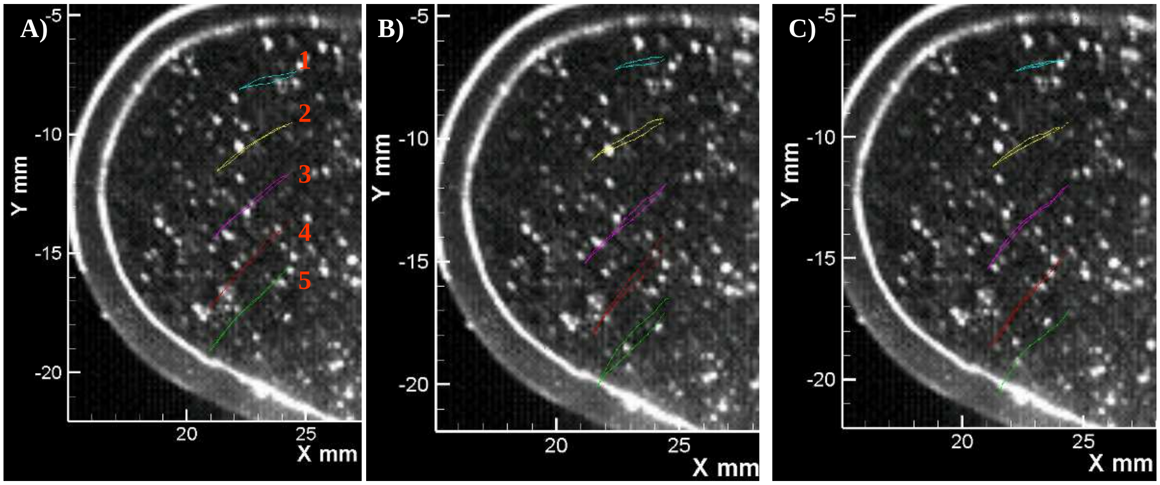

Figure 8.13: Pathlines in Healthy Left Alveolus for First Cycle (A), Second Cycle (B) and Third Cycle (C).

Figures 8.13 and 8.14 show the pathlines for the breathing cycles for the left and right alveolus, respectively. The pathlines' location at the end of inhale was examined for each alveolus in all three cycles, shown in Table 8.4, where the pathline numbering convention is shown in Figure 8.13A and 8.14A. The average pathlines' coordinates at the end of inhale was used in determination of diffusion time, which is used for comparison between the healthy and emphysema alveolar sac geometry.

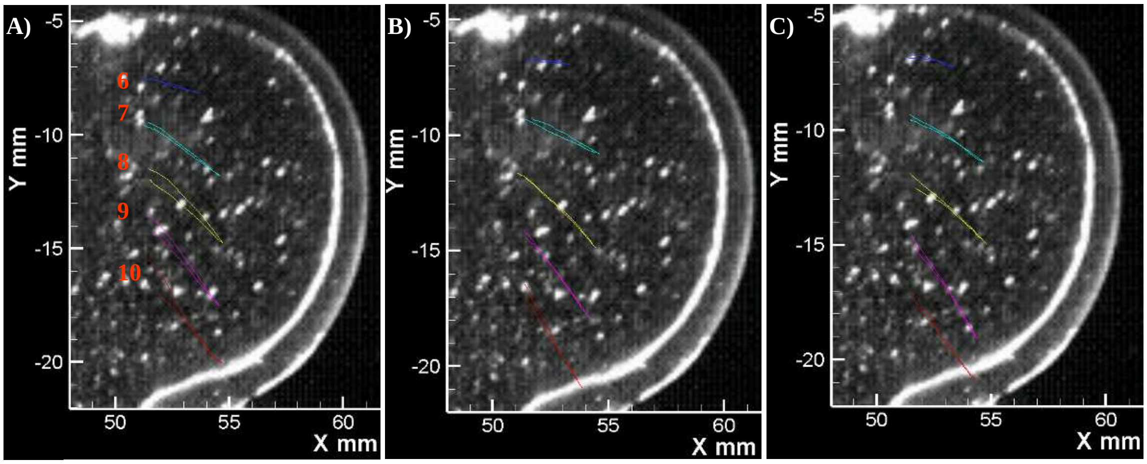

Figure 8.14: Pathlines in Healthy Right Alveolus for First Cycle (A), Second Cycle (B) and Third Cycle (C).

Table 8.4: Healthy Pathline End of Inhale Coordinates for Right and Left Alveoli

	Coordinates (mm)							
	Cycle 1		Cycle 2		Cycle 3		Average	
Pathline	x	y	x	y	x	y	x^*_2	y^*_2
1	22.20	-8.10	22.40	-7.20	22.20	-7.30	22.27	-7.53
2	21.30	-11.50	21.50	-10.40	22.25	-11.20	21.68	-11.03
3	21.00	-14.45	21.20	-15.00	21.05	-15.45	21.08	-14.97
4	21.00	-17.35	21.40	-18.10	21.15	-18.65	21.18	-18.03
5	20.95	-19.10	21.65	-20.10	Outside Solution Field		21.30	-19.60
6	53.75	-8.20	53.40	-7.00	53.40	-7.25	53.52	-7.48
7	54.60	-11.30	54.60	-10.80	54.70	-11.40	54.63	-11.17
8	54.70	-14.75	54.50	-14.90	54.80	-15.00	54.67	-14.88
9	54.60	-17.50	54.25	-18.00	54.40	-19.10	54.42	-18.20
10	54.70	-20.00	53.90	-21.00	54.30	-20.40	54.30	-20.47

*x_2 and y_2 were used in Table 8.11.

8.1.3 Pathlines at the Bottom of the Alveolar Sac

Because of the complexity of the geometry in the bottom half of the alveolar sac, it was desirable to determine if irreversible flow was occurring in this section. Pathlines were plotted in the bottom section of the healthy alveolar sac. The pathlines on the bottom of the healthy alveolar sac were started at two y levels, -34 mm and -45 mm. Ten pathlines were plotted, evenly spaced, between x-coordinates of 25 mm to 52.1 mm. The time separation between vector data files was 0.4 seconds, and the delta time ranged from 0.02 seconds to 0.2 seconds. Figure 8.15 shows the pathlines in the bottom section. From Figure 8.15, it can be seen that even in the more defined areas of the model the pathlines are reversible. It can also be noticed that the pathlines are pulling to the left side of the model. In order to determine if this occurrence was due to PIV error, or if the pulling was actually occurring, a particle tracking analysis was performed.

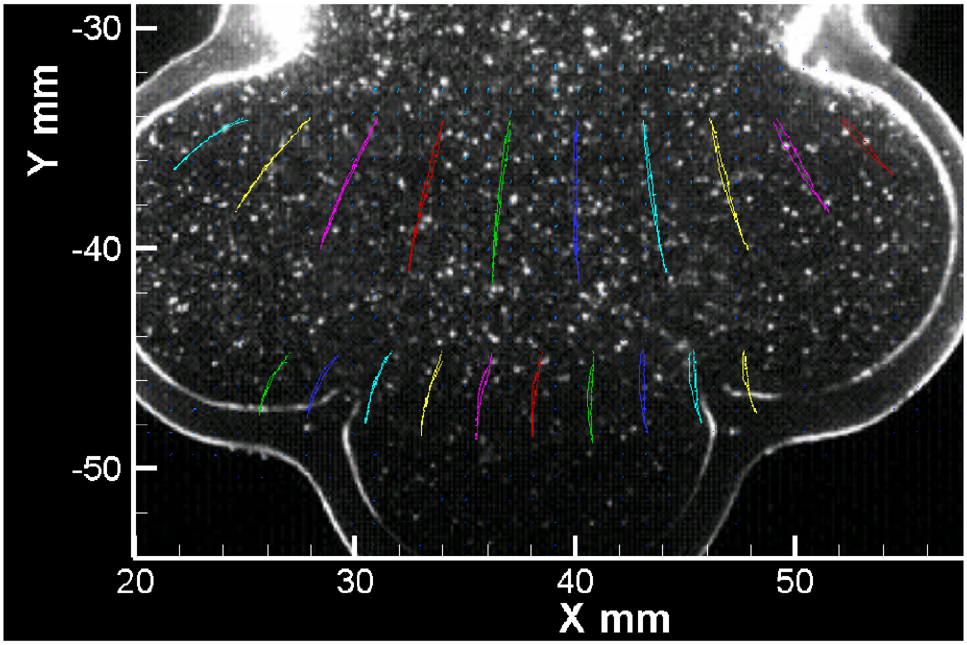

Figure 8.15: Pathlines in the Bottom Section of the Healthy Alveolar Sac

.

The pathlines in the bottom section of the alveolar sac were pulling to the left, Figure 8.15; therefore it needed to be determined if the pathlines pulling to the left of the model was a result of PIV error or if the flow was actually pulling to the left. At exhale all the pathlines return on a path to the right of inhale. An analysis was performed, by tracking a neutrally buoyant particle, using Image J, in order to determine if the behavior was an error or if the pulling was actually occurring during the simulation. One of the neutrally buoyant PIV seeding particles was chosen and tracked at 0.4 second increments, as described in detail in Section 8.1.2.1. Figure 8.16 shows the results from the analysis, where Figure 8.16A is the results from the particle tracking technique using image J and Figure 8.16B is the result from the PIV vector analysis technique. The pathline returned at exhale on the right side of the inhale pathline, which was shown for both techniques. There were several possible reasons why the pulling may have been occurring. The first reason was

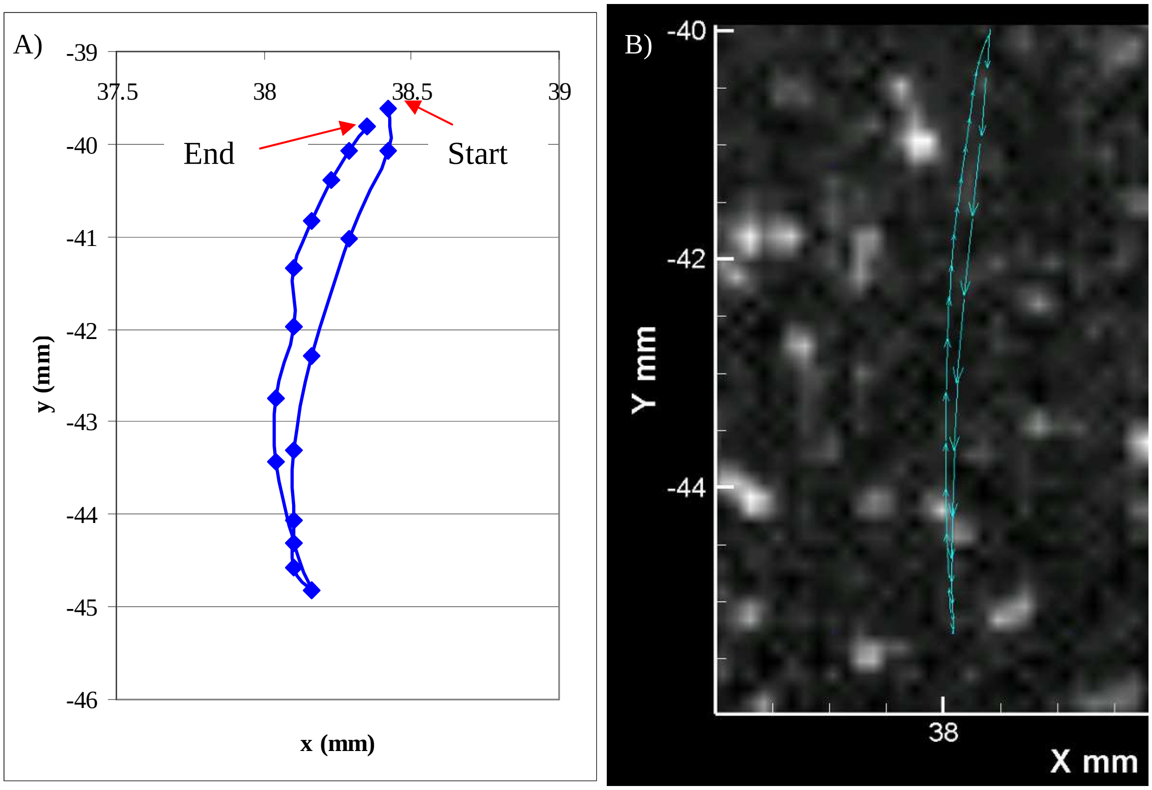

Figure 8.16: Pathline of Neutrally Buoyant Particle Tracked with Particle Tracking Technique Using Image J (A) and Pathline using PIV Vector Analysis Technique (B).

that there was a variation of material thickness on the bottom alveolus, where the right side was thicker then the right. Another reason may be that the model was attached to the test rig slightly crooked, Section 8.1. The final reason was that the pump may have been pushing and / or pulling the model. From the analysis it was concluded that the model was pulling slightly to the left. Because the pulling was small, it was determined that the pulling did not influence the overall conclusions.

8.2 Pathline Results of Emphysema Alveolar Sac

The fluid behavior in the emphysematic alveolar sac geometry needed to be determined. The emphysema alveolar sac was not symmetric; therefore there were several different places that could be chosen for the analysis. It was decided to examine the flow field in the middle of the alveolar sac, at the datum plane that would display an entire alveolus. The datum plane chosen sliced the alveolar sac such that the alveoli on the top and bottom row on the left side were sliced in half, as shown in Figure 8.17. Figure 8.17 also expresses the coordinates for the emphysema alveolar sac. There is approximately 0.2 mm error in the measurements. The emphysematic alveolar sac fluid flow would be compared to the healthy alveolar sac. To allow for a good comparison, the pathlines in the

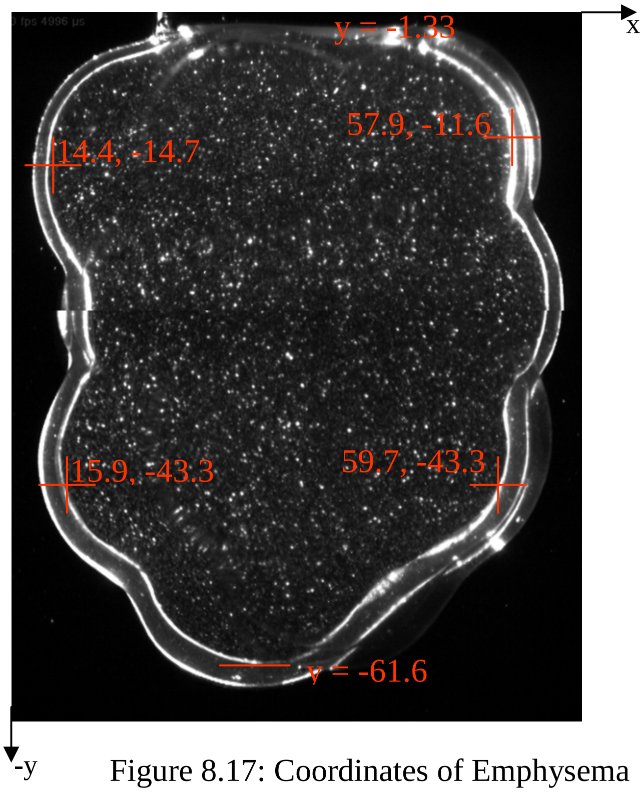

Figure 8.17: Coordinates of Emphysema Alveolar Sac. All dimensions are in mm.

emphysematic alveolar sac were plotted such that they their begin position, at the beginning of inhale, would be the same as the healthy alveolar sac. Pathlines were plotted in the emphysematic alveolar sac in two areas; near the top of the alveolar sac and close to the top alveoli. The pathlines would allow for visualization of the flow field and be used for an estimation of particle diffusion.

8.2.1 Pathlines Beginning at the Duct Entrance

Whether there was irreversible flow in the emphysema alveolar sac and the location of the pathline at the end of inhale needed to be determined, which was used for particle diffusion estimation. The flow characteristics were visualized by use of pathlines. The pathlines released near the duct of the alveolar sac were at -4.698 mm, or 3.428 mm from the top datum, in order to match the start position of the same pathlines in the healthy alveolar sac. The emphysematic alveolar sac cycle time was 11 seconds, where the healthy alveolar sac's cycle time was 8 seconds. Because the results from the two models were compared to each other, it was desirable to analyze the emphysematic sac at the same average times as the healthy sac. The time separation resolution for the pathlines beginning at the top of the model was 0.275 seconds. The delta time ranged between 0.02 and 0.2 seconds. The distance traveled into the model by pathline 6 is shown in Table 8.5, where the pathline numbering system is expressed in Figure 8.18. Figures 8.18, 8.19 and 8.20 shows the pathlines beginning at the duct entrance for cycles 1, 2 and 3, respectively. There is a 1.02 mm difference in the pathline distance, the difference in the position of the pathline at the beginning of inhale and the end of inhale, between the first and second cycles, as shown in Table 8.5. The small difference signifies there is good agreement between the three cycles. Table 8.6 shows the coordinates of the pathlines at the end of inhale for all three cycles as well as average coordinates. Again, at the end of exhale the particles did not return precisely to their position at the beginning of inhale. In the first cycle, Figure 8.18, the pathlines at the end of exhale did not return exactly to their beginning point of the pathlines at the beginning of inhale, the pathlines were short by a maximum of 4.3 mm. In the second and third cycle, Figures 8.15 and 8.16, respectively, the pathlines passed the start position at the beginning of inhale at the end of exhale by a maximum of 2 mm.   It is predicted that the reason this occurred is for the same reason shown in the healthy alveolar sac model (Section 8.1.13); a small amount of error in the PIV analysis can significantly influence the position of the pathlines at the end of exhale. It was concluded, that like the healthy alveolar sac model, the pathlines beginning at the duct entrance are reversible. The average coordinates of the pathlines at the end of inhale were used in Section 8.3.2 in the particle diffusion analysis.

Table 8.5: Comparison of the Distance in Between the Beginning of Inhale and the End of Inhale for Pathline #6

	1st Cycle	2nd Cycle	3rd Cycle	Average (mm)
Distance Traveled (mm)	26.25	25.27	25.70	25.74

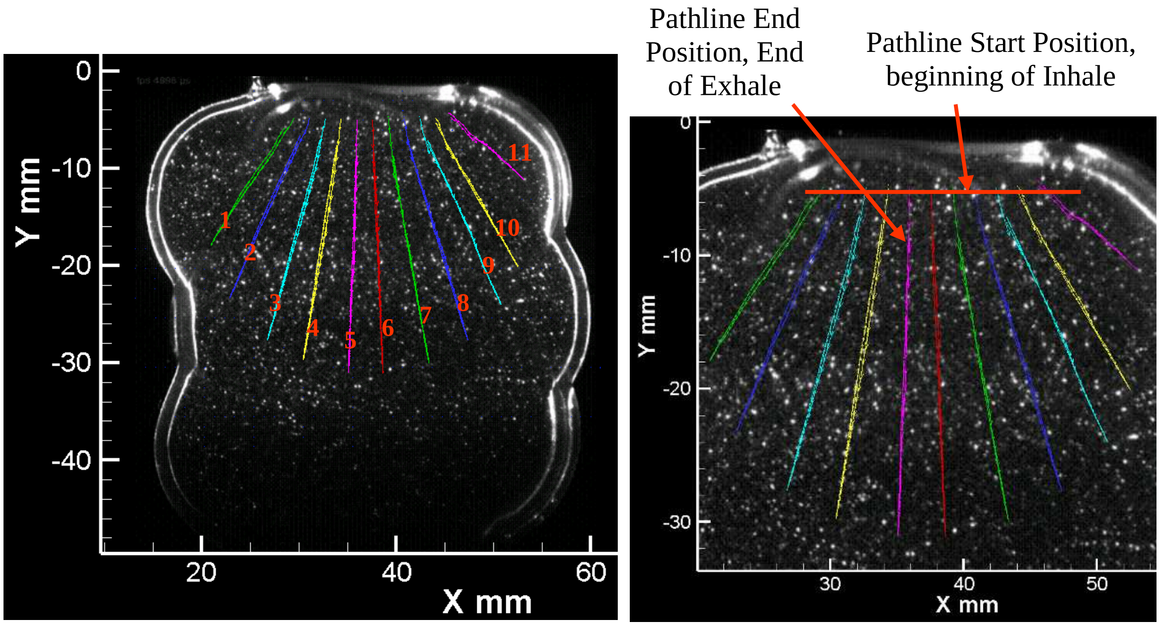

Figure 8.18: Pathlines for Emphysematic Alveolar Sac for 1st Breathing Cycle.

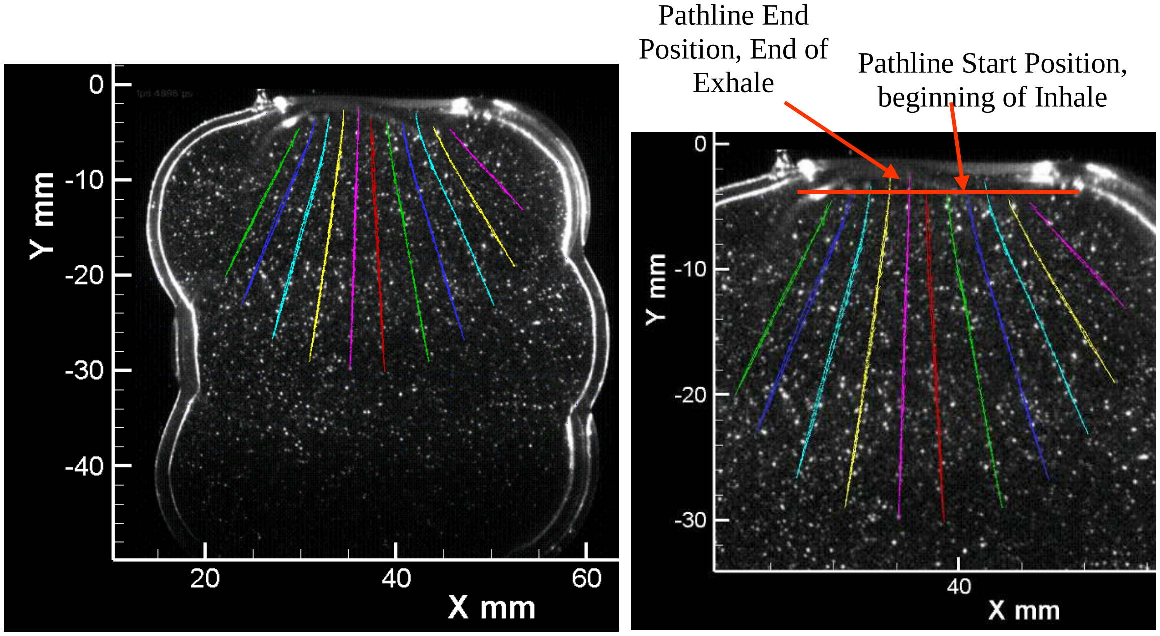

Pathline End Position, End of Exhale

Pathline Start Position, beginning of Inhale

Figure 8.19: Pathlines for Emphysematic Alveolar Sac for 2nd Breathing Cycle.

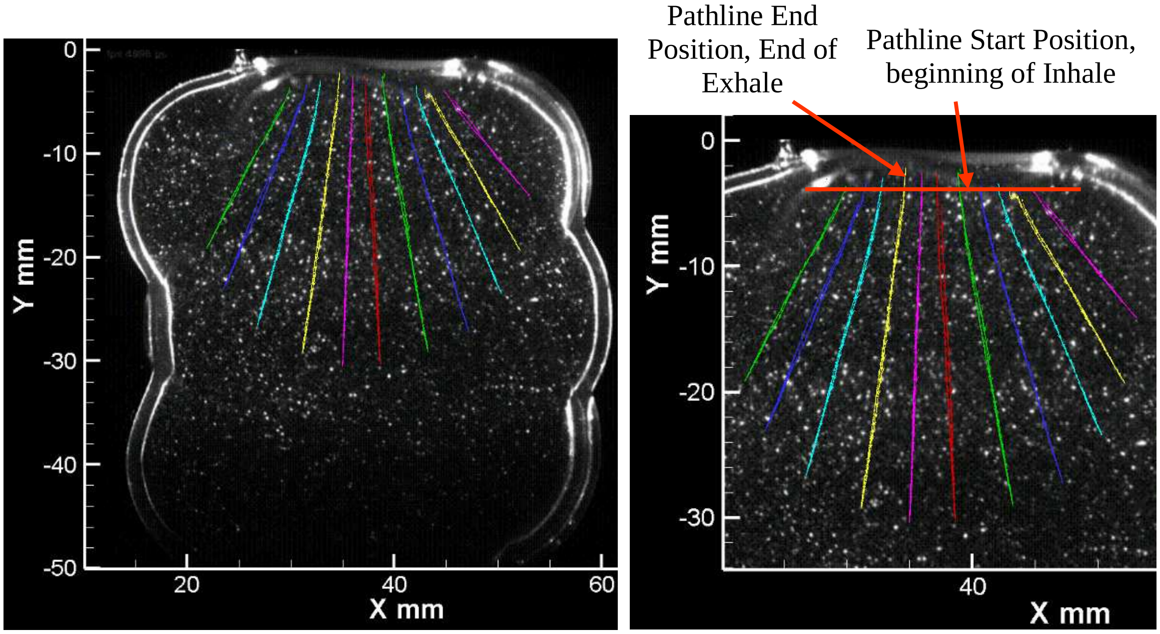

Pathline End Position, End of Exhale

Pathline Start Position, beginning of Inhale

Figure 8.20: Pathlines for Emphysematic Alveolar Sac for 3rd Breathing Cycle.

Table 8.6: Emphysema Pathline End of Inhale Coordinates

	Coordinates (mm)							
	Cycle 1		Cycle 2		Cycle 3		Average	
Pathline	x	y	x	y	x	y	x^*_2	y^*_2
1	20.95	-17.90	22.15	-20.05	21.90	-19.10	21.67	-19.02
2	22.90	-23.30	23.80	-23.20	23.50	-23.10	23.40	-23.20
3	26.80	-27.60	27.05	-26.60	26.80	-26.70	26.88	-26.97
4	30.40	-29.70	30.90	-29.00	31.15	-29.20	30.82	-29.30
5	35.10	-31.00	35.20	-30.00	35.00	-30.40	35.10	-30.47
6	35.10	-31.00	38.80	-30.05	38.60	-30.30	37.50	-30.45
7	43.35	-29.95	43.50	-29.00	43.20	-29.00	43.35	-29.32
8	47.35	-27.70	47.10	-26.75	47.20	-27.20	47.22	-27.22
9	50.75	-24.00	50.30	-23.15	50.30	-23.40	50.45	-23.52
10	52.50	-20.05	52.40	-19.05	52.10	-19.30	52.33	-19.47
11	53.10	-11.20	53.30	-13.10	53.05	-14.10	53.15	-12.80

*x_2 and y_2 were used in Table 8.12.

8.2.2 Pathlines Inside Top Two Alveoli

A determination of irreversibility, as well as a way to compare the emphysema geometry to the healthy alveolar sac geometry, was needed. An examination of the fluid behavior was performed in the emphysematic alveolar sac. Pathlines were plotted close to the top alveoli in order to visualize the flow. The pathlines released near the alveoli were released at the same distance away, from the closest alveolar wall, as the healthy alveolar sac. The x-coordinate for the left alveolus was 22.01 mm, with 5 pathlines ranging of a y-coordinate of -6.03 mm to -13.7 mm. The x-coordinate for the right alveolus was 49.7 mm with the 5 pathlines ranging from -5.7 mm to -15.4 mm. The time separation resolution for the pathlines was 0.55 seconds. Delta time, the time separating the frames analyzed using cross correlation, ranged between 0.02 and 0.2 seconds, where a larger delta time was used in most cases. The irreversibility and pathline location at the end of inhale analysis was performed on these pathlines.

8.2.2.1 Irreversible Flow Analysis

If irreversible flow occurs, it is most likely to happen inside the alveoli (Tsuda et al., 1999). Pathlines were plotted for the third cycle over three breathing iterations; the cycle data was used three times consecutively. The third cycle was chosen because the pathlines were closest to the average. Plotting the pathlines over three iterations allowed for irreversible flow to be distinguishable and allow for calculation of increased residence time, if irreversible flow was occurring. The end of exhale position of the pathline after the first cycle was used for the beginning of inhale start position of the pathline for the second cycle. Figure 8.21 shows the pathlines over the three iterations for third breathing cycle. From Figure 8.21, it can assumed that the even though the pathlines seem to be slightly irreversible, irreversibility was not actually occurring. The irreversible looking flow is most likely due to PIV vector analysis error, as was shown for the healthy alveolar sac, Section 8.1.2.1.

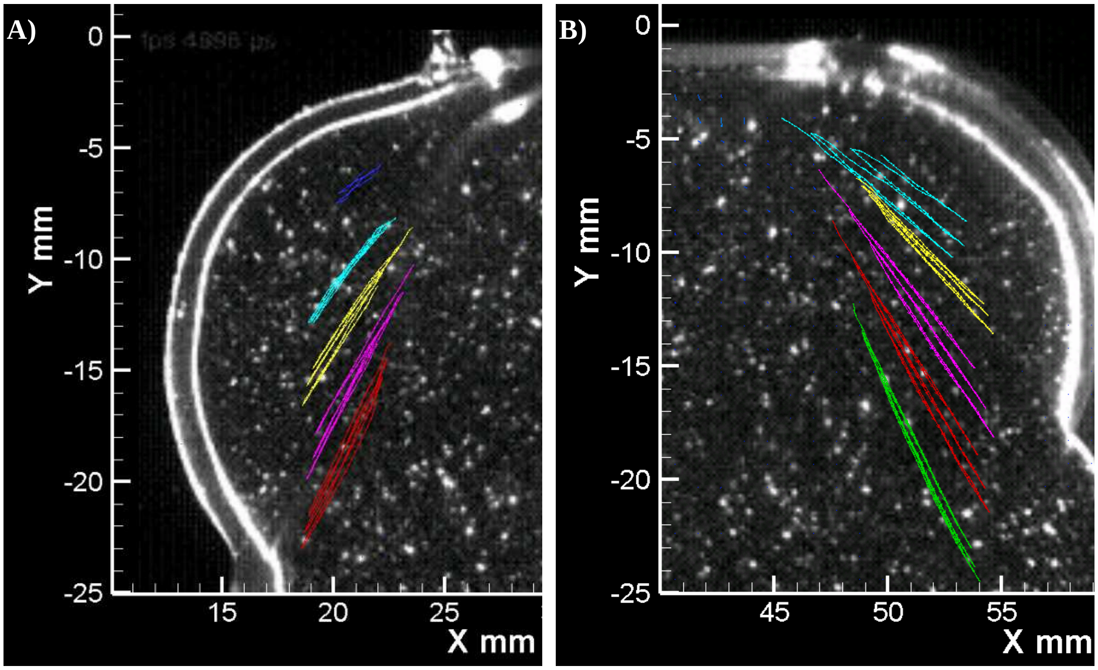

Figure 8.21: Pathlines of Three Cycles in the Emphysematic Alveolar Sac for the Left Alveolus (A) and the Right Alveolus (B).

8.2.2.2 Pathline Location at End of Inhale

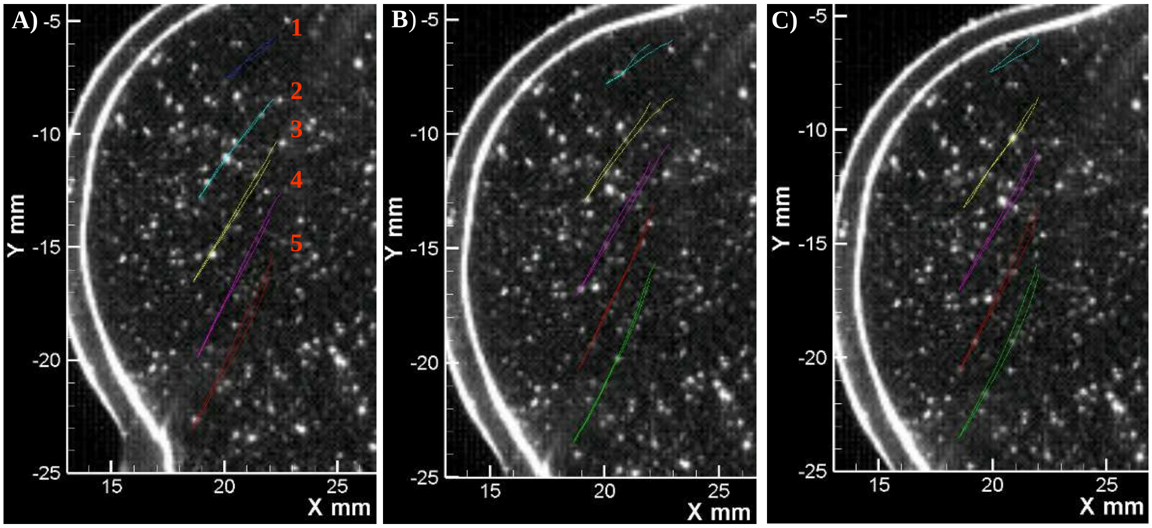

Figure 8.22: Pathlines in Emphysematic Left Alveolus for First Cycle (A), Second Cycle (B) and Third Cycle (C).

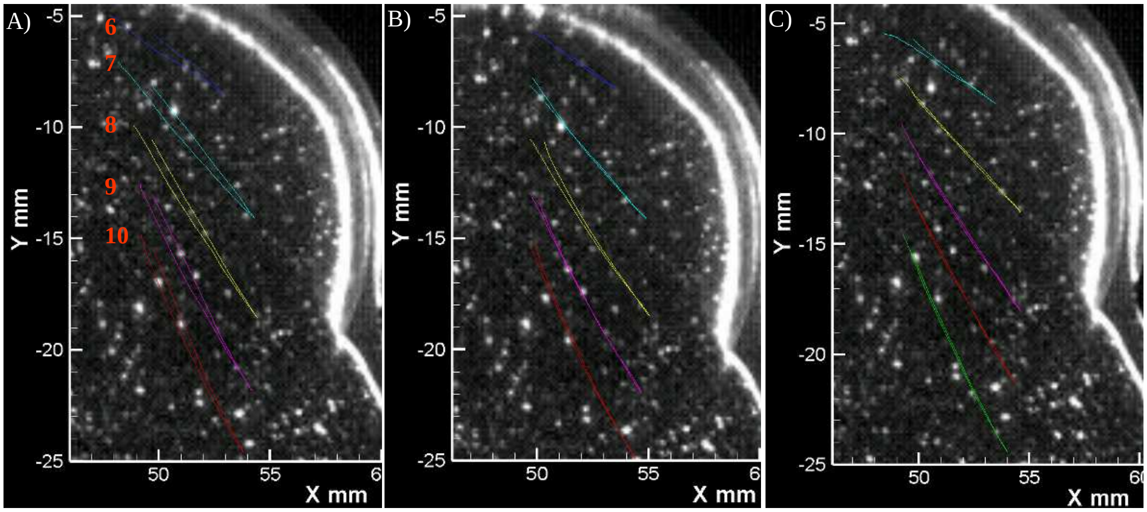

Figure 8.23: Pathlines in Emphysematic Right Alveolus for First Cycle (A), Second Cycle (B) and Third Cycle (C).

The location of each pathline at the end of inhale was needed in order to estimate particle diffusion and compare to the healthy alveolar sac. In order to calculate the average across all three cycles, the pathlines were plotted for breathing cycles 1, 2 and 3. Figures 8.22 and 8.23 express the pathlines for a breathing cycle for the left and right alveolus, respectively. Both figures reinforce the assumption that irreversible flow is unlikely. Table 8.7 shows the coordinates of the pathlines at the end of inhale for all three cycles as well as the average between the cycles. The average pathlines coordinates at the end of inhale was used in determination of diffusion time, which is used for comparison between the healthy and emphysema alveolar sac geometry.

Table 8.7: Emphysema Pathline End of Inhale Coordinates

	Coordinates (mm)							
	Cycle 1		Cycle 2		Cycle 3		Average	
Pathline	x	y	x	y	x	y	x*$_2$	y*$_2$
1	20.10	-7.80	19.90	-7.45	20.10	-7.50	20.03	-7.58
2	19.15	-12.90	18.70	-13.40	18.90	-12.80	18.92	-13.03
3	18.75	-17.10	18.50	-17.05	18.60	-16.50	18.62	-16.88
4	18.80	-20.40	18.55	-20.50	18.58	-19.90	18.64	-20.27
5	18.60	-23.50	18.50	-23.50	18.60	-23.00	18.57	-23.33
6	52.92	-8.50	53.60	-8.25	54.45	-8.60	53.66	-8.45
7	54.30	-14.05	54.90	-14.10	54.60	-13.55	54.60	-13.90
8	54.45	-18.55	55.05	-18.50	54.50	-18.10	54.67	-18.38
9	54.20	-21.80	54.70	-21.95	54.40	-19.10	54.43	-20.95
10	53.80	-24.65	54.45	-24.95	54.00	-24.50	54.08	-24.70

*x_2 and y_2 were used in Table 8.13.

8.3 Particle Diffusion

In order to link the pathline results to actual particle deposition, particle diffusion behavior was examined. Diffusive particles move from an area of high concentration to an area of low concentration by diffusion. The distance a particle travels is

$$x_{rms} = \sqrt{2Dt} \tag{8.1}$$

where x_{rms} is the average Brownian displacement, D is the diffusion coefficient and t is the time it takes to travel the average distance to where the particle is diffusing to. The diffusion coefficient is given by

$$D = \frac{kTC_c}{3\pi\mu d_p} \tag{8.2}$$

where k is the Boltzmann's constant, T is the temperature of the environment, C_c is the slip correction factor, μ is the dynamic viscosity of the environment and d_p is the diameter of the particle (Hinds, 1999). The diffusion coefficient for various sized particles is shown in Table 8.8. The range of particles was chosen because of their high possibility to reach the alveolar region of the lung. Larger particles are governed by other forces, sedimentation and impaction, and therefore have a higher chance of depositing in the upper airways. Also, it can be assumed that for these size particles the diffusive forces are much greater then sedimentation or gravitational forces, and therefore the sedimentation and gravitational forces can be neglected. The distance traveled, based on time, by the small particle is shown in Table 8.9. The data presented in Table 8.9 is used in Figure # in Section # to estimate particle diffusion. Particle Diffusion was calculated for both the healthy and emphysematic alveolar sacs based on the distance between where the pathline ended at the end of inhale and the distance towards the alveolar wall.

Table 8.8: Diffusion Coefficient for Different Sized Particles

Boltzmann's Constant, k	1.38E-23	J/K
Body Temperature, T	37	C
Body Temperature, T	310	K
Dynamics Viscosity of Air at Body Temperature, μ	1.87E-05	Pa-s
Particle Size (μm)	Slip Correction Factor, Cc (Hinds, 1999)	Diffusion Coefficient, D (Equa. 8.2) (m/s)
0.1	2.928	7.11E-10
0.08	3.47	1.05E-09
0.06	4.384	1.77E-09
0.04	6.229	3.78E-09
0.02	11.801	1.43E-08
0.01	22.976	5.58E-08

Table 8.9: Average Brownian Displacement (μm)

	Time (sec)			
Particle Size (μm)	1	3	5	7
0.1	37.71	65.32	84.32	99.77
0.08	45.90	79.50	102.63	121.43
0.06	59.57	103.18	133.20	157.61
0.04	86.97	150.63	194.46	230.09
0.02	169.28	293.21	378.53	447.89
0.01	334.05	578.59	746.96	883.81

8.3.1 Diffusion in Healthy Alveolar Sac

An estimation of particle diffusion time, based on the location of the pathlines at the end of inhale, was desired. The first step, in determining the diffusion, was establishing the location of the pathline with respect to the alveolar wall, the surface to where the particle would need to diffuse to. Table 8.10 shows the distance, x_3 and y_3, between location of the pathline at the end of inhale, x_2 and y_2 (Table 8.2), from each pathline that began at the duct, to the closest radial wall at the end of inhale for the healthy alveolar sac. Table 8.11 expresses the distance between pathlines, which were released inside the alveoli, location at the end of inhale and the distance to the closest radial wall. The closest radial wall represented the shortest two dimensional distance a particle would have to travel in order to diffuse to the alveolar wall. The x_1 and y_1 measurements were the coordinates for the wall closest to the pathline. The measurement between the pathline and the wall were taken with Image J for when the alveolar sac was completely expanded. The completely expanded sac was used because it represented the geometry at the end of inhale. In order to convert the large scale model that was used for the PIV analysis, to the small scale model, which represented an in vivo alveolar sac, the shortest distance from pathline to wall, needed to be converted. The in vivo small scale distance was the length of the distance between the pathline and the wall divided by the scale of the model, 75. The in vivo scale length was used in determining particle diffusion time and distance.

Table 8.10: Healthy Alveolar Sac: Distance to Closest Alveolar Wall from Pathlines, Beginning at Duct, at End of Inhale

	Coordinates of the Alveolar Wall Closest to the Pathline (mm)		Distance Between The Pathline at End of Inhale and Closest Radial Alveolar Wall (mm)		Shortest Distance From Pathline to Wall	
					$\sqrt{x_3^2 + y_3^2}$ (mm)	In Vivo - Small Scale Length (μm)
Pathline	x_1	y_1	$x_3 = x_2* - x_1$	$y_3 = y_2* - y_1$		
1	17.30	-15.58	5.80	1.85	6.09	81.16
2	22.18	-22.83	2.94	2.46	3.83	51.11
3	22.57	-25.33	4.90	-0.04	4.90	65.29
4	22.18	-28.29	8.29	-0.14	8.29	110.51
5	23.34	-30.35	10.76	-0.20	10.76	143.49
6	23.28	-30.67	14.17	-0.36	14.17	189.00
7	55.49	-30.29	-14.29	-0.24	14.29	190.56
8	56.01	-28.49	-10.84	-0.11	10.84	144.59
9	56.20	-26.17	-8.18	0.19	8.19	109.14
10	55.43	-21.86	-5.06	0.13	5.06	67.53
11	60.44	-14.73	-7.94	-0.15	7.94	105.89

* x_2 and y_3 are from Table 8.2

Table 8.11: Healthy Alveolar Sac: Distance to Closest Alveolar Wall from Pathlines at End of Inhale Inside Alveoli

	Coordinates of the Alveolar Wall Closest to the Pathline (mm)		Distance Between The Pathline at End of Inhale and Closest Radial Alveolar Wall (mm)		Shortest Distance From Pathline to Wall	
					$\sqrt{x_3^2 + y_3^2}$ (mm)	In Vivo - Small Scale Distance (μm)
Pathline	x_1	x_1	$x_3 = x_2* - x_1$	$y_3 = y_2* - y_1$		
1	21.41	-5.02	0.86	-2.51	2.66	35.40
2	15.24	-10.80	6.44	-0.23	6.45	85.97
3	16.33	-17.17	4.75	2.20	5.24	69.86
4	18.07	-19.55	3.11	1.52	3.46	46.17
5	19.23	-20.58	2.07	0.98	2.29	30.54
6	54.59	-5.02	-1.07	-2.46	2.69	35.83
7	60.44	-11.12	-5.81	-0.05	5.81	77.42
8	60.38	-14.98	-5.71	0.10	5.71	76.19
9	56.71	-21.48	-2.29	3.28	4.00	53.36
10	54.98	-21.99	-0.68	1.52	1.67	22.24

* x_2 and y_2 are from Table 8.4

The second step in determining the particle diffusion was determining the time needed for a particle traveling on each pathline to diffuse to the closest wall. Equa. 8.2 were used for the time calculation, based on the in vivo length small scale distance, and the diffusion coefficient for different size particles (Table 8.8). Figure 8.24 shows the time for diffusion, based on the in vivo length (Table 8.10), for each size particle entering at the duct of the alveolar sac. Figure 8.25 expresses the time for diffusion to take place, based on the in vivo length (Table 8.11), for different size particles that are inside the alveoli. From Figure 8.24 it can be seen that particles of all sizes, which enter through the alveolar duct, will reach the alveolar wall within 4 seconds if they are traveling on pathlines 2, 3 and 10. Also, particles of all sizes will reach the alveolar wall in 10 seconds, is traveling on pathlines 1, 2 3, 4, 9, 10 and 11. For pathlines 5 and 8 particles larger then 0.08 μm will not make it to the closet alveolar wall in ten seconds. Particles traveling on pathline 6 and 7 will not make it to the closest alveolar wall if they are greater then 0.05 μm. From Figure 8.25 it can be noted that all particles will deposit within 6 seconds, for particles that begin inside the alveoli. Within the 4 second time frame, all particles traveling on pathlines 1, 4, 5, 6, 9 and 10 will be able to diffuse to the closest alveolar wall. Particles larger then 0.08 μm will not have enough time to diffuse to the alveolar wall within 4 seconds if traveling on pathline 2 or 3. The diffusion analysis for the healthy alveolar sac gives a good estimation of diffusion from the position of a particle at the end of inhale to the closest radial wall. The diffusion time was compared to the emphysema time (Section 8.3.2).

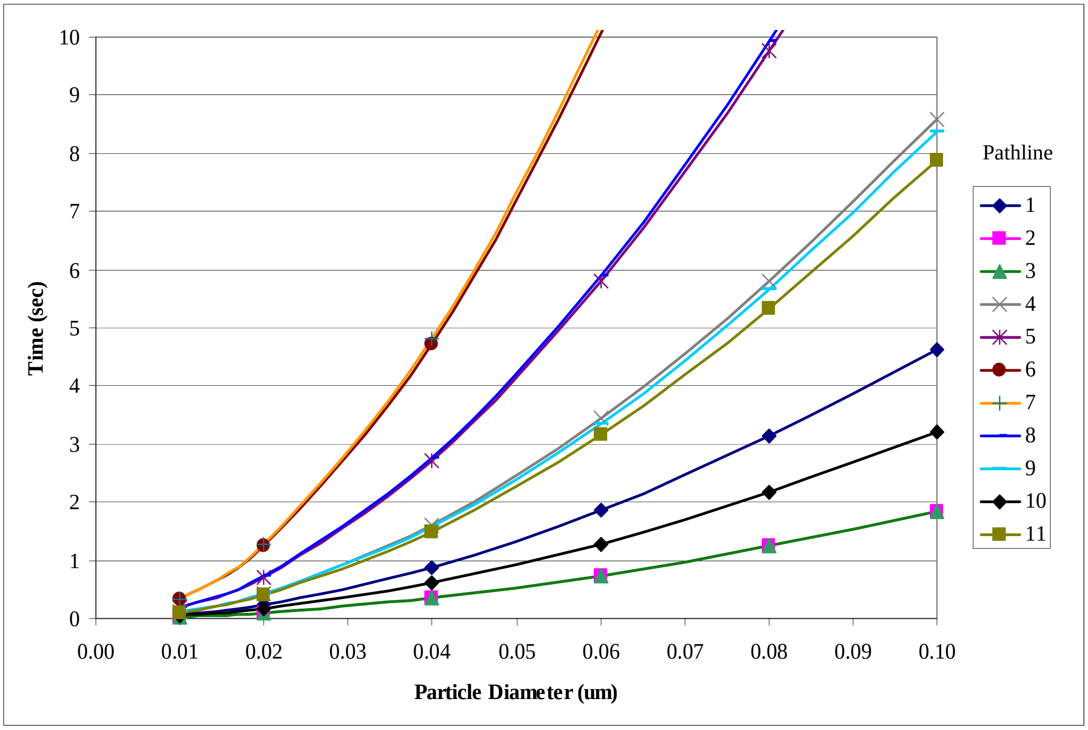

Figure 8.24: Healthy Alveolar Sac Diffusion Time Using Distance from Pathlines Location at the End of Inhale to the Closest Radial Alveolar Wall for Pathlines Beginning at Alveolar Duct.

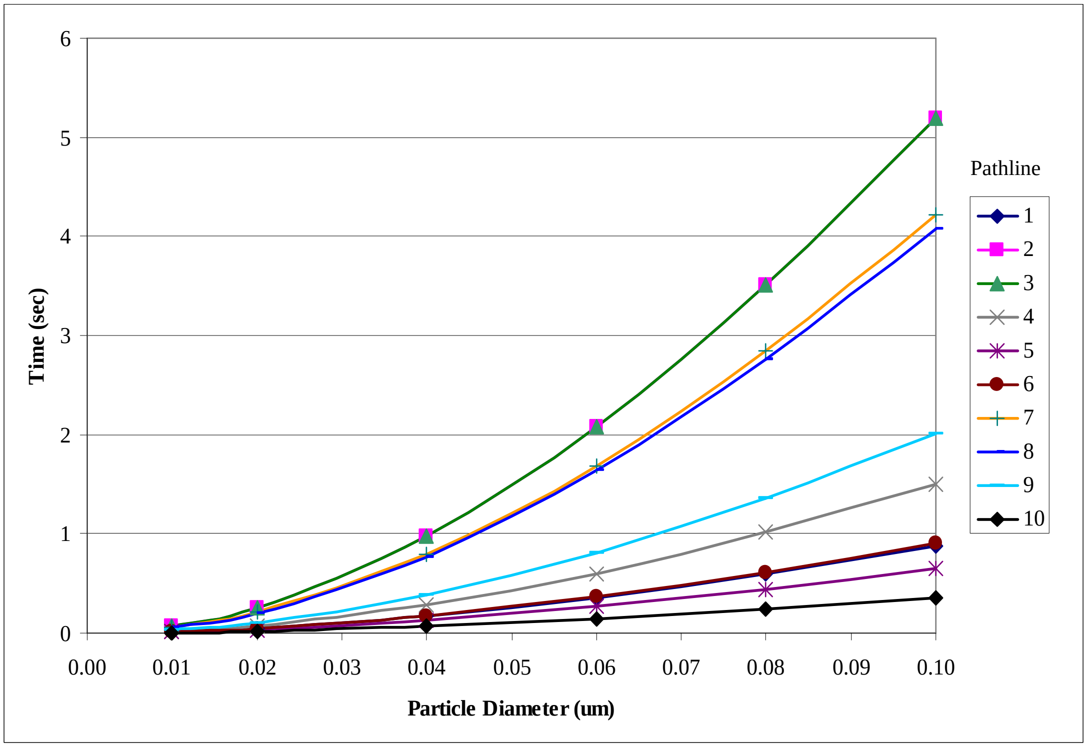

Figure 8.25: Healthy Alveolar Sac Diffusion Time Using Distance from Pathlines Location at the End of Inhale to the Closest Radial Alveolar Wall for Pathlines Beginning Inside Top Two Alveoli.

8.3.2 Diffusion in Emphysematic Alveolar Sac

A comparison between the healthy and emphysematic alveolar sac needed to be made for particle diffusion. A length scale is needed in order to determine diffusion, therefore the location of the pathline with respect to the alveolar wall, the surface to where the particle needs to diffuse to, was calculated. Table 8.12 shows the distance, x_3 and y_3, between location of the pathline at the end of inhale, x_2 and y_2 (Table 8.6), from each pathline that began at the duct, to the closest radial wall at the end of inhale for the healthy alveolar sac. Table 8.13 expresses the distance between pathlines, which were released inside the alveoli, location at the end of inhale and the distance to the closest radial wall. The x_1 and y_1 measurements were the coordinates for the wall closest to the pathline. The measurement between the pathline and the wall were taken with Image J for when the alveolar sac was completely expanded. The in vivo small scale distance is the length of the distance between the pathline and the wall divided by the scale of the model, 75. The in vivo scale length was used in determining particle diffusion time and distance.

Table 8.12: Healthy Alveolar Sac: Distance to Closest Alveolar Wall from Pathlines, Beginning at Duct, at End of Inhale

	Coordinates of the Alveolar Wall Closest to the Pathline (mm)		Distance Between The Pathline at End of Inhale and Closest Radial Alveolar Wall (mm)		Shortest Distance From Pathline to Wall	
					$\sqrt{x_3^2 + y_3^2}$ (mm)	In Vivo - Small Scale Length (μm)
Pathline	x_1	x_1	$x_3 = x_2^* - x_1$	$x_3 = y_2^* - y_1$		
1	12.95	-18.93	8.72	-0.09	8.72	116.23
2	13.27	-22.99	10.13	-0.21	10.13	135.10
3	13.91	-26.61	12.97	-0.36	12.98	173.04
4	14.10	-29.15	16.72	-0.15	16.72	222.90
5	14.01	-30.73	21.09	0.26	21.09	281.22
6	14.01	-30.73	23.49	0.28	23.49	313.22
7	62.48	-27.24	-19.13	-2.08	19.24	256.57
8	62.36	-29.92	-15.14	2.70	15.38	205.10
9	61.72	-23.05	-11.27	-0.47	11.28	150.40
10	60.29	-19.18	-7.96	-0.29	7.96	106.16
11	59.37	-12.51	-6.22	-0.29	6.23	83.02

* x_2 and y_2 are from Table 8.6

Table 8.13: Healthy Alveolar Sac: Distance to Closest Alveolar Wall from Pathlines at End of Inhale Inside Alveoli

	Coordinates of the Alveolar Wall Closest to the Pathline (mm)		Distance Between The Pathline at End of Inhale and Closest Radial Alveolar Wall (mm)		Shortest Distance From Pathline to Wall	
					$\sqrt{x_3^2 + y_3^2}$ (mm)	In Vivo - Small Scale Length (μm)
Pathline	x_1	x_1	$x_3 = x_2* - x_1$	$x_3 = x_2* - x_1$		
1	18.80	-6.10	1.23	-1.48	1.93	25.72
2	14.80	-10.92	4.12	-2.11	4.63	61.70
3	13.08	-16.64	5.54	-0.24	5.54	73.89
4	13.02	-20.32	5.62	0.05	5.62	74.98
5	13.40	-23.39	5.17	0.06	5.17	68.89
6	55.31	-6.86	-1.65	-1.59	2.29	30.58
7	59.18	-12.26	-4.58	-1.64	4.86	64.86
8	60.33	-18.35	-5.66	-0.03	5.66	75.51
9	60.45	-20.45	-6.02	-0.50	6.04	80.50
10	61.91	-23.56	-7.83	-1.14	7.91	105.46

* x_2 and y_3 are from Table 8.7

The diffusion time, based on the pathline and the in vivo length, needed to be calculated for different particle sizes. The calculation was completed by using the Brownian Diffusion Equation, Equa. 8.1. Figure 8.26 expresses the diffusion time based on particle size and the in vivo length, the distance between the pathline at the end of inhale and the closest radial alveolar wall, for the pathlines beginning at the duct entrance. Figure 8.27 shows the diffusion time for the pathlines beginning in the top two alveoli. From Figure 8.26 it can be observed that for the emphysema alveolar sac all particles will diffuse to the closest alveolar wall in the 10 second time frame for pathlines 1, 10 and 11. Within 4 seconds, particles less then 0.08 μm will be able to diffuse to the closest alveolar wall for pathline 11. For pathlines 1 and 10 particles less then 0.06 μm will diffuse in 4 seconds. Particles traveling on pathlines 2, 3 and 9 will deposit on the closest alveolar wall in 4 seconds if they are less then 0.04 μm. Only particles less then 0.02 μm will deposit in 4 seconds if they are traveling on pathlines 4, 5, 6, 7 or 8. From Figure 8.27 all particles will deposit to the closest wall if they are on pathlines 1, 2, 3, 4, 5, 6, 7 or 8. For pathlines 9 and 10, only particles less then 0.06 μm will deposit on the alveolar wall in the 0.04 seconds. A comparison of the diffusion estimation for the emphysematic and healthy alveolar sacs, based on the location of the pathline at end of inhale and the closest radial wall, is made in Section 8.4.

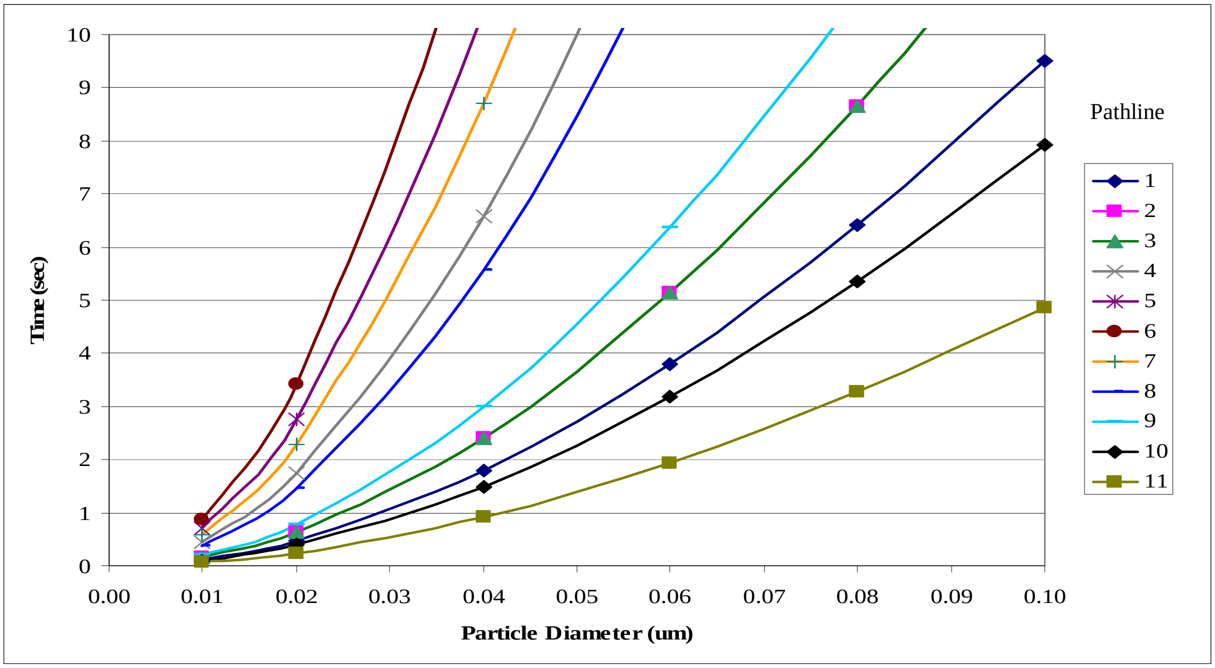

Figure 8.26: Emphysematic Alveolar Sac Diffusion Time to Closest Alveolar Wall for Top Pathlines.

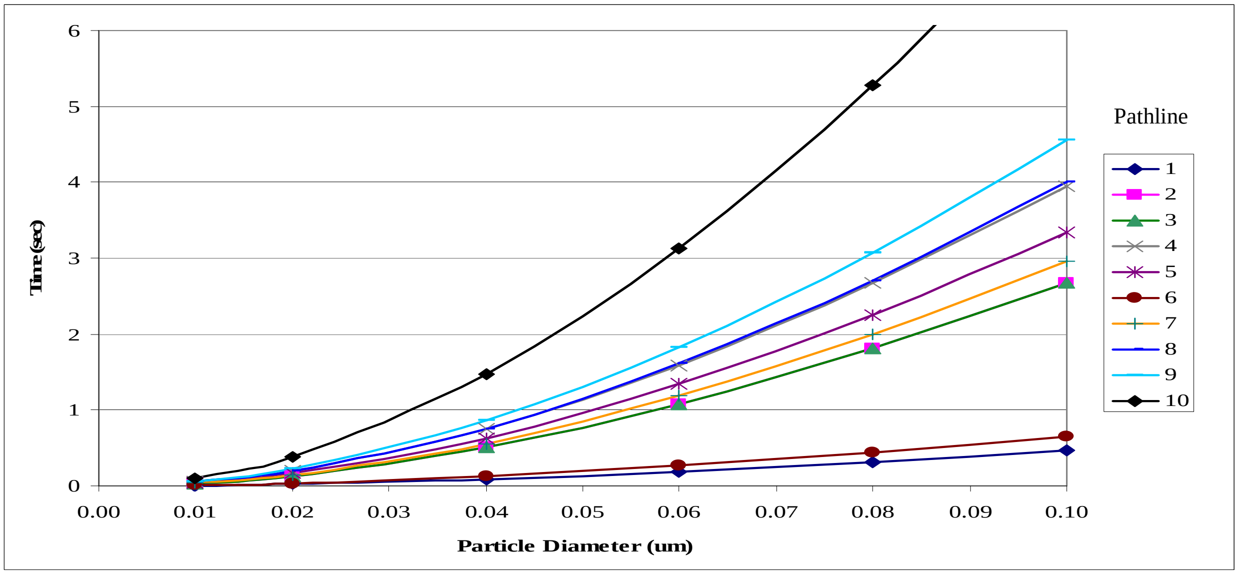

Figure 8.27: Emphysematic Alveolar Sac Diffusion Time to Closest Alveolar Wall for Pathlines Inside Top Alveoli.

8.4 Comparison Between Healthy and Emphysema Alveolar Sacs

A comparison of the distance the middle pathline traveled into the alveolar sacs, the behavior of the pathlines near the alveoli and the distance for diffusion was compared for the healthy and emphysematic alveolar sac models. The comparison links the differences in the fluid flow based on the different geometries.

First, the distance of travel into the alveolar sac, for a pathline starting at the duct, was compared between the different alveolar sac geometries. The average middle pathline, pathline 6, for the healthy alveolar sac was 24.97 mm and the average distance for the emphysematic alveolar sac was 25.74 mm. Both alveolar sacs expanded by thirty percent, but the emphysematic alveolar sac has a larger initial volume. The maximum volume intake of the healthy alveolar sac was 13.3 ml and the maximum volume intake by the emphysematic alveolar sac was 18.2 ml. Even though the initial volume, and therefore the volume intake from a breath were much greater in the emphysematic geometry, the distance the middle pathline traveled was not much different between the two different geometries. It therefore was concluded that the geometry difference was influencing the pathline travel.

A comparison between the healthy and emphysematic alveolar sacs needed to be made based on the location of the pathline at the end of inhale and the closest radial wall. From Figure 8.24, healthy alveolar sac, and Figure 8.26, emphysematic alveolar sac, the following observations can be made about the pathlines that begin at the top of the alveolar sacs. The distance between the closest wall for the healthy alveolar sac was approximately 1.5 times closer then for the emphysema alveolar sac. For the healthy alveolar sac all particles will diffuse to the closest alveolar wall in the 10 second time frame for pathlines 1, 2, 3, 4, 9, 10 and 11, for the emphysematic alveolar sac only pathlines 1, 10 and 11 will there be enough time for all the particles diffuse. For the middle pathline in the healthy alveolar sac, pathline 6, particles larger then 0.04 μm will not deposit in the 10 second time frame. Conversely, for the emphysematic alveolar sac only particles less then 0.02 μm on pathline 6 will be able to diffuse to the closest wall. Particles greater then 0.06 μm will not deposit in the 10 second for the two pathlines furthest from the alveolar wall, pathlines 6 and 7, and for emphysematic the 5 furthest pathlines, pathlines 4, 5, 6, 7 and 8 will not deposit for particle sizes greater then 0.06 μm.

A comparison between the healthy and emphysematic geometry can also be made for the pathlines that begin inside the top two alveoli, Figure 8.25 for the healthy alveolar sac and Figure 8.27 for the emphysematic alveolar sac. For the healthy alveolar sac all particles will deposit in less then 6 seconds, while in the emphysematic particles on pathline 10 will not have enough time to deposit. Four pathlines, pathlines 3, 5, 6 and 10, will deposit for all particle sizes in less then 1 second in the healthy alveolar sac model. For the emphysematic alveolar sac model only two particles on pathlines 1 and 6 will deposit to the closest alveolar wall in less then 1 second.

An approximate amount of time was needed to be determined for each particle size to diffuse. The approximate time was determined based on the longest and shortest radial distance from the pathline at the end of inhale to the alveolar wall. Pathline 1, for the healthy alveolar sac (Table 8.2), and pathline 11, for the emphysematic alveolar sac (Table 8.4), was chosen to represent the shortest distance needed to reach the alveolar wall. Pathline 6, in both geometries, was chosen to represent the longest radial distance to reach the alveolar wall. The distance for pathline 6 was determined from the end position of the pathline at the end of inhale and the distance to bottom point of the alveolar sac. Figure 8.28 expresses the theoretical diffusion distance for different side particles during the range of time for a typical breath. The graph was computed based on the Brownian Diffusion Equation (Equa. 9.1) and Table 8.9. Comparing the Brownian diffusion distance to the radial distance from the end point of the pathline at the end of inhale will give the approximate amount of time is needed for each particle size to diffuse. From the comparison it can be seen that particle size of at least 0.02 μm will be able to diffuse to the alveolar walls for a breath time of 5 seconds for the healthy alveolar model. The emphysematic model will need 7 seconds for particles less then 0.02 μm to diffuse to the all of the alveolar walls. The larger sized particles will not have enough time to diffuse to all of the alveolar walls. Particles sizes greater then 0.08 μm will not even be able to diffuse the shortest radial distance, for times less then 3 seconds, for either the healthy or the emphysematic alveolar sacs. These particles that do not reach the walls after a first initial breath may travel in the model, due to diffusion, and venture off of the pathline that entered the model through the top. Once a particle ventures off the original pathline it will become trapped in the model, and therefore it will not be exhaled. The particle will then stay in the alveolar sac longer and will potentially be able to deposit eventually.

From the analysis it can be noted that in the healthy alveolar sac model the pathlines travel closer to the alveolar walls and therefore there is a potential for greater particle deposition efficiency. A numerical analysis would be able to better predict actual deposit efficiency.

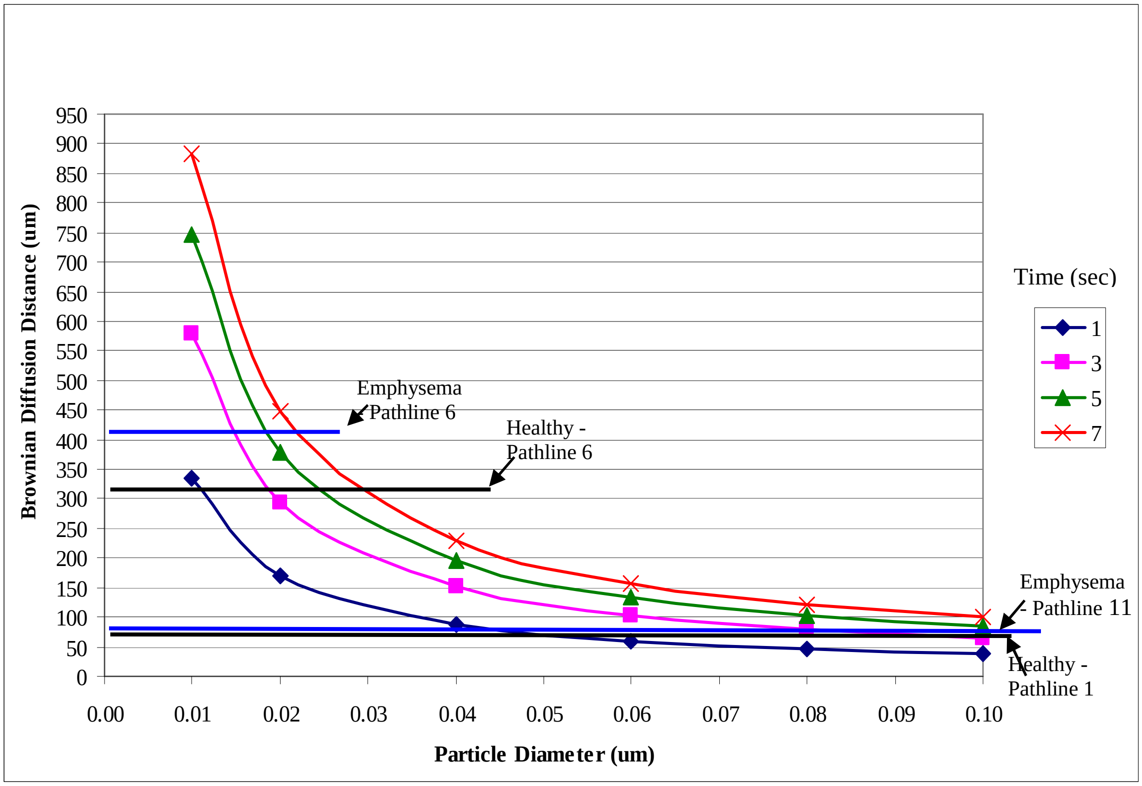

Figure 8.28: Theoretical Brownian Diffusion Distance for Particle Size and Time.

Chapter 9
Discussion

9.1 Comparison to Literature

An examination was performed in order to compare the results found in this work to research published in literature. The first comparison investigated the flow rate ratio relationship developed by Tsuda et al. (1995) and Tippe and Tsuda (1999). The articles found, in their expanding torus alveoli models, that the flow pattern is dependent on the ratio between the flow rate inside an alveolus and the flow rate in the duct. They showed that there was no recirculation, and therefore reversible flow, with a flow rate ratio of approximately 0.06, but recirculation, and therefore irreversible flow, did occur for flow rates ratios smaller then 0.06. It was concluded, by the authors, that the flow rate ratio increases as the distance into the acinus region increases, and therefore there is no recirculation regions in the distal area of the lung. By observation of the fluid flow within the alveolar sac model, it can be noticed that even though the flow rate is much smaller inside the alveolus, the ratio of the flow rate between the duct and the alveolus was not as small as 0.06. The pathlines for an entire cycle inside the alveolus were approximately a fifth of the length of the pathlines. Even though the exact flow rate ratio was not calculated in this work, it is concluded that the flow rate ratio is greater then 0.06 and therefore matches the theory presented by Tsuda et al. (1995) and Tippe and Tsuda (1999).

To determine the influence of the geometry on the flow patterns, a comparison was made with articles, which also examined the shape of the alveolus on the flow patterns. Tsuda et al. (1995) and Karl et al. (2004) examined the flow patterns based on the shape of the alveolus. The alveoli in the healthy and emphysematic models, in this work, were comparable to the shape that the articles used, for the depth to mouth diameter ratio of the models was within the range presented by the articles. It was shown, in their work, that circulation was dependent on the alveolar shape. Circulation decreased as the depth to mouth diameter ratio decreased in the research presented by Tsuda et al. (1995). Karl et al. (2004) found there was recirculation on all of the alveolus models, but the size and location of the recirculation changed depending on the depth to mouth diameter ratio. A direct comparison between the results form this work and the results presented by the articles, could not be completed, because the articles related their results to both the alveolus depth to mouth diameter ratios and the flow rate ratio. The flow rate ratio was not computed in this work. Although, this is the case, some observations were made. The depth to mouth ratio, in this work, was comparable to the smaller depth to mouth diameter ratio presented by Tsuda et al. (1995). Recirculation was not present inside the alveolus for the small depth to mouth diameter ratio in this work or the research presented by Tsuda et al. (1995). Karl et al. (2004) determined that there was recirculation in all of the models, even with the small depth to mouth diameter ratio. The results presented by Karl et al. (2004) differed from this work, because the model presented by the authors was stationary, while the model in this work expanded.

In order to justify the conclusion that there was less particle diffusion in emphysema then in healthy, a comparison was made with Strum and Hofmann (2004) and Sweeney et al.

(1987). Strum and Hofmann (2004) determined that there was less particle deposition in emphysema then in healthy in their mathematical model. A direct comparison could not be made, based on percentage or particles deposited, because deposition percentage was not calculated in this work. Even though a direct comparison was not made, the conclusions between the results from this work and the results from Strum and Hofmann (2004) are the same, there was less particle deposition in the emphysema alveolar sac geometry. Sweeney et al. (1987) determined there was less particle deposition in hamsters with emphysema when compared to healthy hamsters. Therefore, the result that there is less particle deposition in emphysema agrees with the literature.

9.2 Limitations of Work

There were several limitations in this study and are presented in the following section. The first limitation was due to the test rig. The pump on the test rig did not have a feedback loop, and therefore the pump control was limited. A feedback loop would bring more confidence that the pump was expanding and contracting with good accuracy. Figure 5.7 showed that there was some delay for the pump to change directions; a feedback loop would help with the acceleration problem. The pump also had a tendency to begin skipping after several cycles, which made it difficult to gather data for more then a few cycles. A feedback loop would correct the skipping problem. The pump was also located on the side of the test rig. It was not proven, in this study, whether or not the pump was pulling or pushing the models. The pathline results in the models showed that there was a problem with one side of the model expanding more then the other side, but it was not determined the exact cause of the problem. Further analysis would determine whether the location of the pump did create a problem. Another limitation of the test rig was the inability to re-mix the neutrally buoyant particles without completely dismantling the apparatus. Even though the particles did not rise during the experimentation time, the particle rise did become a problem if more images needed to be taken with the model at a later date. If another experiment needed to be performed, the entire setup would have to be dismantled and re-setup, which was time consuming. Finally, it was difficult to attach the hollow cast model to the apparatus. It was not possible to attach the model with perfect alignment, such that the hollow cast was not crooked. It was shown, in Section 8.1, that the healthy alveolar sac hollow cast was slightly crooked, which may have impacted the pathline results by pulling them to one side. Improving the test rig conditions would allow for more confident results in the fluid flow patterns.

The second limitation was the hollow cast geometry. It was shown that the alveolar sac models were a good representation to data found in literature, but the depth to mouth diameter ratio for the healthy alveolar sac could be increased from approximately 0.8 to 1.0, to better match that reported in the literature, as shown in Figure 3.14. Also, the healthy geometry was based off of an idealized alveolar sac. The geometry was derived based off of Weibel (1964) and Haefeli-Bleuer and Weibel (1988). The articles presented the geometry based off of a population average, but only seven lungs were used. Also, the geometry was determined from lung casting. The castings may not accurately represent the alveolar geometry, because the surface tension in the lung is different with the casting material. It was assumed, that an alveolus was a perfect sphere, but from the scanning electron microscope image, Figure 1.3, an alveolus is not a perfect sphere. The fluid flow patterns may change if more realistic geometry was used. In addition, the alveolar sac geometries only represented the 23rd generation of the lung. Particle diffusion was calculated with the necessary assumption that particles actually did travel to the 23rd generation. In order more accurately predict particle deposition; the particles should be examined in a model including the entire path from the trachea to the alveoli to get accurate flow and particle conditions at the alveolar duct entrance.

There were limitations in the manufacturing process of making the aluminum casts and the hollow cast. The aluminum cast had surface divets and rough spots that were not present in the CAD model, and the spherical alveoli were off from the CAD shape by approximately ±0.5 mm. A professional casting company would be better able to create an aluminum cast that represented the CAD models. In addition, it was difficult to create a uniform and predictable hollow cast thickness. The dipping process was difficult to execute and provide consistent results.

The material properties of the model material were unknown. It was not determined exactly how the model was deforming or whether it represented the same behavior in vivo. Perfecting the manufacturing process and understanding the material properties would allow for a better comparison between computational and experimental work, as well as being to more accurately link the results to what is occurring in the body.

There were limitations in the number of experimental parameters that were adjusted within the scope of this work. In order to represent all of the changes that occur with emphysema, a diseased emphysema breathing cycle should be used. In the diseased state, the emphysema patient has a longer expiration time then in health. Other breathing conditions could be simulated in order to determine the changes in the flow field and particle diffusion. Only one breathing cycle was tested for both healthy and emphysema. The breathing curve used represented a typical healthy adult. However, intersubject variability is significant among subjects, particularly as a function of diseased conditions, age and activity level. These changes would alter the flow field and ultimately the particle deposition predictions.

A validation was performed between CFD and PIV for the simple balloon geometry. It was shown that near the top of the balloon model, there was good velocity vector profile correlation at the high velocity and low acceleration areas. There was not as high of a correlation for the high acceleration areas. Improving the pump acceleration problem with a controller would improve the results. Also, it was determined that there was about 0.2 second error in determining what photographed frame represented what time in the breathing cycle, Section 6.4. Reducing timing error would allow for a better correlation between the numerical and PIV results.

The velocity vector plots were only plotted in the top section of the balloon model. Because the pathlines travel deep in the model, it would be desirable to validate the velocity in the bottom areas of the balloon model.

There were several limitations in the analysis of the alveolar sac models. The first was due to the laser light reflection on the alveolar walls. The reflection created very bright areas, which made it difficult for the cross correlation algorithm to determine accurate velocity vectors close to the walls. It was shown, in Section 8.1.2.1, that the errors near the alveolus wall made the pathlines appear irreversible, when in fact they were not. A high pass filter could be purchased in order to reduce the reflection glare.

In Section 7.3.2 it was estimated that there was a maximum uncertainty of 1.4 mm in the pathlines for the simple balloon geometry. Even though the uncertainty was applied to the alveolar sac models, it was difficult to conclude that the same amount of uncertainty exists with the alveolar sac models, because of the geometry differences. CFD analysis should be performed on the healthy and emphysema models and compared to the PIV results of this work to better quantify the uncertainty.

The results of the alveolar sacs were used to estimate in vivo diffusion. By linking the experimental model to in vivo conclusions, it was assumed the fluid scaling performed in Section 4.1 was correct. Performing a numerical analysis on the in vivo sized models and comparing results to the experimental scaled up models would allow for the fluid scaling theory to be validated.

The correlation between the flow field and particle behavior contained limitations. Particle diffusion to the alveolar wall was estimated by use of an average Brownian diffusion equation, but an exact percentage of particle deposition could not be estimated. The diffusion analysis was computed based on the length to the radial wall and the time period of a breath. Unless the time used is for a breath hold, the particle could be traveling with the fluid and the diffusion conclusions could change. The diffusion could be under or over estimated depending on the direction of diffusion relative to the direction of convection. In order to better be able to accurately predict particle deposition, a computational model that incorporated the moving fluid as well as particle diffusion would be needed.

Despite the limitations, conclusions could still be drawn from this work. The relationship between the pathlines for healthy and emphysema was shown and compared. In both alveolar sacs it was shown that the fluid flow was reversible. These results are significant since they contradict what has been presented in the literature. Even though the same breathing curve was used in the emphysema and healthy alveolar sacs, the reversible results probably will not change if a diseased breathing curve was used in the emphysema case. It was also shown that the emphysema pathlines do not come as close to the alveolar walls, as they do with healthy. Even though there was approximately 1.4 mm uncertainty, based on the balloon analysis, in the pathline length, the difference between the healthy and emphysema was larger then the possible uncertainty. Diffusion was estimated, and it was concluded that diffusion was greater in health, which is consistent with results presented in the literature.

9.3 Future Work

The study of fluid flow, and particle behavior, in the acinar region is not complete and therefore there is sufficient opportunities for future work to be completed. The first opportunity is to perform a structural analysis on the hollow cast material. This analysis would allow for a complete understanding of how the models expanded and contracted. Material properties of alveolar tissue was unknown, therefore a study could be completed in determining the material properties. This knowledge would allow for a better link between PIV or numerical experimentation and what is occurring in the body.

Although validation was completed on the simple balloon model, validation of the alveolar sac models was not completed. In order to draw more confident results, a validation would need to be performed. A computational analysis could be completed on the alveolar sac models. In order to link the results of the large scale model to in vivo alveolar sacs, a model and / or animal experiments could be performed. Once a numerical model is developed, and validated with PIV, other flow parameters, such as flow rate, tidal volume, and time of breath, could be adjusted on the model.

As discussed in the limitation section, geometry could be created that better represents the in-homogeneities on the alveolar region of the lung. For example, the fluid flow in different shaped alveoli could be examined. Other in-homogeneities, such as non-uniform expansion due to alveoli touching each other in the lung, would better be able to represent the fluid flow within the lung. It was shown, in Section 7.2, that model thickness variation does influence the expansion of the model, therefore non-uniform expansion could be developed by altering the thickness of the hollow casts. In order to analyze more complicated geometries, three dimensional PIV should be implemented. The three dimensional analysis would be able to better predict the highly three dimensional flow field.

To more accurately understand particle diffusion in the alveolar region of the lung, a numerical diffusion simulation could be performed. The numerical simulation could implement concentration gradients and therefore predict diffusion behavior based on the gradients. Also, particle convection, due to the moving fluid, could be modeled with the particle deposition. A stronger link between the flow field and particle deposition can be determined by a numerical analysis.

9.4 Summary and Conclusion

The relationship between how the fluid flow changes and how this influences particle deposition in emphysema is not fully understood. There have been some studies that have implied that there was difference between healthy and emphysema, but more research needed to be conducted to draw more accurate conclusions. A better understanding of particle deposition will aid in inhaled medication drug development, as well as improving risk assessment of inhaled pathogens. The first goal of this thesis was to determine if irreversible flow was occurring in realistic healthy and emphysema alveolar sac geometries. The second goal was to link the fluid flow analysis to particle deposition by diffusion, and compare the diffusion between healthy and emphysema.

In this work, three models were developed. A simple balloon model was used for validation between numerical and PIV analysis. The uncertainty, in the experimental technique, was theorized with the simple balloon model. Two alveolar sac geometries were used, representing healthy and emphysema alveolar sacs. It was determined that the geometry was comparable to literature, based on the depth to mouth diameter and effective airway diameter. To link the small scale in vivo geometry to the large scale experiment, fluid scaling was performed. The fluid scaling theory was developed and applied to the alveolar sac models. To simulate realistic breathing conditions, a realistic breathing curve was acquired and applied to the models. Particle diffusion was estimated for particle diameters within the range of 0.1 μm and 0.01 μm. The fluid flow and particle diffusion was compared between the two alveolar sac geometries and conclusions were made and linked to disease presence.

It was found, in this work, that irreversible flow was not present in the alveolar sac region of the lung for both the healthy and emphysema case. It was found that the pathlines in the healthy alveolar sac came closer to the walls then in the emphysema alveolar sac. For the pathlines that began at the duct entrance, the pathlines came approximately 1.5 times closer to the wall in the healthy case when compared to emphysema. Because the pathline traveled closer to the alveolar walls, the particle diffusion was greater in the healthy then emphysema. In the healthy geometry particles with a diameter of 0.02 μm will be able to diffuse to all of the alveolar walls within a 5 second time frame, where in emphysema 7 seconds would be needed. It was concluded that the diseased geometry does influence the fluid flow within the alveolar sac and therefore the possible particle deposition. Also, it was shown, that it is important to consider geometry in numerical or experimental models that predict fluid flow and particle deposition in the alveolar region of the lung.

With this thesis, it was shown that PIV can be conducted on an expanding geometry subject to unsteady flow. The research performed will lead to future work that will be able to incorporate different alveolar geometries, flow rates, frequency of a breath, and tidal volume. It was shown, in this research, that the expansion and contraction behavior is dependent on the thickness of the model. Therefore, if the thickness of model is able to be controlled, and therefore non uniform expansion could be performed, localized diseased states could be modeled by altering the material thickness.

Overall, this thesis was successful in comparing healthy and emphysema geometries, as well as developing techniques which could be used in continuation of the study of fluid flow and particle deposition within the alveolar region of the lung.

the lung.

References

Barkley, Russell. Personal Correspondence. Imaging Science. Rochester Institute of Technology.

Beachey, W. Respiratory Care Anatomy and Physiology. Mosby-Year Book Inc., 1998.

Brand, P., Rieger, C., Schulz, H., Beinert, T., Heyder, J. Aerosol bolus dispersion in healthy subjects. *The European respiratory journal.* 10:460-467,1997.

Carcamo, Nelsy. Personal Correspondence. Laboratory Science Technology Program, Department of Science and Mathematics, National Technical Institute for the Deaf, Rochester Institute of Technology.

Choi, J. and Chong, K. Mathematical analysis of particle deposition in human lungs: an improved single path transport model. *Inhalation Technology*. 19:925-939, 2007.

COMSOL Multiphysics User Guide. Version 3.3. COMSOL, August 2006.

Dailey, H., and Ghadiali, S. Fluid-structure analysis of microparticle transport in deformable pulmonary alveoli. *Journal of Aerosol Science.* 38:269-288, 2007.

Darquenne, C., Prisk, G. Aerosols in the study of convective acinar mixing. *Respiratory Physiology and Neurobiology*. 148: 207-216, 2005.

Greaves IA and Colebatch HJ. Elastic behavior and structure of normal and emphysematous lungs post mortem. *Am.Rev.Respir.Dis.* 121: 1: 127-136, 1980.

Grippi, M. Pulmonary Pathophysiology. Lippincott Williams and Wilkens, 1995.

Insight 3G Users Guide. P/N 1980511, Revision F. TSI, May 2007.

Haber, S., Yitzhak, D., Tsuda, A. Gravitational deposition in a rhythmically expanding and contracting alveolus. *Journal of Applied Physiology*. 95: 657-671, 2003.

Haefeli-Bleuer B and Weibel ER. Morphometry of the human pulmonary acinus. *Anat.Rec.* 220: 4: 401-414, 1988.

Huang, H., Dabiri, D., Gharib, M. On errors of digital particle image velocimetry. *Measurement Science Technology*. 8:1427-1440,1997.

Heyder, J., Blanchard, J., Feldman, H., Brian, J. Convective mixing in human respiratory tract: estimates with aerosol boli. *Journal of Applied Physiology*. 64:1273-1278,1988.

Hinds, W., Aerosol Technology: Properties, Behavior and Measurement of Airborne Particles, 2nd Edition. Wiley, 1999.

Laser Lab Instruments Optical Chopper, Thorlabs.

Karl, A., Henry, F., Tsuda, A. Low Reynolds number viscous flow in an alveolated duct. *Journal of Biomechanical Engineering*. 126:420-429,2004.

Keane, R. and Adrian, R. Theory of cross-correlation analysis of PIV images. *Applied Scientific Researc*. 49: 191-215, 1992.

Klingele, T G Staub,N C. Alveolar shape changes with volume in isolated, air-filled lobes of cat lung. *Journal of Applied Physiology*. 28: 411, 1970.

Kohlhaufl, M., Brand, P., Meyer, Th., Scheuch, G., Weber, N., Haubinger, K., Schulz, J., Heyder, J., Detection of impaired intrapulmonary convective mixing by aerosol bolus dispersion in patients with emphysema. *European journal of medical research*. 2:121-128,1997.

Levitzky, M. Pulmonary Physiology, 6th Edition. McGraw-Hill, 2003.

Marieb, E. and Hoehn, K. Human Anatomy and Physiology: 7th Edition. Pearson, 2007.

Mercer, R R Laco, J M Crapo,J D. Three-dimensional reconstruction of alveoli in the rat lung for pressure-volume relationships. *Journal of Applied Physiology*. 62: 1480, 1987.

MotionPro X Users Manual. Redlake Imaging Cooperation, 2007.

Pruyne, A. The mapping of velocity profiles in a three generation lung model using particle image Velocimetry flow analysis technique. *MS Thesis*. Mechanical Engineering. RIT. 2004.

Raffel, M., Willert.C., and Kompwnhans. Particle Image Velocimetry: A Practical Guide. Springer, 1998.

Strum, R., and Hofmann, W. Stochastic simulation of alveolar particle deposition in lungs affected by different types of emphysema. *Journal of Aerosol Medicine*. 17: 357-372, 2004.

Sweeney, T., Brain, J., Leavitt, S., Godleski, J. Emphysema alters the deposition pattern of inhaled particles in hamsters. *American Journal of Pathology*. 128:19-28, 1987.

Tippe, A., Tsuda, A. Recirculationg flow in an expanding alveolar model: experimental evidence of flow-induced mixing of aerosols in the pulmonary acinus. *Journal of Aerosol Science.* 31:979-986, 1999.

Tsuda, A., Butler J., Fredberg, J. Effects of alveolated duct structure on aerosol kinetics I. Diffusional deposition in the absence of gravity. *Journal of Applied Physiology.* 76: 2497-2509, 1994.

Tsuda, A., Henry, F., Butler J. Chaotic mixing of alveolated duct flow in rhythmically expanding pulmonary acinus. *Journal of Applied Physiology*. 79: 1055-1063, 1995.

Tsuda, A., Otani, Y., Butler, J. Acinar flow irreversibility caused by perturbations in reversible alveolar wall motion. *Journal of Applied Physiology* 86:977-984, 1999.

Tsuda, A., Rogers, R., Hydon, P., Butler, J. Chaotic mixing deep in the lung. *PNAS.* 99:10173-10178, 2002.

Waldron, Matthew. Personal Correspondence. Electrical Engineering. Rochester Institute of Technology.

Weibel ER. Morphometrics of the lung. Handbook of applied physiology. *Respiration.* 1964.

Weinstein, Steven Dr. Personal Correspondence. Mechanical Engineering, Rochester Institute of Technology.

Womersley, J.R. Method for the calculation of velocity, rate flow, and viscous drag in arteries when the pressure gradient is known. *Journal of Physiology*. 127:553–563, 1955.

Zeltner, T., Sweeney, T., Skornik, W., Feldman, H., Brian, J. Retention and clearance of 0.9um particles inhaled by hamsters during rest or exercise. *Journal of Applied Physiology*. 70:1137-1145,1995.

Appendix

Appendix A
Emphysema Report

1.0 Introduction:

Mechanical properties of a lung change significantly due to age and disease. The alteration of these properties can impair a person's ability to function normally. With diseases, such as emphysema, the tissue of the lung is damaged. This damaged tissue becomes worse with the severity of emphysema. Understanding how the lung tissue changes with the severity of emphysema is important in understanding the mechanical properties of the lung.

The lung consists of twenty three lung generations, figure 1. At each generation the airway bifurcates to form two more air ducts. Generations 17 – 23 consist of the respiratory zone, where the walls of the bronchioles contain substantially greater numbers of alveoli toward the distal end of the lung, ending in the alveolar sacs. The alveoli are important, for oxygen diffuses across the capillary walls and into the blood stream. When a person inhales and exhales the respiratory zone expands and contracts in order to draw the air into the lung.

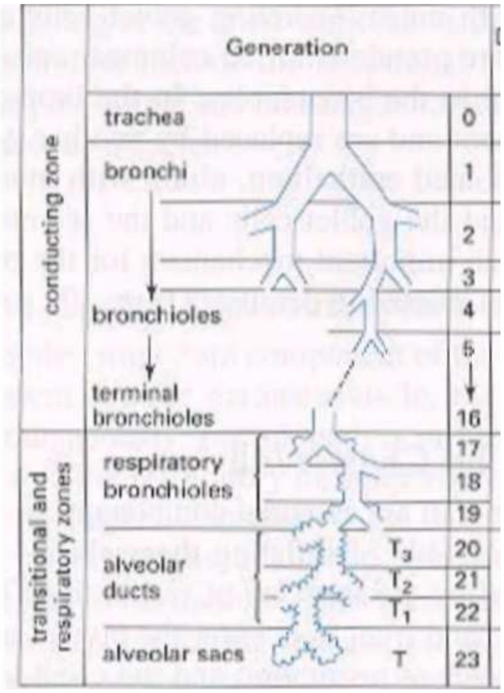

Figure 1: Airway Generation (Grippe, 1965)

1.1 Emphysema:

With Emphysema the elastic properties of the respiratory zone are damaged. The damaged tissue loses structure and therefore causes the individual alveoli to merge and expand. The new alveoli then have an increased volume, but decreased surface area in which oxygen can diffuse (Grippi, 1995). The elastic recoil is significantly changed, much like an overstretched rubber band; if an overstretched rubber band is released it will not return to its original shape, because of the damage created by overstretching. An emphysematous lung acts much like an overstretched rubber band, the tissue is damaged and overtime the damaged tissue loses its original elastic properties. The individual alveoli do not return to their original shape, and therefore remain in an expanded state. Figure 2 expresses the difference between a healthy (part "a") acinus and an acinus with emphysema (part "b"). It can be noticed from the picture that the alveoli have become expanded and merged.

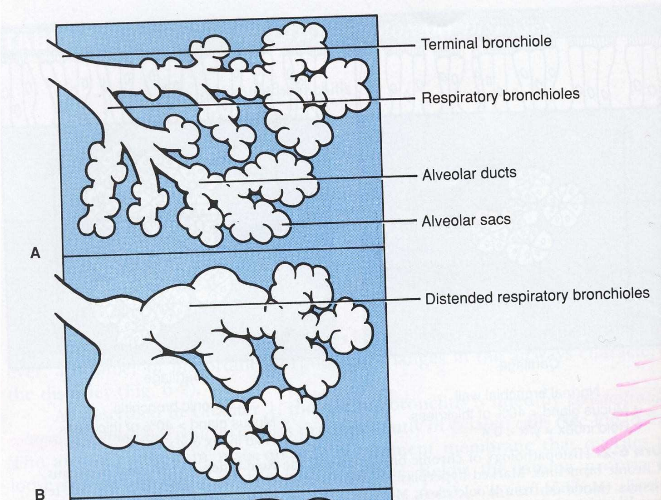

Figure 2: Grippi (1995)

Figure 3 is an example of an emphysematous section of a lung that has significant tissue damage. The section of the lung is open to atmosphere and therefore should be completely deflated. As it can be seen from figure 3, the alveoli on the left side of the sectioned lung do not look deflated, for their elastic properties have been damaged due to the tissue damage that occurs with emphysema, and therefore hold their original shape (Greaves and Colebatch (1980).

Figure 3: Emphysematous Lung (Greaves and Colebatch (1980))

1.2 Educational Significance:

Because of the damaged tissue the respiratory zone is unable to expand and contract, as it would in a normal lung, therefore changing the mechanical properties that drive the flow of air into the respiratory zone. The exact understanding on how the fluid acts in the respiratory zone, or acinus, is unknown and there is much research in trying to understand the exact fluid properties.

The research study that is being performed is a part of preliminary work that will compare fluid flow in a healthy alveolar sac to alveolar sacs with different degrees of emphysema. Two models, numerical and physical, will be created of the acinus region and fluid properties will be studied using computational dynamics and particle image velocimetry.

2.0 Body:

The elastic properties of the lung have been measured several different ways; by evaluation of the pressure-volume curve, static recoil pressure, and observation of elastic fibers in humans and animals.

2.1 Quantifying the Degree of Emphysema

The amount of emphysema present is quantified using many different techniques. In order to fully understand data that is obtained from articles, it must be understood how the amount of emphysema was quantified.

Thurlbeck et al. (1970) described three methods to quantify emphysema; Dunnill Point Count, Ryder Grid, and Picture Grading. With the Dunnill grading method the extent of involvement of emphysema is measured, not the severity of emphysema. With the Ryder

Grid method the severity of the emphysema is measured, not the spread or extent of involvement of the emphysema. Photographs of the lung are compared to standard photographs in the Picture Grading method. The Picture Grading method is like the Ryder Grid method, for it measures the severity of emphysema. What exactly is measured or observed is not given in Thurlbeck's work.

Lung density scans can measure the density of the lung and therefore quantify the extent of emphysema. The more emphysematous a lung is the lower the lung density, because of the enlarged airspaces. An EMI, electromagnetic imaging, number is assigned based on the lung density. The more negative the EMI number, the greater the emphysema (Gugger (1991)).

2.2 Pressure – Volume Analysis

There have been several studies that look at the pressure – volume relationship of the lung. Figure 4 expresses the pressure – volume relationship or a normal lung, where the lung is represented by the dotted line.

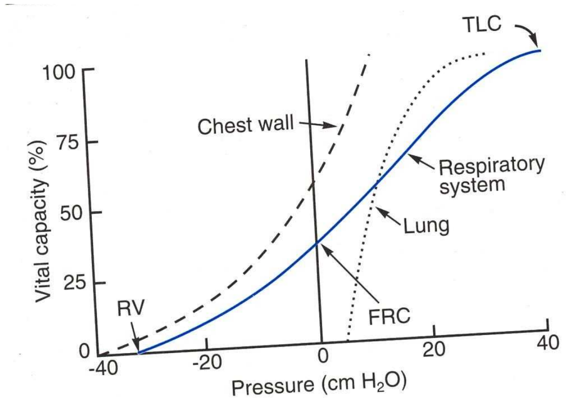

Figure 4: Pressure – Volume Curve (Grippe (1995))

Elastic properties of the lung can be determined by pressure – volume analysis, and the properties determined can be compared to the amount of emphysema present. The pressure and volume measurements can be obtained different ways, analyzed differently; and therefore produce different results. The different results may be due to whether the measurements were taken pre or post death, if the patient had other pulmonary diseases other than emphysema, and how the amount of emphysema was quantified.

Theoretically the pressure – volume curve should change with varying degrees of emphysema, because with emphysema there are air pockets and therefore the volume at the beginning of a breathing cycle, functional residual capacity, would increase with emphysema. In order for the lung to expand to the total lung capacity, it would take a different pressure because it would not need to increase in volume as much as a normal lung. Also, if the elastic properties of the alveolar walls are damaged then they would respond differently to pressure (Grippi (1995)).

The most common function to describe the pressure volume curve is expressed in equation 1, where V is the lung volume, P is the static recoil pressure, and several constants are defined; A, the volume asymptote, B, the volume at which the pressure is zero and K. The constant, K, describes the shape of the pressure volume curve independently of lung volume and is linearly related to the mean alveolar size (Greaves and Colebatch (1980)).

$$V = A - Be^{-KP}, \quad \text{Equation 1}$$

Table 1 summarizes the literature articles that studied pressure – volume relationships based on the exponential equation, equation 1. It can be noted that half the articles showed that the coefficient K is related to emphysema or the linear mean intercept, a diameter used to measure the airspace of alveolar sacs. The other half of the articles did not show a correlation with the K coefficient.

Table 1: Summary of articles that looked at pressure – volume and the exponential equation expressed in equation 1.

Article	**State of Lung for Pressure - Volume Measurements (Alive or Post Mortem)**	**How was Emphysema Measured?**	**Analysis of K (K or ln(K))**	**What was K compared to?**	**Correlation Coefficient of K and Emphysema**	**P - Value**
Petty et al. (1987)	Post Mortem	Picture Grading of Thurlbeck et al. (1970)	K	Amount of Emphysema, based on grade	None Given	Not Significant - exact number not given
Osborne et al. (1988)	Alive	Picture Grading of Thurlbeck et al. (1967)	K and ln (K)	Amount of Emphysema, based on grade	None Given	Not Significant - exact number not given
			K and ln (K)	Linear mean intercept	0.37 (For both K and ln (K)	K - Less than 0.01. ln(K) - Less than 0.005
Greaves and Colebatch (1980)	Post Mortem - 8 - 24 hours after death	Picture Grading of Thurlbeck et al. (1970)	K	Linear mean intercept	0.9	Was not given
Gugger et al. (1991)	Alive	Electromagnetic Imaging (EMI) Number	ln(K)	EMI Numbers	-0.6	0.001

Both Petty et al. (1987) and Osborne et al. (1988) determined that there was not a correlation between the K coefficient and the amount of emphysema. Also both researchers used the Picture Grading method to determine amount of emphysema present. Petty et al. (1987) inflated the lungs to 20 cm H_2O, where the volume of air that the lung contained was defined as the total lung capacity. Air was removed at increments of 2 cm H_2O, where the volume of the lung was measured at each increment. Eighteen healthy and twenty one lungs containing mild amounts of emphysema were used in the analysis. Because the lungs did not have much emphysema present it may be assumed that that is the reason why a correlation was not found for amount of emphysema and the K coefficient.

Osborne et al. (1988) contained a wider range of emphysematous lungs, fourteen healthy, seven mild, eleven moderate and ten containing severe emphysema. Osborne also measured the pressure and volume increments with live patients, which may create error because of the variance that occurs when doing any live test. The linear mean intercept was measured from lobes that were removed during surgery. The measurements were taken at areas that did not contain obvious areas of emphysema, which may the reason why there was not a correlation between the K coefficient and linear mean intercept, because the measurement of the linear mean intercept would not have been an accurate representation of emphysema. Figure 5 shows the graph generated by Osborne et al. (1988), and therefore noticed that there does not seem to be a relationship between K and emphysema score (increased emphysema score, an increase in severity of emphysema).

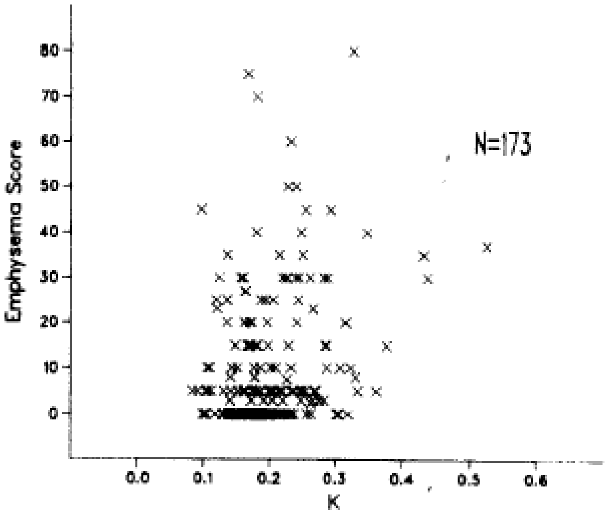

Figure 5: Osborne et al. (1988)

Contrastingly both Greaves and Colebatch (1980) and Gugger et al. (1991) determined that there is a correlation between amount of emphysema and the coefficient K. Gugger et al. (1991) used lung density scans to measure the EMI value and quantified the amount of emphysema based on the EMI value. Gugger measured pressure – volume from live patients, twelve healthy and twenty four with varying degrees of emphysema. Figure 6 expresses ln(K) as a function of EMI number, where it can be seen that there is a relationship between ln(K) and amount of emphysema present. Gugger argues that ln(K) should be used, instead of K, in order to obtain a relationship between emphysema and the constant, K. Also, using lung density scans, the amount of emphysema present can be more accurate, because the data obtained from CT scans is more quantitative.

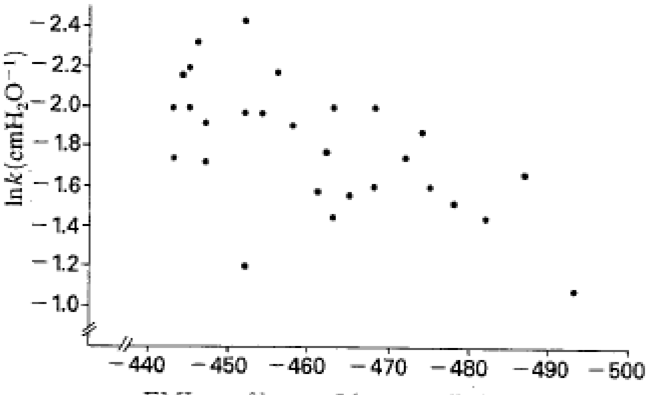

Figure 6: Gugger et al. (1991)

Greaves and Colebatch (1980) determined that K is related to emphysema in the study of 14 normal, 1 moderate, and 6 severe emphysematous excised lungs. The relationship between K coefficient and linear mean intercept is expressed in figure 7.

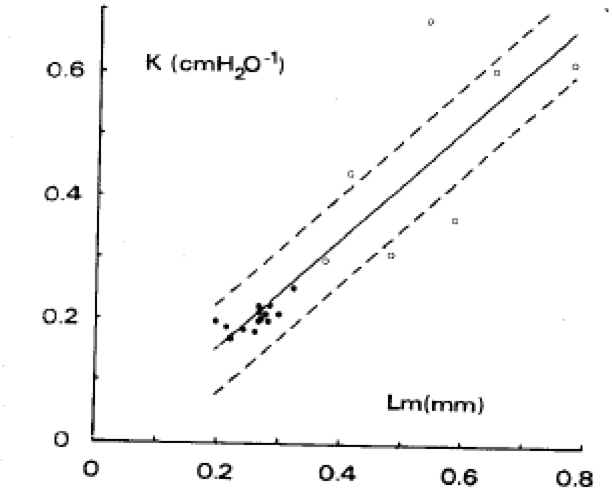

Figure 7: Greaves and Colebatch (1980)

Greaves and Colebatch (1980) determined a function to describe the constant K, where %E is the percent of emphysema present; equation 2. Therefore, theoretically, this equation could be used with any percent emphysema data generated using the Picture Grading technique that Thurlbeck et al. (1970) describes.

$$K(cmH_2O^{-1}) = 3.196*10^{-3}*\%E + 0.2531, \quad \text{Equation 2}$$

As described by Osborne et al. (1980), even though it is known that in emphysema there is an increase in alveolar size, linear mean intercept, and therefore the elastic tissue in the wall of the alveoli is affected, it was experimentally determined that in some cases a highly emphysematous lung would also have high values of K but in other cases the opposite was true, a high emphysematous lung would have low values of K. The reasoning behind this observation is that it is true that K will increase with an increase in airspace and therefore an increase in emphysema but if there is airway obstruction or airway closure due to the disease there will be a decrease in expired volume and therefore a decrease in K. Therefore the measurement of the shape of the pressure-volume curve cannot alone be a measurement of the degree of emphysema present in a lung.

Another study had been performed in order to look at the pressure – volume relationship. Niewoehner et al. (1975) measured the change of pressure as a function of volume in fifty most mortem lungs. Thirty eight of the lungs were healthy, nine with mild emphysema, and three with severe emphysema; each lung was measured within twenty four hours after death at room temperature. The degree of emphysema was determined by a point system that was derived in Nierwoehner et al. (1974). The lungs were inflated to a pressure of 15 – 20 cm H_2O, and the volume was recorded after a ten second time frame. The lungs were deflated at ten percent volume increments and the pressure was measured after a ten second wait. The exponential function that best described the pressure-volume curve is expressed in equation 3, where P is the pressure, α_1 is the lung size, α_2 describes the elasticity and V is the lung volume.

$$P = \alpha_1 e^{\alpha 2V} \quad , \text{ Equation 3}$$

It was found that the derived exponential function related correlated with the data, the correlation coefficient exceeded 0.995. The study showed that with emphysema the lung size, $\alpha_{1,}$ changed significantly when comparing emphysematous lungs to normal lungs. Contrastingly the elastic properties did not change significantly between the emphysematous and normal lungs.

2.3 Elastic Coefficient

Studies have been performed in order to describe the elastic behavior of emphysematous lungs macroscopically. Park et al (1970) evaluated 27 patients; their pulmonary function before death and the extent of the emphysema after death. The amount of Emphysema was determined by observing sections of each lung and assigning a grade between zero and four, based on observation. The lungs were categorized based on the percentage of maximum emphysema, grade 4. It was found that the extent of emphysema was closely related to the elasticity coefficient; which is shown in equation 4.

$$\text{Elastic Coefficient} = \frac{\text{Pressure of lung recoil at maximal inflation}}{\text{Total Lung Capacity / Predicted Total Lung Capacity}} \quad , \text{ Equation 4}$$

Figure 8 expresses the elastic coefficient based on the extent of emphysema present, where the correlation coefficient is -0.71. The relationship between the elastic coefficient and the amount of emphysema present is significant, for the p value is less than 0.001.

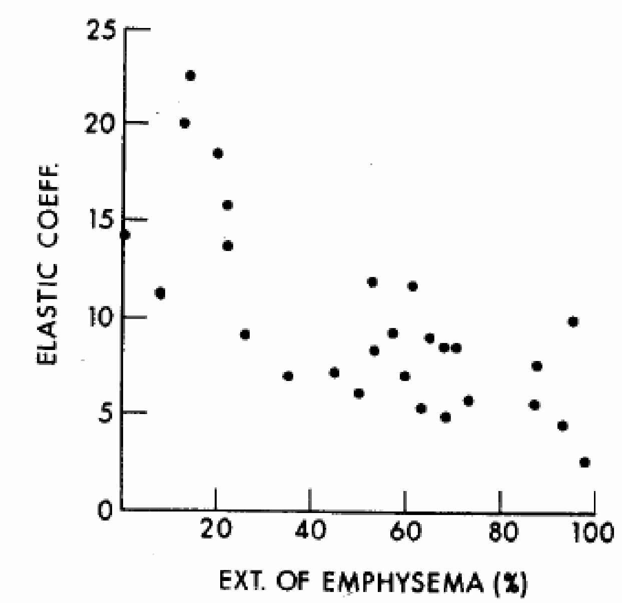

Figure 8 Park et al. (1970)

2.4 Elastic Recoil Pressure

Elastic Recoil Pressure of a lung is a measurable quantity that can describe the elastic properties of the lung. Predicted static recoil is determined from healthy lungs, and therefore the percentage of predicted recoil is a measurement of the recoil pressure measured from the diseased lungs compared to the healthy lung (Silvers (1980)). Figure 9 expresses the theoretical difference between a normal and emphysematous lung, and the relationship between percent total lung capacity and static recoil pressure.

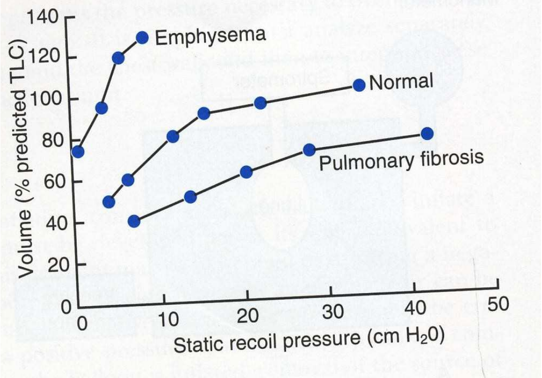

Figure 9: Healthy and Diseased Pressure – Volume Graph (Grippe (1995))

Table 2 expresses the literatures that have measured static recoil pressure and their determination of the correlation between the recoil pressure and other lung qualities that determine amount of emphysema.

Table 2: Summary of articles that measured static recoil pressure

Article	**State of lung for static recoil pressure measurement (Post Mortem or Alive)**	**How was Emphysema Measured?**	**Percent Predicted Static Recoil (Pst) or Static Recoil?**	**What was it compared to?**	**Correlation Coefficient**	**P - Value (Less than)**
Petty et al. (1987)	Post Mortem	Picture Grading of Thurlbeck et al. (1970)	Percent Predicted Static Recoil Pressure (Pst)	Mean bronchiolar internal diameter	0.517	0.001
Silvers et al. (1980)	Post Mortem- 48 hours after death	Picture Grading of Thurlbeck et al. (1970)	Percent Predicted Static Recoil Pressure (Pst)	Grade of Emphysema	-0.696	0.01
Osborne et al. (1988)	Alive	Picture Grading of Thurlbeck et al. (1967)	Maximum Static Elastic Recoil Pressure	Linear Mean Intercept	0.39	0.005
			Percent Predicted Static Recoil Pressure (Pst)		0.33	0.025
Gugger et al. (1991)	Alive	Electromagnetic Imaging (EMI) Number	Percent Predicted Static Recoil Pressure (Pst)	EMI	-0.65	0.001

From table 2 it can be determined that the correlation between static recoil pressure and emphysema are weak for most cases. Even though the correlation is weak, it is shown that there is significant difference between normal elastic recoil pressure and emphysematous elastic recoil pressure. Therefore it can be determined that elastic recoil pressure can not determine the extent of emphysema, but the elastic recoil pressure does change with emphysema.

Silvers et al (1980) proved that the elastic recoil pressure does change with emphysema. In the study that was performed, sixty five excised lungs were examined and graded based on the degree of emphysema present. The lungs were separated in three categories; twenty three normal lungs, twenty four lungs with emphysema score that is less than five, and eighteen lungs with an emphysema score greater than five. Even though the lungs were analyzed outside of a live person, the data was proven to be comparable to that found in live subjects. In order to account for a wide range of aged lungs, the static recoil pressure was corrected based on factors determined by pervious studies. It was determined that there is a negative correlation, -0.696 between the predicted static recoil pressure at ninety percent total lung capacity and degree of emphysema, figure 10. The correlation suggests that even though the static recoil pressure changes with emphysema, there is not a strong correlation between static recoil pressure and degree of emphysema.

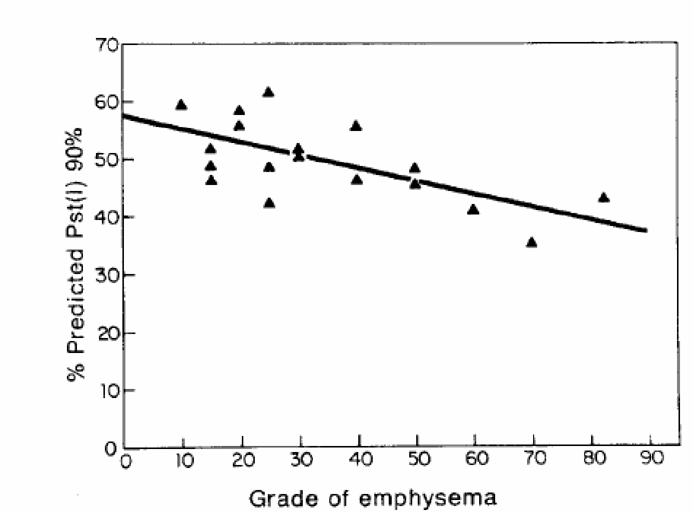

Figure 10: Relationship of Predicted Static Recoil Pressure Based on Grade of Emphysema (Silvers et al. (1980))

Petty et al. (1987) measured the elastic recoil pressure and analyzed a pressure-volume curve of eighteen normal and twenty one lungs containing mild emphysema.

The predicted static recoil pressure was determined by equations 5 -9, which corrects for age.

$$\begin{aligned} Pst_{50} &= (-0.048)age + 4.691 \\ Pst_{60} &= (-0.060)age + 6.341 \\ Pst_{70} &= (-0.070)age + 8.339 \quad \text{, Equations 5 - 9} \\ Pst_{80} &= (-0.074)age + 10.789 \\ Pst_{90} &= (-0.069)age + 13.980 \end{aligned}$$

The percent static recoil pressure was compared between the normal and emphysematous lungs for lung volumes of 50, 60, 70, 80 and 90 percent total lung capacity. It was determined there was a significant difference between predicted elastic recoil and the recoil in emphysematous lungs. Figure 11 expresses the percent predicted recoil pressure for a lung capacity of 70 percent. The static recoil is compared to mean internal diameter of the bronchiole, for this diameter changes with emphysema (Petty et al. (1987)).

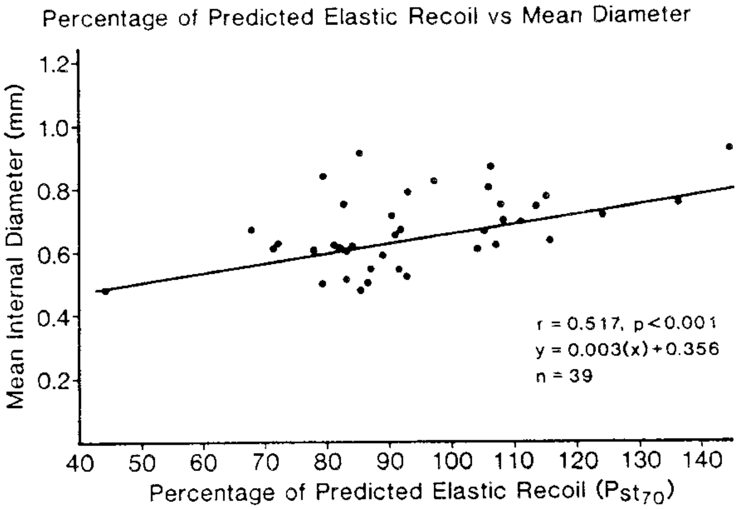

Figure 11: Petty et al. (1987)

2.5 Elastic Fibers

Tissue damage in the lung is due to an excess of proteolytic activity. The excess of proteolytic is caused by an increase in protease levels, decrease in antiprotease level, or a combination of both. The proteolyic destroys the collagen and elastin fibers in the lung, and therefore causes the reduced elastic properties. Also the tissue cannot hold its original shape and therefore deforms, which results in alveoli merging and the alveoli becoming larger (Grippe (1995)). Figure 12 is a graphical example of the balance that is needed between protease, and how a change in protease can result in emphysema.

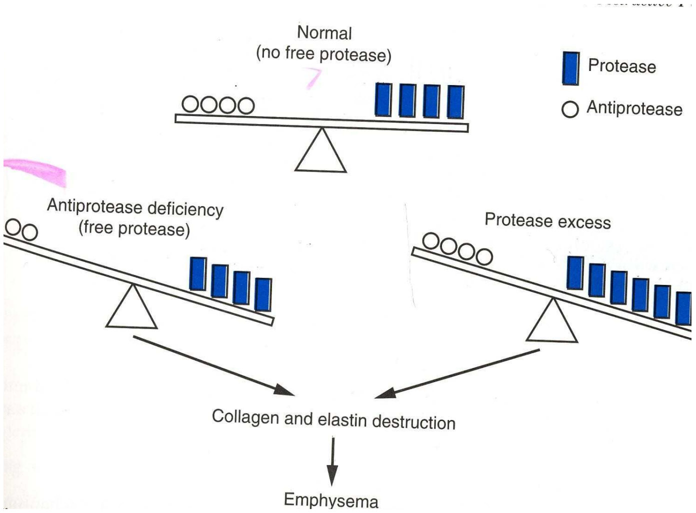

Figure 12: Representation of Protease levels (Grippe (1995)).

2.51 Human

Even though the elastin and collagen fibers are theoretically destroyed with emphysema, there is controversy in how the destruction changes the fibers. Two different researcher teams determined two different conclusions on how emphysema changes the physical properties, mainly the thickness and length, of the elastin fibers.

Fukuda et al. (1988) compared the elastic fibers of excised healthy and diseased human lungs. Three normal lungs and three centriacinar emphysema lungs were studied. The grade of emphysema was not mentioned, but only areas of obvious emphysematous lesions were used in the study. Sections of the lungs obtained were examined by use of an electron microscopy. The antielastin antibody, which was used in preparation of the lungs, reacts with the elastic fibers of the amorphous part of the tissue. The reaction allows for these fibers to be observed under the electron microscopy. It was found that the thickness of the alveoli's wall was much greater with those that had emphysema, due to the merging of alveoli that occurs with emphysema. Also, the elastic fibers were of various sizes in the normal lung, with elastic fibers rarely matching the thickness of the alveolar walls. In contrast, the emphysematous lung tissue contained much thicker elastic fibers, which may be a result of the merging of alveoli. Also the elastic fibers of the diseased lungs contained deposits of electron-dense granular materials. Figures 13 (normal) and 14 (emphysematous) show the difference between a healthy alveoli section and that that contains emphysema. It can be noted that the alveoli merged with the diseased cross section and there are collections of elastic fibers, represented by black circles, due to the reconstruction of the alveoli created by the merge.

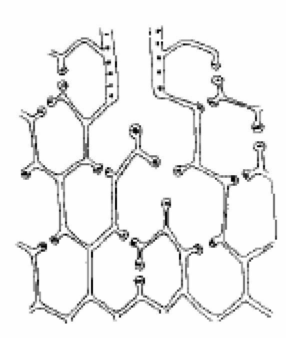

Figure 13: Normal Alveolar Section (Fukuda et al. (1988))

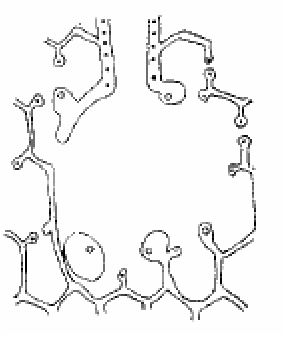

Figure 14: Emphysematous Alveolar Section (Fukuda et al. (1988))

Niewoehner and Kleinerman (1976) studied the length and diameter of elastic fibers in thirty three lungs, nine of which contained mild emphysema. The lungs were inflated to a pressure of 25cm H_2O, and sectioned based on their inflation volume. The elastic fibers were stained and examined using a microscope. It was determined that the diameter and the length of the elastic fibers of the emphysematous lungs did not change significantly from the average length and diameter of age relative, healthy lungs.

The reason why there may be a difference in the two findings may be a result of how severe the emphysema was in the lungs that were studied. The work of Fuduka et al. (1988) did not report the grade of emphysema, and therefore it may be assumed that lungs that were used were various range of emphysema. Niewoehner and Kleinerman (1976) did report the amount of emphysema, mild emphysema. Therefore the lungs that were used in the study have not have had enough damage to cause the change in shape of the elastin fibers. Also, with mild emphysema, alveoli may not have merged yet, and therefore the elastin fibers would not have changed.

2.52 Elastic Fibers – Animal

Mechanical properties of normal and emphysematous lungs can be compared using lung tissue obtained from laboratory rats. In order to induce emphysema like properties rats are given elastase. It has been proven that elastase induced rats will have the same tissue destruction that is seen with emphysema (Hautamaki et al. (2004)). Mechanical properties such as the stress – strain behavior, change in shape of the elastin and collagen fibers, and resistance and elastance of the wall tissue can be measured from the rat lungs.

Kononov et al. (2001) studied the stress – strain behavior of normal and elastase induced rats. Figure 15 represents the stress-strain behavior of both normal and emphysematous lungs, measured from the post mortem rat lungs.

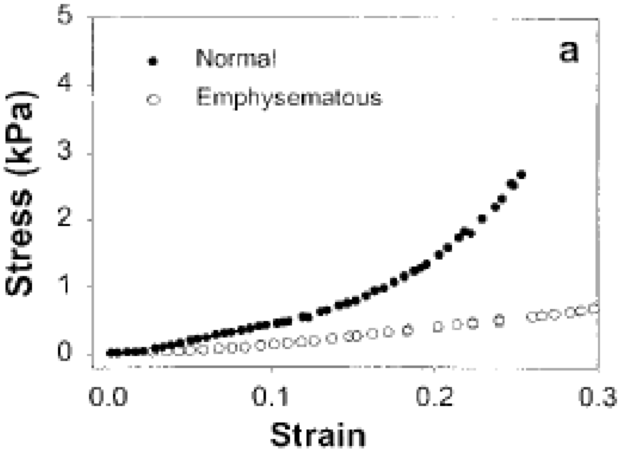

Figure 15: Kononov et al. (2001)

The actual elastin fiber and cells within the elastin change under loading. Figure 16 shows a magnified elastin fiber under loading. Parts “a” and “b” express a normal fiber under loading, where “a” experiences no strain, and “b” is elongated forty percent. It can be noticed that the shape of the cells within the elastin fibers are more oval shaped in the strained fiber. Parts “e” and ‘f” are an emphysematous elastin fiber, where “e” is experiencing no strain, and “b” is experiencing forty percent strain. It can be noted that not only are the cells larger in the emphysematous fiber, but the cells become much more oval shape under loading. Also the elasitin and collegen fibers thickened with the emphysematous lungs (Kononov et al. (2001).

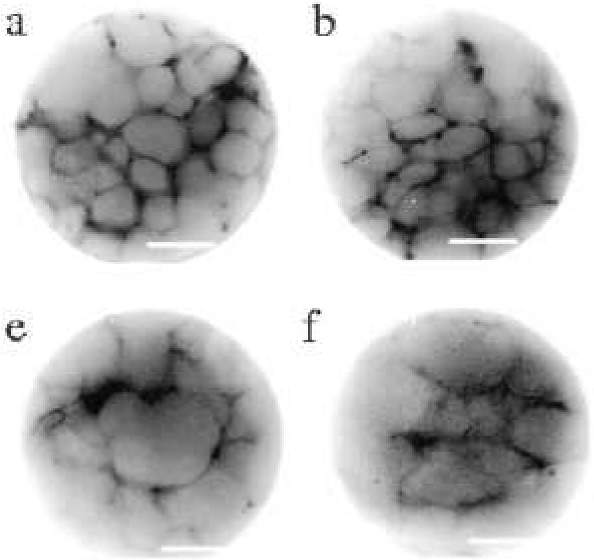

Figure 16: Kononov et al. (2001)

Kononov et al. (2001) hypothesized that because the cells of emphysematous tissue are damaged, it would be much easier to cause tissue destruction. The tissue destruction would lead to the reason as to why the tissue of emphysematous lung plastically deforms, which causes the alveoli to merge and create enlarged airspaces. Figure 17 shows how under loading of increased strain of 10 percent that the fibers merge. In part “a” the fibers are easy to distinguish, but in part “b”, after loading, they become merged. This would lead to plastic deformation.

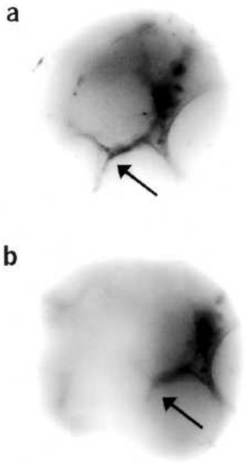

Figure 17: Kononov et al. (2001)

Brewer et al. (2003) studied normal and elastase-treated rats in order to look at the behavior of the elastin fibers under loading. Figure 18 shows the mechanical behavior of the normal and elastase-treated rat lung. The restistance in the emphysematous lung was greater than the normal lung. Also, the elastance, which is expressed in equation 10, decreased in the emphysematous lung.

$$Elas\tan ce = -2\pi f \quad \text{, Equation 10}$$

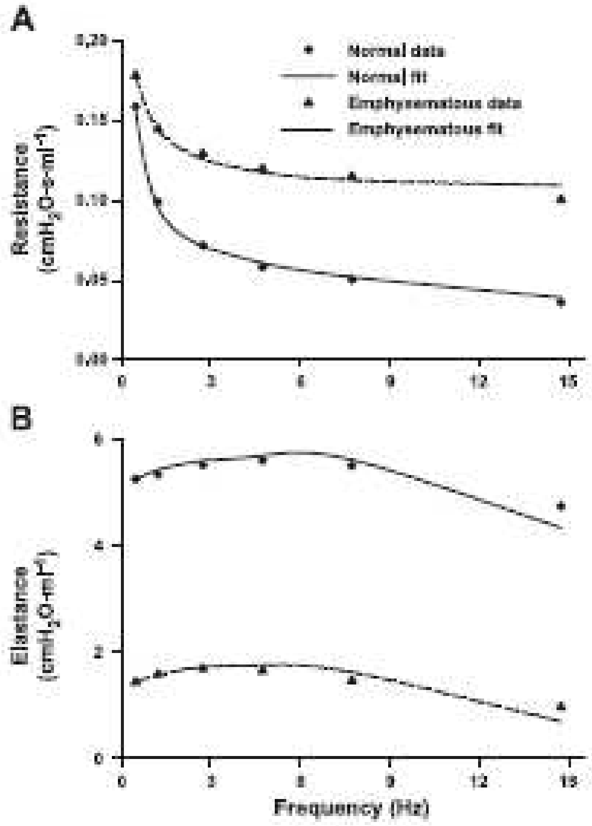

Figure 18: Mechanical Properties of Normal and Emphysema Rats (Brewer (2003))

Conclusion:

In order to fully understand the mechanical properties of the lung, many different types of research and tests have to be understood. Pressure – volume analysis, elastic recoil pressure, and examination of elastic fibers are different ways to look at elastic properties. Even though many of these techniques are repeatable, many different results can be obtained, because in most cases human lungs are used in the analysis. Each person is different and therefore even if standards are used in classification of severity of emphysema and in the test procedure, the results may vary from one study to another. Also, in many cases, a lung does not contain only emphysema, but other pulmonary diseases. These other pulmonary diseases may also alter mechanical properties and therefore the test results do not match the predicted results.

The understandings of the mechanical properties of the lung are significant, for complete understanding would lead to mechanical understanding of a diseased lung. There are sufficient models, numerical, analytical, and experimental, that look at fluid flow in healthy lungs, but models that look at fluid flow in emphysematous lung are non-existent. Therefore if tissue properties are well known, and therefore mechanical properties are known, emphysematous models can be developed.

References

Brewer KK, Sakai H, Alencar AM, Majumdar A, Arold SP, Lutchen KR, Ingenito EP and Suki B. Lung and alveolar wall elastic and hysteretic behavior in rats: effects of in vivo elastase treatment. *J.Appl.Physiol.* 95: 1926-1936, 2003.

Fukuda Y, Masuda Y, Ishizaki M, Masugi Y and Ferrans VJ. Morphogenesis of abnormal elastic fibers in lungs of patients with panacinar and centriacinar emphysema. *Hum.Pathol.* 20: 652-659, 1989.

Greaves IA and Colebatch HJ. Elastic behavior and structure of normal and emphysematous lungs post mortem. *Am.Rev.Respir.Dis.* 121: 1: 127-136, 1980.

Grippi . *Pulmonary Pathophysiology.* 1995.

Gugger M, Gould G, Sudlow MF, Wraith PK and MacNee W. Extent of pulmonary emphysema in man and its relation to the loss of elastic recoil. *Clin.Sci.* 80: 4: 353-358, 1991.

Hautamaki, R D Kobayashi, D K Senior, R M Shapiro,S D. Requirement for macrophage elastase for cigarette smoke-induced emphysema in mice. *Science.* 277: 2002, 1997.

Kononov, S Brewer, K Sakai, H Cavalcante, F S Sabayanagam, C R Ingenito, E P Suki,B. Roles of mechanical forces and collagen failure in the development of elastase-induced emphysema. 164: 1920, 2001.

Niewoehner, D E Kleinerman, J Liotta,L. Elastic behavior of postmortem human lungs: effects of aging and mild emphysema. *Jour. Appl. Physiologoy.* 39: 943, 1975.

Niewoehner, D E Kleinerman,J. Morphometric study of elastic fibers in normal and emphysematous human lungs. *Am.Rev.Respir.Dis.* 115: 15, 1977.

Osborne S, Hogg JC, Wright JL, Coppin C and Pare PD. Exponential analysis of the pressure-volume curve. Correlation with mean linear intercept and emphysema in human lungs. *Am.Rev.Respir.Dis.* 137: 5: 1083-1088, 1988.

Park SS, Janis M, Shim CS and Williams, Henry M. Jr. Relationship of Brochitis and Emphysema to Altered Pulmonary Function. *Am.Rev.Respir.Dis.* 102: 927, 1970.

Petty, T L Silvers, G W Stanford,R E. Mild emphysema is associated with reduced elastic recoil and increased lung size but not with air-flow limitation. *Am.Rev.Respir.Dis.* 136: 867, 1987.

Silvers G, Petty T and Stanford R. Elastic recoil changes in early emphysema. *Thorax.* 35: 7: 490-495, 1980.

Thurlbeck, W M Dunnill, M S Hartung, W Heard, B E Heppleston, A G Ryder,R C. A comparison of three methods of measuring emphysema. *Human Pathology.* 1: 215, 1970.

Appendix B
Matlab Program: Image Recognition and Definition

Developed by: Matthew Waldron (Electrical Engineering, Rochester Institute of Technology)

```
%function [ curve, crvRaw ] = gbmp_to_curve( file_name )
%image reading
clear
filename = input ('prompt \n','s')

pic=imread(filename);
crvRaw=zeros(1,size(pic,2));
for k=1:size(pic,2)
    for i=1:size(pic,1)
        if pic(i,k)<125
            crvRaw(k)=size(pic,1)-i;
            break;
        end
    end
end
%filtering and smoothing
curve(1)=crvRaw(size(crvRaw,2)-
1)+3*crvRaw(size(crvRaw,2))+7*crvRaw(1)+3*crvRaw(2)+crvRaw(3);
curve(2)=crvRaw(size(crvRaw,2))+3*crvRaw(1)+7*crvRaw(2)+3*crvRaw(3)+crvRaw
(4);
for k=3:(size(crvRaw,2)-2)
    curve(k)=crvRaw(k-2)+3*crvRaw(k-
1)+7*crvRaw(k)+3*crvRaw(k+1)+crvRaw(k+2);
end
curve(size(crvRaw,2)-1)=crvRaw(size(crvRaw,2)-3)+3*crvRaw(size(crvRaw,2)-
2)+7*crvRaw(size(crvRaw,2)-1)+3*crvRaw(size(crvRaw,2))+crvRaw(1);
curve(size(crvRaw,2))=crvRaw(size(crvRaw,2)-2)+3*crvRaw(size(crvRaw,2)-
1)+7*crvRaw(size(crvRaw,2))+3*crvRaw(1)+crvRaw(2);
%normalize
curve=curve/(max(curve)-min(curve))-min(curve)/(max(curve)-min(curve));

curve = curve'
```